

# OPTIMISATION OF OZONE GENERATION USING DIELECTRIC BARRIER DISCHARGE

---

A thesis presented in fulfilment of the requirement for  
the degree of

**Doctor of Philosophy**

**Yingjia Zhou, Msc**

2017

Department of Electronic and Electrical Engineering

University of Strathclyde

Glasgow, UK

The place of useful learning

The University of Strathclyde is a charitable body, registered in Scotland, number SC015263

**REF** UK TOP 20 RESEARCH-  
INTENSIVE UNIVERSITY

**THE** UK UNIVERSITY OF THE  
YEAR WINNER

**THE** UK ENTREPRENEURIAL  
UNIVERSITY OF THE  
YEAR WINNER

# Declaration of Authenticity and Author's Rights

‘This thesis is the result of the author’s original research. It has been composed by the author and has not been previously submitted for examination which has led to the award of a degree.’

‘The copyright of this thesis belongs to the author under the terms of the United Kingdom Copyright Acts as qualified by University of Strathclyde Regulation 3.50. Due acknowledgement must always be made of the use of any material contained in, or derived from, this thesis.’

Signed:

Date:

# Acknowledgements

I would firstly show my sincere respect to Dr. Tao Wang for his supervision, guidance and encouragement throughout the entire study of this research. Thanks for giving me this opportunity to do my favourite research. His stringent and careful attitude towards work inspire me a lot. Also, his spirit of perseverance and his strong enterprise affect me of commitment to excellence in my future life. Many thanks to Dr. Qing Chun Ren and the Strathclyde Faculty of Engineering for the financial support.

I would also like to show my respect to Professor Scott MacGregor for his encouragement and support. I would like to thank Dr. Mark P Wilson for his encouragement and help on my academic papers. Many thanks to Dr. Michelle MacLean for her help. Many thanks to Dr. Igor Timoshkin and Dr. Martin Given for their continuous help and advices in the research.

I would like to show my gratitude to my parents for their patience and thoughtful kindness when I suffer setbacks. Their encouragement makes me insist to carry on my research career. I would like to thank all the technicians in the mechanical workshop and electrical workshop of Electronic and Electrical Engineering Department and the storage room in TIC building: David Griffin, Sean Doak, Andy Carlin, Frank May, James Tollan, Peter Costello and Charles Doyle. Thanks to Mrs. Maureen Cooper for all her help in ordering experiment equipment and organising conference trips.

Thanks to all my colleagues in the HVT Research Group. I would like to show my especially gratitude to Dr. Guangming Huang for his patient advice and help in my research. Also I would like to thank my group mates Mr Linghe Zhou and Miss Yiyi Zhao for their selfless help in my research. Many thanks to all the students that I supervised to let me continually add my knowledge and experience to be a better researcher.

Finally, I would like to thank Professor Yi-Kang Pu for his deep guidance and his enlightenment in my research.

# Abstract

The aims of the research include understanding the fundamental kinetics of ozone generation using dielectric barrier discharge and investigating the potential to optimize the process to improve ozone generation efficiency.

The kinetics of ozone generation and its limitations are reviewed. The discharge characteristics of single filaments are investigated by analysing its equivalent circuit and the distribution of current magnitude. The parallel-plane electrode is used for the investigation of the relationship between current distribution, reduced electric field and ozone generation efficiency. The maximum ozone efficiency of the experiment is 207 g/kWh at the reduced electric field of 120 Td. With the increase of reduced electric field from 120 Td to 280 Td, the ozone generation efficiency drops to 109 g/kWh. The meshed electrode configuration was employed to optimize the ozone efficiency. The highest ozone efficiency achieved is over 330 g/kWh at  $\sim 100$  Td which is twice higher than the commercial ozone generator. It is found that the distribution of external current amplitude using meshed electrode is narrower compared to planar plates. To further understand ozone generation kinetics, the gas discharge is generated at cryogenic temperature of  $-183$  °C using liquid oxygen. The liquid ozone is produced and the highest ozone efficiency achieved is  $\sim 460$  g/kWh. The ozone dissociation reactions involving atomic oxygen and free electrons and the humidity effect at cryogenic temperature of  $-183$  °C were effectively limited.

# Contents

---

Abstract.....	III
1 Introduction .....	1
1.1 Motivation and research objectives.....	1
1.2 Overview of ozone generation.....	1
1.2.1 Properties of Ozone.....	1
1.2.2 Ozone applications.....	1
1.3 Ozone generation kinetics.....	5
1.3.1 Ozone generation reactions.....	5
1.3.2 Ozone generation limitations using electric discharges.....	7
1.3.3 Ozone efficiency obtained in laboratory.....	12
1.4 Thesis outline.....	13
2 Experimental Instruments and Setup.....	15
2.1 Introduction.....	15
2.2 Gas system design.....	15
2.3 Power supply.....	18
2.3.1 50 Hz power supply.....	18
2.3.2 5 kHz power supply.....	18
2.4 Electrical diagnostics.....	20
2.4.1 Voltage measurement.....	20
2.4.2 Current measurement.....	21
2.4.3 Data logging and processing.....	22
2.5 Optical diagnostics.....	23
2.5.1 Light emission intensity.....	23
2.5.2 Emission spectrum.....	24
2.6 Discharge energy measurement.....	26
2.7 Ozone measurement.....	29

2.7.1	Ozone measurement.....	29
2.7.2	Ozone concentration .....	30
2.7.3	Ozone generation calculation.....	31
3	Discharge Development of Dielectric Barrier Discharge .....	34
3.1	Introduction.....	34
3.2	Electrical properties of filamentary discharge .....	35
3.2.1	Experimental setup.....	35
3.2.2	Analysis of external current .....	37
3.2.3	Development of filamentary discharge .....	43
3.3	Single filament development .....	51
3.3.1	Equivalent circuit of single filament.....	51
3.3.2	Effect of the stray capacitance .....	53
3.4	Discharge behaviour in the first three cycles .....	57
3.4.1	Lissajous Figure analysis .....	57
3.4.2	Current and voltage waveform analysis.....	60
3.5	Electrical properties of APGD .....	62
3.5.1	Test cell design and experimental setup.....	62
3.5.2	Discharge characteristics.....	62
3.6	Conclusion .....	68
4	Current Distribution and Ozone Efficiency using Planar Electrodes .....	70
4.1	Introduction.....	70
4.1.1	Motivation.....	70
4.1.2	Objectives .....	71
4.2	Experimental setup.....	71
4.2.1	Test cell design.....	71
4.2.2	Experimental arrangement .....	72
4.3	Current amplitude distribution analysis .....	74
4.3.1	Applied voltage and current distribution analysis.....	75

4.3.2	Gas pressure with current distribution analysis .....	78
4.3.3	Barrier thickness and current distribution analysis .....	80
4.4	Ozone efficiency analysis .....	81
4.4.1	Ozone generation versus dew point .....	81
4.4.2	Ozone generation versus applied voltage.....	84
4.4.3	Ozone generation versus gap length .....	87
4.4.4	Ozone generation versus gas pressure.....	90
4.4.5	Ozone generation versus dielectric barrier thickness.....	92
4.4.6	Ozone efficiency versus reduced electric field .....	94
4.5	Conclusions.....	98
5	Current Amplitude Distribution and Ozone Efficiency using Meshed Electrodes .....	100
5.1	Introduction.....	100
5.2	Experimental setup.....	100
5.2.1	Test cell design.....	100
5.2.2	Experimental arrangement .....	101
5.3	Discharge characteristics.....	103
5.3.1	Current and voltage waveforms .....	103
5.3.2	Lissajous Figure analysis .....	104
5.4	Current and ozone efficiency analysis under different conditions.....	106
5.4.1	Discharges at different voltages .....	106
5.4.2	Discharges under different gas pressures .....	114
5.5	Ozone efficiency versus reduced electric field .....	120
5.6	Ozone generation and mesh aperture size .....	124
5.6.1	Ozone efficiency .....	124
5.6.2	Discharge characteristics analysis.....	127
5.7	A comparison of planar electrode and meshed electrode.....	128
5.7.1	Ozone efficiency versus reduced electric field .....	128
5.7.2	Current amplitude distribution analysis .....	130

5.8	Conclusion .....	132
6	Ozone Generation Technology below -80 °C.....	134
6.1	Introduction.....	134
6.1.1	Motivation.....	134
6.1.2	Objectives .....	134
6.1.3	Properties of liquid ozone and liquid oxygen .....	135
6.2	Experimental setup.....	135
6.2.1	Test cell design.....	135
6.2.2	Experimental setup.....	137
6.3	Ozone generation with 50 Hz power supply .....	139
6.3.1	Ozone generation in air .....	139
6.3.2	Current amplitude distribution using air .....	147
6.3.3	Ozone efficiency in oxygen .....	152
6.3.4	Current amplitude distribution in oxygen .....	159
6.4	Ozone generation with 5 kHz power supply .....	165
6.4.1	Ozone concentration analysis.....	165
6.4.2	Ozone efficiency analysis .....	167
6.5	Discussion.....	168
6.6	Conclusion .....	169
7	Conclusion and Future Work.....	171
7.1	Conclusion .....	171
7.2	Highlights of the results .....	176
7.3	Future work.....	176
8	Published Papers.....	178
8.1	Journal papers .....	178
8.2	Conference papers.....	178
9	Appendix .....	179
10	Reference .....	196

# 1 Introduction

## 1.1 Motivation and research objectives

The aim of this research is to optimize the ozone generation using oxygen-fed dielectric barrier discharge. To achieve this aim, there are following objectives:

- Analyse the kinetics of ozone generation process including ozone formation and dissociation.
- Investigate the limitations of ozone efficiency.
- Investigate electrical characteristics of DBDs including accurate measurement of external current, determination of single filament current and the charge transfer distribution of a single filament discharge.
- Investigate filament current distributions and their relationships to ozone efficiency using planar electrode and meshed electrode.
- Investigate ozone generation performance under low temperature.

## 1.2 Overview of ozone generation

### 1.2.1 Properties of Ozone

Ozone is a colourless gas with a molar mass of 48 g/mol [1], a density of  $\rho_{ozone} = 2.144 \text{ g/L}$  at standard temperature and pressure (STP,  $T=273\text{K}$  and  $P= 1 \text{ atm}$  pressure) and a boiling point of  $-112 \text{ }^\circ\text{C}$ . Liquid ozone is blue-violet colour and becomes a deep violet colour in the solid phase below  $-193 \text{ }^\circ\text{C}$ . Ozone is a bent molecule with a single bond and a double bond which is easy to lose an oxygen atom and converted back to oxygen. Consequently, ozone is a strong oxidant, of which the oxidation-reduction potential (ORP) is  $2.07 \text{ V}$ , which is higher than that of hydrogen peroxides ( $1.77 \text{ V}$ ) and chlorine ( $1.36 \text{ V}$ ). Ozone molecule is a polar molecule with a dipole moment of  $0.53 \text{ D}$  ( $1 \text{ D} = 10^{-18} \text{ statC}\cdot\text{cm}$ ) in the gas phase [2].

### 1.2.2 Ozone applications

Ozone is an environmentally- friendly oxidant that is widely used for industrial applications, such as the following listed purpose:

- Water treatment: water disinfection.

- Air purification: flue gas emission from industry (DeNO<sub>x</sub>).
- Pulp bleaching for chlorine-free production of paper.
- Micro pollutants decontamination.
- Inorganics by-products disinfection [3].
- Medical use: ozone therapy, surgery, dental care and manufacture of pharmaceuticals.

Nowadays, the increasing environmental problems (wastewater discharges, exhaust emissions) led to the increase of ozone applications. As a strong disinfectant, ozone has been widely used for disinfection, decolouration, and toxic compound degradation [4]. The past and current situations of ozone application of water treatment are discussed below.

The ability of ozone to disinfect polluted water was recognized in 1886 by de Meritens [5]. A few years later, the German firm Siemens and Halske, manufacturers of electrical equipment, contacted local Prussian officials who were willing to test ozone's application for the disinfection of drinking water. Accordingly, a pilot plant was constructed at Martinikenfelde, Germany. Froelich reported in 1891 that tests at this site showed ozone to be effective against bacteria [5]. Most ozone applications (since 1891 to 1950s) were for both disinfection and taste control. However, application of ozone for other purposes were investigated during the pre-World War I era. Treatment engineers reported observations of colour removal and iron and manganese oxidation following ozonation. In Britain, a few ozone plants had been installed prior to 1960 to treat high-quality groundwater in areas where it was considered inappropriate to "contaminate" such supplies by using marginal chlorination [6].

Based on current knowledge of ozone's reactions with synthetic organic chemicals (SOCs), it was proposed that ozone could be used to effectively control certain types of organic compounds [7]. For instance, Bisphenol A (BPA) decontamination is a very important application of ozone in recent years. BPA is an endocrine-disrupting compound (EDC), which can cause a significant harm to human health [8]. Ozone has been found to be highly effective for the removal of BPA [9].

According to the investigation of ozone generator installation in EA<sub>3</sub>G (European African Asian Australian Group) [10], during 1990-2004, the application of ozone for drinking water treatment was weighted 72.9% with an ozone capacity of 14,381 kg/h, the industrial wastewater was weighted 7.9% with an ozone capacity of 1124 kg/h, the municipal wastewater was weighted 1% with an ozone capacity of 751 kg/h, the application of industrial production was weighted 7.9% with an ozone capacity of 1697 kg/h [11]. Since 1990, the

growth rate of ozone generators has been about 6% and the mean capacity per installation increased from 20 kg/h to 32 kg/h [10].

In the U.S., the early applications of ozone were typically at small plants trying to solve site-specific problems [12]. Only recently has the U.S. water treatment industry fully accepted ozonation, opening the way to larger-scale applications [13].

In Western Europe, ozone facilities are located in different-size plants (from 10 m<sup>3</sup>/h to over 30,000 m<sup>3</sup>/h with the ozone production from 227.1 m<sup>3</sup>/d to over 720×10<sup>3</sup> m<sup>3</sup>/d) [14]. For instance, in France, as of 1990s, over 700 French water plants are equipped with operating ozone systems. The largest ozonation plants are located in the greater Paris area where 12 water plants with total ozone output capacity greater than 500 kg/h using air as the feed gas, which are able to treat a daily flow of 3,000,000 m<sup>3</sup> to serve more than 10 million people. Ozone remains the choice for drinking water disinfection in France with most major cities using this treatment [15]. In Switzerland, since the 1950s, ozone has been used in over 80 Swiss water plants to disinfect slightly contaminated groundwater and spring water and to oxidize the organics in heavily contaminated surface water. Since 1980, there has been a 25 % increase in the number of ozone installations [16]. About 40 % of the plants use ozone to treat surface water [17].

In Asia, the first large ozonation facilities were installed in Japan and Singapore during the 1970s [18]. During the following decade, Japanese water utilities using ozone, such as Chiba Prefecture (which operates the largest ozone plants in Japan- 38 kg/h), installed granular activated carbon (GAC) filters downstream of the ozonation step. Japan has more than 17,000 water treatment plants producing more than 16 billion m<sup>3</sup> of treated water [18]. Public water works which are designed to supply water to less than 50,000 residents constitute 97.5 % of the total water works in Japan, and of them 93.7 % are serving a population of less than 5,000. As of 2004, there was approximately 800 kg/h ozone capacity in operation for drinking water treatment in Japan [19]. 85% of the capacity was from domestically produced ozone generators. The most common use of ozone for drinking water treatment in Japan is odor reduction followed by trihalomethane (THM) removal [20]. Furthermore, for the industrial waste water treatment, the number of ozone plants increases from 3 in 1980s to 65 in 2010s [19] with the waste water treatment capacity of 3 million m<sup>3</sup>.

For future study, new regulations on disinfection and its by-products, which are emerging as a result of the 1986 Amendments to the Safe Drinking Water Act (PL 99-339), are expected

to further increase the water industry's interest in ozone technology. In Europe, the EEC regulations on drinking water quality also lead to an increasing interest in ozone use [10].

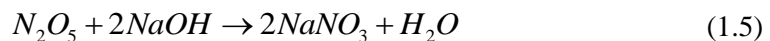
Ozone can also be applied to decompose  $NO_x$  (95 %  $NO$  and 5 %  $NO_2$ ) [21]. The two main methods being used for exhaust gas treatment are ozonation with wet scrubbing, and ozonation with selective catalytic reduction SCR. For both methods, the exhaust gas reacts with ozone first and then, the produced gas passes through the wet scrubbing solution or SCR bed.

For ozonation with wet scrubbing technology, ozone reacts with  $NO_x$  to convert  $NO_x$  to  $NO_3$  as shown in (1.1) and (1.2) [22] with high ozone concentration. The  $NO_3$  then reacts with  $NO_2$  to convert to  $N_2O_5$  as shown in (1.3) [23].

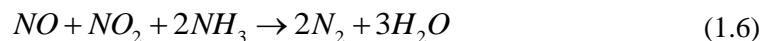


At present, there is one commercially-available de $NO_x$  technology, named LoTO $_x$ <sup>TM</sup> [24] which can reduce the concentration of  $NO_x$  between 52-163 °C. Later on, Cannon Technology Inc. cooperated with BOC gases to apply this technology to the small industrial boiler to degrade pollutants such as  $SO_2$ ,  $NO_x$ , Hg and CO.

Also, the ozonation can be applied with aqueous alkali. The produced nitrides then pass into alkaline solution (NaOH and ammonium hydroxide solution) for absorption. According to Zhang et. al [25] and Jakubiak et. al [26] research results, using ozonation method accompanied by absorption of NaOH solution, the De $NO_x$  efficiency reached 99%. The reaction of  $NO_x$  and NaOH can be written as (1.4)(1.5)



However, using ozonation technology accompanied by ammonium hydroxide absorption, the removal rates can only reach 84.33 %. The reaction of  $NO_x$  and  $NH_3$  can be written as:



Once  $NO$  has been converted to  $NO_2$ , the main reaction changes to (1.7):



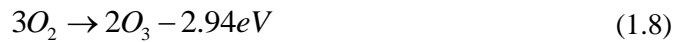
Ozone is a clean oxidant without creating secondary pollution and has a strong ability of synergistic removal of many pollutants. However, considering the financial cost, using ozone generation is more expensive than other alternative options. The high cost limits the application of ozone in environmental field. To optimise its generation efficiency and increase ozone concentration become crucial.

### 1.3 Ozone generation kinetics

In industry, the most commonly used method of ozone generation is dielectric barrier discharge which was first developed by Siemens in 1857 [27]. A dielectric barrier discharge is a non-thermal plasma discharge with two metallic electrodes separated by one or two dielectric barriers [28]. The dielectric barrier across two electrodes can efficiently limit the charge transfer in a discharge into the electrodes and the charges are distributed over the dielectric barrier surface to build the reversed electric field to extinguish the discharge. The ozone generator uses high voltage power supply of a few kilovolts and under 5 kHz to generate filamentary discharges in pure oxygen or air.

#### 1.3.1 Ozone generation reactions

Theoretically, two ozone molecules are produced by three oxygen molecules with an efficiency of 1220 g/kWh [29] as expressed in (1.8)



1.47 eV is needed to produce one ozone molecule.

While, the detailed process is a two-step procedure (1.9)(1.10),



The 2.2 eV in (1.10) is transferred to kinetic energy before finally being released as heat. Compared with the theoretical value, the ozone generation efficiency according to (1.9) to (1.10) is only 698 g/kWh, 2.57 eV is needed for production of an ozone molecule.

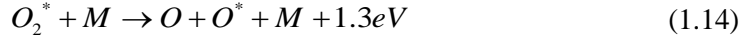
For oxygen-fed ozone generation, the reactions between oxygen species and electrons can initiate 76 major reactions [30].

Oxygen molecules react with electrons at 6.0 eV as shown in (1.11)(1.12),

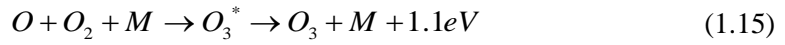


where  $M$  is the third body and is an oxygen molecule here.

Oxygen molecules react with electrons at  $8.4eV$  as shown in (1.13)(1.14),



Ozone formation progresses as shown in (1.15)(1.16),



$$k_1 = 6.0 \times 10^{-34} \left( \frac{T}{300} \right)^{-2.8} [O_2] (cm^6 s^{-1}) \quad (1.16)$$

Where  $k_i$  is the reaction rate coefficient, which is the integration of the collision cross section into the velocity distribution. The loss of  $O$ ,  $O_2$  and  $M$  is shown in (1.17),

$$\frac{dN(O)}{dt} = \frac{dN(O_2)}{dt} = \frac{dN(M)}{dt} = k_1 N(O) N(O_2) N(M) \quad (1.17)$$

The rate coefficient  $k_i$  is the function of energy distribution that is not related to the density of the particle as shown in (1.18),

$$k_i = A e^{\frac{-E_a}{RT}} \quad (1.18)$$

where  $E_a$  is the activation energy,  $R$  is the gas constant which is  $8.31 Jmol^{-1} K^{-1}$  and  $A$  is the pre-exponential factor and  $T$  is the temperature in  $K$ . In (1.16), the reaction rate coefficient is related to the temperature and the concentration of oxygen molecules.

Ozone is formed by the combination of atomic oxygen and molecular oxygen via a three-step process. First, the excitation of oxygen molecules takes place. In the presence of an applied electric field, the seed electrons existing in the gas due to natural radiation can initiate electron avalanches. The produced electrons collide with ground state oxygen molecules to excited  $O_2(A^3\Sigma_u^+)$  absorbing  $6.0 eV$  according to (1.11), and to excited  $O_2(B^3\Sigma_u^-)$  with  $8.4 eV$  according to (1.13).

Next, the excited state oxygen molecule collides with a third body to dissociate it into two oxygen atoms. With excitation energy of 6.0 eV, an oxygen molecule is dissociated into two ground states of oxygen atoms, as shown in (1.12). With excitation energy of 8.4 eV, an oxygen molecule is dissociated into one ground state oxygen atom  $O(^3P)$  and an excited state oxygen atom  $O(^1D)$  carrying 1.97 eV as shown in (1.14).

Finally, a three-body reaction occurs, in which the produced oxygen atoms react with oxygen molecules and a third body  $M$  to produce vibrationally excited ozone molecules. These ozone molecules are quenched into ground state ozone molecules as shown in (1.15) within a microsecond [31]. The rate coefficient of (1.15) is shown in (1.16).

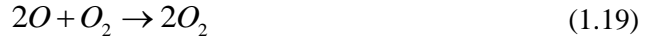
Comparing the electron energy efficiency with theoretical value shown in (1.8), without considering other losses, the maximum electron energy efficiency for 6.0 eV reaction is 598 g/kWh and the maximum electron energy efficiency for 8.4 eV reaction is only 427 g/kWh.

### 1.3.2 Ozone generation limitations using electric discharges

At present, the typical commercial efficiency of ozone generators is 90 g/kWh using dry air and 180 g/kWh using oxygen [32]. The losses consist of the ozone dissociation by electron collision, ozone decomposition with atomic oxygen and ion losses.

#### A. Ozone decomposition with atomic oxygen

Some unstoppable reactions that occur at the same time are shown below [33].



$$k_2 = 1.3 \times 10^{-32} \left(\frac{300}{T}\right) e^{-\frac{170}{T}} (cm^6 s^{-1}) \quad (1.20)$$



$$k_3 = 2.0 \times 10^{-11} e^{-\frac{2300}{T}} (cm^3 s^{-1}) \quad (1.22)$$



$$k_4 = 1.2 \times 10^{-10} (cm^3 s^{-1}) \quad (1.24)$$

Two oxygen atoms combine to form an oxygen molecule as shown in (1.19); thus, the energy used for the production of atomic oxygen is wasted though the probability of this reaction occurring is very low due to the low concentration of oxygen atoms ( $10^{15}$  to  $10^{14}$ ). Also, an

oxygen atom reacts with an ozone molecule to dissociate it into two oxygen molecules as shown in (1.21) and (1.23).

### B. Electron collisions with ozone molecules

The average electron energy in a filamentary DBD is between 1 eV and 10 eV [34]. The majority of low energy electrons collide with ozone molecules and dissociate ozone molecules into oxygen molecules and oxygen atoms. The corresponding reactions (1.25) to (1.27) are shown below [35][36][37]:



With the increment of electron energy, the produced species by electron collision with ozone molecules are different. With 1.1 eV, electrons collide with ozone molecules to dissociate ozone molecules to oxygen molecules and oxygen atoms. With continuous increasing the electron energy up to 3.07 eV, the extra energy can excite oxygen molecules to different excited states. Once the electron energy is above 3.07 eV, oxygen atoms can be generated to excited states. With further increase of the electron energy to above 5.17 eV, the ozone molecules are dissociated into three oxygen atoms [38].

### C. Ion losses

The maximum ozone efficiency achieved by the calculation is shown in Figure 1.1 [2]. Considering reaction losses and without ion losses, the maximum ozone efficiency is ~ 410 g/kWh with the total energy being carried by electrons. However, the electrons across the gap are produced by the ionization process. In the meantime, the produced ions move to the opposite polarity electrode under the electric field. If only 55% of the total energy is carried by electrons [2], the maximum ozone efficiency calculated is only ~ 230 g/kWh.

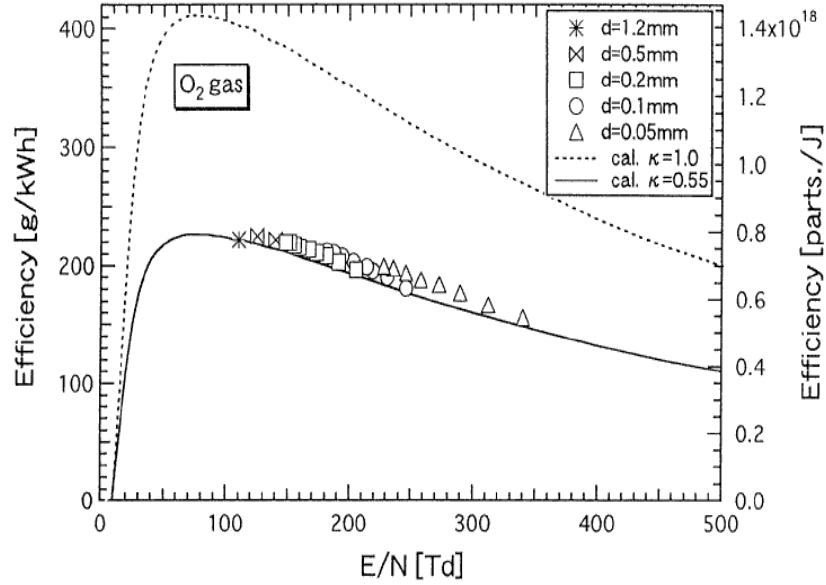


Figure 1.1 Ozone efficiency as a function of E/N [2].

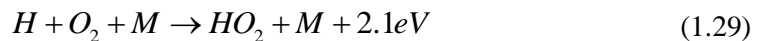
The maximum experimental result achieved is  $\sim 220$  g/kWh at  $\sim 110$  Td and decreases gradually with the increase of the reduced electric field from 110 Td. The experimental results (symbols) in Figure 1.1 have a strong agreement with the calculated results (solid line) [2].

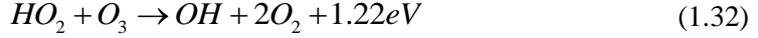
Comparing the electron energy efficiency with the theoretical value, according to the experimental results, one ozone molecule needs  $8.15$  eV to form, which decreases the ozone efficiency to 18% of the theoretical value.

#### D. Water vapour effect

According to Rideal's research, ozone efficiency can increase by 50% by using dry air rather than air with a dew point of  $5.5$  °C [39]. Humidity has a negative effect on ozone generation due to the change of micro-discharge characteristics and the catalytic reactions dissociating ozone.

As water vapour can react with electrons to produce  $H$  and  $OH$  species [3] as shown in (1.28), hydrogen atoms react with oxygen molecules further to produce  $HO_2$  as shown in (1.29) which react further with ozone molecules, as shown in (1.30) to (1.32), to decrease the ozone concentration.





Decreasing the dew point of the feed gas can increase ozone efficiency. In addition, the experimental results of Sease [40] show that ozone efficiency was 50% greater at a dew point of  $-80^\circ\text{C}$  than that obtained at  $-5^\circ\text{C}$ , which is due to the fact that the reactions between electrons and water vapour and the reactions between ozone molecules and OH, HO<sub>2</sub> can increase the ozone dissociation processes. Also, the water vapour can increase the surface conductivity of the dielectric leading to the higher amplitude of discharge current. The microdischarges with longer discharge time and higher current can produce a concentration ratio of atomic oxygen and oxygen molecules that is higher than  $10^{-4}$  which leads to a decrease in ozone generation efficiency. In the commercial ozone generator, the dew point is required to be lower than  $-60^\circ\text{C}$ .

### E. Temperature effect

It is known that the reaction rate coefficient in the plasma-chemical reaction depends upon temperature. Overall, the ozone formation and dissociation reactions can be simplified as shown in (1.33) to (1.36):



$$k_f = 6.9 \times 10^{-34} \left(\frac{300}{T}\right)^{1.25} (\text{cm}^6 \text{s}^{-1}) \quad (1.34)$$



$$k_d = 2.0 \times 10^{-11} \exp\left(\frac{-2300}{T}\right) (\text{cm}^3 \text{s}^{-1}) \quad (1.36)$$

For a reaction shown as (1.37):



The reaction rate  $r$  is formed as follows (1.38):

$$r = k(T)[A]^M [B]^N \quad (1.38)$$

where  $M$  and  $N$  are the partial orders of the reaction.

To increase the gas temperature from 300 K to 350 K,

$$\frac{r_{f_1}}{r_{f_2}} = \frac{6.9 \times 10^{-34} N(O)N(O_2)N(O_2)}{6.9 \times 10^{-34} \times \left(\frac{300}{350}\right)^{1.25} N(O)N(O_2)N(O_2)} = 1.2 \quad (1.39)$$

$$\frac{r_{d_1}}{r_{d_2}} = \frac{2.0 \times 10^{-11} \times \exp\left(-\frac{2300}{300}\right) N(O)N(O_2)N(O_2)}{2.0 \times 10^{-11} \times \exp\left(-\frac{2300}{350}\right) N(O)N(O_2)N(O_2)} = 0.33 \quad (1.40)$$

The ozone decomposition rate increases by three times while the ozone generation rate decreases by 17.5%, which indicates that it is important to control the temperature in the test cell.

Figure 1.2 shows the effect of the gas temperature on ozone efficiency at different concentrations of atomic oxygen. The ozone production decreases at the same temperature when increasing the ratio of  $[O]/[O_2]$ , represented by  $x_{10}$ . If the ratio of  $[O]/[O_2]$  is higher than  $10^{-4}$ , then ozone production in the gas phase decreases rapidly [4] when the temperature is increased from 161 K. With an increase of the temperature to 600 K, the ozone concentration also decreases at the ratio of  $10^{-4}$ .

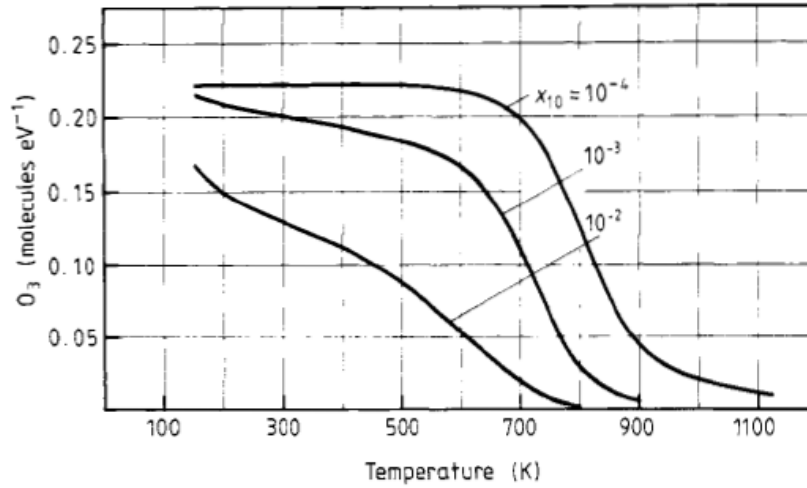


Figure 1.2 The effect of the gas temperature on the efficiency of ozone generation [4].

The research has been undertaken to demonstrate that a cooling system is required to keep the gas temperature low [41][42][43]. Here, the average temperature increase is  $\Delta T_g$ , which is determined by the power input to the test cell, and the heat removed via the cooled electrode and kept at the coolant temperature [43].

$$\Delta T_g = \frac{1}{3} \frac{d}{K} \frac{P}{F} (1 - \eta) \quad (1.41)$$

Where  $d$  is the gap length,  $k$  is the heat conductivity of the feed gas,  $P/F$  is the power density ( $P$  is the input power,  $F$  is the electrode surface area) and  $\eta$  is ozone efficiency. The average gas temperature in the gap is shown in (1.42).

$$T_g = T_w + \Delta T_g \quad (1.42)$$

From (1.42), it can be seen that a smaller discharge gap can decrease the average temperature in the gap. In addition, based on numerical modelling [43], it has been shown that the gas temperature increases with an increase of the discharge gap length. The gas temperature of the gas in the discharge channel can reach tens of degrees higher than the ambient gas temperature. According to Jodzis's research [42], faster gas flow is beneficial for heat exchange in the ozone generator.

### 1.3.3 Ozone efficiency obtained in laboratory

In attempts to increase ozone efficiency, pulsed power supply with nanosecond regime duration was used for ozone generation to avoid ion loss. The optimum ozone efficiency could reach 544 g/kWh when oxygen-fed, and 239 g/kWh when air-fed. With pulse duration of the order of nanoseconds, ion movement is effectively restricted, reducing the energy loss [44]. Moreover, the optimized ozone efficiency of 400-600 g/kWh was achieved at cryogenic temperature [45][46]. The electron collision with ozone, temperature effect and humidity effect under cryogenic temperature were limited. Besides electrical discharge method, the photochemistry of  $O_3$  generation by vacuum ultra violet has been characterised. Using a 172 nm xenon excimer lamp, photons with an energy of 7.22 eV are generated. These photons can dissociate oxygen effectively but have low cross-section with ozone molecule. The corresponding reaction efficiency could reach 497 g/kWh [47]. However, the exorbitant price, low ozone concentration and short lifetime of the excimer lamp restrict its application in industry.

Both energy efficiency and ozone concentration are important for ozone generation as lower concentration will lead to oxygen loss while lower energy efficiency will consume more electricity. In addition, the power supply needs to be scaled up to tens or hundreds of kilowatts for industrial application. To achieve high energy efficiency and high ozone concentration at the same time, it is necessary to investigate the micro-discharge behaviours and their relationships to the ozone generation process.

## 1.4 Thesis outline

This thesis is divided into eight chapters and the contents of each chapter are listed below:

In **Chapter 2**, the essential experimental setup and methods are introduced.

**Chapter 3** is the fundamental study of filament development. The accurate external current measurement is developed. The discharge characteristics of two types of DBD, atmospheric pressure glow discharge and filamentary discharge, are investigated. The more detailed analysis of single filamentary discharge is investigated. A detailed equivalent circuit for single filament discharge is developed to understand the relationship between external current and filament current. Finally, the discharge behaviors in the first few cycles following power-on are investigated for better understanding of the establishment of a filamentary discharge.

**Chapter 4** discusses the distribution of external current amplitude and ozone generation under different generator parameters. Firstly, the relationship of current distribution with applied voltage, gas pressure and barrier thickness is investigated. Secondly the ozone generation efficiency is investigated for its relationship with applied voltage, gap length, gas pressure and barrier thickness. Finally, the relationship between ozone efficiency and the reduced electric field is investigated.

**Chapter 5** details the ozone generation using meshed electrodes. The mechanism of discharge using meshed electrodes is discussed, including the discharge mode and filament current characteristics. The investigation is undertaken to find the relationship between ozone efficiency and current distribution by changing mesh aperture, applied voltage and gas pressure. At the end of the chapter, a comparison of ozone generation efficiency versus reduced electric field under meshed electrode and planar electrode is made. A discussion is made to demonstrate the advantages of using meshed electrode for ozone generation.

In **Chapter 6**, the advanced ozone generation technology under low temperature is investigated. The experiment is carried out at 50 Hz and 5 kHz respectively. The current distribution and ozone efficiency in air and oxygen are investigated respectively. With air fed, the current distribution at low temperature of -80 °C to -183 °C and the corresponding ozone efficiency are investigated at 50 Hz. When oxygen-fed, the liquid ozone is produced at cryogenic temperature of -183 °C. The calculation of ozone concentration and efficiency are introduced. Also, current distribution at different operating zone is investigated.

**Chapter 7** summarises the results achieved in the research and concludes the potential methods to optimize ozone generation. At the end of the chapter, the future work is recommended for improved ozone generation.

## 2 Experimental Instruments and Setup

### 2.1 Introduction

In this chapter, the experimental setup and equipment, gas supply system and power supplies are described. The electrical diagnostics, such as the measurement of voltage, current and discharge energy are introduced; the optical diagnostics were used to determine the light emission intensity and spectrum; the ozone measurement and ozone efficiency analysis are described.

### 2.2 Gas system design

#### A. Feed gas property

Table 2.1 shows the properties of the oxygen cylinder [48].

Table 2.1 The specification of feed gas.

Supplier	Type of Gas	Purity	Dew Point
BOC	Compressed Oxygen	99.5%	-40 °C

#### B. Gas supply system

The gas path schematic is shown in Figure 2.1. All tubes and tube connectors on this board are made from stainless steel 316 to prevent ozone corrosion. The stainless-steel tube size is ¼ inch. The gas flow rate is controlled by the needle valve and measured by a gas flow meter; the gas pressure and humidity are measured by the pressure gauge and dew- point hygrometer individually. The test cell gas outlet is connected to the ozone monitor for ozone concentration measurement, and the ozone off-gas is destroyed by an ozone destructor before discharge to the atmosphere.

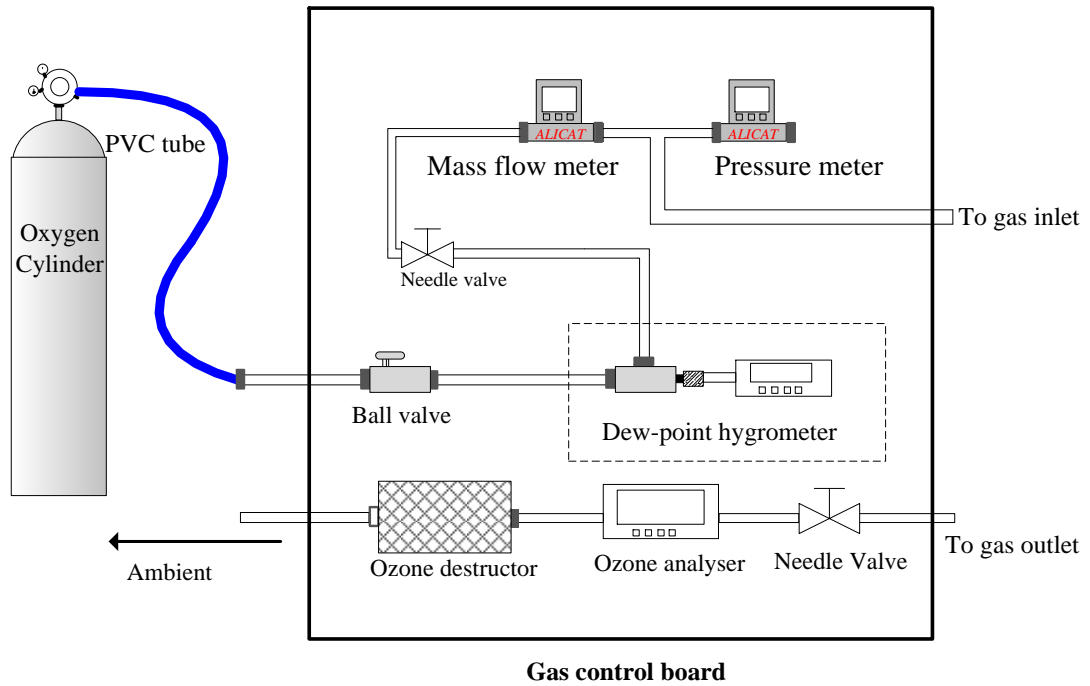


Figure 2.1 The configuration of the gas control board.

Instrument specifications:

1) Gas flow meter:

The mass flow meter is the Alicat Scientific Mass Flow Meter Model M-10 SLPM-D. Table 2.2 shows the general specifications of the mass flow meter.

Table 2.2 The specifications of the gas flow meter [49].

Full Scale	Operating Range	Accuracy	Repeatability	Operating Temperature
10 SLPM	0.5% to 100% Full Scale	$\pm(0.8\%$ of Full Scale Reading + 0.2% of Full Scale)	$\pm 0.2\%$ Full Scale	-10 to +60 °C

2) Pressure Meter:

The pressure meter is the Alicat Scientific Pressure Meter Model P- 2Bar- D. Table 2.3 shows the general specifications of the pressure gauge.

Table 2.3 The specifications of the pressure meter [50].

<b>Full Scale</b>	<b>Operating Range</b>	<b>Accuracy</b>	<b>Repeatability</b>	<b>Operating Temperature</b>
2 Bar (absolute)	0.5% to 100%	$\pm 0.25\%$	$\pm 0.08\%$	-10 to +60 °C
	Full Scale		Full Scale	

### 3) Hygrometer:

A hygrometer is an instrument that is used to measure the moisture content of the atmosphere. In this experiment, an Easidew [51] on-line hygrometer from Mitchell Instruments is connected next to the ball valve. It is a capacitance-type dew point measurement system with a capacitive sensor. The transmitter relays the current loop signal (4 – 20 mA) to the monitor. Table 2.4 shows the specifications of the hygrometer:

Table 2.4 The specifications of the hygrometer.

Measurement range	-100 to +20° C dew point
Accuracy(dp)	$\pm 2^\circ$ C dew point
Repeatability	0.5 ° C dew point
Operating humidity	0-100 % RH
Operating temperature	-40 to +60° C (Sensor); 0 to 50° C (Monitor)
Flow rate	1 to 5 <i>NL/min</i> <sup>[1]</sup> mounted in standard sampling block

<sup>1</sup> NL/min stands for normal litres per minute.

## 2.3 Power supply

In this section, the 50 Hz and 5 kHz power supplies used in the research are described.

### 2.3.1 50 Hz power supply

The 50 Hz AC power supply has been used to determine the ozone efficiency in a low-temperature experiment. Figure 2.2 shows the components of a 50 Hz high-voltage AC power supply. The 230 V 50 Hz AC power source is connected via an auto-transformer that can adjust the voltage output from 0 to 230 V. Following the auto-transformer, a high-voltage transformer is connected in the circuit; the ratio of the high-voltage transformer is 1:50 with the output voltage stepped up to 12 kV. After the high voltage transformer, a current-limiting resistor of 600 k $\Omega$  is connected in series to limit the charging current, as shown in Figure 2.2.

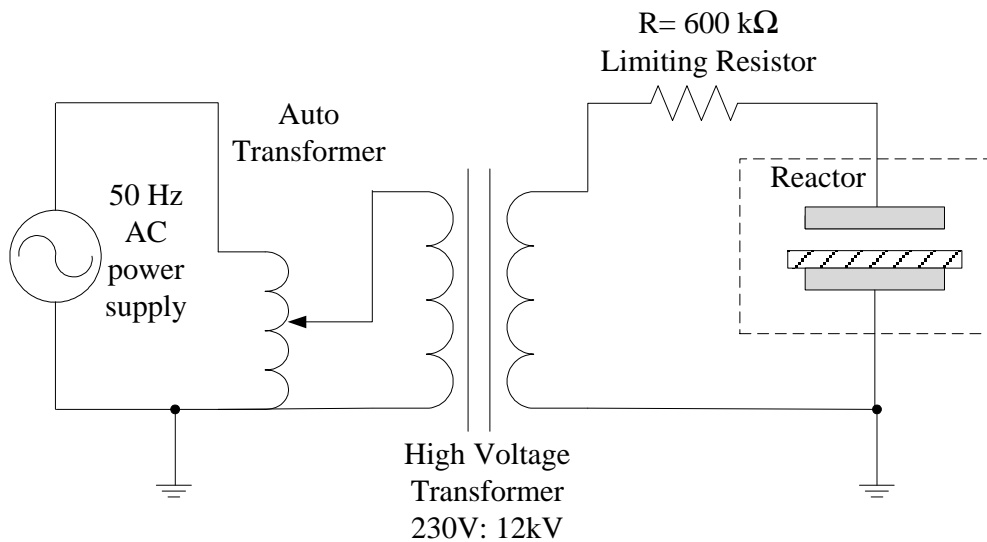


Figure 2.2 The schematic of the 50 Hz power supply.

### 2.3.2 5 kHz power supply

A smart high-frequency power supply was used to adjust the voltage output at the desired frequency and number of cycles. The steady state and transient ozone generation were investigated using the 5 kHz AC power supply.

The model of the smart linear AC power source is 112AMX from Pacific Power instrument [52], a high-performance linear AC power source. It can operate using either 1 phase (0 to 150 V<sub>L-N</sub>) or 2 phases (0 – 300 V<sub>L-L</sub>). Table 2.5 shows the specifications of the power source.

Table 2.5 The specifications of the high-frequency power supply.

Output Frequency	Line Regulation	Load Regulation	Output Distortion	Ripple and Noise	Response Time
20-5000 Hz	0.1% max for a $\pm 10\%$ change	0.25% 20 to 2000 Hz. 0.50% 2000 to 5000 Hz.	0.25% THD <sub>avg</sub> 20 to 5000 Hz.	-72 dB	5 $\mu$ s typically.

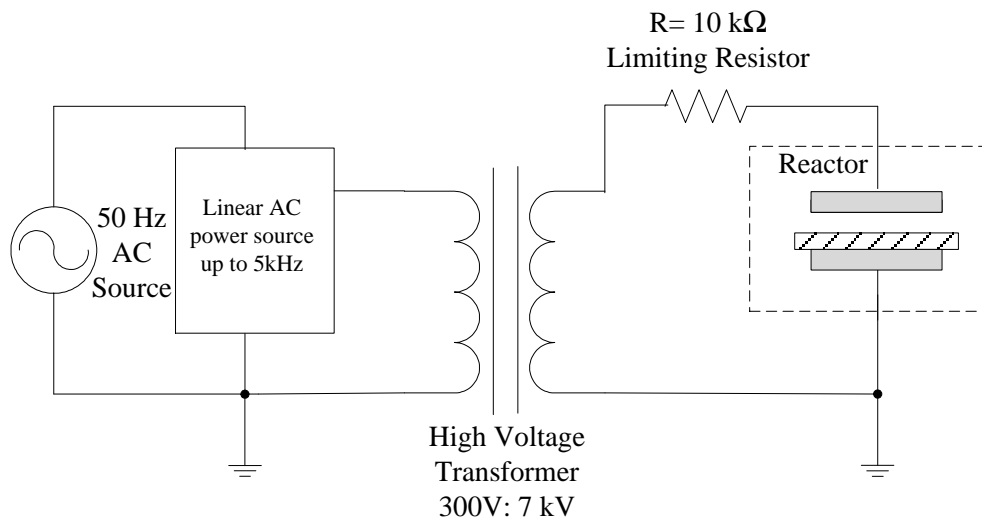


Figure 2.3 The schematic of the high-frequency power supply.

The transient programmes (few cycles) can be set up to vary from continuous true sine output to true discontinuous AC output. The power supply can generate a continuous transient AC output with 100-cycle to analyse the ozone efficiency using different electrodes. The power supply can generate a discontinuous transient voltage output of 1 cycle, 2 cycles and 10 cycles to analyse the filament current development with time. Figure 2.3 shows the circuit diagram using the linear AC power source.

The power supply is connected to a step-up transformer (ratio of 1:22) as shown in Figure 2.3. The maximum output of the transformer is 10 kV<sub>rms</sub>, with an operating frequency of 3 kHz to 30 kHz. To prevent overvoltage across the limiting resistor, the value of the limiting resistor is chosen to be much lower than the impedance of the test cell. The capacitance of the test cell in the research is in the order of pico-farads and the limiting resistor is 10 k $\Omega$ .

## 2.4 Electrical diagnostics

In this section, the diagnostics of the current, voltage and energy measurements are discussed.

### 2.4.1 Voltage measurement

A high-voltage probe is connected in parallel to the test cell to determine the voltage across the test cell as shown in Figure 2.4. Two different high voltage probes are used in the research for different applications. The specifications are discussed in the following subsection.

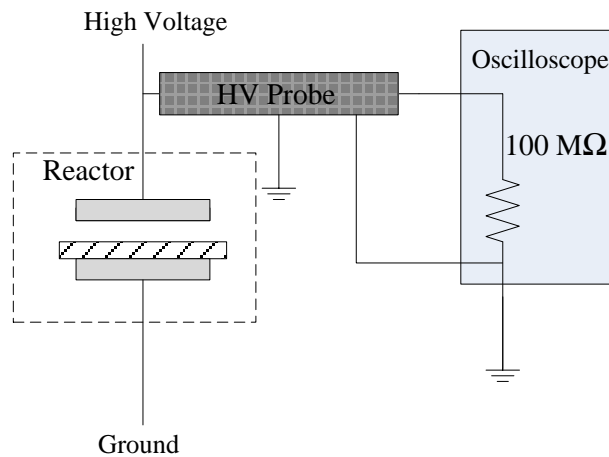


Figure 2.4 High-voltage side measurement configuration.

#### *Tektronix P6015A high-voltage probe*

This high-voltage probe is used to determine the voltage input to calculate the Lissajous figure (which is described in detail in Section 2.6) and the input power. The technical specifications are listed in Table 2.6 below:

Table 2.6 The specifications of the P6015A probe.

Maximum input voltage	Bandwidth (-3dB)	Rise Time	DC attenuation	Input resistance	Input capacitance	Delay Time
20 kV DC 40 kV Pulse	75 MHz	$\leq 4.67$ ns	1000:1	100 M $\Omega$	$\leq 3$ pF	14.7 ns

Teledyne LeCroy PPE 6 kV high-voltage probe

The LeCroy PPE 6 kV probe is used to analyse the single filament development process in more depth, as the bandwidth of the probe is much higher, the filament development occurs in nanoseconds, thus requiring rapid response rate and high bandwidth. Table 2.7 shows the specifications of the probe.

Table 2.7 The specifications of the PPR 6 kV probe.

<b>Maximum input voltage</b>	<b>Bandwidth (-3dB)</b>	<b>Rise Time</b>	<b>DC attenuation</b>	<b>Input resistance</b>	<b>Input capacitance</b>
6 kV DC and Impulse	400 MHz	$\leq 0.9$ ns	1000:1	50 M $\Omega$	$\leq 6$ pF

## 2.4.2 Current measurement

The oscillation in the circuit due to unmatched impedance can strongly affect the output current waveform and leads to distortion. To reduce and minimise the effect of oscillations, a high-bandwidth coaxial cable (RG405) is used for ns pulsed current measurement in the research. Table 2.8 shows the general specifications.

Table 2.8 General specifications of the RG405 cable.

<b>Capacitance</b>	<b>Impedance (<math>\Omega</math>)</b>	<b>Maximum operating frequency (GHz)</b>	<b>Maximum operating voltage (<math>V_{RMS}</math>)</b>
95.1 pF/m	$50 \pm 1.5$	20	1,500

The coaxial cable has three components: an inner conductor consisting of silver-plated copper-clad steel, a dielectric layer constructed of PTFE and an outer conductor formed by a seamless copper tube. The ground electrode of the test cell is connected to the inner conductor of the cable. The outer conductor of the cable is connected to the ground as shown in Figure 2.5.

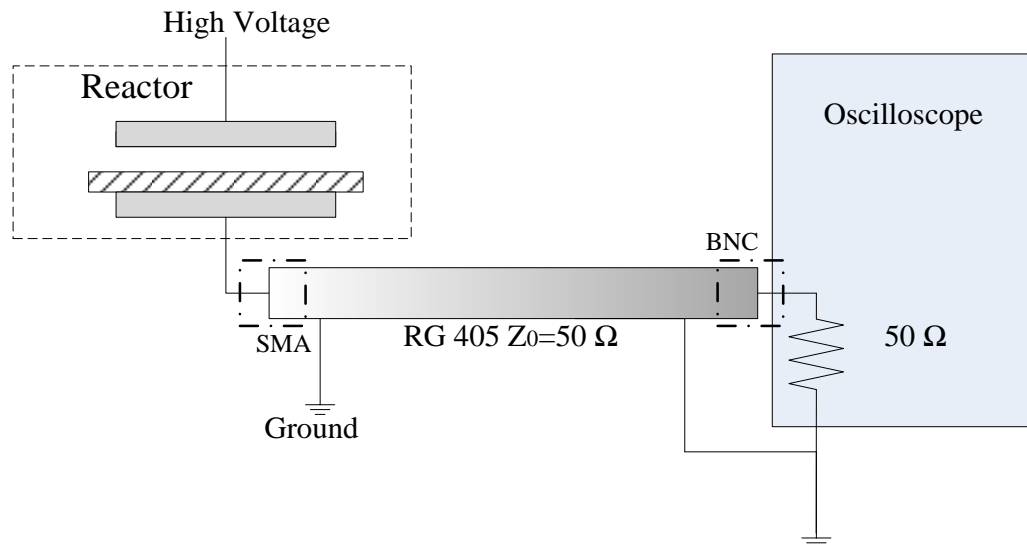


Figure 2.5 Current measurement using coaxial cable.

### 2.4.3 Data logging and processing

A WaveRunner 625 Zi oscilloscope from *LeCroy* is used to log the voltage and current data and perform the basic mathematical calculations. This oscilloscope is suitable for investigating the nanosecond filament current properties and for analysing the Lissajous figure accurately. Table 2.9 shows the specifications of the oscilloscope.

#### Trigger function:

The oscilloscope can record the voltage and current waveforms of the first few cycles up to 100 cycles after switching on the power supply. The information is used to analyse the transient behaviour of the discharge.

By setting the trigger function to pattern mode (both voltage and current are greater than zero), the positive current distribution histogram can be plotted automatically.

#### Functional measurement and calculation:

The math mode is used to perform the integration and differential function. The energy of a single pulse can be calculated using the integration mode. The oscilloscope can output a histogram of the peak current amplitude and its average. In the experiments, the voltage probes are connected to the oscilloscope via a DC 1 M $\Omega$  input. The RG405 coaxial cable is connected to the oscilloscope via a DC 50  $\Omega$  input.

Table 2.9 The specifications of WaveRunner 625 Zi.

Analog Bandwidth @ 50 $\Omega$ (-3dB)	2.5 GHz ( $\geq 5$ mV/div)
Analog Bandwidth @ 1 M $\Omega$ (-3dB)	500 MHz
Rise Time (10 – 90 %, 50 $\Omega$ )	160 ps
Maximum Input Voltage	50 $\Omega$ : $5V_{\text{rms}} \pm 10V_{\text{peak}}$ 1 M $\Omega$ : $400V_{\text{max}}$ .
Maximum Trigger Rate	1,000,000 waveforms/second (in Sequence Mode)
Time/Division Range	20 ps/div-1.6ks/div with standard memory
Sample Rate/Channel	20 Gs/s on 4 Channel, 40Gs/s on 2 Channel
Standard Memory (4 Ch/ 2 Ch/ 1 Ch)	16Mb / 32Mb/ 32Mb

## 2.5 Optical diagnostics

In this thesis, the optical diagnostics analyse the light emission spectrum and intensity of the dielectric barrier discharge.

### 2.5.1 Light emission intensity

#### A. Optical fibre

A 600  $\mu\text{m}$  core diameter optical fibre from Ocean Optics is used. The wavelength range is from 200 nm to 1100 nm. The buffer is made of polyimide. The jacket is stainless-steel. The acceptance angle is  $12.7^\circ$  in air with a 0.22 numerical aperture.

#### B. Photomultiplier tube (PMT)

The photosensor module used in this experiment is Hamamatsu H10721-01 with a Multiakali photocathode. It contains a metal-packaged PMT and a high-voltage power supply system. The electric circuit of the power supply is shown in Figure 2.6. The PMT has high gain, wide dynamic range and high-speed response. The spectral response is 230 nm to 870 nm. The window material is borosilicate glass.

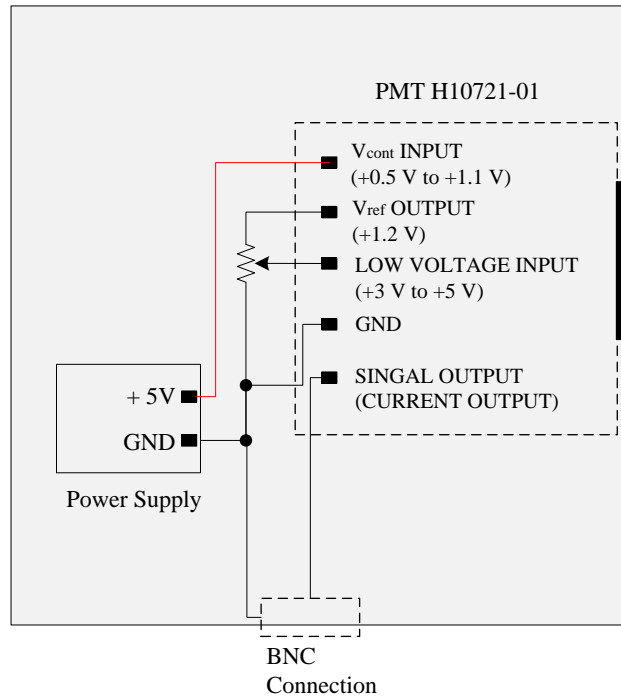


Figure 2.6 The electrical circuit of the PMT.

There are four input channels:  $V_{cont}$  is the control voltage (+ 0.5 to + 1.1V);  $V_{ref}$  is the reference voltage (constant+1.2 V); LOW VOLTAGE INPUT is connected to the power supply (+3 to +5 V), and GND is connected to the ground. The output channel is connected to a BNC connector. To adjust the voltage range of  $V_{cont}$ , a potentiometer is used.

The required input voltage of PMT is 5  $V_{DC}$  which is connected to the 9  $V_{DC}$  battery. An L78S05CV positive voltage regulator stabilises the continuous 5  $V_{DC}$  output that is connected to the PMT module. The output signal of the PMT is connected via a BNC connector to the oscilloscope using a RG214 cable of 50  $\Omega$ .

### 2.5.2 Emission spectrum

The light emission spectra of the discharges were measured using a HR4000 Spectrometer from Ocean Optics. There are five components in the spectrometer box: entrance slit, collimating mirror, grating, focusing mirror, and exit slit.

The entrance slit is used to transfer the light from the optical fibre. After the slit, there is a filter (Point B) that is set to pre-determined wavelength regions before entering the optical bench. Light from the entrance slit passes through the filter to a collimating mirror which focuses the light toward the grating in parallel. The grating splits the light into different wavelengths. Different size of grating can make a difference in the resolution of the

spectrometer and the accuracy of measurement. The light is directed to the exit slit through a focusing mirror.

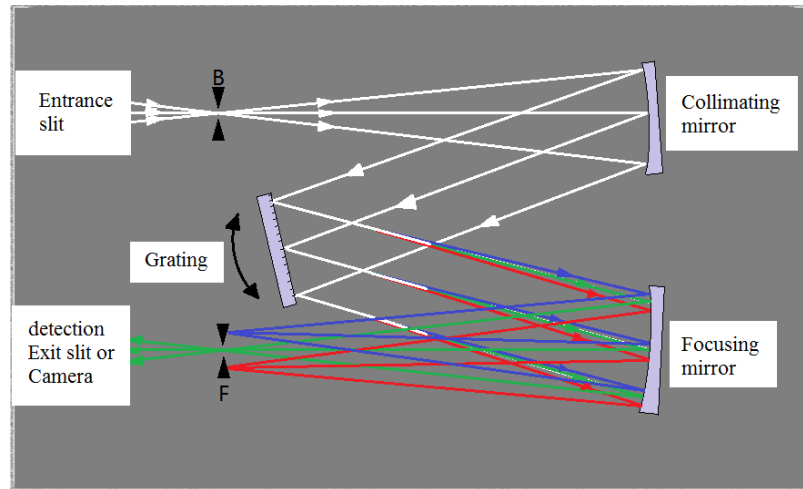


Figure 2.7 The arrangement of the spectrometer.

The specifications of HR4000 are shown in Table 2.10:

Table 2.10 The specifications of the HR4000 spectrometer.

Detector	
Type	Toshiba TCD 1304AP
Pixels	3648
Detection Range	190-1100 nm
Wavelength range	200-1100 nm
Slit	25 $\mu\text{m}$
Optical resolution:	$\sim 1.09$ nm (FWHM)
Grating	HC-1

Optical resolution can be calculated using:

$$\text{Optical Resolution} = \text{Dispersion} \times \text{Pixel resolution}$$

where dispersion is  $\sim 0.25$  nm/Pixel and Pixel resolution is 4.4.

## 2.6 Discharge energy measurement

The Lissajous figure is used to calculate charge transfer and the total energy per cycle. A measurement capacitor is connected in series with the test cell to measure the voltage across this measurement capacitor ( $V_m$ ). The equivalent circuit of the discharge indicates that, once the discharge has occurred, the gap voltage will decrease. Following the discharge, the gap voltage is replenished by the power supply. The total charge transfer can be shown by the increase of the voltage across the measurement capacitor.

Figure 2.8 shows the schematic diagram of the measurement circuit. The measurement capacitor is normally greater than 50 times [53] the total equivalent capacitance of the test cell. The capacitance range of the test cell is approximately in the range of tens of pico-farads; in this case, the measurement capacitor was chosen as  $15\text{ nF}$ .

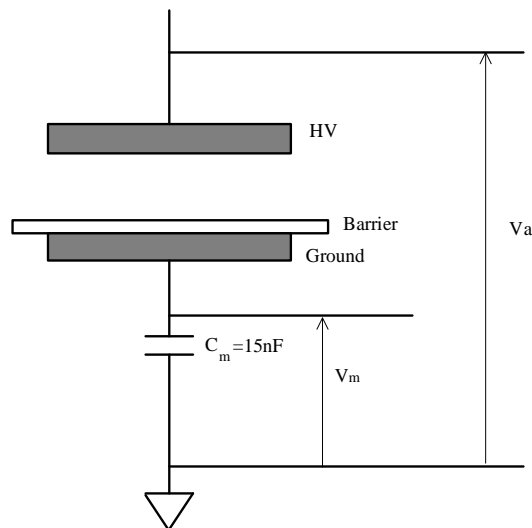


Figure 2.8 Electrical circuit of energy measurement using Lissajous figure.

Figure 2.9 shows the equivalent circuit. The gas gap can be treated as a gap capacitance ( $C_g$ ) and the dielectric barrier can be treated as dielectric capacitance ( $C_d$ ) in series with the gap capacitance. The value of the gap capacitance and the dielectric capacitance can be determined by the Lissajous figure. The detailed analysis is introduced in Chapter 3.

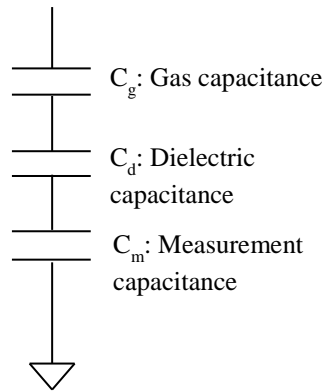


Figure 2.9 Equivalent circuit with a measurement capacitor.

Figure 2.10 shows the Lissajous figure measured for a DBD discharge. The x axis is the voltage across the test cell and the y axis is the charge transfer ( $Q_m$ ). The schematic of the Lissajous figure is shown in Figure 2.10. For a dielectric barrier discharge with constant breakdown voltage during the active phase, this U-Q diagram is ideally a parallelogram with four sharp points labelled A, B, C and D. The discharge in the positive cycle starts at point A and continues to point B. Once the applied voltage reaches the peak amplitude, the discharge stops. For the negative cycle, the discharge occurs from point C to point D and is extinguished once the amplitude of the applied voltage reaches the peak. The slope of AB line and DC line is the same, which is the equivalent dielectric capacitance ( $C_d$ ). From point B to point C, the electric field of the test cell decreases and the slope of BC line is the equivalent total capacitance ( $C_t$ ), the same as the slope of DA line. The enclosed area is the energy input of a full cycle. The breakdown voltage ( $V_b$ ) can be determined when the voltage across the measuring capacitance is equal to zero.

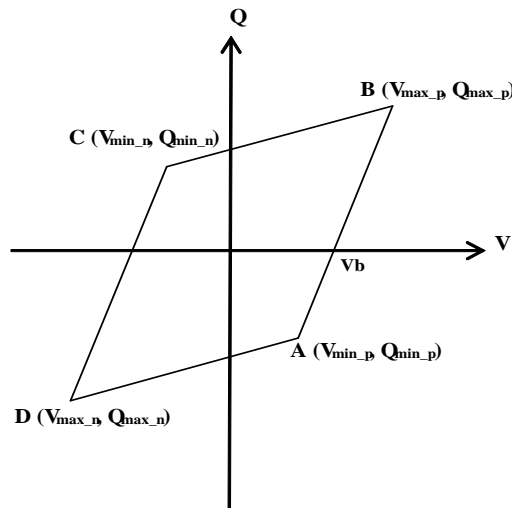


Figure 2.10 Lissajous figure of planar electrode DBD discharge.

The voltage change across the measuring capacitance is related to the charge transfer (2.1):

$$Q = Q_m = C_m V_m \quad (2.1)$$

The total energy input per cycle in  $J$  is obtained by (2.2)

$$E = 4C_d V_b \left( V_{\max} - \frac{C_d + C_g}{C_d} V_b \right) \quad (2.2)$$

### A. Steady-state

The input power in  $W$  can be determined as (2.3):

$$P = f \times E \quad (2.3)$$

where  $f$  is the applied frequency.

### B. Transient state

To ensure accurate energy measurements, all 100 cycles of the applied voltage waveform and voltage across  $C_m$  were recorded using the oscilloscope. Figure 2.11 shows the Lissajous figure measured for the 100 cycles superimposed.

Subsequently, based on the six points selected in Figure 2.11, the equivalent gap capacitance,  $C_g$ , the barrier capacitance,  $C_d$ , the breakdown voltage,  $V_b$ , and the maximum voltage,  $V_{\max}$ , of each cycle can be calculated individually using Matlab. The energy of the  $i^{\text{th}}$  cycle can be calculated using (2.4):

$$E_i = 4C_{d_i} V_{b_i} \left( V_{\max_i} - \frac{C_{g_i} + C_{d_i}}{C_{d_i}} V_{b_i} \right) \quad (2.4)$$

The total energy input of the 100 cycles is calculated using (2.5):

$$E_{total} = E_1 + E_2 + \dots + E_{100} \quad (2.5)$$

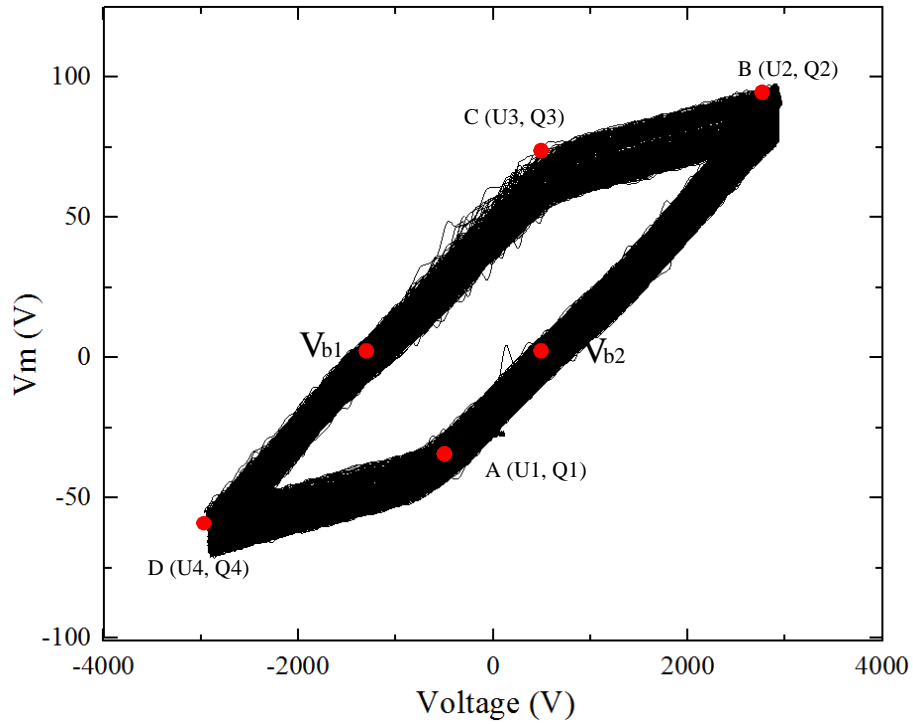


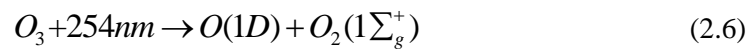
Figure 2.11 Sampled superimposed Lissajous figure for all 100 cycles.

## 2.7 Ozone measurement

In order to determine the ozone production, gas flow and ozone concentration need to be measured. The following sections introduce how to determine the ozone production and ozone generation efficiency.

### 2.7.1 Ozone measurement

The photons of wavelength 254 nm react with ozone molecules, as shown in (2.6)



The ozone dissociation rate coefficient is a parameter to determine the reaction rate, which is related to the absorption cross section  $\sigma$ .

The absorption cross section is the probability of an absorption process. It indicates the ability of a molecule to absorb a photon at a certain wavelength. The absorption is defined as (2.7) by the Beer-Lambert absorption law:

$$I = I_0 \exp(-\sigma dn) \quad (2.7)$$

where  $I$  is the transmitted light intensity,  $I_0$  is the incident light intensity,  $d$  is the absorption path length (in cm),  $n$  is the concentration of ozone (in  $\text{molecule} / \text{cm}^3$ ) and  $\sigma$  is the absorption cross section (in  $\text{cm}^2 \text{molecule}^{-1}$ ).

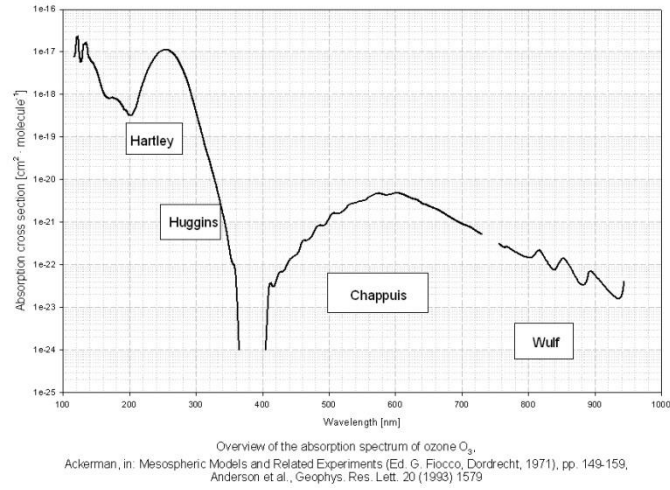


Figure 2.12 Absorption cross section of ozone in ultraviolet and the visible part of the spectrum [54] [55].

Figure 2.12 shows the absorption cross section of ozone under different wavelengths from VUV to the visible band. The absorption cross section at room temperature is  $\sim 1.15 \times 10^{-17}$  at 253.7 nm.

### 2.7.2 Ozone concentration

Ozone concentration detection is usually performed using a low-pressure mercury lamp that produces 253.7 nm emission. An ozone analyser is a dual-beam photometer based on a microprocessor to measure ozone concentration in air ( $M=29.0$ ) or oxygen ( $M=32.0$ ). It measures the UV intensity  $I_{\text{ozone}}$  through the measurement channel (with ozone) and the UV intensity  $I_{\text{ref}}$  from the reference channel (without ozone), in addition to the temperature and pressure. The ozone concentration  $n_{\text{ozone}}$  is written as (2.8):

$$n_{\text{ozone}(\text{molecules}/\text{cm}^3)} = (\sigma d)^{-1} \ln \frac{I_{\text{ozone}}}{I_{\text{ref}}} \quad (2.8)$$

For the steady-state ozone concentration measurement, the MINI-HICON Ozone Analyser from INUSA was used with higher ozone concentration range. For the transient ozone concentration measurement ( $\leq 10,000$  ppm<sub>v</sub>), the BMT 964 ozone analyser is used. Table 2.11 shows the specifications of both ozone analysers.

Table 2.11 Specifications of ozone analysers.

	MINI-HICON	BMT 964
<b>UV Light Source</b>	Low-pressure mercury vapour lamp	Low-pressure mercury lamp, burnt-in for 300 h
<b>Units of Measure</b>	$\text{g/m}^3$ , $\text{g/Nm}^3$ , % wt/wt	$\text{g/Nm}^3$ , % wt/wt, ppm
<b>Range</b>	0 to 400 $\text{g/Nm}^3$	0 to 10,000 ppm
<b>Sample Flow</b>	0.2 to 15 SLPM	0.1 to 1 SLPM
<b>Response Time</b>	0.5 s or 2 Hz sampling rate	0.03 s (analogue output), 0.3 s (display)
<b>Accuracy</b>	0.1 $\text{g/Nm}^3$	0.4% of measurement + 0.1% of scale
<b>Repeatability Error</b>	1% of measurement	0.2% of measurement
<b>Operating Condition</b>	5 to 45 and 0 to 95% RH (non-condensing)	0 to 50 (non-condensing)

For the steady-state analysis, the ozone concentration is obtained directly from the display panel. The transient ozone concentration data are logged by connecting the ozone analyser to the computer using the RS232 serial interface.

### 2.7.3 Ozone generation calculation

Under the STP conditions, the molar volume of ozone gas is equal to 22.4  $L/mol$ . The molar mass of ozone is 48  $g/mol$  and the molar mass of oxygen is 32  $g/mol$ , respectively. The density of ozone is  $\rho_{ozone}=2.14$   $g/L$  and the density of oxygen is  $\rho_{oxygen}=1.43$   $g/L$ .

$$n_{ozone(mol/cm^3)} = \frac{n_{ozone(molecules/cm^3)}}{A} \quad (2.9)$$

where  $A$  is the Avogadro constant ( $6.02 \times 10^{23}$ ).

The ozone concentration in grams per cubic meter is in  $c[O_3]_{g/m^3}$  expressed as (2.10)

$$c[O_3]_{(g/m^3)} = 48 \times 10^6 \times n_{ozone(mol/cm^3)} \quad (2.10)$$

The unit of grams of ozone per normal cubic meter is usually written as  $c[O_3]_{g/Nm^3}$  as calculated in (2.11)

$$c[O_3]_{(g/Nm^3)} = c[O_3]_{(g/m^3)} \times \frac{T_2}{T_1} \times \frac{P_1}{P_2} \quad (2.11)$$

The terms  $T_1$  and  $P_1$  refers to standard temperature 273 K and 1 atm.  $T_2$  and  $P_2$  refer to the measured temperature and pressure.

Another unit of measurement used in the experiment is ppm<sub>v</sub>, which stands for parts per million by volume, written as  $c[O_3]_{ppmv}$ , expressed as (2.12). For the STP condition,

$$c[O_3]_{ppmv} = 22.4 \times 10^3 \times n_{ozone(mol/cm^3)} \quad (2.12)$$

### A. Steady state

The ozone weight percentage in a gas mixture is shown in (2.13)

$$c[O_3]_{wt\%} = \frac{c[O_3]_{(g/Nm^3)}}{c[O_3]_{(g/Nm^3)} - \frac{\rho_{oxygen}}{\rho_{ozone}} \times c[O_3]_{(g/Nm^3)} + \rho_{oxygen}} \quad (2.13)$$

The ozone production per hour is expressed as  $[O_3]$  in unit of g/h as shown in (2.14)

$$[O_3] = FL \times \frac{32}{22.4} \times c[O_3]_{wt\%} \times 60 \quad (2.14)$$

where  $FL$  is the gas flow rate in standard litres per minute.

The ozone efficiency is the amount of ozone produced in g per kWh, expressed as (2.15)

$$\eta = \frac{[O_3] \times 1000}{P} \quad (2.15)$$

### B. Transient state

The ozone concentration in the transient state is shown in Figure 2.13:

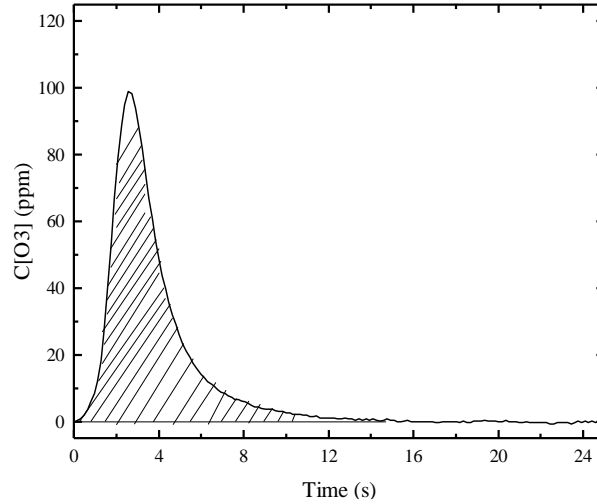


Figure 2.13 The sampled transient ozone concentration.

The transient ozone concentration is measured in  $c[O_3]'_{ppmv}$ .

The total ozone generated in  $g$  can be calculated by the integration of ozone production in real time, as shown in (2.16)

$$[O_3]' = FL' \times \frac{\int_0^t C[O_3]_{ppmv} dt}{466.43} \quad (2.16)$$

where  $FL'$  is the gas flow rate in standard  $m^3$  per second and  $1 g/m^3 = 466.43 ppm_v$ .

The ozone efficiency of transient state in  $g/kWh$  is expressed as (2.17)

$$\eta = \frac{[O_3]'}{E_{total}} \quad (2.17)$$

Where  $E_{total}$  is calculated using (2.4) and (2.5).

## **3 Discharge Development of Dielectric Barrier Discharge**

### **3.1 Introduction**

Dielectric barrier discharge (DBD) is the most conventional method for ozone generation. DBD is a transient self-sustained discharge between two electrodes with one or more dielectric barriers. The discharge occurs at a location once the electric field is strong enough to ignite gas breakdown. The most common mode of discharge is a filamentary discharge [56]. Electrical charge will accumulate on the dielectric barrier to extinguish the discharge filament.

The advantage of DBD is that a large number of high energy electrons can be generated at a low gas temperature. Much of the progress on ozone generation using DBD was made in the past 50 years, especially after the evolution of power electronics technology. However, despite the knowledge in generating ozone efficiently and in understanding the electrical properties of DBD, it is still not possible to provide a quantitative theoretical description of the filamentary DBD behaviour and its relationship to ozone generation. It is difficult to investigate experimentally the dynamics of the discharge filaments, which have a short duration of tens of nanoseconds.

In this chapter, the filamentary DBD is investigated to understand the characteristics of the discharge as a preparation for ozone-generation research. The properties of filamentary discharges including breakdown voltage, filament current and charge transfer are discussed. The charge accumulation per half cycle is analysed in detail. The equivalent circuit for a single filament development is investigated to determine the relationship between the external current and the filament current during a single filament. The charge accumulation from a single filament is also investigated. The discharge characteristics at power on (first several cycles) were investigated for a better understanding of the establishment of steady state discharge in DBD. The atmospheric pressure glow discharge (APGD) is investigated for its discharge characteristics and applications for ozone generation.

## 3.2 Electrical properties of filamentary discharge

### 3.2.1 Experimental setup

#### A. Test cell design

A planar electrode configuration is used to analyse the characteristics of dielectric barrier discharge. Two stainless steel planar plates were chosen as electrodes. The diameter of the electrodes is 30 mm with 10 mm depth. To avoid spark discharges, the edges of the electrodes were profiled, with a radius of 1.5 mm. The dielectric barrier is attached to the ground electrode, which is a borosilicate glass with a rectangular cross-section. The test cell design is shown in Figure 3.1.

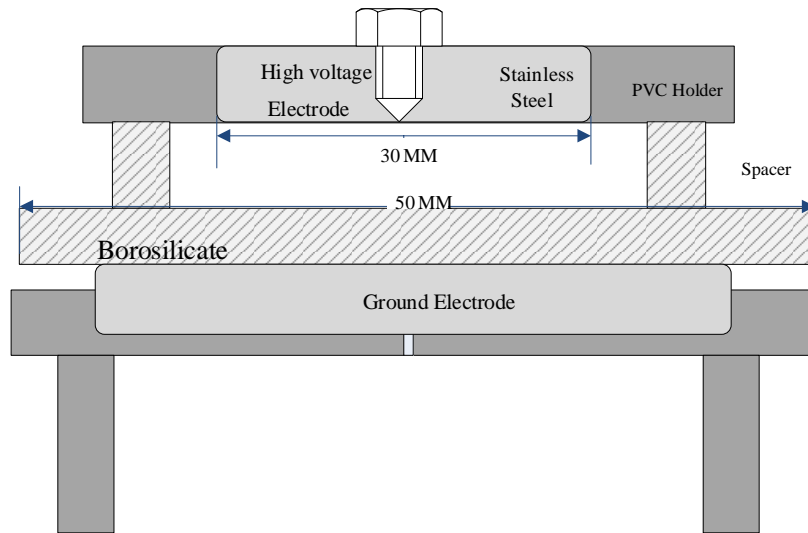


Figure 3.1 Test cell design.

The equivalent dielectric capacitance can be calculated based on the planar capacitance formula (3.1):

$$C = \frac{\epsilon_r \epsilon_0 A}{d} \quad (3.1)$$

where  $A$  is the area of the electrode and  $d$  is the thickness of the glass. The relative permittivity of borosilicate glass is 6.7. The equivalent barrier capacitance is calculated to be 139 pF. The gap length is 0.15 mm. The equivalent gap capacitance is calculated to be 43 pF.

#### B. Experimental arrangement

The 5-kHz power supply is connected to a 1:22 high-frequency transformer to increase the voltage. The output of the transformer is connected to the test cell, via a 10 k $\Omega$  current-limiting resistor. The voltage waveform is monitored using a Teledyne LeCroy PPE 6 kV

1000:1 high-voltage probe with a bandwidth of 400 MHz. The current signal was measured by a RG 405 coaxial cable. The voltage across the measurement capacitor is measured by a PP008 10:1 passive probe from LeCroy. Figure 3.2 shows the experimental setup diagram.

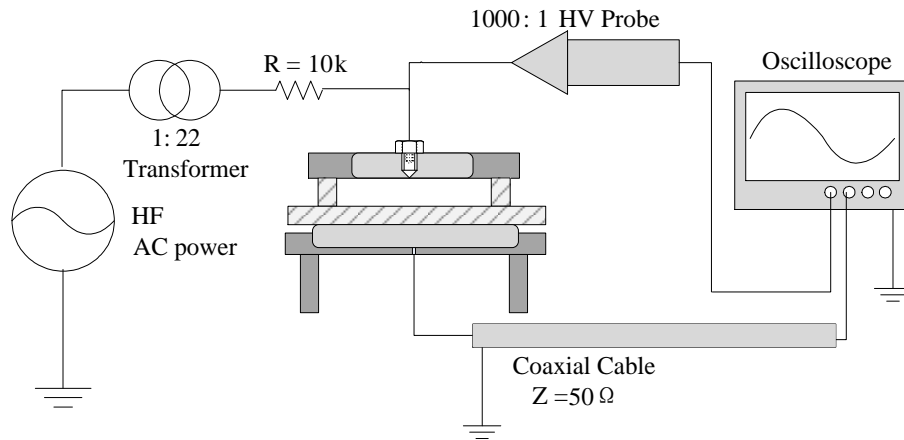


Figure 3.2 Experimental setup diagram.

Due to the difference in the cable length and signal propagation speed when measuring voltage and current, the measured waveforms are not synchronized. To relate the voltage and current signals accurately, it is necessary to synchronise the voltage signal and current signals. The calibration process sets the voltage signal as the reference and the pulsed current is synchronised with the voltage drop as shown in Figure 3.3.

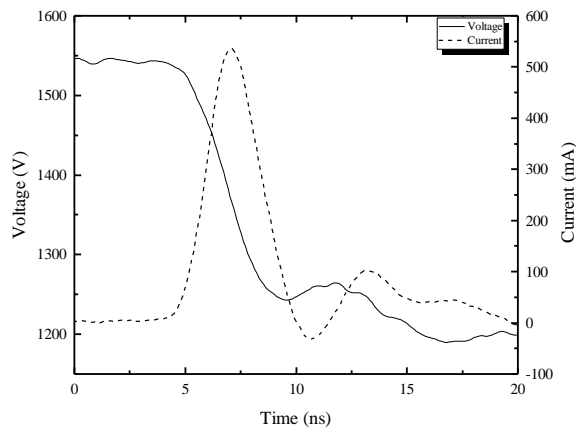


Figure 3.3 The calibration of current (dashed line) and voltage (solid line) waveform by using 0.3 mm barrier thickness and 0.15 mm gap length in the DBD configuration.

### 3.2.2 Analysis of external current

#### A. Accuracy of the external current measurement

The external current is measured with a duration of nanoseconds which is electron current. The charging current following the discharge can distort to the external current. Without the limiting resistor, the power supply charges the test cell quickly once there is a voltage drop across the test cell. To determine the distortion from the charging current, a comparison is made by changing the value of limiting resistor.

In this experiment, the current limiting resistor is changed from 0, 10 k $\Omega$  and 24 M $\Omega$ . By applying the same voltage to the test cell, the external current and the corresponding voltage drop are investigated. The results under no limiting resistor are shown in Figure 3.4.

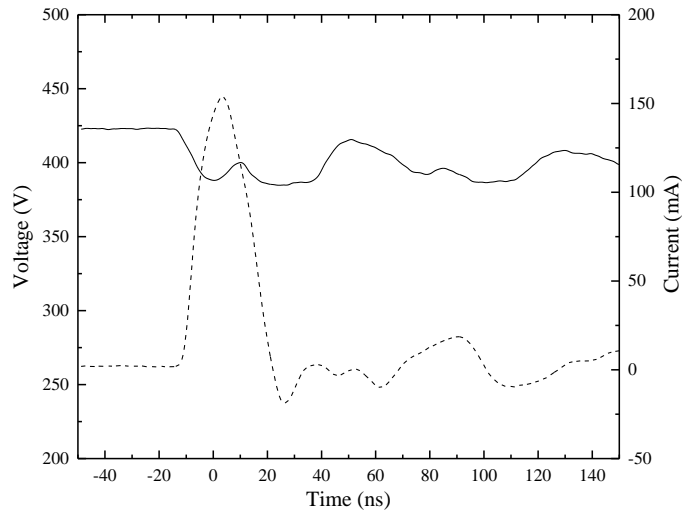


Figure 3.4 The sampled external current (dashed line) and the corresponding voltage drop (solid line) without a limiting resistor.

The total pulse current duration is 40 ns (full duration) with an amplitude of 160 mA, while the voltage drop is only 30 V in a duration of 10 ns. Once the discharge is extinguished, the discharge current should drop to zero. Figure 3.4 shows that there is still a current after the voltage drops to its lowest value. The current is identified as the charging current, which joins the discharge current. To separate the discharge current from the charging current, a 10 k $\Omega$  limiting resistor is added in series between the secondary side of the transformer and the high-voltage side of the test cell. The sampled external current and the corresponding voltage drop are shown in Figure 3.5.

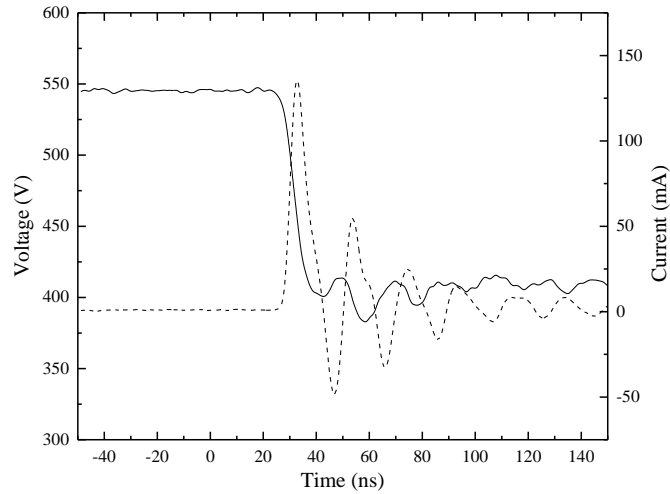


Figure 3.5 The sampled external current (dashed line) and corresponding voltage drop (solid line) with a  $10\text{ k}\Omega$  limiting resistor electric circuit.

After adding the limiting resistor, the voltage drop is much greater than that without a limiting resistor. The voltage drop from a single filament shown in Figure 3.5 is  $150\text{ V}$  in  $11\text{ ns}$ . The amplitude of the external current is  $150\text{ mA}$ , with a duration of  $11\text{ ns}$ . The duration of the current is the same as that of the voltage drop. Consequently, the external current measurement can be made more accurate by adding a reasonable limiting resistor. When the  $10\text{ k}\Omega$  limiting resistor is replaced by a  $24\text{ M}\Omega$  limiting resistor, the sampled external current and the corresponding voltage drop are shown in Figure 3.6.

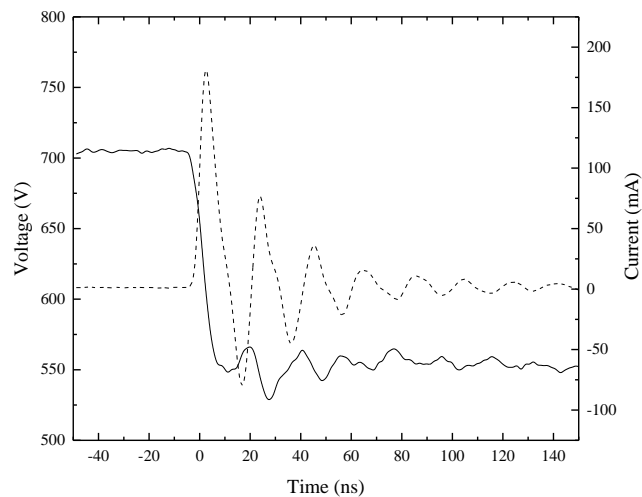


Figure 3.6 The sampled external current (dashed line) and corresponding voltage drop (solid line) with a  $24\text{ M}\Omega$  limiting resistor electric circuit.

The amplitude of the voltage drop is approximately 150 V in a duration of 10 ns; the corresponding amplitude of the external current of approximately 200 mA and a duration of 10 ns. It is confirmed that the charging current can be removed from the discharge current by adding the limiting resistor, which enabled the accurate measurement of discharge current.

In Figure 3.6, the pulsed current has a full pulse width of 10 ns with amplitude of 175 mA. An oscillation is observed at the tail of the current, which may be due to unmatched impedance in the circuit or the electromagnetic interference. To determine the electromagnetic interference to the measurement, an antenna was used to measure the influence of electromagnetic radiation during the discharge period. Figure 3.7 shows the circuit configuration.

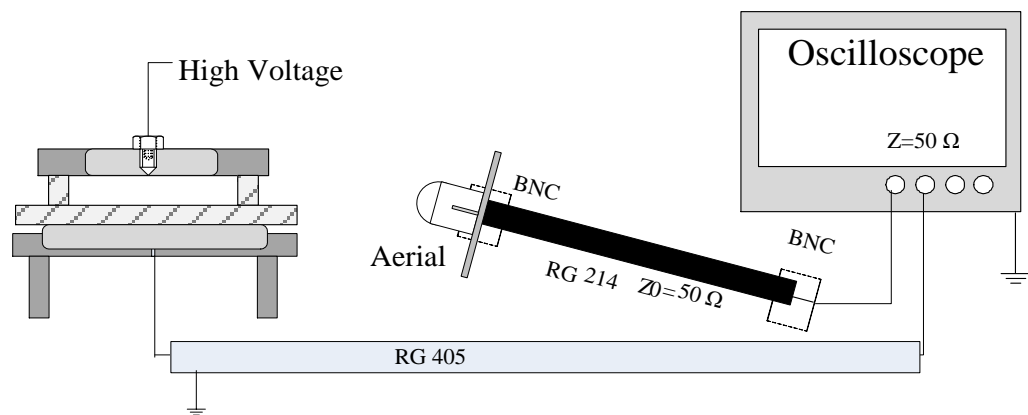


Figure 3.7 Circuit diagram to measure the electromagnetic signal of single filament discharge.

The FFT analysis was performed to determine whether the oscillation at the tail of the filament current is caused by the electromagnetic interference. Figure 3.8 shows the sampled single pulsed current with the corresponding EM signal.

The FFT analysis of the current waveform showed that, there are three peaks at 10 MHz, 50 MHz, and 85 MHz. The FFT analysis of the EM signal showed that there were two peaks at 50 MHz and 85 MHz, respectively. This proves that the current oscillation at the current tail is due to EM interference. The electromagnetic coupling is unavoidable because the EM waves are transmitted to the ground electrode and measured by the oscilloscope.

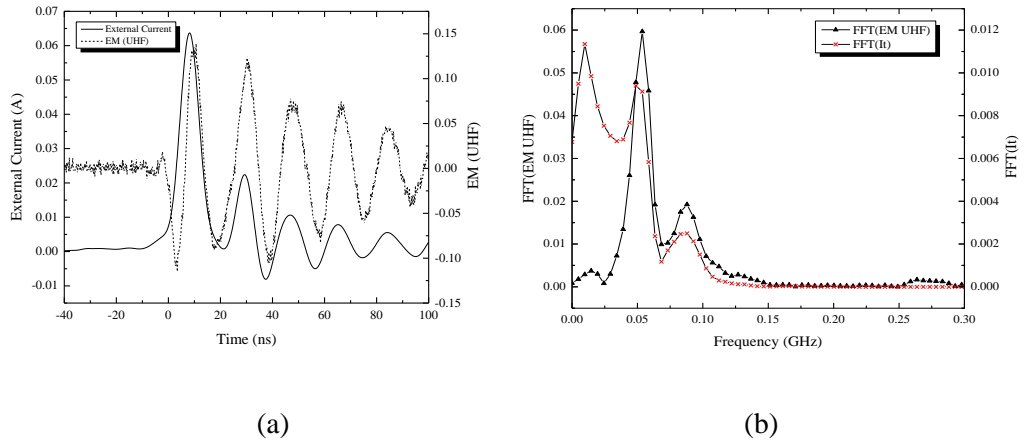


Figure 3.8(a) The sampled external current (solid line) and the EM signal (dotted line) (b) the corresponding red line of crosses for the external current and the line of black triangles for the EM signal.

To minimise the noise in the current measurement, a  $50 \Omega$  SMA connector is inserted into the test cell ground electrode. At the bottom of the ground electrode, there is a 1 mm diameter hole, and the needle of the SMA connector is plugged directly into the hole. For the current measurement,  $50 \Omega$  input impedance is chosen in the oscilloscope. Figure 3.9 shows an optimised external current waveform of a single filament with the corresponding PMT signal.

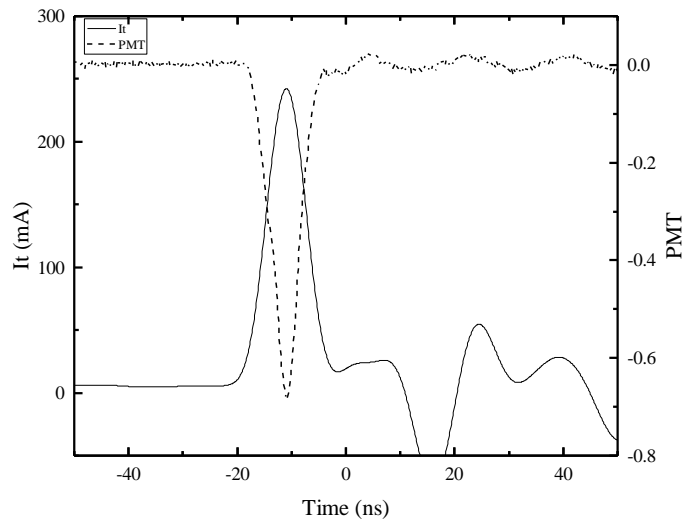


Figure 3.9 Sampled single optimised external current (solid line) and the corresponding PMT signal (dashed line).

The relationship between the voltage drop and the external current will be investigated in the following section (Section 3.2.3).

To ensure that the light emission from the discharge can be detected, the distance between the optical fibre and the test cell should be constantly the same during each experiment, and the fibre height should be aligned with the discharge gap. Figure 3.10 shows the PMT measurement circuit.

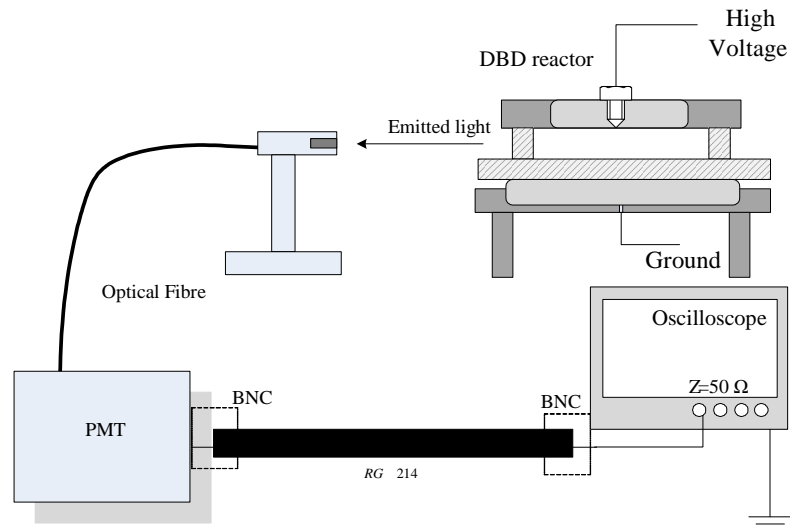


Figure 3.10 The PMT signal measurement system.

The experiment is carried out open to air with a 0.15 mm barrier thickness and a 0.3 mm gap. The applied voltage is 3.5 kV<sub>p</sub> at 5 kHz. The sampled current of a quarter cycle and the corresponding PMT signal are plotted in Figure 3.11.

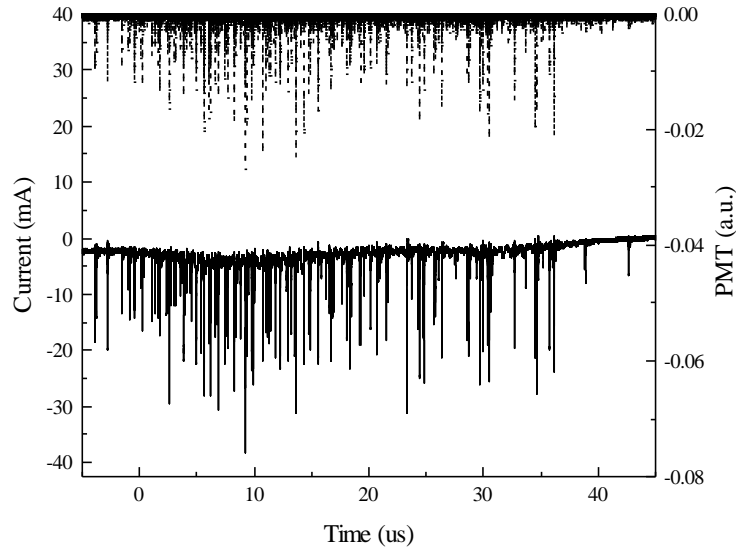


Figure 3.11 The sampled quarter-discharge cycle with the external current waveform (solid line) and the PMT signal (dashed line).

Each discharge current corresponds to a PMT pulse signal. The higher amplitude of the external current corresponds to a higher intensity PMT signal.

### B. External current amplitude distribution

Meanwhile, an investigation has been made to analyse the current amplitude distribution by capturing 5,000 single impulse currents. Figure 3.12 shows a distribution measured at 1 bar with a dielectric barrier thickness of 0.15 mm, and a gap length of 0.15 mm at 3 kV<sub>p</sub> applied voltage.

It shows a normal distribution with an average peak current of approximately 41 mA, with 40% weighted standard deviation. The most repeatable peak current level is in the range of 20 mA to 40 mA. The investigation of the distribution of external current amplitude and its relationship with ozone generation will be investigated in the following chapters.

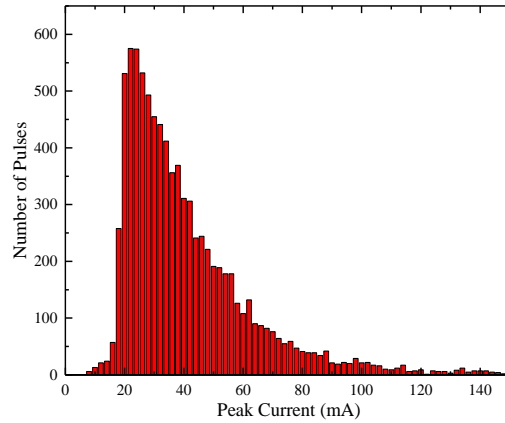


Figure 3.12 The sampled external current distribution of the positive discharge cycle with a dielectric barrier 0.15 mm thick and a gap length of 0.15 mm at 3 kV<sub>p</sub> applied voltage.

### 3.2.3 Development of filamentary discharge

#### A. Voltage and current waveforms

Figure 3.13 shows a sampled full cycle of current and voltage waveforms.

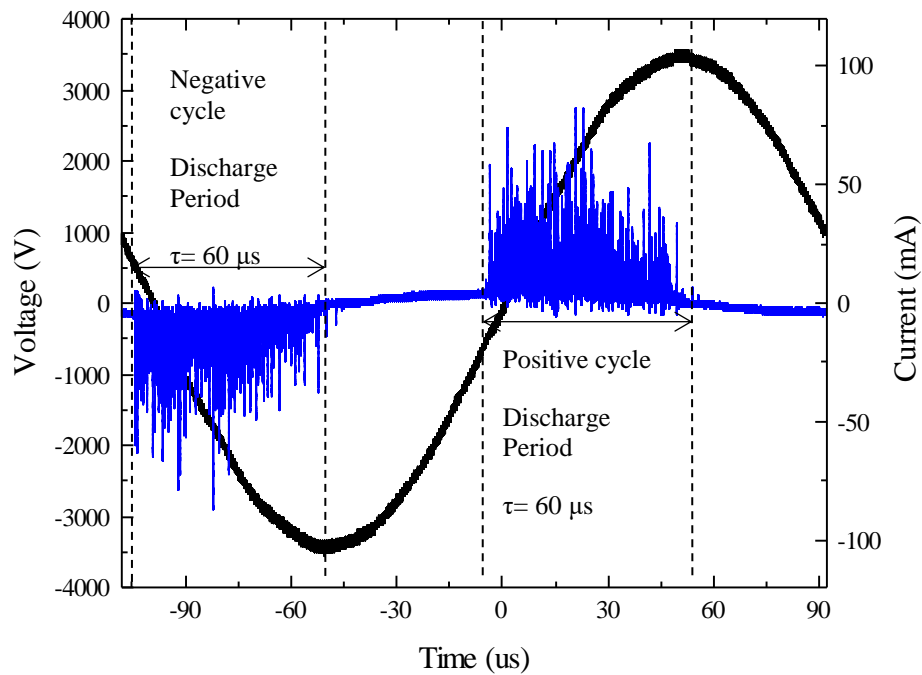


Figure 3.13 The sampled current and voltage waveform with 0.3 mm barrier thickness, 0.15 mm gap, 5 kHz and a 3.5 kV<sub>p</sub> power supply.

In the inter-electrode gap, once the electric field is sufficiently high to initiate gas breakdown, the electric field around the head of the avalanche increases dramatically, increasing the

number of ionising collisions. The discharge is developed on the rising edge once the voltage across the gap reaches the required breakdown voltage. For a gas breakdown, the electron avalanche is developed in a time scale of ps to ns.

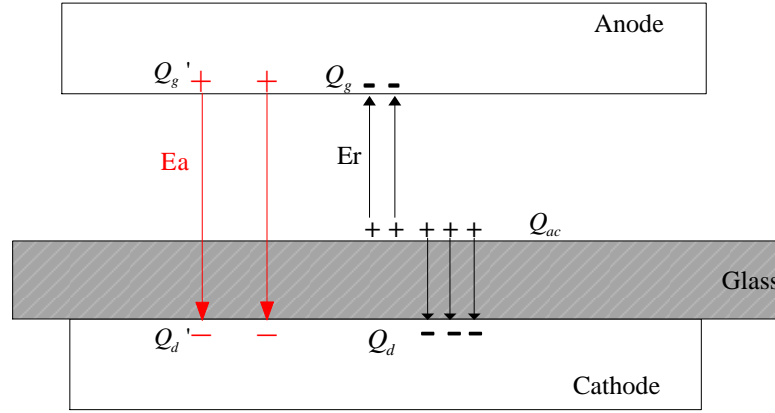


Figure 3.14 The electric field distribution of DBD.

Figure 3.14 shows the electric field distribution at the end of a quarter cycle discharge. During the discharge, the positive ions at the head of the streamer move to the barrier surface and accumulate. The total accumulated charge on the barrier is  $Q_{ac}$ . Some of the accumulated charge develops an electric field with the cathode, which induced  $Q_d$  and the remaining accumulated charge forms the reversed electric field  $E_r$  with the induced charge  $Q_g$  in anode as shown in (3.2).

$$Q_{ac}(t) = -[Q_d(t) + Q_g(t)] \quad (3.2)$$

The charge distribution is dependent on the gap capacitance and dielectric capacitance, as shown in (3.3).

$$\frac{Q_d}{Q_g} = \frac{C_d}{C_g} \quad (3.3)$$

According to (3.2) and (3.3), the induced charge  $Q_d$  and  $Q_g$  can be calculated as shown in (3.4) and (3.5).

$$|Q_d| = |Q_{ac}| \frac{C_d}{C_d + C_g} \quad (3.4)$$

$$|Q_g| = |Q_{ac}| \frac{C_g}{C_d + C_g} \quad (3.5)$$

With the increment of the applied voltage during the discharge phase, the discharge gap behaved like a variable resistor, the voltage across the barrier increasing continuously and the voltage across the gap remaining the same, which is the breakdown voltage  $V_b$  [57]. The electric field across the gap  $E_g$  is equal to the breakdown electric field  $E_b$ .

The charge produced by the power supply is  $Q_g'$  of anode and  $Q_d'$  of cathode, respectively, and obey (3.6).

$$Q_g' = -(Q_d') = C_t \cdot V_a \quad (3.6)$$

During the falling edge of the applied voltage, the applied electric field  $E_a$  across the gap reduces and no discharge occurs as shown in Figure 3.13. When increasing the applied voltage, the discharge can develop before the voltage changes polarity. The amount of accumulated charge on the barrier surface increases with the applied voltage, as a result, the surface charge density increases leading to much stronger reversed electric field  $E_r$ , which is high enough to initiate the gap breakdown during the falling edge. Once the polarity of the applied voltage is reversed, the applied electric field adds to the reversed electric field  $E_r$  produced by the accumulated charge, increasing the net electric field across the gap.

### **B. The parameters from Lissajous Figure**

Apart from calculating the energy input per cycle, Lissajous figure can also show many discharge parameters such as breakdown voltage, dielectric barrier capacitance, total capacitance and the charge transfer.

Figure 3.15 shows a sampled Lissajous figure measured with a 0.3 mm barrier thickness and a 0.15 mm gap at 3.5 kV<sub>p</sub>.

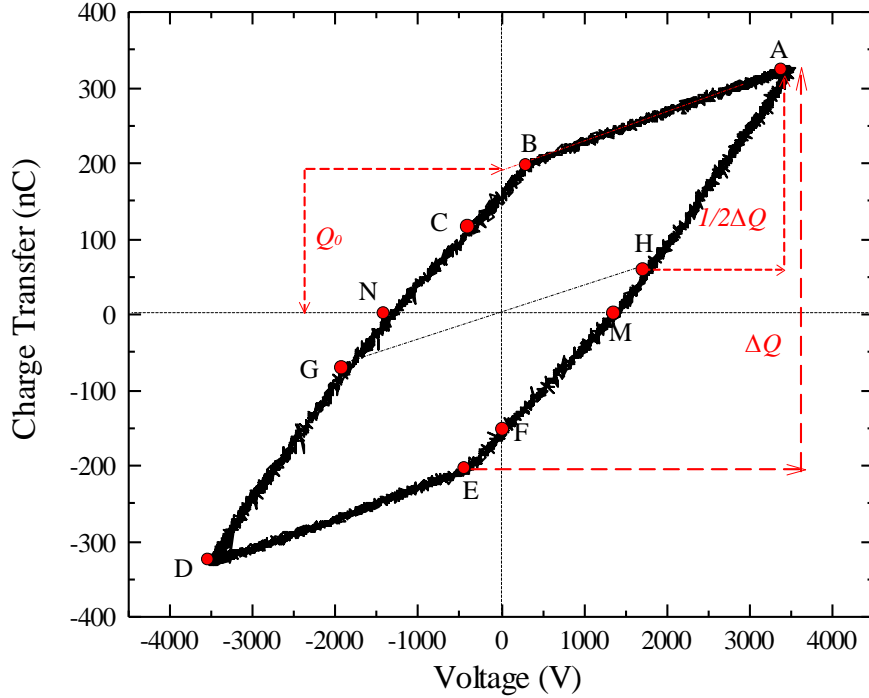


Figure 3.15 The sampled Lissajous figure with all the essential labels with a 0.3 mm barrier thickness and a 0.15 mm gap at 3.5 kV<sub>p</sub>.

The positive cycle from point E to point B is analysed and the analysis methodology for the negative cycle from point B to point E is the same.

The segment A-C corresponds to the non-discharge phase. As a result, the slope of A-C is the total capacitance of the test cell. The  $Q$ - $V$  relationship can be described by equation (3.7):

$$Q(t) = C_t \cdot V_a(t) + Q_0 \quad (3.7)$$

where  $Q_0$ , shown in Figure 3.15, is the total charge induced in the cathode at the point A by the accumulated charge on the dielectric surface,  $Q_{ac}$ .

The positive discharge phase is represented by the segments of F-A of which the charge transfer leads to voltage increase across the dielectric barrier. The slope of F-A is the dielectric capacitance. It can be seen that, when  $Q(t)$  is equal to zero, the applied voltage is equal to the gap voltage. Therefore, from the Lissajous figure, the gap discharge voltage,  $V_b$ , can be read from the points M and N, where the line segments of F-A and C-D intersect with the  $x$ -axis as shown in (3.8).

$$Q(t) = C_d \cdot (V_a(t) - V_b) \quad (3.8)$$

The charge across the dielectric barrier capacitance is equal to its capacitance,  $C_d$ , multiplied by the voltage, which is equal to  $V_a(t) - V_b$ . According to Figure 3.14, the charge transfer  $Q(t)$  is the sum of  $Q_d$  and  $Q_d'$  with opposite polarity,

$$Q(t) = -(Q_d + Q_d') \quad (3.9)$$

The breakdown voltage is  $V_b = 1.3 \text{ kV}$ ,  $C_d = 139 \text{ pF}$  and  $C_g = 53 \text{ pF}$ .

The measured gap capacitance is 23% greater than the calculated capacitance (section 3.2.1). The difference between the calculated gap capacitance and the measured gap capacitance is due to: the accuracy of the Vernier in measuring the gap length or the error of the calculated discharge area. Based on the gas breakdown curve, the discharge voltage was found to be close to the gas breakdown voltage at 0.15 mm (1.2 kV) calculated according to (3.10), based on Paschen's law:

$$V_b = 6.72\sqrt{pd} + 24.36(pd) \text{ kV} \quad (3.10)$$

Where  $V_b$  is breakdown voltage in kV,  $p$  is the gas pressure in bar,  $d$  represents the distance in cm between the electrodes. The electric field across the gap is 87 kV/cm.

At point E, the local negative ions deposited on the dielectric surface will be neutralized first before the positive ions accumulate and extinguish the filament. The net electric field across the gap is sufficiently strong to ignite the positive discharge which gives (3.11):

$$E_g = E_r + E_a = E_b \quad (3.11)$$

The charge accumulation and the reversed electric field are shown in Figure 3.16.

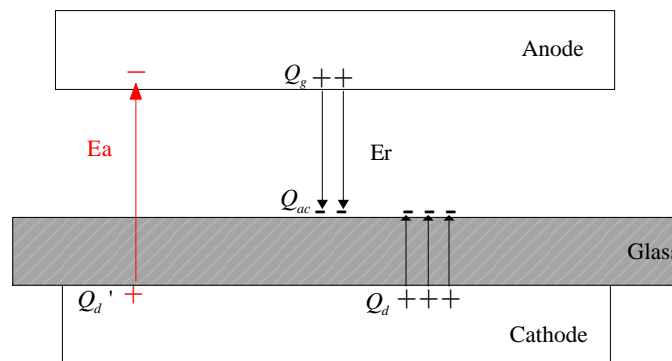


Figure 3.16 The charge distribution across the test cell at point E.

At point E,  $Q_E = -202 \text{ nC}$  and  $V_a = -266 \text{ V}$ , based on (3.4) (3.6) and (3.9), all the related charge can be calculated.

$$Q_E = -(Q_d' + Q_d) = C_t V_a + Q_{ac} \frac{C_d}{C_d + C_g} \quad (3.12)$$

$$Q_d' = -Q_g' = 11nC \quad (3.12a)$$

$$Q_d = |Q_E| - Q_d' = 191nC \quad (3.12b)$$

$$Q_{ac} = -Q_d \frac{C_d + C_g}{C_d} = -264nC \quad (3.12c)$$

$$Q_g = |Q_{ac}| - Q_d = 73nC \quad (3.12d)$$

The applied field can be calculated as (3.13):

$$E_a = \frac{V_g}{d_g} = -13kV / cm \quad (3.13)$$

The reversed electric field is shown in (3.14):

$$E_r = \frac{V_r}{d_g} = \frac{Q_g}{C_g} = 92kV / cm \quad (3.14)$$

The net electric field is shown in (3.15):

$$E_g = E_r + E_a = 79kV / cm \quad (3.15)$$

Once the discharge develops at point F, the applied voltage is equal to zero. The electric field across the gap is the reversed electric field produced by the accumulated charge.

$$E_g = E_r \quad (3.16)$$

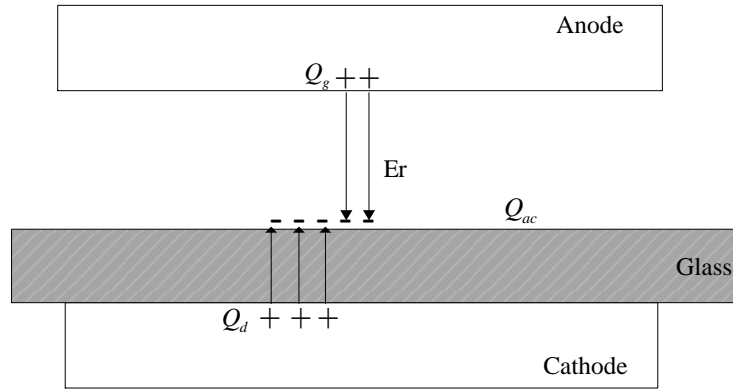


Figure 3.17 The charge distribution across the test cell at point F.

Once the charge across the measurement capacitor is zero at point M, the amount of induced charge  $Q_d$  is equal to the charge induced by power supply  $Q_d'$  as shown in (3.17).

$$Q_M = Q_d' + Q_d = 0 \quad (3.17)$$

According to (3.8), the voltage across the barrier is equal to zero. The voltage across the test cell is equal to the gap voltage which is the gas breakdown voltage. The gap electric field is written as (3.18):

$$E_g = E_r + E_a \quad (3.18)$$

The charge accumulation and the reversed electric field at point M are shown in Figure 3.18.

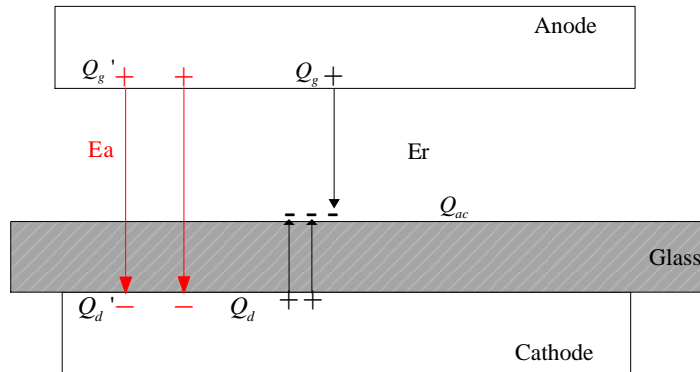


Figure 3.18 The charge distribution across the test cell at point M.

With the increase of voltage to point H, the charge transfer is half of the total charge transfer  $\Delta Q$ , there is no net charge on the barrier surface. The charge on the ground electrode is induced by the applied voltage. The electric field across the gap is equal to the applied electric field.

$$E_g = E_a \quad (3.19)$$

The charge accumulation and the reversed electric field are shown in Figure 3.19.

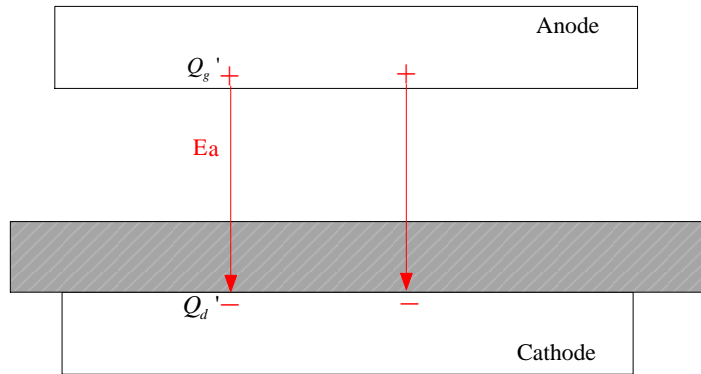


Figure 3.19 The charge distribution across the test cell at point H.

The net charge accumulation between H and A increases with the increase of applied voltage. The direction of the reversed electric field changes due to a positive net charge accumulation. Further decrease of the applied voltage will reduce the gap electric field, leading to the end of discharge in the positive cycle.

$$E_g = E_a - E_r < E_b \quad (3.20)$$

The charge accumulation and the reversed electric field are shown in Figure 3.14.

The charge at points E, F, M, H and A can be calculated and measured by the equations.

Table 3.1 The parameters of each point in Lissajous figure.

	<b>E</b>	<b>F</b>	<b>M</b>	<b>H</b>	<b>A</b>
<b><math>V_a</math> (V)</b>	-266	0	1295	1800	3487
<b><math>Q</math> (nC)</b>	-202	-172	0	63	328
<b><math>Q_{ac}</math> (nC)</b>	-264	237	72	0	260
<b><math>Q_d</math> (nC)</b>	191	172	52	0	-189
<b><math>Q_g</math> (nC)</b>	73	65	20	0	71
<b><math>Q_d'</math> (nC)</b>	11	0	-52	-77	-139
<b><math>Q_g'</math> (nC)</b>	-11	0	52	77	139
<b><math>E_a</math> (kV/cm)</b>	-13	0	63	90	-167
<b><math>E_r</math> (kV/cm)</b>	92	82	25	0	84
<b><math>E_g</math> (kV/cm)</b>	79	82	88	90	83

Based on the calculation results, once the positive discharge happens at point F, the average net electric field across the gap is 84.4 kV/cm with the standard deviation of 4.5 kV/cm. The experimental results are close to the calculated result 87 kV/cm. The amount of the charge transfer increased from -202 nC to 328 nC and the amount of the accumulated charges remains at ~260 nC. The results confirm the analysis of the Lissajous figure. During the discharge phase, the gap voltage remains at the breakdown voltage.

### 3.3 Single filament development

#### 3.3.1 Equivalent circuit of single filament

When the local electric field in the gap exceeds the threshold field of the breakdown, a pulsed discharge of ns duration occurs and the diameter of the filament channel is in the range of 0.1 mm to 1 mm [58].

For each filamentary discharge, it develops in a certain space in the gap, with a corresponding capacitance of  $C_g''$  and the charge will accumulate on the barrier surface with a corresponding capacitance  $C_d''$ . The remaining gap capacitance and the dielectric capacitance can be represented by  $C_g'$  and  $C_d'$ . The total capacitance of  $C_g'$  and  $C_d'$  is named as  $C_t'$ . In addition, there is a stray capacitance in the electric circuit. Figure 3.20 shows the equivalent circuit for a single filament development.

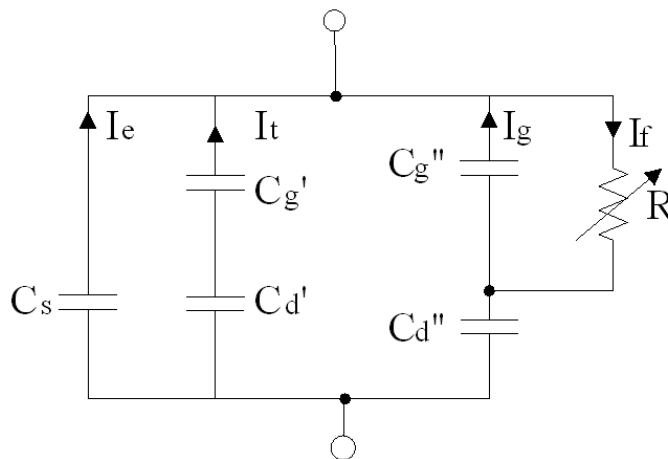


Figure 3.20 Equivalent circuit for a single filamentary discharge.

As the streamer discharge occurs in the gas gap, the voltage across the filament channel drops. Due to the limiting resistor in series with the test cell, the power supply cannot replenish the voltage drop across  $C_g''$ . In this case, the voltage across  $C_t'$  and  $C_s$  drops to replenish the energy

loss in the discharge until the reversed electric field is strong enough to extinguish the filament. In Figure 3.20, the current flowing through the  $C_t'$  sub-circuit is  $I_t$ , the current flowing through the  $C_s$  sub-circuit is  $I_e$ , and the current through  $C_g''$  is  $I_g$ . The total filament current is  $I_f$  described in (3.21):

$$I_f = I_e + I_t + I_g \quad (3.21)$$

The external current,  $I_e$ , measured using a coaxial cable, is the current flowing through the stray capacitance,  $C_s$ . The voltage drop across  $C_t'$  is the same as the voltage drop across the stray capacitance. As  $C_t'$  is much greater than  $C_g''$  and  $C_d''$  in series, the value of  $C_t'$  can be assumed to be the total capacitance,  $C_t$ . In this case, the filament current can be rewritten as in (3.22):

$$I_f = I_e + C_t \frac{dV_a}{dt} + C_g'' \frac{dV_g''}{dt} \quad (3.22)$$

where  $V_a$  is the applied voltage across the test cell and  $V_g''$  is the voltage across  $C_g''$ . Here, the integration of the current flowing through  $C_s$  and  $C_t'$  is the charge transferred onto the barrier surface, causing the voltage to increase across the barrier. When the voltage drops across  $C_g''$  and the accumulated charges on the barrier builds the reversed electric field, the discharge is extinguished. For a given electric circuit of a test cell,  $C_s$  is a fixed value. The ratio between the current is expressed by (3.23).

$$\frac{I_g}{I_e + I_t} = \frac{Q_{g\_single}}{Q_{d\_single}} = \frac{\Delta V_g'' \times C_g''}{\Delta V_a (C_t + C_s)} \quad (3.23)$$

As the discharge area of each filament is variable, the ratio of the two currents is also variable. For a large ozone generator with total capacitance in nF range, the filament current can be approximated as the sum of  $I_e$  and  $I_t$ .

$$I_f = C_s \frac{dV_a}{dt} + C_t \frac{dV_a}{dt} \quad (3.24)$$

The distribution characteristics of the external current are identical to that of the filament current.

## 3.3.2 Effect of the stray capacitance

A zig-zag line is measured in Lissajous figure during the discharge, as shown in Figure 3.21. The discharge process can clearly be identified from A to B, the segment B to C represents the charging process by the power supply.

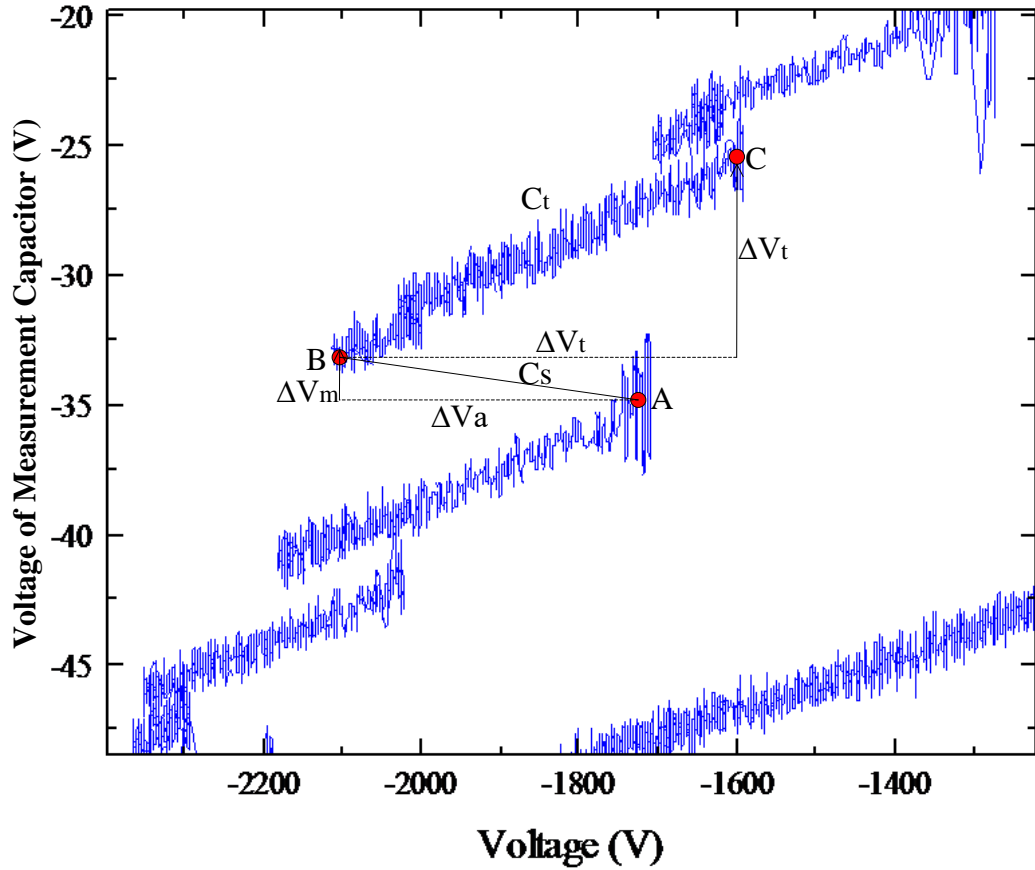


Figure 3.21 A part of Lissajous figure and the analysis of the filament current development progress.

In a few nanoseconds, a voltage  $\Delta V_m$ , 1.7 V, develops across the measurement capacitor,  $C_m$ , and the charge transfer is  $\sim 5$  nC. A corresponding voltage drop,  $\Delta V_a$ , 384 V, across  $C_s$  is developed. The charge transfer through the stray capacitance is shown in (3.25):

$$\Delta Q_s = \Delta V_a \times C_s = 5nC \quad (3.25)$$

where  $C_s$  can be calculated as 13 pF.

The voltage drop across  $C_t'$  can be determined using (3.26):

$$\Delta V_t = \Delta V_a - \Delta V_m = 382V \quad (3.26)$$

At this time,  $C_s$  and  $C_t'$  are both transferring charge to  $C_d''$ , meaning that the charge that increases the barrier voltage accumulated on  $C_d''$  is  $\Delta Q_s + \Delta Q_t$ .

$$\Delta Q_s + \Delta Q_t = \Delta V_a (C_s + C_t') = 20nC \quad (3.27)$$

Here  $C_t'$  is closed to  $C_t$ . In this figure,  $C_t$  can be calculated as 37 pF which is in close agreement with the calculation based on Figure 3.15.

After the filament is extinguished, the power supply will charge the circuit until the voltage across the test cell and the electric field across the gap recover. As  $C_g''$  is much lower than  $C_t'$ , the total charge transfer from the power supply can be estimated as  $\Delta Q_t$ . The charge transferred to the test cell is shown in (3.28):

$$\Delta Q_t = \Delta V_a \times \left( C_t + \frac{C_g'' C_d''}{C_g'' + C_d''} \right) = 14nC \quad (3.28)$$

From the equivalent circuit, the transferred charge  $\Delta Q_g''$  from  $C_g''$  is equal to the charge accumulated on the dielectric barrier surface forming the reversed electric field distinguishing the filament accumulating on the barrier to form the reversed electric field  $E_r$ . For a single filament, the total charge transfer  $\Delta Q_f$  is described by (3.29):

$$\Delta Q_f = \Delta Q_s + \Delta Q_t + \Delta Q_g'' \quad (3.29)$$

The external current measured is supplied by the stray capacitance. By determining the voltage drop  $\Delta V_s$  and the external current  $I_e$ , the stray capacitance can be calculated using (3.30):

$$I_e = C_s \frac{dV_a}{dt} \quad (3.30)$$

Figure 3.22 shows the sampled Lissajous figure with the stray capacitance of 13 pF. In Figure 3.23,  $C_s$  is changed manually by adding a 1 nF capacitor in parallel with the test cell and  $C_m$  and the stray capacitance is 1.14 nF. The applied voltage is 3 kV<sub>p</sub> at 5 kHz.

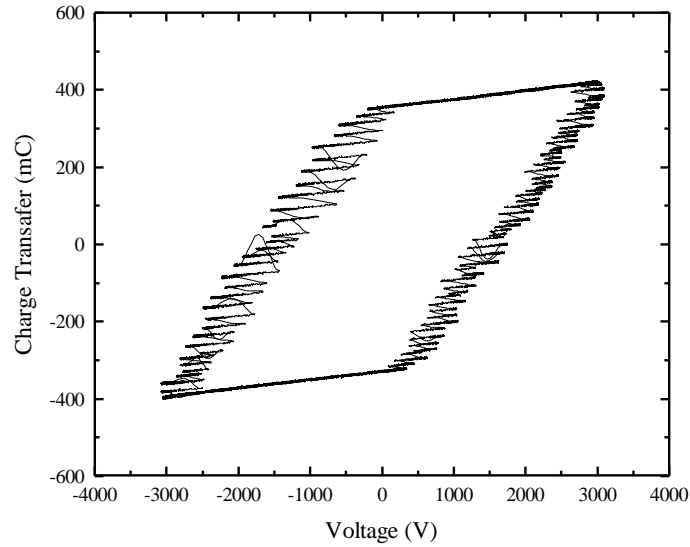


Figure 3.22 The sampled Lissajous figure at 5 kHz with 3 kV<sub>p</sub> power supply without an added 1 nF capacitance. The gap length is 0.15 mm and the barrier thickness is 0.15 mm.

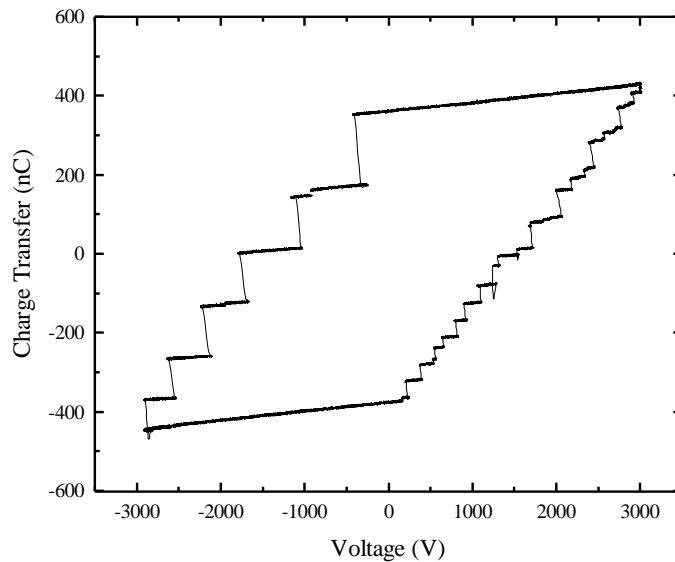


Figure 3.23 The sampled Lissajous figure at 5 kHz and 3 kV<sub>p</sub> power supply with an added 1.14 nF capacitance. The gap length is 0.15 mm and the barrier thickness is 0.15 mm.

By adding a 1 nF capacitor, but without changing the applied voltage, the charge transfer of a quarter-cycle remains 745 nC. The number of filamentary discharge and the voltage drop of each filament decrease dramatically. Figure 3.24 and Figure 3.25 show the sampled external current and voltage drop of a single filament. When adding the stray capacitance, the discharge time of a single filament increases from ~15 ns to ~70 ns. The amplitude of the external current reaches over 1 A.

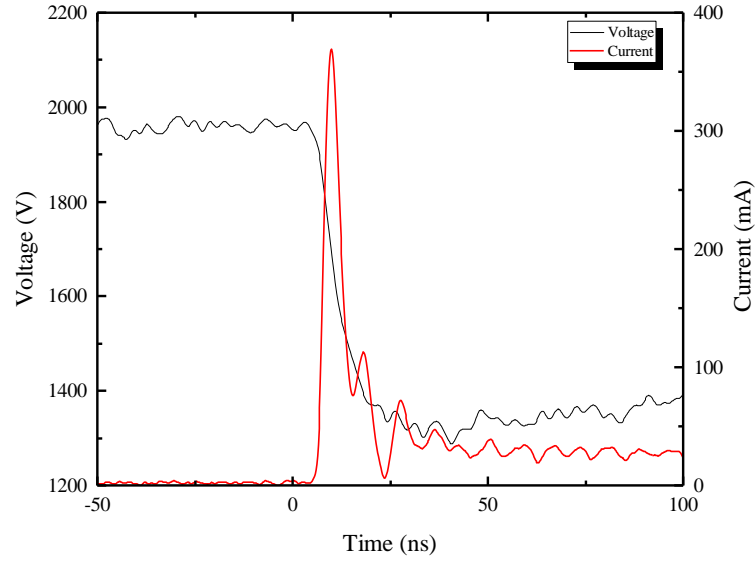


Figure 3.24 The sampled single external current with voltage drop without added capacitor in parallel to the test cell.

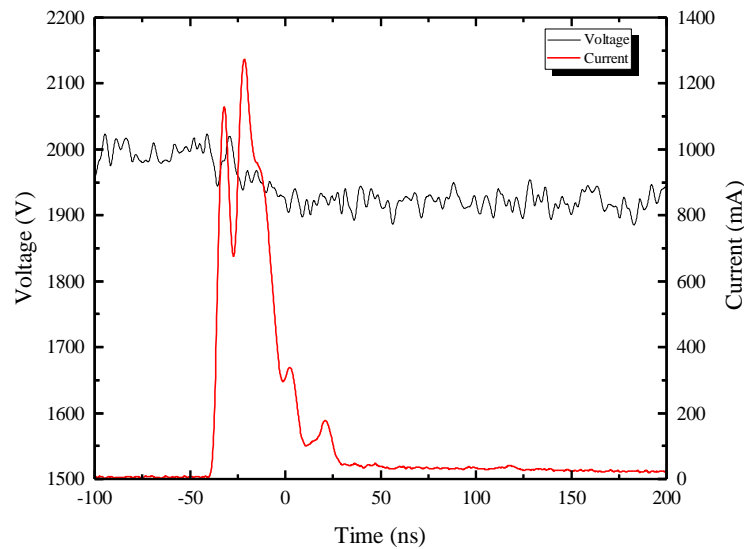


Figure 3.25 The sampled external current and voltage drop with the added 1 nF capacitor.

The total charge transfer per filament increases when adding a capacitor while the voltage drop across the test cell decreases. The criteria for extinguishing the filament depend on the electric field across the gap. Since  $C_d''$  is in series with  $C_g''$ , the charge transfer across  $C_d''$  is equal to the total charge transfer of  $C_r$  and  $C_s$  in parallel. As  $C_r$  in this case is much lower than the stray capacitance  $C_s$  (1.14 nF) while the voltage across  $C_r$  is the same as  $C_s$ , then  $\Delta Q_s \gg \Delta Q_r$ . The voltage increase across  $C_d''$  is due to the voltage drop across  $C_s$ . Thus, we have (3.31) and (3.32):

$$\Delta V_a C_s = -\Delta V_d C_d \quad (3.31)$$

$$\Delta V_g = \Delta V_a - \Delta V_d = \Delta V_d \left(1 - \frac{C_d C_s}{C_d + C_s}\right) \quad (3.32)$$

For the same  $\Delta V_a$ , a higher  $C_s$  implies more charge transfer to  $C_d$ .

The results indicate that for the same gap length, the required electric field is the same, which means the required voltage across the discharge gap does not change. As the value of the stray capacitance is much greater than the equivalent gap capacitance, the voltage drop across the discharge gap can be replenished rapidly by the stray capacitance. To reach the required electric field for extinguishment, the discharge period must be longer.

In general, for a large ozone generator with a total capacitance in nF range, the filament current can be approximated as the sum of  $I_e$  and  $I_r$ . The distribution characteristics of the external current are identical to those of the filament current.

### 3.4 Discharge behaviour in the first three cycles

In this subchapter, the transient dielectric barrier discharge properties are explored by investigating the current and voltage waveforms and Lissajous figure in the first few cycles.

#### 3.4.1 Lissajous Figure analysis

In the steady state dielectric barrier discharge, the charge accumulation on both discharge phases is equal. The positive discharge phase will produce a  $\Delta Q$  charge to neutralise the  $|\frac{1}{2} \Delta Q|$  charge that accumulated in the preceding discharge phase.

To determine the statistic of charge transfer, the smart power supply is used to generate only one cycle of the power applied to a test cell with 0.3 mm barrier thickness and 0.2 mm gap length. Figure 3.26 shows the Lissajous figure for the first cycle.

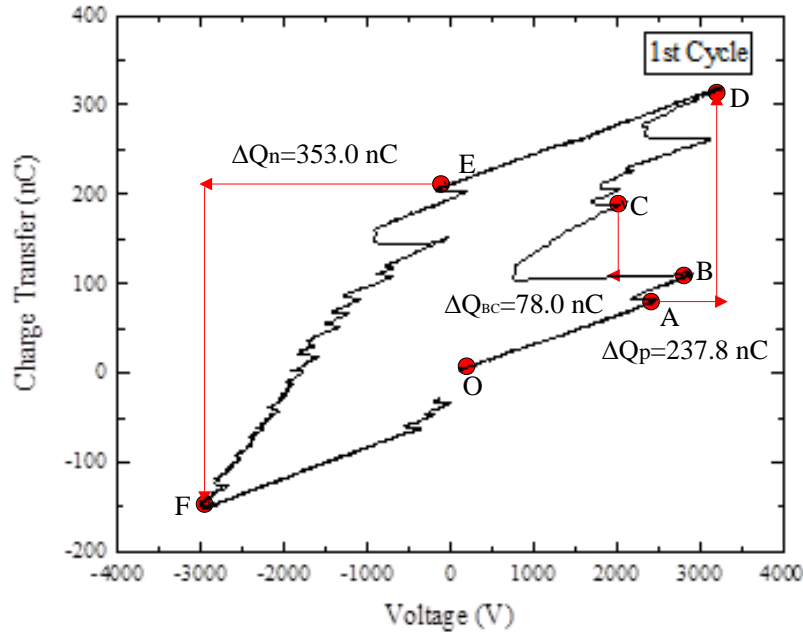


Figure 3.26 The sampled Lissajous figure of the first cycle of discharge.

At point O, the power supply is enabled where the charge transfer  $Q$  is equal to zero and the applied voltage  $V$  is close to zero. With the continuous increase of the voltage to point A, the discharge begins. The first discharge occurred at  $\sim 2.5 \text{ kV}_p$  at this moment the gap voltage is over  $1.8 \text{ kV}$  which is 1.4 times greater than the breakdown voltage ( $1.3 \text{ kV}$ ) at steady state. From point B to C, the voltage drop is more than  $2 \text{ kV}_p$ . The charge transfer  $Q_{BC}$  is approximately  $78 \text{ nC}$ . From point A to point D, the charge transfer is  $237.8 \text{ nC}$ . For the positive discharge in the first cycle, the discharge is strong with higher amplitude of external current and longer discharge time per micro-discharge. Once the applied voltage reached the peak value, the discharge of the positive cycle stopped. At point E, the negative discharge started. When the charge transfer is  $\sim 200 \text{ nC}$ , the applied voltage is  $-200 \text{ V}$  which is much lower than that of the positive discharge phase. For the negative half-cycle, the total charge transfer is approximately  $353 \text{ nC}$ . Due to the non-uniform accumulated charge distribution on the barrier surface in the positive discharge phase, the electron density is not uniform. The negative discharge firstly happens at the point where there is higher electron density. The upcoming discharge should produce double the charge to neutralise the accumulated charge on the barrier surface. As introduced in 3.2.3, half of the charge transfer per discharge cycle is used to neutralize the opposite polarity charges accumulated on the barrier surface, and the other half of the charge transfer per discharge cycle is accumulated on the barrier surface and waiting to be neutralized by the opposite polarity charges. The total charge transfer of the

negative cycle is less than twice the total charge transfer of the positive cycle. In this case, an offset of the charge transfer (150 nC) is observed.

The Lissajous figure for the second cycle was measured, as Figure 3.27 shows.

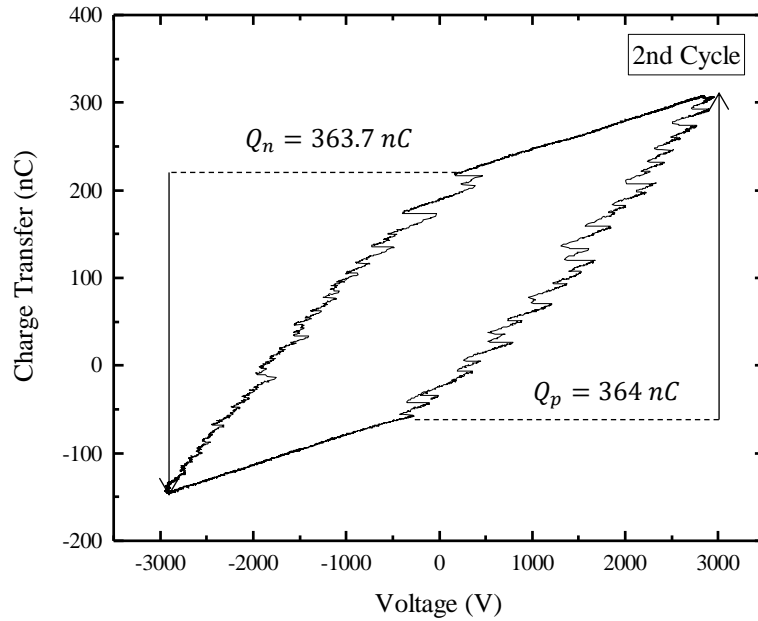


Figure 3.27 The sampled Lissajous figure of the second cycle discharge.

The charge transfer of the positive cycle is 364.0 nC, compared to 363.7 nC in the negative cycle. The offset net charge on the barrier surface remains 150 nC. The offset charge was neutralized with time because of the leakage current through the barrier. Figure 3.28 shows the Lissajous figure of the 100<sup>th</sup> cycle.

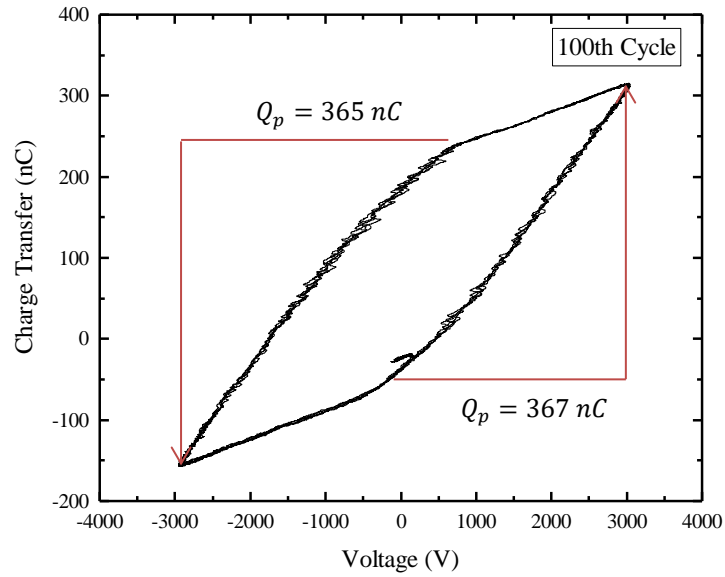


Figure 3.28 The sampled Lissajous figure of the 100<sup>th</sup> cycle.

When comparing the total charge transfer in the 100<sup>th</sup> cycle and the total charge transfer in the second cycle, there is not a significant difference. Thus, it can be said that the discharge is in steady state.

### 3.4.2 Current and voltage waveform analysis

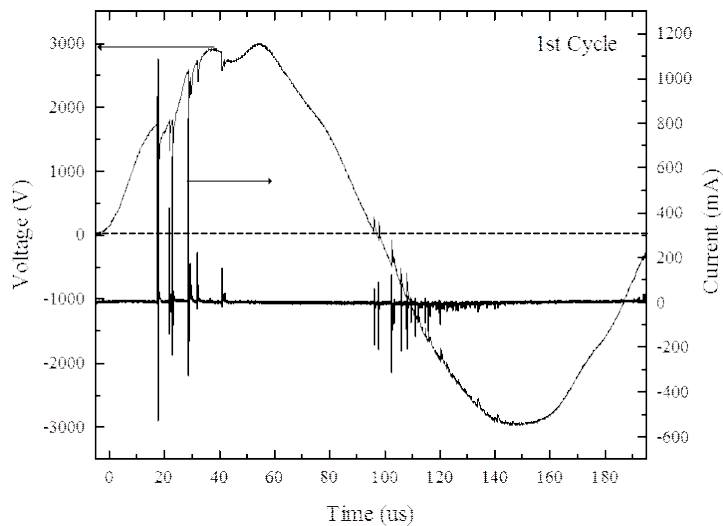


Figure 3.29 The sampled external current and voltage waveforms in the first cycle.

At the beginning of the discharge, without any charge accumulation on the barrier surface, the first discharge occurred when the applied voltage was 1.8 kV<sub>p</sub>. The amplitude of the

external current is over 1 A with an 800 V voltage drop. The duration of the first discharge is  $\sim 30$  ns. In the positive half-cycle, there were seven discharges, which is less than the number of discharges in the steady state. In the negative half-cycle, the discharge is ignited at 0 V. The average amplitude of the external current is much less than it is in the positive half-cycle.

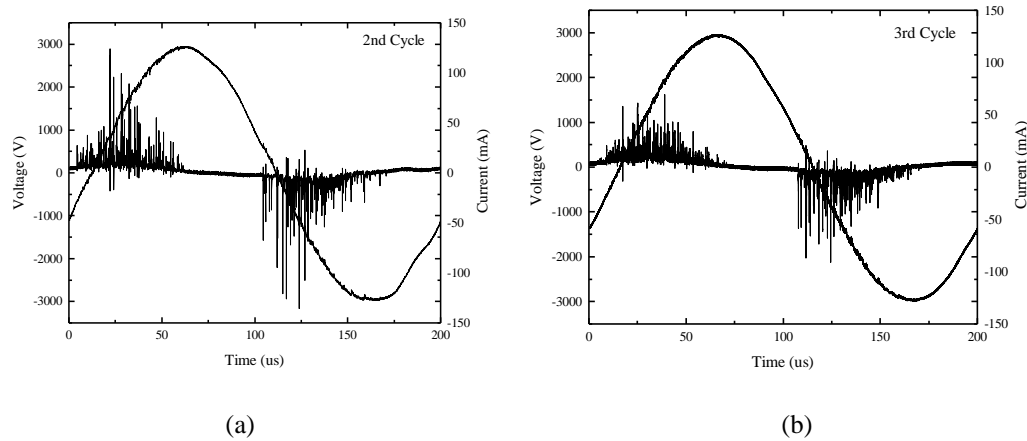


Figure 3.30 The sampled external current and voltage waveforms (a) in the second cycle and (b) in the third cycle.

In the sampled second cycle, the average amplitude of the external current is 48 mA. Compared to the maximum amplitude of the external current in the first cycle, the maximum amplitude in the second cycle is only 125 mA which is 8 times less than the maximum current amplitude of the first cycle. With regard to the positive discharge period, the amplitude of the external current in the second cycle is much lower than the amplitude in the first cycle. The voltage drop of the discharge is below 100 V on average. The average amplitude is 53 mA with a maximum amplitude of only 130 mA. The number of discharges in both the positive and negative cycles increased dramatically compared with the results for the first cycle.

In Figure 3.30 (b), the average amplitude of the external current for the positive discharge period is 28 mA. The distribution of the third cycle becomes more uniform, with a maximum amplitude of 75 mA. In the negative discharge cycle, the average amplitude of the external current is 45 mA. The maximum amplitude for the negative discharge period is only 80 mA. Comparing the current waveform in Figure 3.30 and the current waveform at steady state shown in Figure 3.13, the discharge becomes stable in 3 cycles.

### 3.5 Electrical properties of APGD

In this section, the discharge characteristics of a limited condition are investigated: atmospheric pressure glow discharge (APGD). This type of discharge can be seen as many filamentary discharges occurring at the same time, with the charge moving towards the opposite polarity electrode. According to the current performance, it is a continuous discharge with microseconds time period to produce a uniform electron density across the gap. Massines concluded in his research that the number of electrons in the gap were sufficient to produce the next breakdown under a low electric field, which is a necessary condition to obtain an APGD [59].

#### 3.5.1 Test cell design and experimental setup

The cylindrical test cell that is developed with a dielectric barrier is a quartz tube with a 7 mm inner diameter and a 10 mm outer diameter and is 200 mm length. The high-voltage electrode is a stainless-steel rod with 6.4 mm diameter and 180 mm in length. The gap length is set by a 0.3 mm thick stainless-steel wire around the high-voltage electrode. For the ground electrode, aluminium foil 150 mm in length is attached to the quartz tube. The input gas is pure helium with a flow rate of 0.3 L/min. A 5 kHz smart-power supply is used to generate high frequency power. Figure 3.31 shows the design of the test cell.

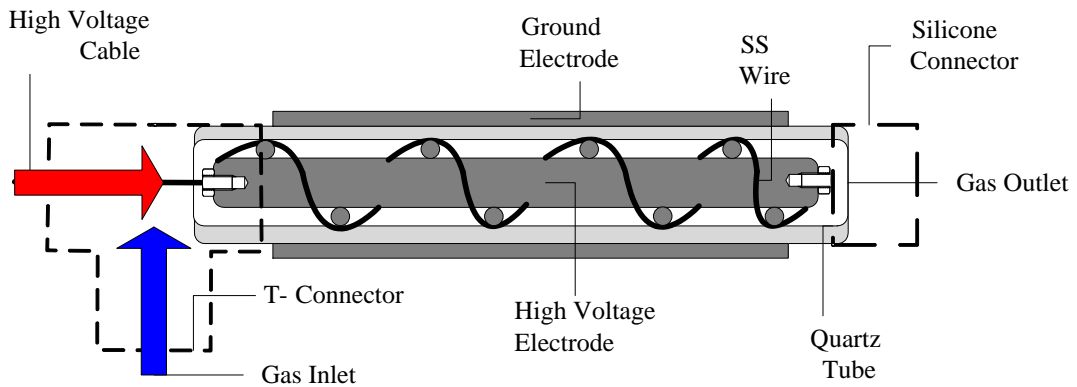


Figure 3.31 The design of the cylindrical test cell.

#### 3.5.2 Discharge characteristics

##### A. Discharge voltage and current

Figure 3.32 shows the sampled current and voltage waveforms of a full cycle with an applied voltage of 2 kV<sub>p</sub> at 5 kHz. The discharge only occurred with the increment of the electric field across the gap. The ignition voltage of the positive cycle is -980 V. For the single pulsed

current, the peak current is below 20 mA in a period of a few microseconds. When continuously increasing the applied voltage, the number of discharges increased.

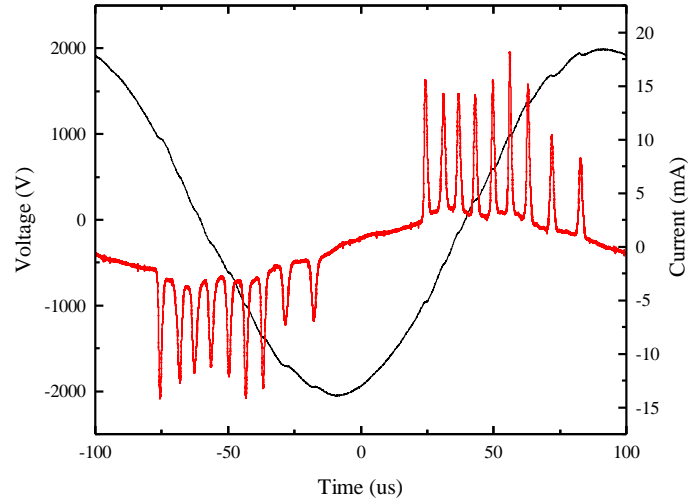
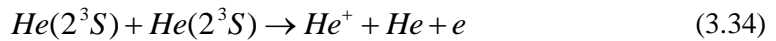


Figure 3.32 A sampled voltage (solid black line) and current (solid red line) waveform at APGD with helium input with 2 kV<sub>p</sub> applied voltage at 5 kHz, 1 atm.

Because of the metastable states of helium,  $He(2^3S) + 19.73 \text{ eV}$  and  $He(2^1S) + 20.61 \text{ eV}$ , the discharge period of a single micro-discharge is longer than nanoseconds. The lifetime of  $He(2^3S)$  is 15  $\mu\text{s}$  [60] and  $He(2^1S)$  is 19.5 ms [61]. The ionisation energy of helium is 24.6 eV [62], which means that the energy needed to ionise the metastable state helium is less than 5 eV. The ionisation processes are shown in (3.33) and (3.34) [63].



The metastable state helium atoms are the source of high-energy electrons. The energy accumulated in the metastable states is released gradually in the discharge channel, and a glow discharge is sustained [64].

The electrical properties of Boeuf's results [65] are shown in Table 3.2.

Table 3.2 The electrical parameters of APGD DBDs.

Conditions	1 atm He
Gas Gap	0.5 cm
Current pulse duration	$> 1 \mu s$
Filament radius	Uniform
Peak current density	$\sim 1 \text{ mA/cm}^2$
Total charge transferred	$13 \text{ nC/cm}^2$
Peak electron density	$< 10^{11} \text{ cm}^{-3}$
Electron energy	1 – 5 eV

According to a numerical model, a density of electrons higher than  $10^6 \text{ cm}^{-3}$  at the breakdown voltage is necessary to obtain an APGD controlled by a dielectric layer. The highest electron density of Massine's experiment is about  $10^{11} \text{ cm}^{-3}$  [59], in agreement with Boeuf's results [65].

#### **B. The effect of water vapour**

Figure 3.33 shows the line spectra of atomic helium at  $2 \text{ kV}_p$  power supply using the Ocean Optic spectrometer. Along these lines, the 656.05 nm is close to a typical line spectrum of atomic hydrogen at 656.27 nm.

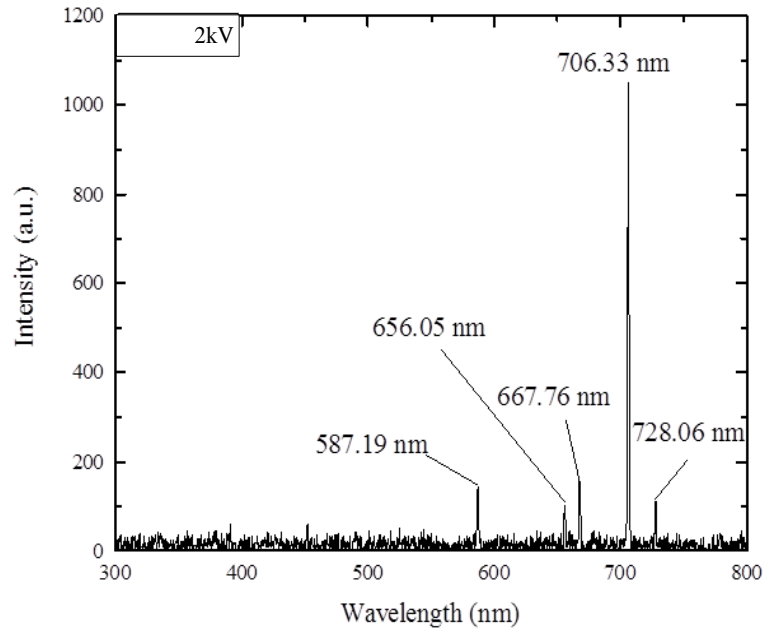


Figure 3.33 The atomic helium spectra using DBD at 5 kHz, 2 kV<sub>p</sub> applied voltage and 1 atm.

Based on the datasheet from NIST [66], the Table 3.3 lists the most proximate atomic line spectra.

Table 3.3 Atomic line spectra comparison between observed database and referenced database.

Lower State	Higher State	Observed Wavelength Air (nm)	Referenced Wavelength on NIST (nm)
He (1s2p)	He (1s3d)	587.19	587.56
H (2s)	H (3p)	656.05	656.27
He (1s2p)	He (1s3d)	667.76	667.82
He (1s2p)	He (1s3s)	706.33	706.52
He (1s2p)	He (1s3s)	728.06	728.13

Because the water vapour can also react with electrons as shown in (1.28), the probability of the ionisation of metastable state helium decreases. By passing helium gas through a copper coil which is immersed in a liquid nitrogen flask, the water vapour is solidified. The current and voltage waveforms at 2 kV<sub>p</sub> without water vapour are shown in Figure 3.34.

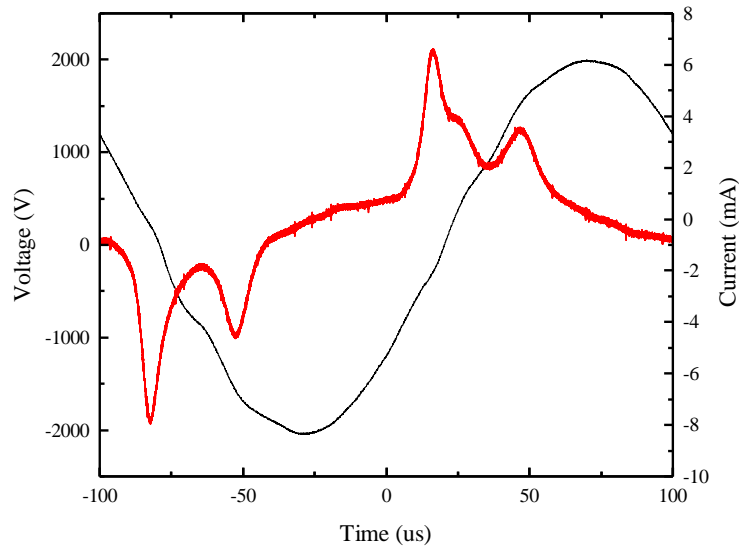


Figure 3.34 The current (solid red line) and voltage (solid black line) waveform of helium discharge without water vapour.

With the same applied voltage and frequency, the discharge period of the positive cycle is  $50 \mu\text{s}$  with the current of only  $7 \text{ mA}$ . The second pulse is ignited immediately after the first pulse with the same discharge duration yet much lower current amplitude. For the negative discharge, the first micro-discharge is ignited at  $-1000 \text{ V}$ . The duration of the current in the negative cycle is the same as that in the positive cycle with  $\sim -8 \text{ mA}$  peak value. The discharges of both positive and negative cycle are consecutive, a residual current is observed in Figure 3.34 after the discharges. The Figure 3.35 shows the line spectra of atomic helium without the humidity effect.

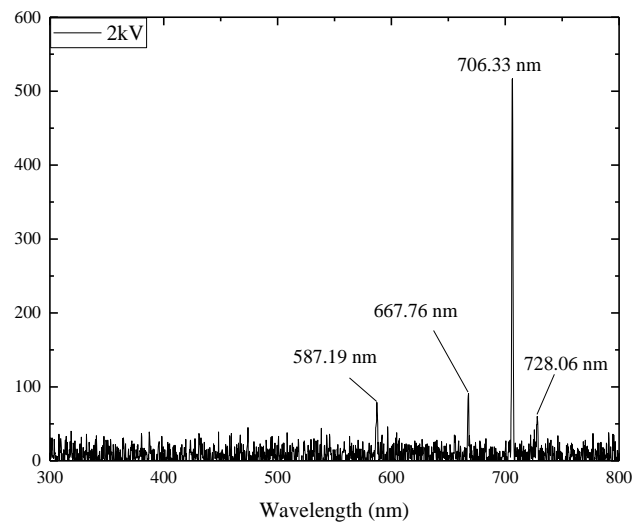


Figure 3.35 The line spectra of atomic helium without humidity effect.

The discharge characteristics of APGD in different gases is investigated by Okazaki *et al.* [67]. According to Kogoma's research [13], ozone efficiency in a homogeneous glow discharge at atmospheric pressure is measured and compared with that in a filamentary discharge. The results showed that the ozone efficiency in APGD is 10% higher than that of filamentary discharge in air. The ozone efficiency in APGD is also 15% higher than that of filamentary discharge in oxygen. Kogoma's team expected that the high ozone efficiency is due to the electron collision with molecules. In a filamentary discharge, the charge density is higher than that in a APGD. The collision efficiency between electrons and molecules in a APGD should be higher than that in a filamentary discharge [68][69] due to the uniform distribution of electrons across the gap. Also, the lower temperature increment in the micro-discharges in APGD can increase the ozone efficiency while along the filamentary discharge, temperature increases may promote the decomposition of ozone.

Nakai *et al.* investigated the APGD discharge generated in air using an alumina barrier at a frequency range of 32 Hz to 1 kHz [70][71]. The ozone efficiency comparison between APGD and filamentary discharge was also investigated. The ozone efficiency in the filamentary mode in pure oxygen was 247 g/kWh, which is much higher than that in the APGD mode (33 g/kWh) with the same specific energy input. The ozone efficiency using APGD discharges remained the same when increasing the specific input energy ( $J/L$ ). The expected reason is the much lower electric field strength in the APGD compared with that in the filamentary discharge. The electrons cannot get enough energy to dissociate oxygen molecules where the elastic collision cross section is between  $4 \times 10^{-16}$  to  $10 \times 10^{-16}$  cm<sup>2</sup> and the electron energy is in the range from 0.1 eV to 5 eV.

According to Nakai's results [71], the authors claimed that as the electron density under APGD is much lower than that under filamentary discharge, the density of oxygen atom is therefore, lower under APGD. The ozone formation rate is much slower. According to the observation, the breakdown voltage of helium under APGD and filamentary modes does not show a big difference. The reduced electric field therefore is the same under the same gap length. The electron energy under the APGD discharge mode is comparable with that under filamentary discharge. Moreover, as the electron distribution is quite uniform, the produced ozone molecules are more likely to collide with electrons to be dissociated. The increment of ozone dissociation leads to the low ozone efficiency of APGD. However, to date, no specific research has clearly indicated the ozone efficiency in different discharge modes.

### 3.6 Conclusion

In this chapter, the dielectric barrier discharge properties were investigated. Measuring the external current accurately is critical in order to improve the analysis of filament development. The optimised ways both by minimising the oscillation in the circuit and by the advanced equivalent circuit analysis have been discussed clearly. To minimise the circuit oscillation, the wires should be as short as possible to reduce the influence of stray capacitance and the impedance of the coaxial cable should be matched. The discharge currents associated with DBD were found to conform to a Gaussian distribution. It is also found that the current associated with one single micro discharge corresponded to one pulsed emitted light signal.

During the development of a micro-discharge, the electrons first leave the cathode within 5 ns to form the electron avalanche, and then, the negative space charge is formed at the anode in 10 ns when the electron avalanches arrive at the anode followed by the development of the reverse propagation towards the cathode. Just before the peak of the total current, the positive streamer develops and the electron density of the central streamer can be  $10^{14} \text{ cm}^{-3}$  [72]. After the accumulated charge on the dielectric barrier establishes a reversed electric field, the filament is extinguished. The reversed electric field to extinguish the filament discharge is related to the voltage drop across the filament. The charge transferred through the discharge gap was verified to be equal to the charge transferred in the external circuit, through the quantitative analysis of the accumulated charge on the dielectric surface.

The determination of the filament current, which contains three parts of the current (the current passing through the stray capacitance, the current due to the voltage drops across the total capacitance and the current due to the voltage drop across the discharge gap channel) is made. The charge transfer from the stray capacitance and the total capacitance can cause the voltage to increase across the affected dielectric barrier.

In addition, the transient state dielectric barrier discharge process is analysed. From the result, we can see that the dielectric barrier discharge can be balanced quickly in the first few cycles. The discharge started from second cycle is more stable. The accumulated charge on the barrier will form a relatively uniform distribution on the barrier surface. A higher current amplitude micro-discharge with more charge transfer can carry more energy, and the increasing number of electrons can reduce the ozone efficiency. In the next chapter, the relationship between the filament current and ozone generation efficiency will be discussed using the planar configuration dielectric barrier discharge.

Finally, a uniform discharge is achieved in helium with much longer discharge period of microseconds compared with that under filamentary discharge. It is found that the reduced electric field under APGD is the same as that of filamentary discharge. The analysis shows that the higher collision frequency of electrons and ozone molecules leads to a decreased ozone efficiency.

The discharge characteristics of DBD help to clarify the better ozone generation discharge environment. The reduced electric field and the current distribution can be manipulated by changing physical and electrical parameters. The relationship between these parameters and ozone efficiency will be investigated in Chapter 4.

## 4 Current Distribution and Ozone Efficiency using Planar Electrodes

### 4.1 Introduction

#### 4.1.1 Motivation

Filamentary DBD is the most commonly used method for industrial ozone generation in recent years. For commercial scale ozone generator, the system operates between one and three bars (normally at two bars) and at 0.5 to 5 kHz with a gap length of 1 mm. The average temperature of the discharge gap can be determined by measuring the temperature of the cooling water. The most commonly used electrode design is the cylindrical type, as shown in Figure 4.1 [73]. The low-loss dielectrics of high breakdown strength such as glass, quartz or ceramic plates are the most commonly used dielectric material. Inside the glass tube is an inner metal coating, which acts as a high-voltage electrode. Outside the quartz tube is a discharge space of between 0.5 and 1 mm radius. With narrow gaps, the electrical field at breakdown can be strongly influenced by varying the gap spacing or the particle density in the gap [74]. The choice of gap length is a compromise between reducing the gap breakdown voltage and increasing the discharge volume for ozone formation. The outer surface of the tube is in contact with a metallic electrode [75]. The outer electrode is made from stainless steel that has been earthed and water cooled. The feed gas streams into the gap between the inner quartz tube and the outer steel tube.

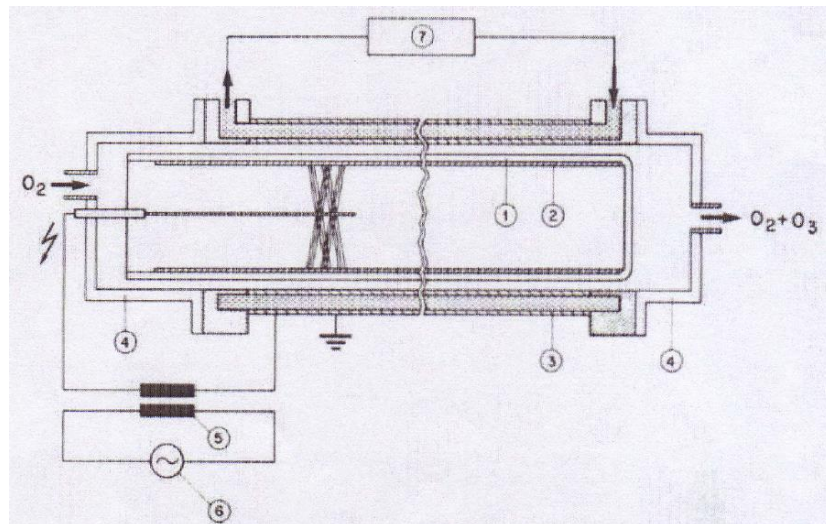


Figure 4.1 Typical electrode configuration of the dielectric barrier discharges [73].

According to the research, the highest ozone efficiency using dielectric barrier discharge at room temperature can be up to 225 g/kWh which corresponds to only 18.4% electron energy efficiency. In industry, the normal ozone efficiency is between 150 g/kWh and 180 g/kWh with ozone production of 100 g/Nm<sup>3</sup> to 150 g/Nm<sup>3</sup> [74]. By changing the discharge gap, the operating pressure, the thickness of the barrier and the cooling water temperature, ozone generation efficiency is optimised, as the filament discharge properties can be tailored to minimise the recombination of oxygen atoms. The current properties are related to the filament discharges, which can affect the ozone generation efficiency. As a result, the investigation of current distribution and ozone generation efficiency was undertaken.

#### 4.1.2 Objectives

In Chapter 4, the external current distribution and the filament current of a single pulse were investigated. The distribution of the charge transfer of a filament was related to the filament radius and the diffusion area on the barrier.

The external current distribution using a planar-plate dielectric barrier discharge is investigated at different applied voltages, gas pressures and barrier thicknesses.

Ozone efficiency was investigated by changing

- The dew point from -40° C to -60° C.
- The applied voltage from 4.5 kV<sub>p</sub> to 6.5 kV<sub>p</sub> in 0.5 kV increments.
- The absolute pressure from 1 bar to 1.6 bar in 0.2 bar increments.
- The gap length from 0.1 mm to 0.3 mm in 0.1 mm increments.

The ozone efficiency (g/kWh) versus the reduced electric field ( $E/N$ ) curve was investigated.

## 4.2 Experimental setup

### 4.2.1 Test cell design

In this experiment, a planar-plate electrode configuration with one barrier was used. A schematic diagram of the test cell is shown in Figure 4.2. Two stainless steel (SS316) plates with a 1 mm thickness and 30 mm diameter formed the electrodes. A square glass cover, with  $\epsilon_r = 6.7$ , was used as a dielectric barrier and was attached to the ground electrode. The length

of the barrier was 50 mm and the thickness was 0.2 mm. Between the barrier and the high-voltage electrode, four lengths of 5 mm square glass were attached at the edge of the barrier as spacers to maintain the gap length. A hole with a diameter of 2 mm at the centre of the high-voltage electrode formed a gas inlet at the top of the test cell. The input gas diffuses to fill the entire gas gap. After the discharge, the gas will pass to the ozone analyser.

The test cell was located centrally in two PTFE lids. The outer diameter of the lids was 150 mm with a 100 mm inner diameter and a 3 mm deep groove in the centre. The thickness of the PTFE was 20 mm. There was a groove at the edge of the bottom lid in which to place a silicone O-ring. There were six screws at the edges of the lids to seal the test cell. The circuit connection consisted of two straight stainless-steel tube connectors with 6 mm holes at the centre of the top and bottom lids. These connectors could be used as gas inlets and outlets. There was a stainless-steel spring in the bottom stainless steel connector. The outer diameter of the spring was 6 mm.

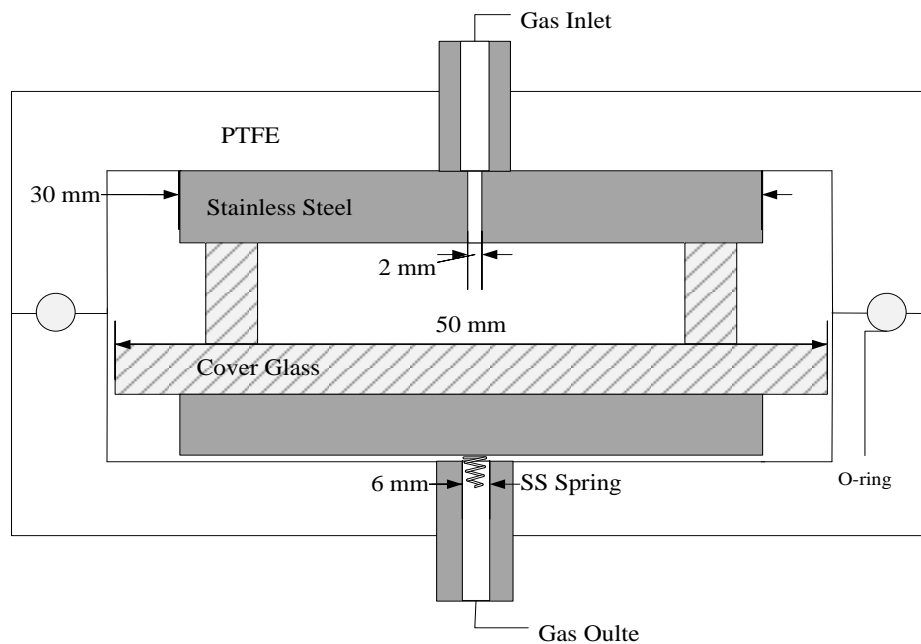


Figure 4.2 Test cell design constructed with 30 mm diameter SS316 stainless steel electrodes and 50 mm diameter cover glass.

#### 4.2.2 Experimental arrangement

Figure 4.3 shows the experimental arrangement. A high-frequency (up to 5 kHz) power supply (Pacific Smart Source 112-AMX) was connected to a 1:22 transformer (up to 7 kV<sub>rms</sub>). A

10 k $\Omega$  current-limiting resistor was connected between the output of the transformer and the test cell. The ground electrode was connected to a digital storage oscilloscope (LeCroy WaveRunner 625 Zi) via a 50  $\Omega$  coaxial cable. A high-voltage probe (Tektronix P6015A 1000:1 3.0 pF 100 M $\Omega$ ) was connected to a high-voltage electrode in parallel to measure the voltage input. The current output was measured using an RG 405 coaxial cable with 18 GHz bandwidth and 50  $\Omega$  impedance connected to the ground electrode. The ozone efficiency was measured by adding a 15 nF capacitor in series with the ground electrode. The voltage across the measurement capacitor was measured using a passive probe.

In front of the gas inlet, a flow meter and a stainless-steel valve were added to control and maintain the gas flow rate and to measure the gas inlet temperature. A hygrometer was connected after the flow meter to measure the gas humidity. A pressure meter was connected after the test cell to measure the pressure. After the pressure meter, a stainless-steel needle valve was added to adjust the pressure in the test cell. An ozone analyser (BMT 964 up to 10,000 ppm) was connected to measure the ozone concentration. Finally, the gas passed through the ozone destructor before being exposed to the air.

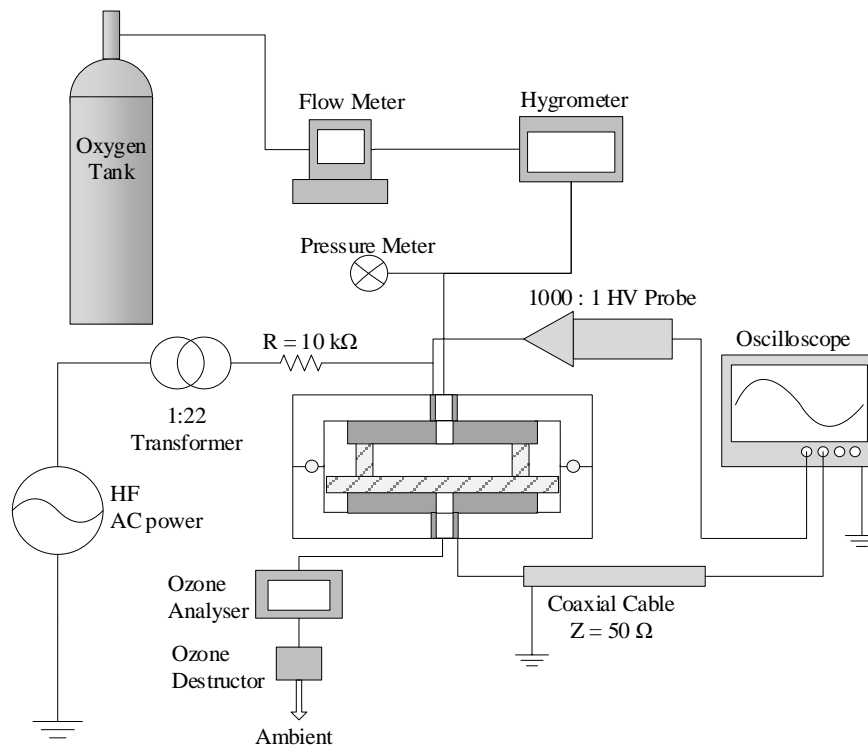


Figure 4.3 Experimental setup.

The calculated gap capacitance and dielectric barrier capacitance are shown in Table 4.1:

Table 4.1 The calculation of equivalent capacitance based on Lissajous figure at different gap lengths and barrier thicknesses.

	<b>0.1 mm</b>	<b>0.2 mm</b>	<b>0.3 mm</b>
Cg (pF)	64.8	54.5	33.27
Cd (pF)	331.4	180.1	133.7

### **A. Energy input**

According to the analysis in Section 1.3.2, an increase in gas temperature leads to an increase in the rate of ozone dissociation, while the ozone production rate reduces. In order to achieve higher ozone efficiency, balancing the temperature in the test cell is crucial. In this experiment, the power supply was only enabled for 100 cycles for each test in order to minimise the influence of gas temperature.

### **B. Current distribution measurement**

To analyse the distribution of the current, the amplitude of the external current was logged by the oscilloscope. It captured 5,000 single pulsed currents to analyse the amplitude of the external current under different conditions and the histogram figure was developed.

## **4.3 Current amplitude distribution analysis**

In this section, the external current distribution was investigated by measuring the peak value at different applied voltages, gas pressures and barrier thicknesses. Figure 4.4 shows the sampled single current and voltage waveforms of a micro-discharge with a 0.2 mm barrier thickness and a 0.2 mm gap.

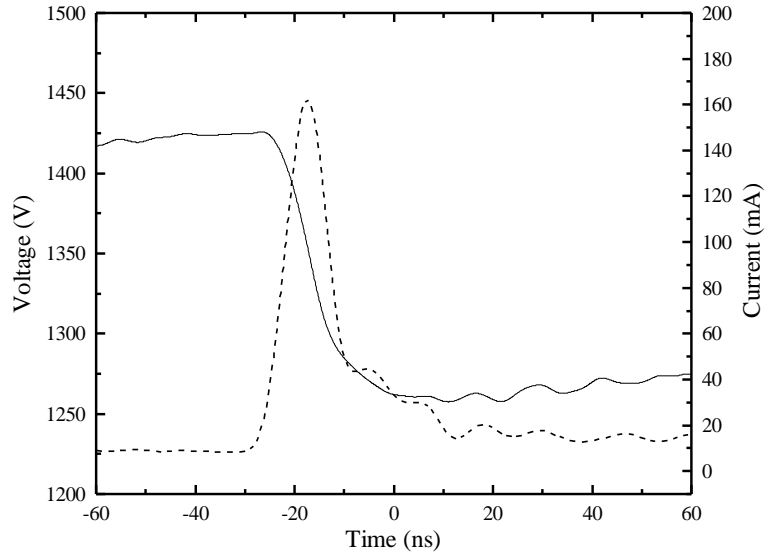


Figure 4.4 Single measured external current (dashed line) with corresponding voltage drops across the stray capacitance (solid line).

The duration of the discharge (fall time) was 15 ns. The amplitude of the external current was ~162 mA with ~150 V voltage drop.

#### 4.3.1 Applied voltage and current distribution analysis

The experiment was carried out with a barrier thickness of 0.2 mm and a gap of 0.2 mm at 1 bar by adjusting the applied voltage from 2 kV<sub>p</sub> to 3.5 kV<sub>p</sub> in 0.5 kV<sub>p</sub> increments. The current distribution at different applied voltages is shown in Figure 4.5.

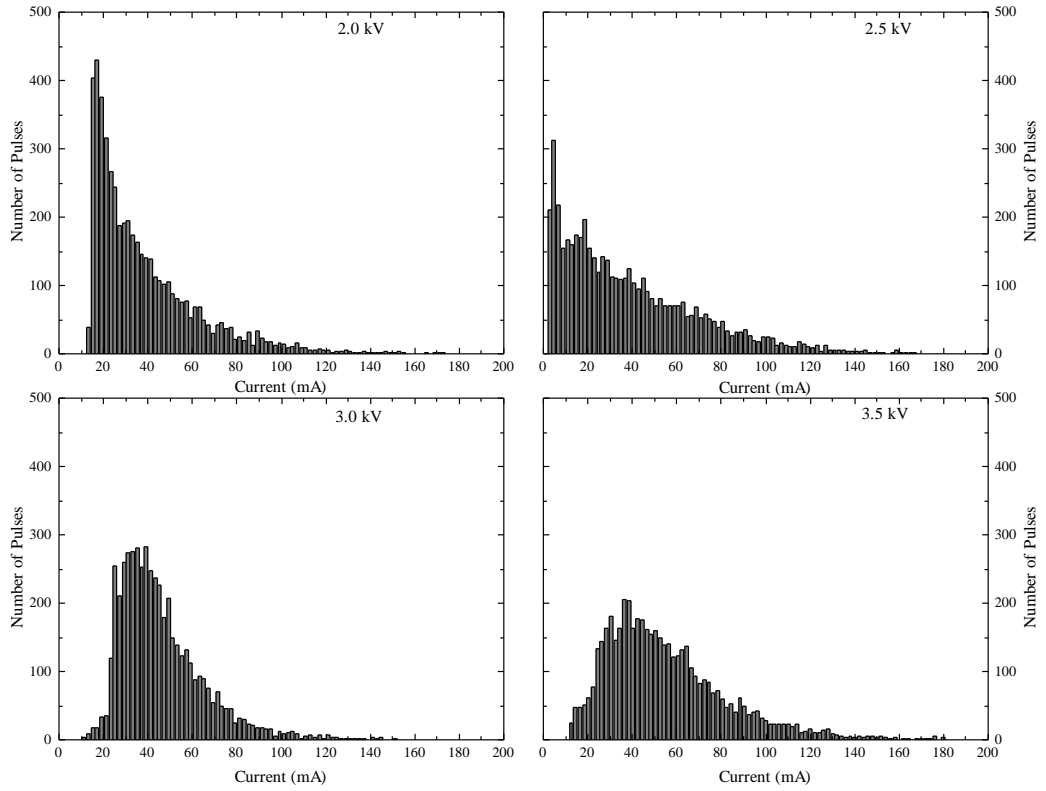


Figure 4.5 The external current distribution at different applied voltages.

Table 4.2 Current analysis under different applied voltage.

Applied Voltage (kV)	Minimum Current(mA)	Peak Current(mA)	Maximum Current(mA)	Average Current (mA)	Peak
2.0	12.6	173.0		38.0	
2.5	2.8	167.0		38.7	
3.0	11.2	151.0		46.1	
3.5	12.4	180.0		55.3	

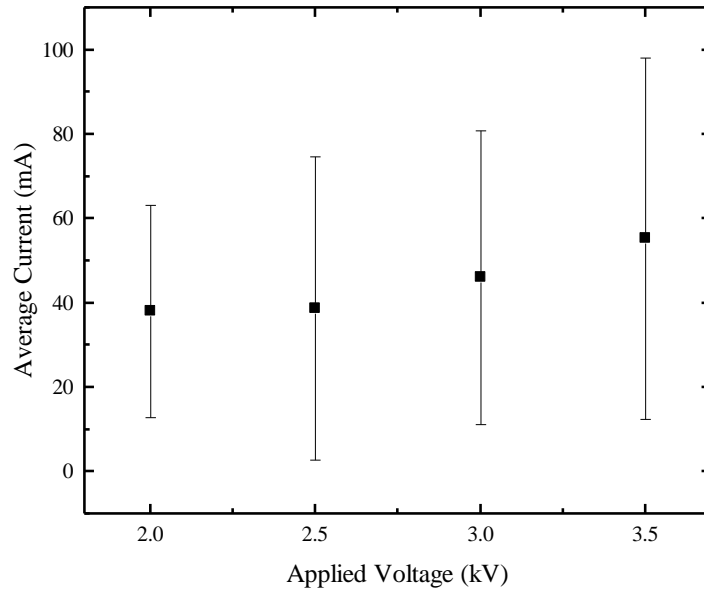


Figure 4.6 The average peak current at different applied voltages.

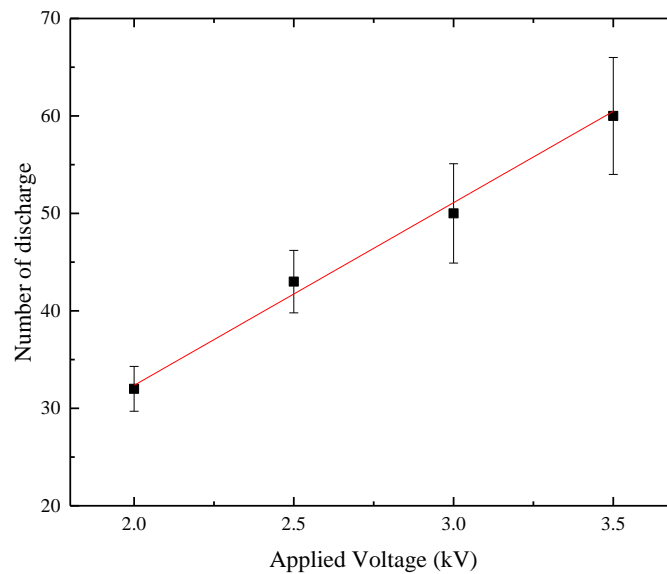


Figure 4.7 Number of micro-discharges of positive cycle at different applied voltage.

With the increment of the applied voltage, the average peak current increased slightly from 38.0 mA to 55.3 mA, as Figure 4.6 shows. The average number of micro-discharges increased with increasing applied voltage amplitude. With the same frequency of the applied voltage, an increase in the amplitude means an increase of the voltage rise rate. The results shown in Figure 4.7 indicate that with increasing rate of voltage rise, the frequency of the micro-discharges increases; hence, the number of micro-discharges increased during one half of a voltage cycle. Because the charge transferred during one single micro-discharge is almost the

same, an increase of the micro-discharge number under higher applied voltage results in increased total charge transferred. Thus, the development of a single filament does not change as a result of the applied voltage.

#### 4.3.2 Gas pressure with current distribution analysis

The experiment was carried out with a barrier thickness of 0.2 mm and a gap of 0.2 mm at 3.0 kV<sub>p</sub> by adjusting the gas pressure from 1.0 bar to 1.6 bar in 0.2 bar increments. Figure 4.8 shows the peak current distribution of 5,000 single pulses at 1 bar and at 1.6 bar.

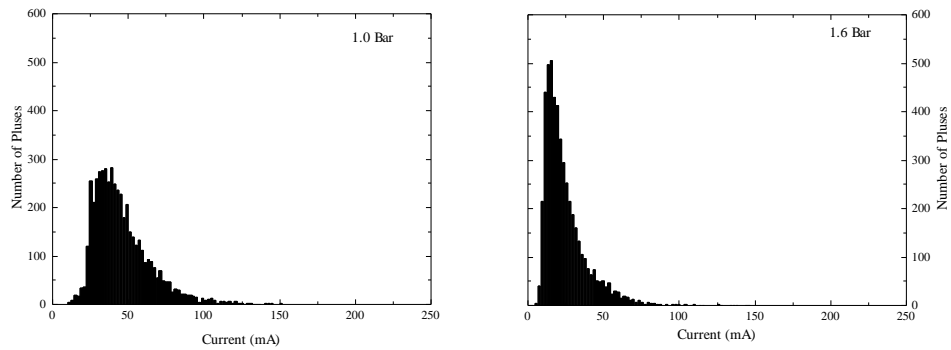


Figure 4.8 The current distribution at 1.0 bar and at 1.6 bar.

In Figure 4.8, the histograms under different pressures display different current distributions. With increasing pressure, the current distribution becomes narrower, and the number of filaments with a measured current between 20 mA and 40 mA was weighted at 83% at 1.6 bar. At 1 bar, although the most likely external current was also between 20 mA and 40 mA, the number of filaments with measured currents in this range was only weighted at 37%. Figure 4.9 shows the average peak current with its standard deviation.

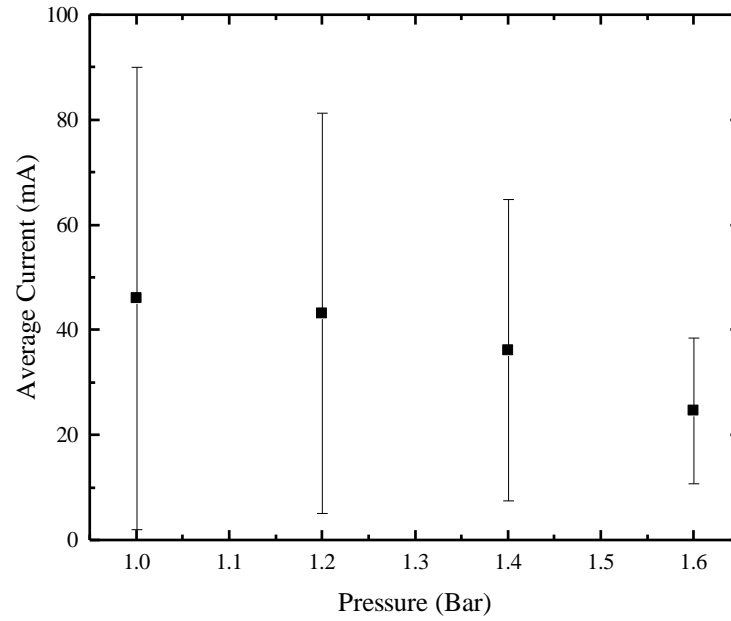


Figure 4.9 The average peak current under different gas pressures.

With an increase in the pressure, the average peak current decreased slightly from 46.1 mA to 24.7 mA, as Figure 4.9 shows. The standard deviation decreased from 44 mA to only 13.8 mA. It was found that the external measured current was lower under higher pressure, the discharge repetition rate increased, and the voltage drop decreased dramatically.

The relationship between current density and pressure is shown in (4.1):

$$j = \left( \frac{pB}{pd - B^*} \right)^2 \quad (4.1)$$

where  $j$  is the current density,  $p$  is the test cell pressure,  $d$  is the gas-electrode gap length,  $B$  is a constant related with electrode material and  $B^*$  is a constant specific to the gas type. In a DBD, the parameters of the electrode material and gas can be constant. In (4.1), increasing the pressure leads to an increased current density. This is because, with increasing pressure, the number density,  $N$ , in a fixed volume test cell increases, meaning that the distance between each molecule is shorter than it was previously.

In this case, with increasing pressure, the mean free path- a parameter to indicate the average distance during the period between two collisions written as  $\bar{\lambda}$  becomes shorter. If the average velocity of the molecules is  $\bar{v}$ , the average distance between the molecules in time is  $\bar{v}t$ . The average collision time is  $\bar{Z}t$ . The mean free path of the same gas molecule is shown in (4.2):

$$\bar{\lambda} = \frac{\bar{v}t}{Zt} = \frac{1}{\sqrt{2N\sigma}} \quad (4.2)$$

The cross-sectional area of the filament channel is smaller with increasing pressure, decreasing the diffusion area of the accumulated electrons, which can lead to the filament being extinguished due to the faster formation of the reversed electric field. According to the measured average peak current results, a decrease in the cross-sectional area of the filament channel can decrease the external peak current.

### 4.3.3 Barrier thickness and current distribution analysis

The current distribution was investigated in 0.2 mm and 1 mm barrier thicknesses. The gap was 0.2 mm. As the applied voltage became different as a result of changing the barrier thickness, the charge transfer remained the same in the experiment.

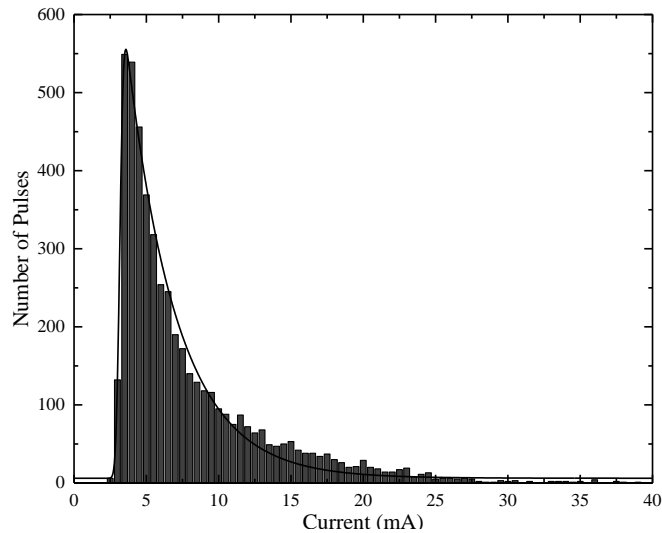


Figure 4.10 The external current distribution with 1 mm barrier thickness, a 0.3 mm gap and 6.5 kV<sub>p</sub> power supply.

When increasing the barrier thickness, the mean peak current at 6.5 kV<sub>p</sub> was less than 10 mA. The maximum current detected was less than 40 mA. Compared with the results in Figure 4.5, the current distribution was more concentrated when the barrier thickness was increased.

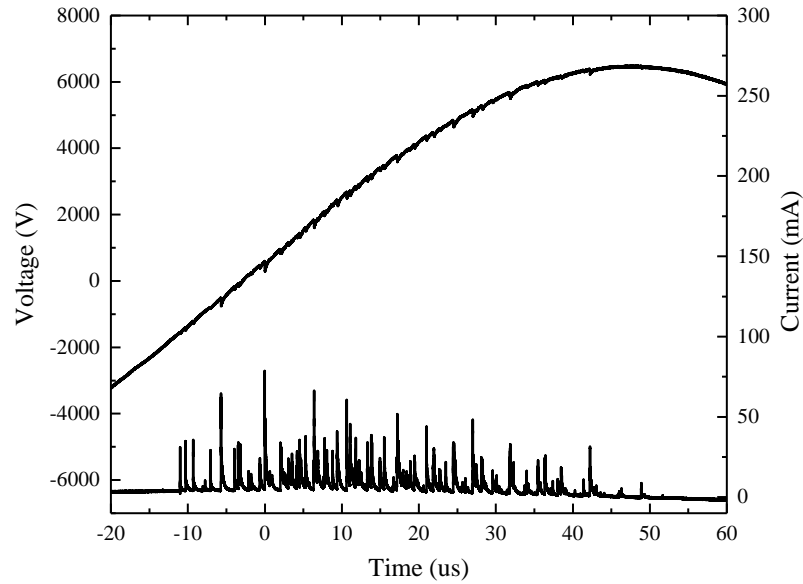


Figure 4.11 Example of a quarter-cycle of current and voltage for a 1 mm barrier, 0.2 mm gap and 6.5 kV<sub>p</sub> supply voltage.

Figure 4.11 shows the half-cycle voltage and current waveforms for 1 mm barrier thickness, 1 bar absolute pressure and 6.5 kV<sub>p</sub> supply voltage. The external current and the voltage drop are much lower when the barrier is thicker.

It was obvious that, when increasing the barrier thickness, the amplitude of the external current decreased. When ions accumulated on the surface of the barrier, there was a redistribution of the electric field on the barrier. Some of the ions will build up the reversed electric field to halt the development of the filament, while the rest of the ions will form an electric field within the barrier to increase the voltage across the barrier. According to the equivalent circuit in Figure 3.20, for the same voltage drop across the filament channel, when increasing the barrier thickness, both the barrier capacitance and the total capacitance decrease, causing the corresponding current flowing through  $C_d''$  and the filament current to reduce.

## 4.4 Ozone efficiency analysis

### 4.4.1 Ozone generation versus dew point

With regard to ozone generation via excimer lamp [76], research shows that the effect of water vapour is crucial. The maximum ozone concentration was increased from approximately 6 wt% at 300 ppm to 13 wt% at 0 ppm. In addition, at a 5 wt% ozone concentration, the ozone efficiency increased from 125 g/kWh at 300 ppm to 200 g/kWh at 0 ppm. The dramatic

increase indicates the negative effect of water vapour on ozone generation. To limit the effect of water vapour in the experiment, the dew point was changed by using liquid nitrogen.

The dew point of the oxygen leaving the cylinder was  $-40^{\circ}\text{C}$ , which corresponded to 127 ppm water vapour. The comparison was made by passing oxygen from the cylinder to a copper coil that was located in the liquid nitrogen.

The dew point was measured from the outlet of the copper coil and was changed by adjusting the depth of the copper coil in the liquid nitrogen. The dew point was changed from  $-40^{\circ}\text{C}$  to  $-60^{\circ}\text{C}$  (11 ppm). The information extracted from the Lissajous figure is presented in Figure 4.12 at under  $-40^{\circ}\text{C}$  and  $-60^{\circ}\text{C}$ , respectively.

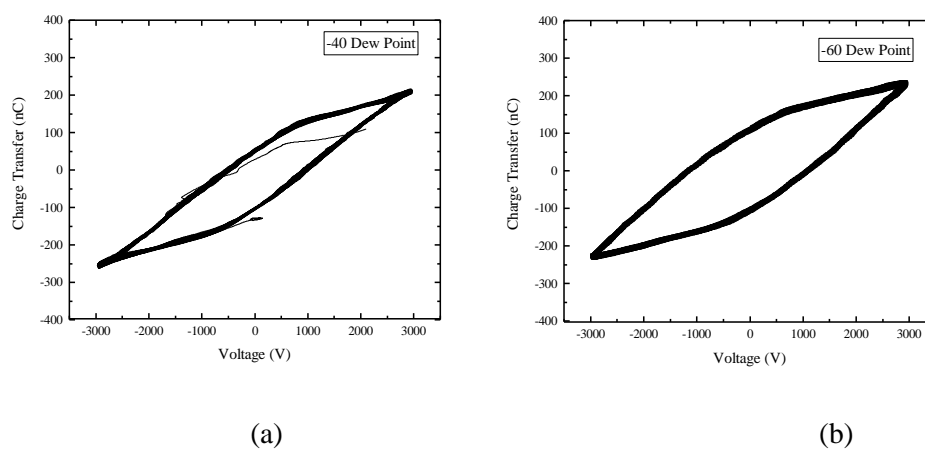


Figure 4.12 100-cycle Lissajous figures with a 0.2 mm gap and 0.3 mm barrier thickness at different dew points of (a)  $-40^{\circ}\text{C}$  and (b)  $-60^{\circ}\text{C}$ , respectively.

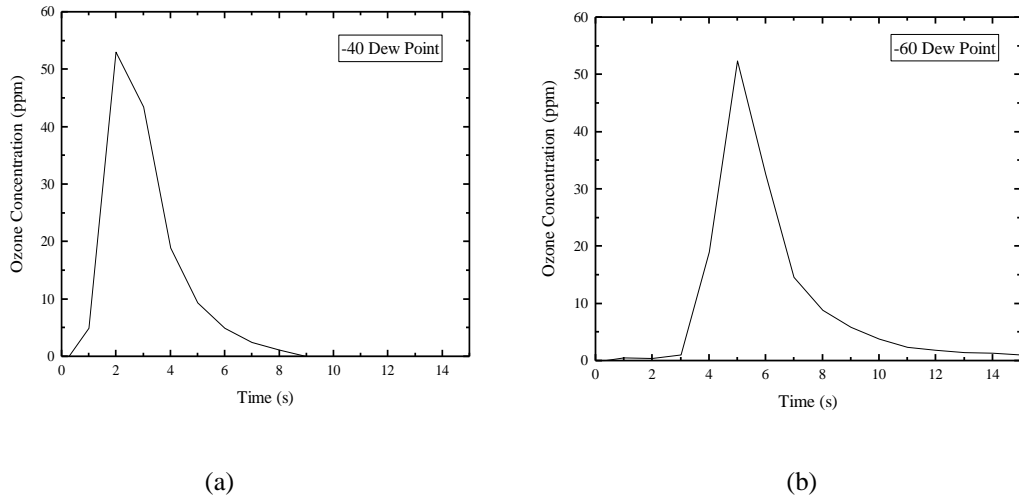


Figure 4.13 The transient ozone concentration of 100 cycles of energy input with a 0.3 mm barrier thickness and a 0.2 mm gap at different dew points of (a) -40 °C and (b) -60 °C.

Table 4.3 The discharge parameters at different dew points.

<b>Dew Point (°C)</b>	<b>Cd (pF)</b>	<b>Cg (pF)</b>	<b>V<sub>b</sub> (V)</b>	<b>Energy Input (mJ)</b>
-40	126.9	42.1	1075	81
-50	128.6	40.8	1101	81
-60	126.8	43.8	1070	80.9

In Table 4.3, when increasing the dew point, the breakdown voltage, the gap capacitance, the dielectric barrier capacitance and the energy input of 100 cycles did not change significantly. In Figure 4.13, the peak value of ozone concentration at -40 °C was 53.0 ppm, while the peak value of ozone concentration at -60 °C was 52.4 ppm. The very small difference in ozone concentration and energy input means the ozone efficiency at different dew points does not change in the 100-cycle energy input.

In the following experiment, the input gas was taken directly from the oxygen cylinder at a -40 °C dew point.

#### 4.4.2 Ozone generation versus applied voltage

To understand the relationship between applied voltage and ozone efficiency, the peak value of the applied voltage was increased from 2 kV<sub>p</sub> to 3.5 kV<sub>p</sub> with a 0.2 mm barrier thickness and a 0.2 mm gap.

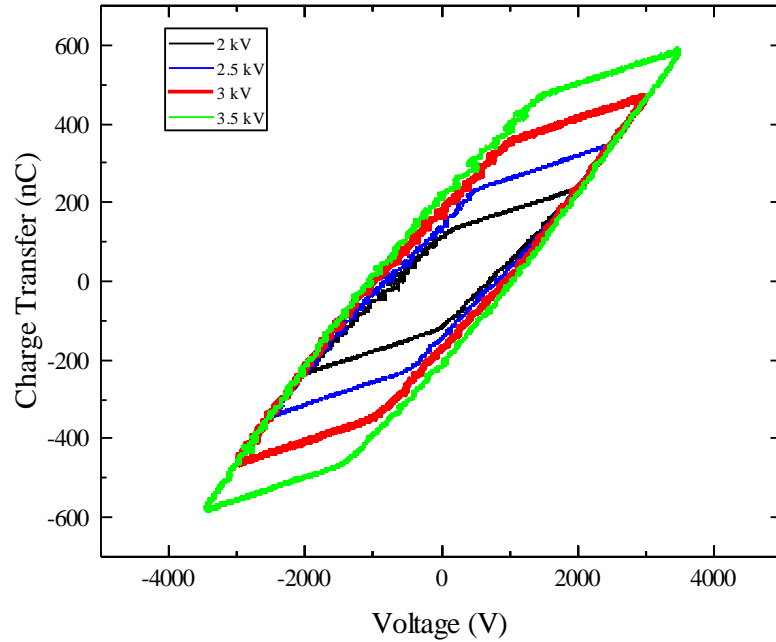


Figure 4.14 The sampled Lissajous figure with a 0.2 mm barrier thickness and a 0.2 mm gap at different applied voltages from 2 kV<sub>p</sub> to 3.5 kV<sub>p</sub>.

From the Lissajous figure shown in Figure 4.14, the breakdown voltage, the gap capacitance, the dielectric barrier capacitance and the energy input can be calculated, as Table 4.4 shows:

Table 4.4 The discharge parameters at different applied voltages.

Applied Voltage (kV)	Cd (pF)	Cg (pF)	Vbreakdown (V)	Energy Input (mJ)
2.0	156.8	54.8	770.0	47.1
2.5	158.9	45.9	801.7	73.9
3.0	164.7	43.5	908.5	101.5
3.5	169.8	42.5	1006.2	132.4

When increasing the applied voltage from 2 kV<sub>p</sub> to 3.5 kV<sub>p</sub>, the total capacitance did not change, while the dielectric barrier capacitance increased and the corresponding gap capacitance decreased. According to the capacitance calculation formula of parallel-plane geometry, the value of the capacitance is only related to the equivalent area and the length of the material.

The breakdown voltage increased from 770 V to 1006 V with the increase of the applied voltage which does not conform to gas breakdown theory. For a gas breakdown, the electron avalanche is developed in a time-frame of ps to ns. In the inter-electrode gap, once the electric field is sufficiently high to initiate gas breakdown, the electric field around the head of the avalanche increases dramatically, increasing the number of ionising collisions.

As the discharge in oxygen was filamentary, the electron distribution on the surface of the barrier was not uniform. With lower supply voltage, only a few discharges occurred during the half-cycle - each discharge was relatively independent, with the charge accumulated on the surface being different each time. There is a certain point with an enhanced local electric field at which the discharge will occur first. When increasing the supply voltage, the number of charges accumulated on the barrier surface increased and the distribution was more uniform, while the value of the equivalent barrier capacitance increased. In this case, the breakdown voltage of the gap was closer to the breakdown voltage of parallel-plane geometry when there was no local field enhancement.

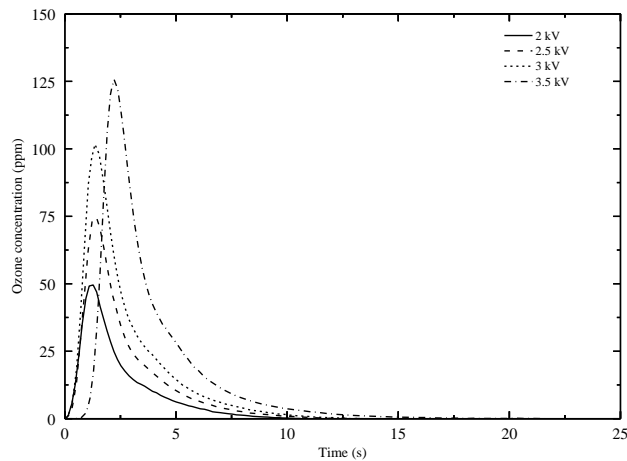


Figure 4.15 The sampled ozone concentration with a 0.2 mm barrier thickness and a 0.2 mm gap at different applied voltages from 2 kV<sub>p</sub> to 3.5 kV<sub>p</sub>.

According to Figure 4.15, for a certain gap length and oxygen flow rate, increasing the supply voltage leads to an increase in the ozone concentration. The ozone production during 100 cycles increases from 164 ppm to 397 ppm with an increase of the applied voltage from 2 kV<sub>p</sub> to 3.5 kV<sub>p</sub>. For a 0.2 mm gap, the ozone efficiency was found to decrease from ~201 g/kWh to ~162 g/kWh when increasing the supply voltage from 2 kV<sub>p</sub> to 3.5 kV<sub>p</sub>, as shown in Figure 4.16, while the reduced electric field increased from 128 Td to 186 Td as shown in Figure 4.17. When increasing the applied voltage, the charge transfer increases; in this case, the produced ozone can increase as well, while the dissociation process increases significantly, decreasing the total ozone efficiency.

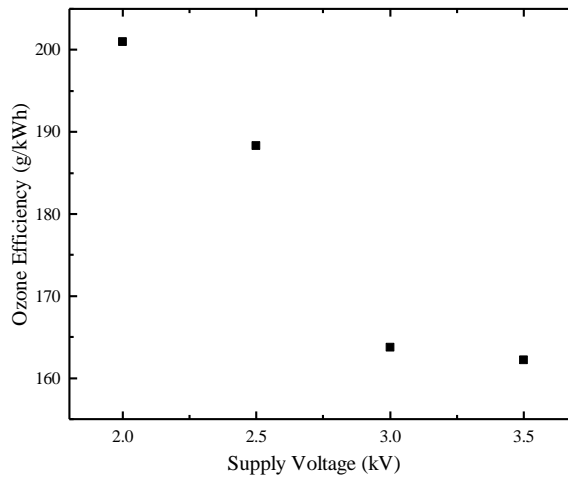


Figure 4.16 The ozone efficiency at different applied voltages.

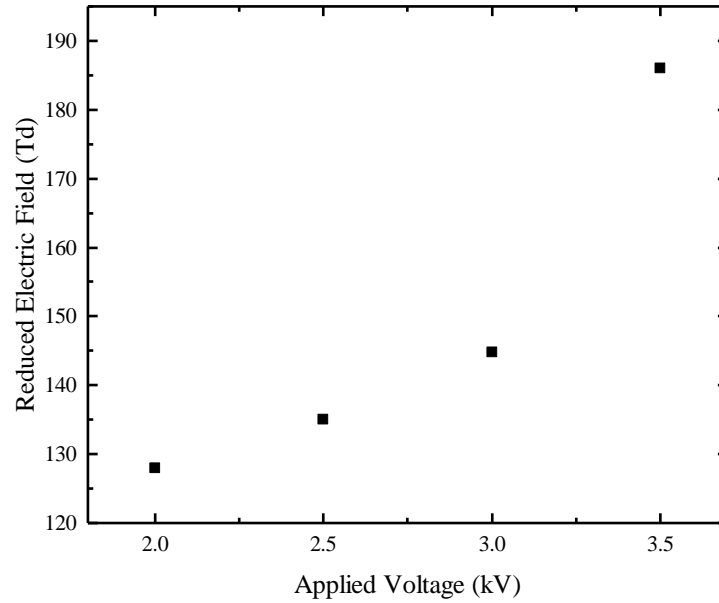


Figure 4.17 Reduced electric field versus applied voltage.

#### 4.4.3 Ozone generation versus gap length

To understand the relationship between ozone efficiency and gap length, the gap length was increased from 0.1 mm to 0.3 mm in 0.1 mm increments. The experiment was carried out using a 0.2 mm thick barrier with 3.0 kV<sub>p</sub> applied voltage at 5 kHz.

Table 4.5 The discharge parameters at different gap lengths.

Gap length (mm)	C <sub>d</sub> (pF)	C <sub>g</sub> (pF)	V <sub>b</sub> (V)	Energy Input per 100 cycle (mJ)
0.1	183	47.5	683.5	103
0.2	169.8	44.7	875.2	98
0.3	172	29.3	1184.9	126

Figure 4.18 shows the ozone concentration at different gap lengths.

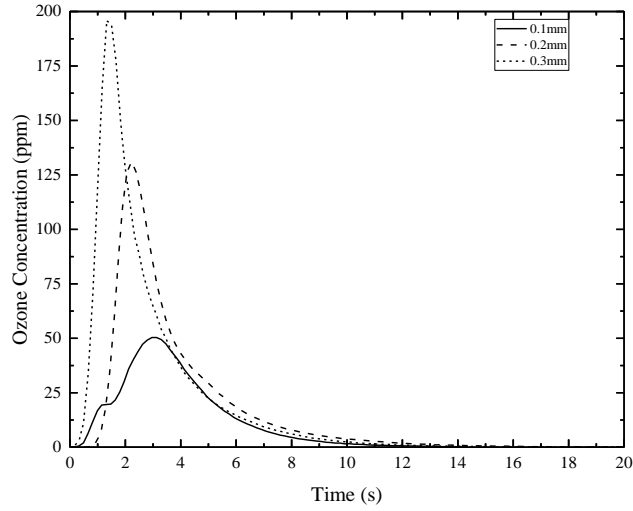


Figure 4.18 The ozone concentration at 100 cycles with a 0.1 mm gap length (solid line), a 0.2 mm gas distance (dashed line) and a 0.3 mm gap length (dotted line).

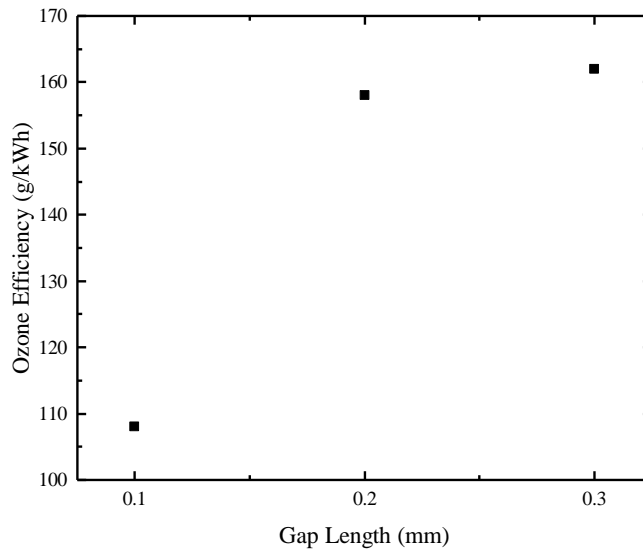


Figure 4.19 The relationship between gap length (mm) and ozone efficiency (g/kWh) with 3 kV<sub>p</sub> voltage supply and 0.2 mm barrier thickness.

For a given supply voltage, increasing the gap size from 0.1 mm to 0.3 mm led to an increase in the ozone efficiency. For instance, at 3 kV<sub>p</sub> input voltage, the ozone efficiency increased from ~109 g/kWh to ~162 g/kWh.

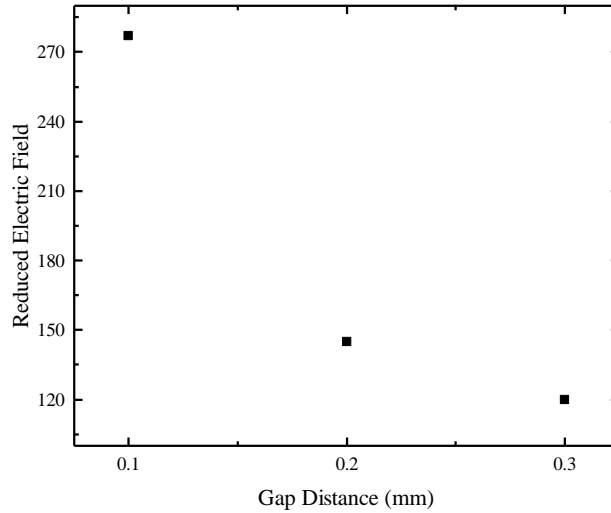


Figure 4.20 Reduced electric field versus gap length.

When increasing the gap length, the electric field decreases from ~277 Td to ~123 Td at 3 kV<sub>p</sub> supply voltage as shown in Figure 4.20; when increasing the reduced electric field, the ozone concentration decreases. The input energy for the different gap sizes studied here did not change significantly at the same supply voltage (from 0.10 J to 0.12 J), while the ozone concentration decreased dramatically when the reduced electric field increased. In summary, it can be said that increasing the reduced electric field above the optimal value leads to a higher increase in the rate of ozone dissociation than in the rate of ozone formation, resulting in reduced ozone efficiency.

Without considering the ionic current component in the filament current due to its small contribution [30], the current density,  $j$ , can be calculated from (4.3):

$$j = e \cdot N_e \cdot v_d \quad (4.3)$$

where  $N_e$  is the electron density, and  $v_d$  is the electron drift velocity.

It can be deduced that the increase of filamentary current with increasing gap length results from the joint effects of the electron density and electron drift velocity at different gap lengths. The electron density and the electron drift velocity distribution are related to the reduced electric field  $E/N$  [77][78]. The effects of discharge gap length and gas pressure on the characteristics of micro-discharges have also been investigated by other researchers. Using a numerical method, Braun *et al.* [33] reported that the radius of the micro-discharge increased with increasing gap length. For longer gap length, with larger micro-discharge radius, the transferred charge of a single filament and the micro-discharge energy both increase. The

filamentary current pulse duration represents the time taken for a reverse electrical field to be established by accumulated charge that is high enough to terminate the discharge. With a longer discharge gap, more time is needed to establish the reverse electrical field to extinguish the discharge while the ozone efficiency increases with the increment of gap length. Comparing these two parameters (gap size and supply voltage), the ozone efficiency decreases with an increase in the reduced electric field in the range of  $\sim 123$  Td to  $\sim 277$  Td.

#### 4.4.4 Ozone generation versus gas pressure

To analyse the relationship between ozone efficiency and absolute pressure, the pressure was increased from 1 bar to 1.6 bar in 0.2 bar increments. With a 0.2 mm gap size and a 0.2 mm barrier thickness, the ozone efficiency was measured under various absolute pressures. The supply voltage was 3 kV<sub>p</sub>, and the frequency was 5 kHz.

Table 4.6 The discharge parameters under different gas pressures.

Gas Pressure(bar)	Cd (pF)	Cg (pF)	Vbreakdown (V)	Energy Input (mJ)
1.2	164.7	43.6	988	85.2
1.4	163.9	43.8	1053.4	78.4
1.6	158.9	42.9	1155.2	76.5

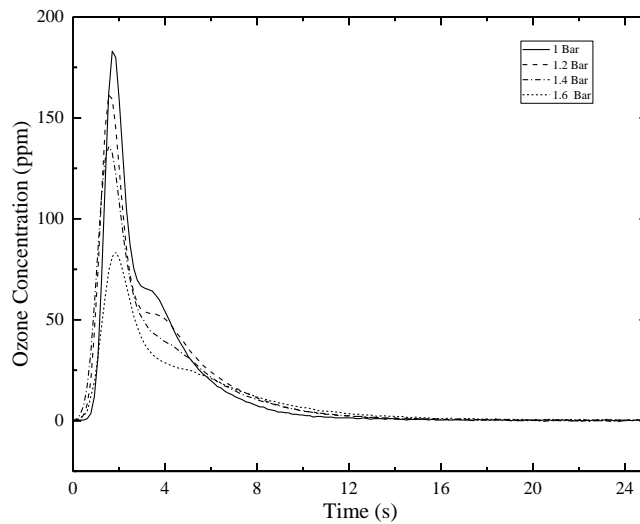


Figure 4.21 The ozone concentration under different gas pressures.

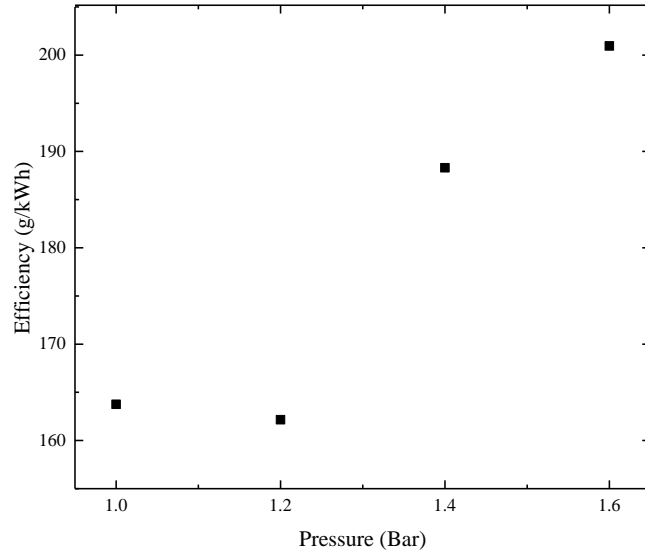


Figure 4.22 The ozone efficiency versus different gas pressures.

When increasing gas pressure, the required breakdown voltage increased from 988 V to 1155 V, while the dielectric capacitance decreased from 165 pF to 159 pF. The energy input decreased from 85.2 mJ to 76.5 mJ. The peak value of ozone efficiency decreased from nearly 180 ppm to only 80 ppm, as shown in Figure 4.21. Meanwhile, it can clearly be seen in Figure 4.22 that, with increasing pressure, the ozone efficiency increased from ~162 g/kWh to ~207 g/kWh.

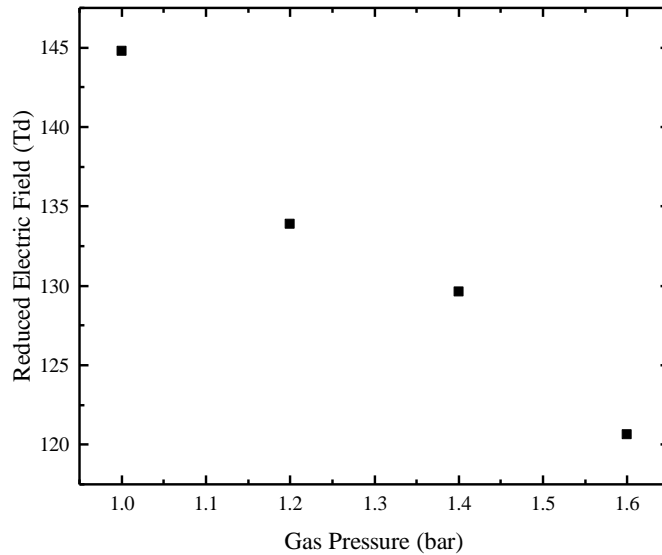


Figure 4.23 Reduced electric field versus gas pressure.

It was found that, when increasing the gas pressure, the reduced electric field decreased to 120 Td from 145 Td, as shown in Figure 4.23. The effect of  $E/N$  on the distributions of electron density and electron drift velocity is complicated and requires further advanced plasma diagnostic techniques or application of the Particle-in-Cell method for numerical simulation [79].

Related to the analysis of the current distribution under different gas pressures, the lower peak current and more concentrated distribution can increase the ozone efficiency. As the filament diameter decreases with the increment of pressure, the number of produced  $O$  atoms also decreases. For the same charge transfer, the discharge number increases with increasing gas pressure. The distribution of  $O$  atoms is more uniform. Accordingly, a good mixture of  $O$  atoms can reduce the dissociation of ozone in a certain area to increase the total ozone efficiency.

#### 4.4.5 Ozone generation versus dielectric barrier thickness

To analyse the relationship between barrier thickness and ozone efficiency, experiments were carried out by changing the barrier thickness from 0.2 mm to 1 mm, with a fixed gap size of 0.3 mm.

In Figure 4.24, the peak ozone efficiency with a 1 mm thick barrier can reach  $\sim 225$  g/kWh when the reduced electric field is  $\sim 130$  Td. Compared to the results of a 0.2 mm thick barrier, according to the fitting line, even at the same reduced electric field, the ozone efficiency increased with the increasing barrier thickness. For instance, the ozone efficiency increased from 188 g/kWh to 213 g/kWh at  $\sim 145$  Td. Moreover, the ozone efficiency increased with the increasing barrier thickness with the same input energy. For instance, with 0.13 J input energy, the ozone efficiency increased from  $\sim 162$  g/kWh in 0.2 mm to  $\sim 185$  g/kWh at 1 mm barrier thickness at 1 bar absolute.

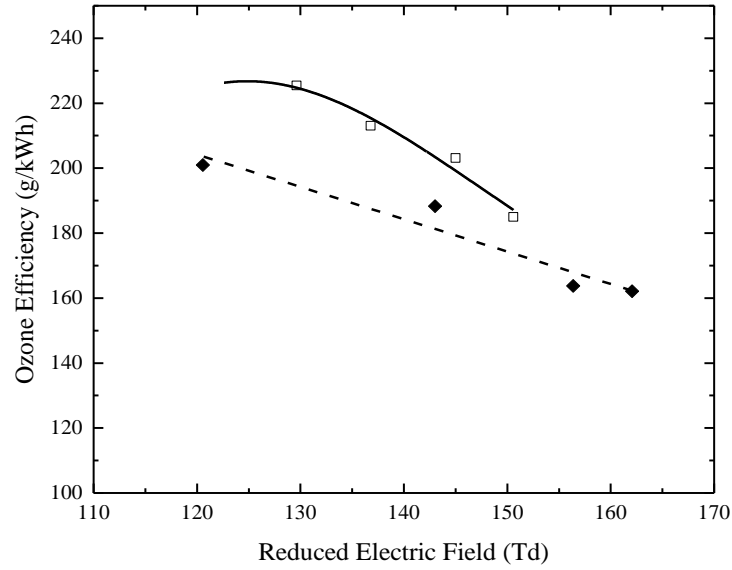


Figure 4.24 The relationship between ozone efficiency and a reduced electric field for a 1 mm barrier (open squares and solid line curve fit) and a 0.2 mm barrier (closed diamonds and dashed line curve fit).

The results shown in Figure 4.25 indicate that the average peak current decreases with the increment of the ozone efficiency. When the pressure was increased, the average external current fell from 25 mA to 11 mA. The rise times were all in the range of 3.9 ns to 4.2 ns. With a decrease in the external current, the ozone efficiency increases. By increasing the barrier thickness, most of the charges form a reversed electric field with the opposite polarity charges. The filament is easier to extinguish. For the same charge transfer, the discharge number increases with the increasing barrier thickness. A more uniform concentration of atomic oxygen can increase the ozone production to increase the ozone efficiency.

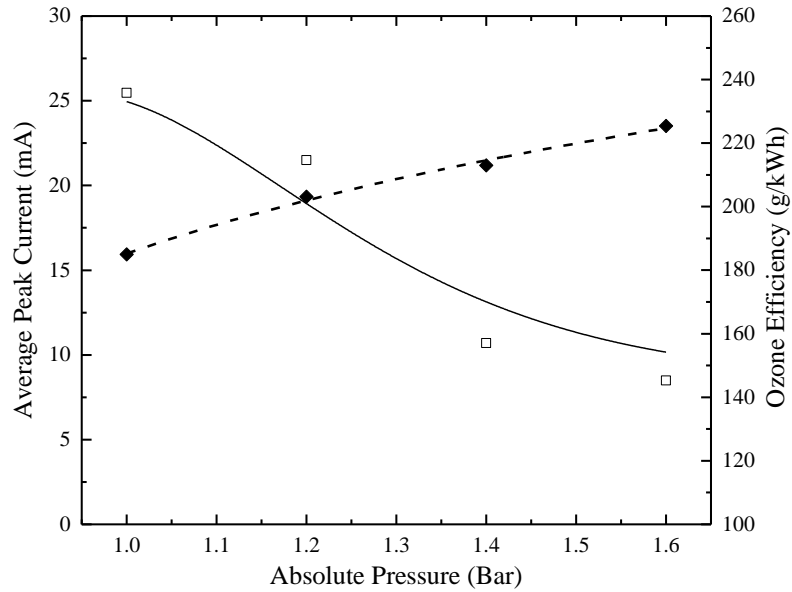


Figure 4.25 Variation of the average peak current (open squares and solid curve fit) and ozone efficiency (closed diamonds and dashed curve fit) with pressure. The dielectric barrier is 1 mm thick, and the gap size is 0.3 mm.

#### 4.4.6 Ozone efficiency versus reduced electric field

The experimental results were gathered by measuring the ozone concentration and the corresponding efficiency at varying voltages and gap sizes to determine the relationship between the reduced electric field ( $E/N$ ) and ozone efficiency.

Ozone efficiency was investigated by changing the gap size from 0.1 mm to 0.3 mm in 0.1 mm increments and changing the peak amplitude of the supply voltage from 2 kV<sub>p</sub> to 3.5 kV<sub>p</sub> in 500-V increments with a 0.2 mm gap size. The results are shown in Figure 4.26.

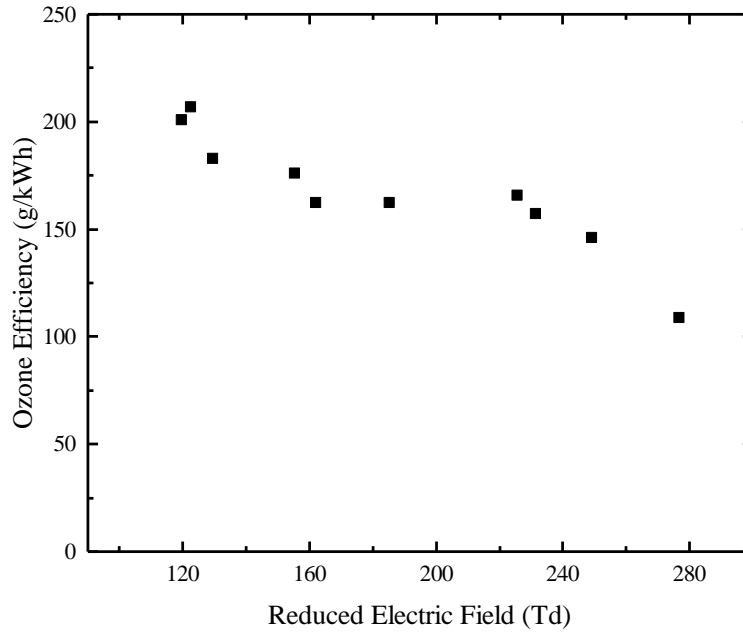


Figure 4.26 The relationship between the reduced electric field (Td) and ozone efficiency (g/kWh).

The optimised ozone efficiency reached in this experiment was  $\sim 207$  g/kWh, which was achieved when the reduced electric field was equal to  $\sim 123$  Td. With the increase of the reduced electric field, the ozone efficiency dropped to  $\sim 109$  g/kWh at  $\sim 277$  Td. A similar result was obtained by Kitayama, demonstrating that ozone efficiency reduces gradually with an increase in the reduced electric field when  $E/N \geq 100Td$ .

Figure 4.27 shows the cross section of electron collisions with oxygen molecules, including elastic collision, momentum transition, rotational excitation, vibrational excitation, dissociation, excitation of metastable states ( $I\Delta g$ ,  $I\Sigma g+$ ) and ionisation [80]. The highest dissociation cross section is  $\sim 0.3 \times 10^{-16}$  cm<sup>2</sup>.

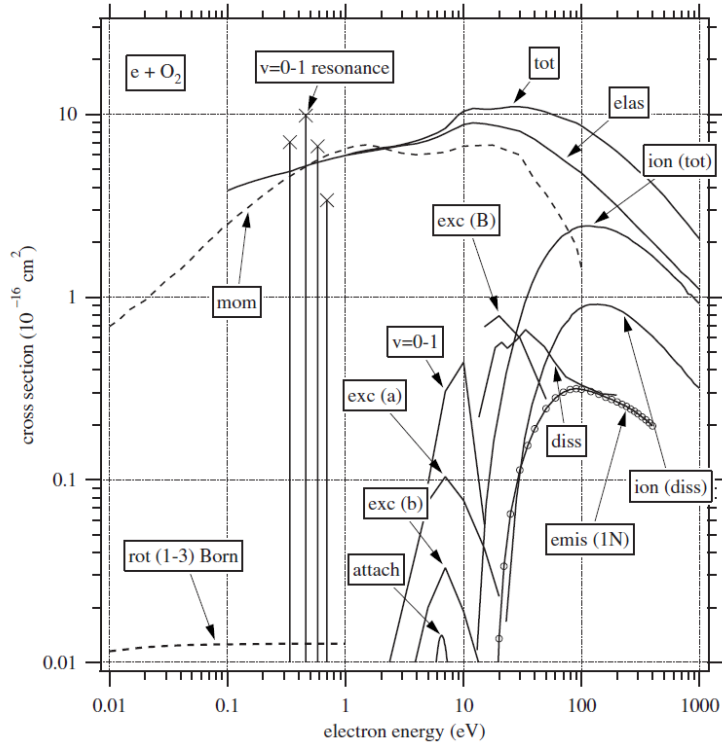


Figure 4.27 The electron cross section with an oxygen molecule [80].

A continuous increase in the electron energy above 12.06 eV causes the ionisation cross section to increase and the dissociation cross section to decrease.

Figure 4.28 shows a more detailed energy branching in oxygen.

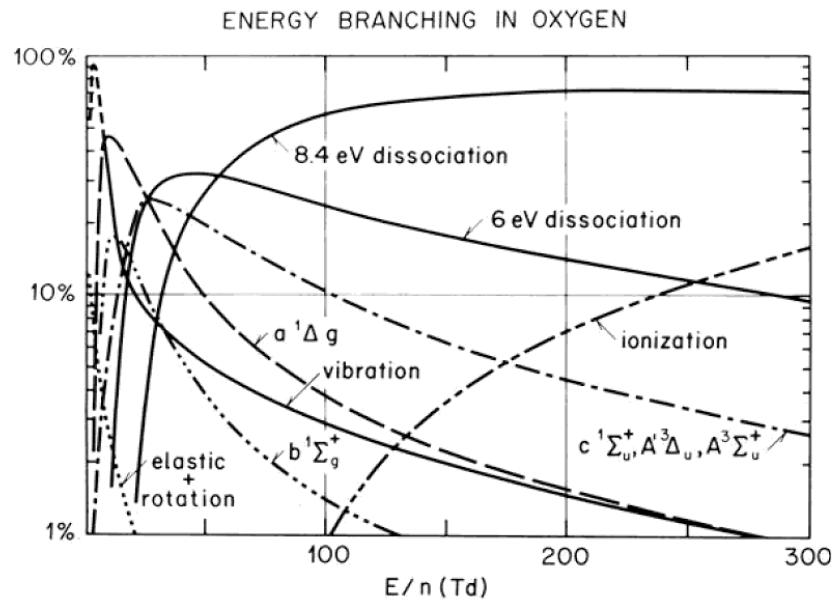


Figure 4.28 Distribution of electron energy branching as a function of the reduced electric field (Td) [41].

With a lower reduced electric field below 30 Td, most of the electron energy is used for the excitation of oxygen molecules. At 30 Td, the probability of a dissociation process with 6 eV increases to over 30% of the total energy branching. When continuously increasing the reduced electric field to 100 Td, the percentages of the probability of vibration, elastic scattering, rotation and excitation decrease dramatically. Simultaneously, the percentage of 8.4 eV dissociation probability increases to 80% [81][82]. Meanwhile, when continuously increasing the reduced electric field, the probability of a 6 eV dissociation process reduces while the ionisation probability increases rapidly. In this case, if the reduced electric field is either less than 80 Td or is higher than 200 Td, ozone efficiency cannot be optimized. When increasing the reduced electric field, the electron energy also increases. The cross section of oxygen ionisation and dissociation increases dramatically, meaning that the number of electrons and  $O$  atoms also increases.

According to the energy branching in Figure 4.28, with an increase in the reduced electric field (above 100 Td), the ionisation process increases. In micro-discharges, part of the energy is dissipated by ions, which is a situation to be avoided. In this case, there is an optimum reduced electric field (discharge strength) that affords a compromise between avoiding the energy losses of ions and minimising chemical-reaction losses. According to the modelling result that was based on 76 reactions (including ground state, excited state and charged particles), the concentration of different species of a single filament are shown in Figure 4.29.

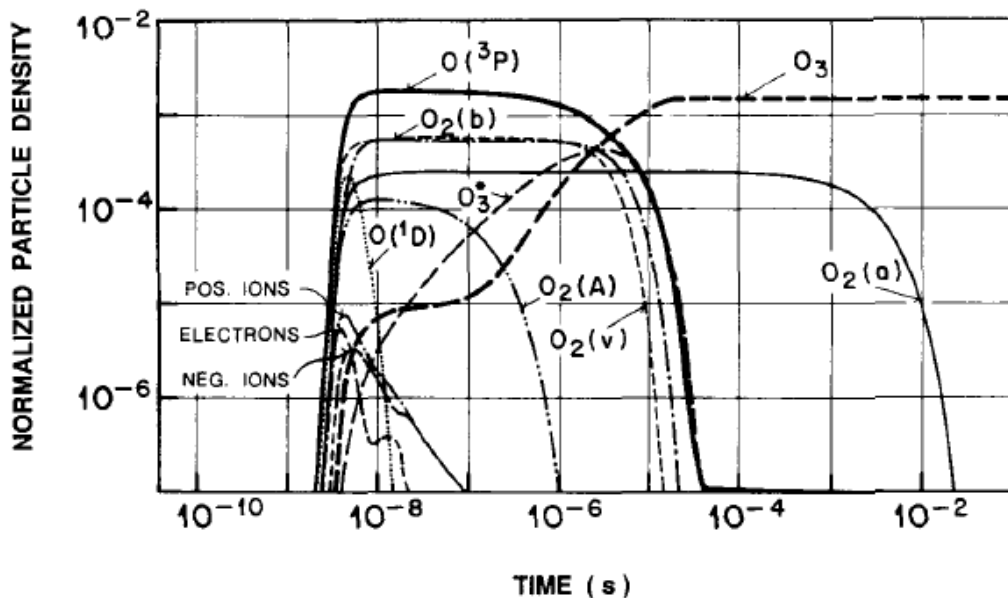


Figure 4.29 The concentration of different species of a single micro-discharge in pure oxygen [74].

Most of the oxygen atoms are produced in the 10-ns discharge. The concentration of ground state  $O(3P)$  is more than that of the excited state  $O(1D)$ , as part of the excited atomic oxygen collides with the third body and returns to the ground state atomic oxygen. Within nanoseconds, when the concentration of  $O(1D)$  starts to decrease, the concentration of  $O_3^*$  increases. After the discharge, the concentration of ground state oxygen starts to decrease gradually after the nanosecond discharge and the ground state ozone concentration increases more rapidly due to the reaction between the ground state  $O$  and the oxygen molecule  $O_2$ , and is also due to the de-excitation of  $O_3^*$ . After microseconds, the normalised density of ozone reaches  $10^{-3}$ . As a result, the majority of ozone molecules are formed within microseconds. When increasing the reduced electric field, the ozone dissociation rate will also increase. In general, the reasonable  $c[O] / c[O_2]$  ratio should be between  $10^{-5}$  and  $10^{-4}$ . In this range, the conversion efficiency  $c[O_3] / c[O]$  can reach 1.

## 4.5 Conclusions

Firstly, the current distribution for different applied voltages, under different gas pressures and for different barrier thicknesses was investigated. It was found that, when increasing the applied voltage, the average peak current did not change significantly. Meanwhile, increasing the gas pressure and the barrier thickness can decrease the amplitude of the external current.

According to the Td versus ozone efficiency curve (Figure 4.24), the ozone efficiency can reach  $\sim 207$  g/kWh at  $\sim 123$  Td. The ozone efficiency then reduces gradually when the reduced electric field is increased from 140 Td to 210 Td. With the continuing increase of the reduced electric field, the ozone efficiency fell rapidly to  $\sim 109$  g/kWh at  $\sim 277$  Td.

For a single filament, the voltage drop across the filament channel leads to the extinguishing of the filament. With increasing pressure, the current distribution becomes narrower and the mean amplitude of the filament current decreases, leading to higher ozone efficiency.

For the same reduced electric field, with lower amplitude of the filament current and narrower current distribution, the ozone efficiency was found to increase as a result of the more uniform distribution of the filaments on the barrier surface. The author is currently working to determine the values of  $C_g''$  and  $C_d''$ , and the affected area of each filament.

The power supply will charge the test cell to recover the electric field across the gap, but the local electric field across the previous gap channel is lower than the average electric field. The next filament will then form at a different position on the electrode surface. When the filament

is extinguished easily, the electron distribution in the gas gap tends to be more uniform, increasing the ozone efficiency. With a higher external current and a strong filament, the electrons produced in the filament channel can react with the oxygen molecules to produce atomic oxygen with a higher density. Meanwhile, most of the oxygen molecules in the gap cannot react with the electrons, and the atomic oxygen produced in the filament channel can react with ozone molecules to reduce the ozone production efficiency.

In summary, for higher ozone efficiency, a low external current and uniform electron distribution in the gap are the key factors.

## 5 Current Amplitude Distribution and Ozone Efficiency using Meshed Electrodes

### 5.1 Introduction

The results using planar electrode DBD showed that an average current amplitude of ~25 mA and narrower distribution of current amplitude can increase ozone efficiency up to 207 g/kWh. With a reduced current amplitude, the charge transfer of each filament decreases leading to a greater number of discharges in a cycle.

In this chapter, meshed electrodes are used to optimise the current amplitude distribution and ozone efficiency using dielectric barrier discharge. By changing the applied voltage, mesh aperture size and gas pressure, the current amplitude distribution of 10,000 single discharges was investigated for its relationship to ozone generation efficiency. In addition, the relationship between reduced electric field and ozone efficiency was determined. Finally, a comparison of current amplitude distribution and ozone efficiency versus reduced electric field ( $E/N$ ) when using a planar electrode and a meshed electrode was made.

### 5.2 Experimental setup

#### 5.2.1 Test cell design

A schematic of the test cell is shown in Figure 5.1. The entire test cell is sealed in a PTFE holder using a silicon O-ring. Two circular stainless steel (SS316) meshed-plates formed the electrodes. The mesh diameter is 50 mm, the aperture size is 0.96 mm and the wire thickness is 0.45 mm. A round quartz plate is located directly between the two meshed electrodes to form a dielectric barrier with  $\epsilon_r = 3.8$ . The quartz plate diameter is 75 mm and the thickness is 1 mm. At the centre of top and bottom PTFE lids, a stainless-steel connector is located for gas flow and voltage connection.

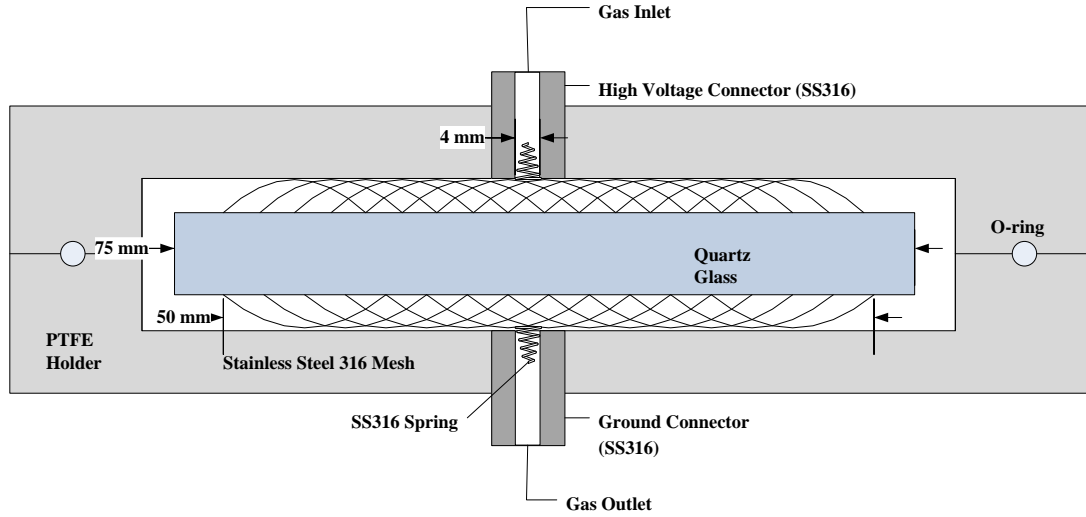


Figure 5.1 Test cell design constructed with a 50 mm diameter, a 0.96 mm aperture size, SS316 stainless steel electrodes and a 75 mm diameter quartz plate.

### 5.2.2 Experimental arrangement

Figure 5.2 shows the experimental setup, similar to that for the experiment in Chapter 3. The experiment was carried out by changing the applied voltage (4.5 kV<sub>p</sub> to 6.5 kV<sub>p</sub> voltage), gas pressure (1.0 bar to 2.0 bar) and mesh aperture size (0.26 mm to 1.7 mm) to analyse the current amplitude distribution, ozone efficiency and the corresponding reduced electric field. In this experiment, the power applied was only enabled for 100 cycles for each test in order to minimise the temperature rise in the discharge gap.

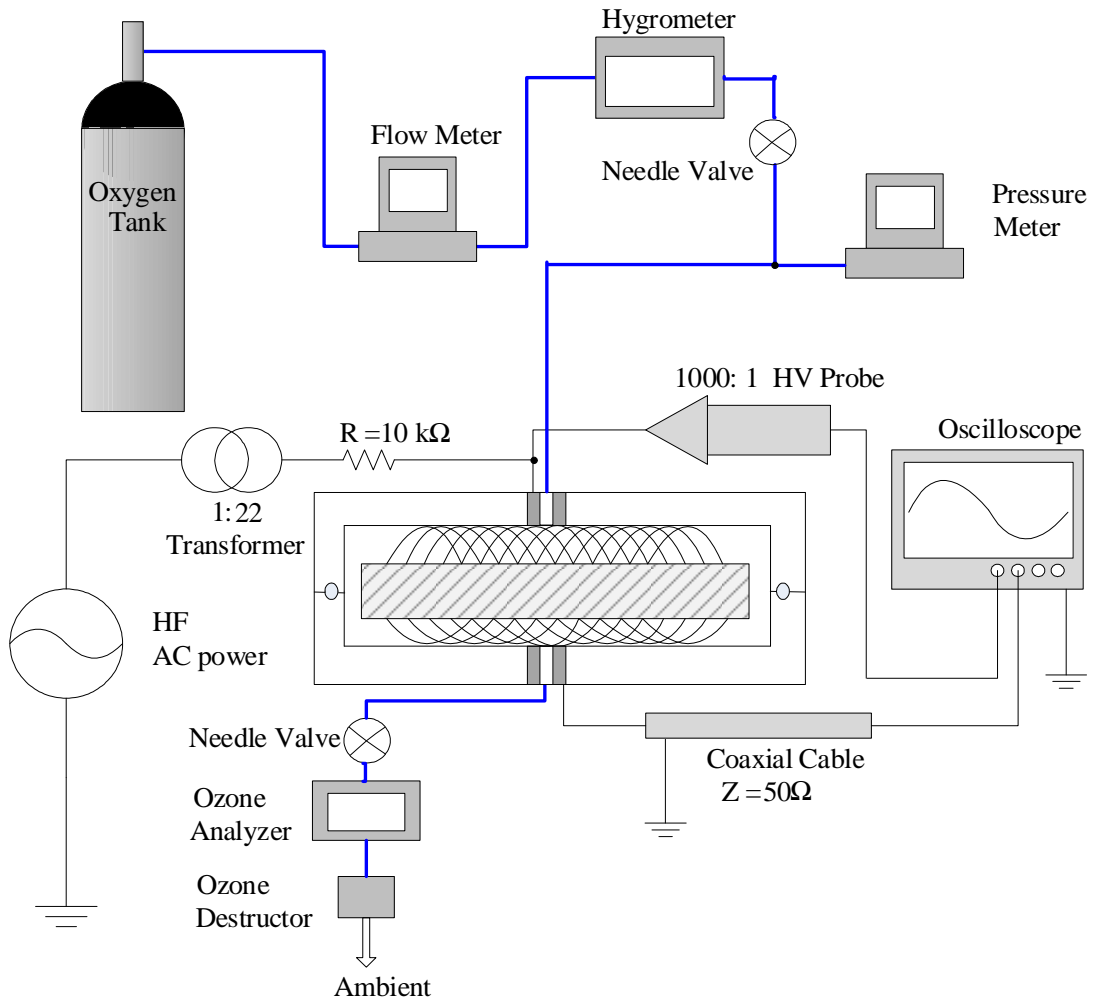


Figure 5.2 Experimental arrangement using mesh electrodes.

### 5.3 Discharge characteristics

#### 5.3.1 Current and voltage waveforms

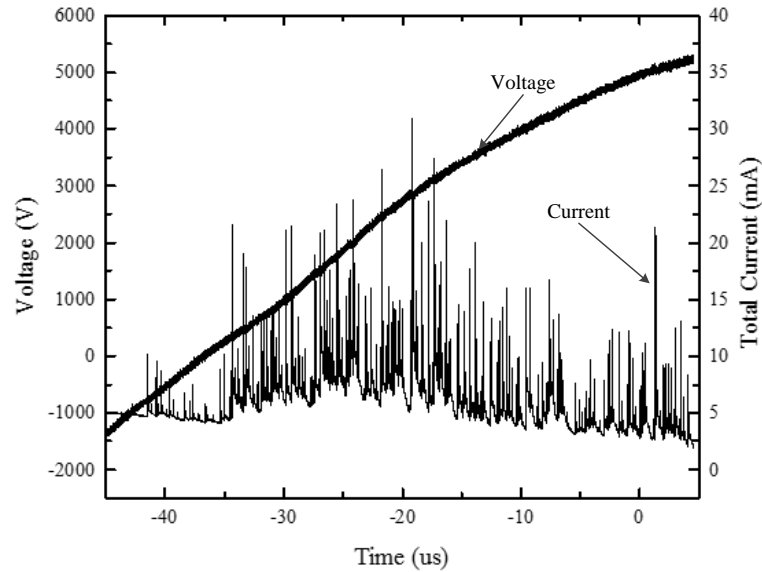


Figure 5.3 The example quarter cycle waveform of voltage and current at  $5.5 \text{ kV}_p$  applied voltage.

Figure 5.3 shows an example of a quarter-cycle waveform of current and voltage at  $5.5 \text{ kV}_p$  applied voltage using  $0.96 \text{ mm}$  aperture size meshed electrodes. The time interval between two discharges (the period between two measured current pulses) is shorter than  $100 \text{ ns}$ . The measured results show that a few discharges can occur almost simultaneously. The shorter single pulsed current duration means the diffusion of deposited charge on the quartz surface is quite limited to extinguish the discharge quickly. The affected area of the single filament is limited as well.

## 5.3.2 Lissajous Figure analysis

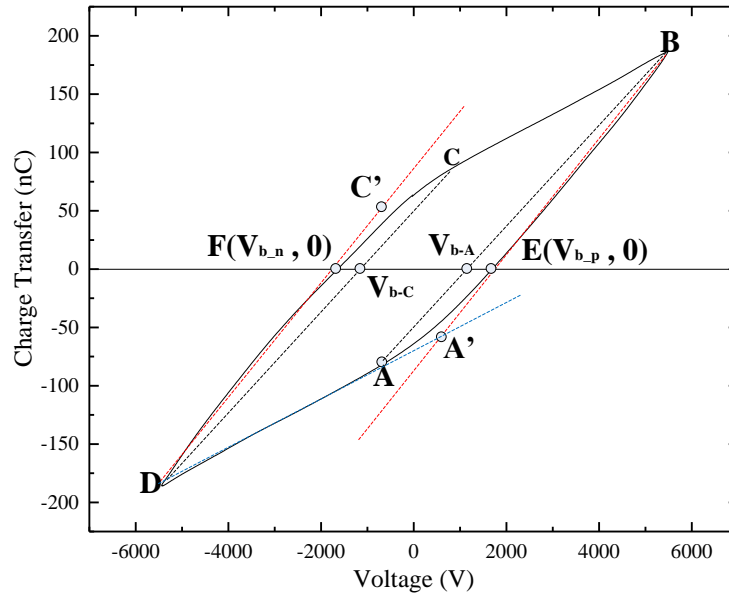


Figure 5.4 Lissajous figure of a 0.96 mm mesh plate test cell discharge with 5.5 kV<sub>p</sub> applied voltage.

#### A. Breakdown voltage

Figure 5.4 shows Lissajous figure at 5.5 kV<sub>p</sub> using 0.96 mm aperture size meshed-electrodes. The segments of A-B and C-D represent the discharge phases and the segments of D-A and B-C represent the non-discharge phases.

According to Figure 5.5, the gap length  $d_g$  between the dielectric barrier and the meshed electrodes is variable. The electric field across the entire gap is  $E_g$ . The maximum gap length on each side is the mesh wire thickness,  $d_w$ . With the continuous increase of the applied voltage  $V_A$ , the electric field across the gap increased, enabling gas breakdown to happen in longer gaps,  $d_g$ . The total breakdown voltage is the sum of the breakdown voltage across the two gaps above and below the quartz plate.

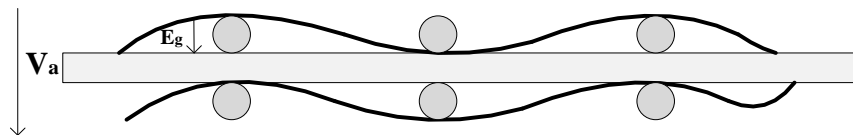


Figure 5.5 The schematic of gas discharge using a mesh plate electrode test cell.

The positive discharge phase starts at point A at -750 V. Drawing a straight line between A and B, the intersection with  $x$ -axis is termed as  $V_{b-A}$ , which is 1080 V. While, in this Lissajous figure, once the charge transfer is equal to zero, the applied voltage at this point (E) is named as  $V_{b-p}$  and is 1670 V.

Extending the lines B-E and D-A, the intersection is named as A'. This implies that the starting discharge point of the equivalent gap length at point B should be A'. The voltage at the intersection A' is 600 V, which is greater than the voltage applied at point A. With increasing applied voltage, the discharge gap length at point B is much longer than that where the discharge happens at point A. According to Figure 5.4, from point A to point E, the breakdown voltage increases gradually. From point E to B, the breakdown voltage does not change significantly.

By using meshed electrodes, the voltage across the test cell when  $y$ -axis  $Q=0$ , is the equivalent breakdown voltage.

### B. Input energy calculation

The equivalent total capacitance  $C_t$  is the slope of DA and CB. The barrier capacitance  $C_d$  is the slope of EB and DF. The energy input per cycle is measured based on these six points selected. The equivalent gap capacitance  $C_g$  can be calculated using the capacitance formula. As the measured Lissajous figure is not an ideal parallelogram, the calculated Lissajous figure area is slightly larger than the actual input energy. The total input energy over 100 cycles can be calculated by summing the energy input of each cycle, calculated as shown in (5.1):

$$E_i = 4C_{d-i}V_{b-i}(V_{\max-i} - \frac{C_{g-i} + C_{d-i}}{C_{d-i}}V_{b-i}) \quad (5.1)$$

### C. Discharge gap length

The equivalent discharge gap length  $d_g$  is calculated by the formula of parallel plate capacitance shown in (5.2):

$$C_g = \frac{\epsilon_0 A}{d_g} \quad (5.2)$$

Here the discharge gap length is the sum of the gap length between the high voltage electrode and barrier and the gap length between the barrier and the ground electrode.

**D. Electric field**

The electric field is equal to the breakdown voltage divided by the gap length, as displayed in (5.3):

$$E = \frac{V_b}{d_g} = \frac{V_b C_g}{\varepsilon_0 A} \quad (5.3)$$

The reduced electric field (Td) can be calculated by dividing the electric field,  $E$ , by the number of particles,  $N$ .

**5.4 Current and ozone efficiency analysis under different conditions**

Discharge characteristics and the corresponding ozone generation efficiency were investigated under various applied voltages and gas pressures. Finally, the relationship between ozone efficiency and reduced electric field was investigated.

**5.4.1 Discharges at different voltages**

The experiment was carried out by changing the applied voltage from 4.5 kV<sub>p</sub> to 6.5 kV<sub>p</sub> in 0.5 kV increments using meshed electrodes with 0.96 mm aperture size at 298 K and 1 bar absolute.

**A. Current amplitude distribution analysis**

From the experimental results using planar electrodes, the current amplitudes conformed to a normal distribution with an average amplitude of tens of milliamps. In this subsection, the current amplitude distribution and the average peak current and its standard deviation are investigated at different applied voltages.

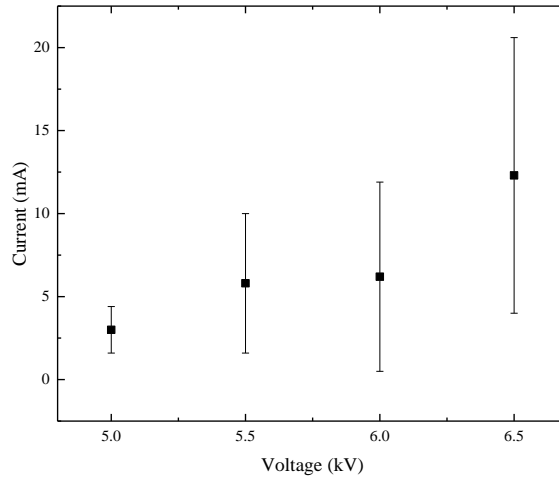


Figure 5.6 The average current with standard deviation at different applied voltages (from 5.0 kV<sub>p</sub> to 6.5 kV<sub>p</sub>) using meshed electrodes with a 0.96 mm aperture size, 0.5 slpm, at 298 K and 1 bar absolute.

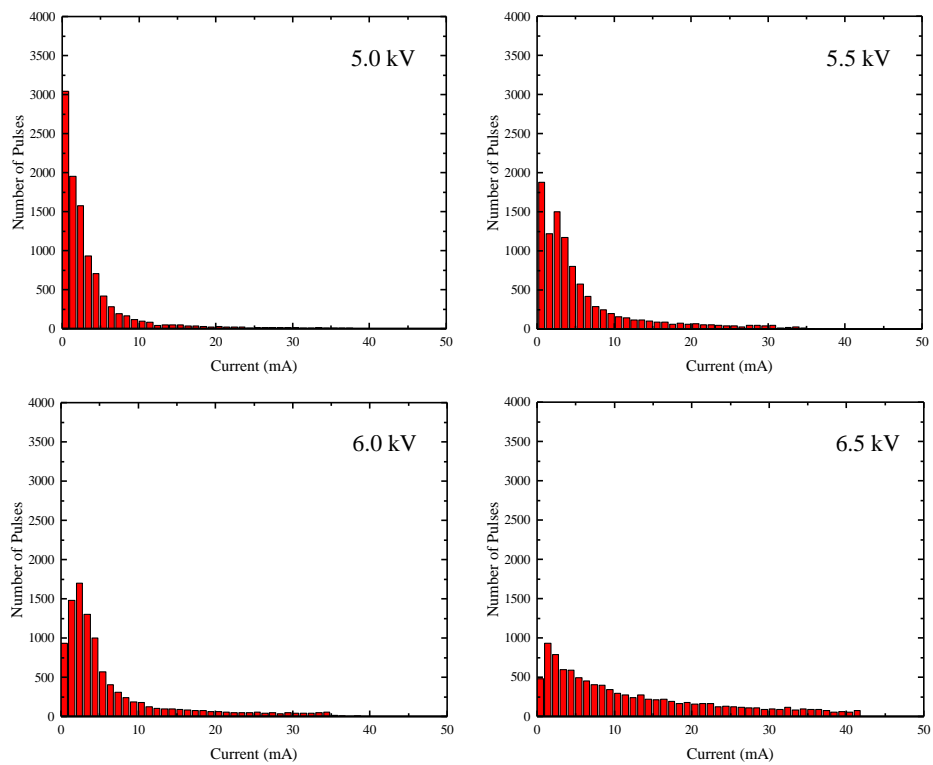


Figure 5.7 The current amplitude distribution at different applied voltages (from 5.0 kV<sub>p</sub> to 6.5 kV<sub>p</sub>) using meshed electrodes with a 0.96 mm aperture size, 0.5 slpm, at 298 K and 1 bar absolute.

Figure 5.6 to Figure 5.7 show the current distribution at 5 kV<sub>p</sub> to 6.5 kV<sub>p</sub>. Each column represents 1 mA interval. With increasing the applied voltage, the mean peak current increases from 3.2 mA to more than 12.3 mA. The amplitude distribution of the external current at a lower applied voltage (4.5 kV<sub>p</sub> to 5 kV<sub>p</sub>) is much narrower than that at a high applied voltage. The maximum number of pulses at 5.0 kV<sub>p</sub> is over 3000 within 1 mA interval. With continuous increasing the applied voltage to 6.5 kV<sub>p</sub>, the maximum number of pulses is only 1000 within 1 mA interval.

For lower applied voltage, the discharge starts to develop at a location with a short gap length. The accumulated charges can only be deposited within a small surface area where the electric field is strongest. With the increase in the applied voltage, the voltage across the gap also increases to ignite the discharge in a location with longer gap length. According to the results of average external current, it shows that by increasing the applied voltage, the amplitude of the external current increases corresponding to increased charge transfer.

### B. Lissajous figure at different applied voltages

The energy input of each experiment was calculated using a Lissajous figure, as shown in Figure 5.8. The waveforms of all 100 cycles were recorded using the oscilloscope and were analysed and calculated in Matlab (see Appendix A).

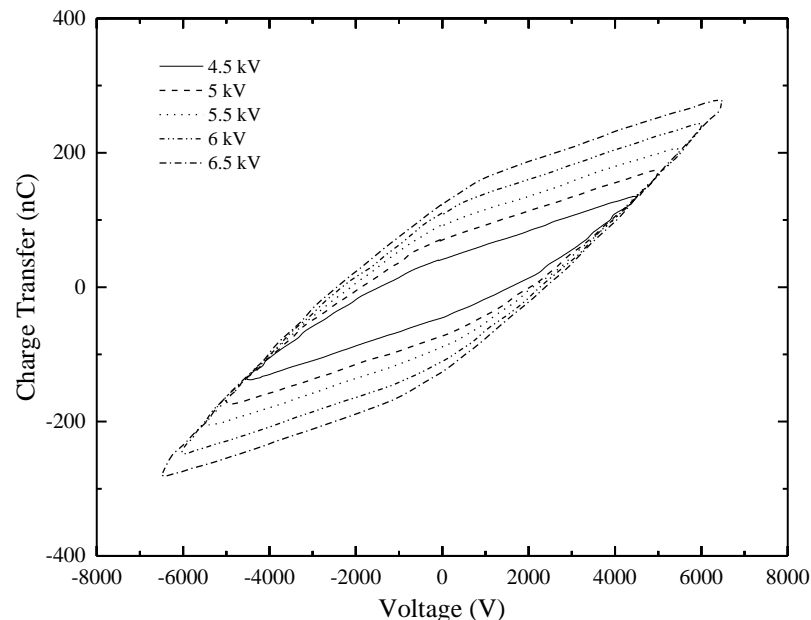


Figure 5.8 The Lissajous figure at different applied voltages (from 4.5 kV<sub>p</sub> to 6.5 kV<sub>p</sub>) with mesh electrodes having an aperture size of 0.96 mm, 0.5 slpm, at 298 K and 1 bar absolute.

Figure 5.9 shows the breakdown voltage under different applied voltages. With an increase of the amplitude of the applied voltage, the equivalent breakdown voltage increases from 1105 V to 2061 V. The higher applied voltage led to the breakdown of longer gaps. By increasing the applied voltage, the total charge transfer increases which increases the density of charge accumulation. The higher density of deposited charge will increase the breakdown voltage, as in the analysis of using planar electrode, though it is not a major cause for increased breakdown voltage here.

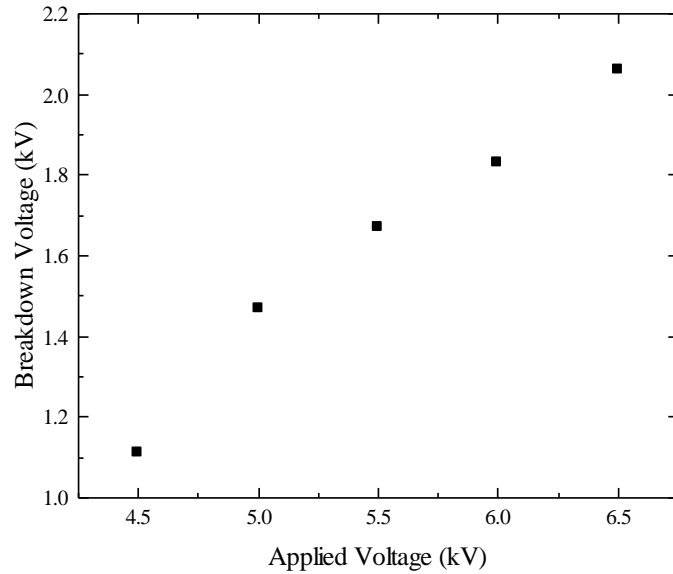


Figure 5.9 Breakdown voltage vs applied voltage using 0.96 mm meshed electrodes, 0.5 slpm, at 298 K and 1 bar absolute.

Table 5.1 Discharge parameters at applied voltages ranging from 4.5 kV<sub>p</sub> to 6.5 kV<sub>p</sub> in 0.5 kV increments using meshed electrodes with a 0.96 mm aperture size.

<b>Applied Voltage (kV<sub>p</sub>)</b>	<b>Input Energy per 100 cycle (mJ)</b>	<b>Breakdown Voltage (kV)</b>	<b>Equivalent Gap length (mm)</b>	<b>Reduced Electric Field (Td)</b>
4.5	28	1105	0.28	133
5.0	56	1465	0.31	138
5.5	84	1671	0.40	153
6.0	112	1826	0.39	161
6.5	136	2061	0.42	179

Table 5.1 summarizes the variation of the input energy, breakdown voltage, equivalent gap length and reduced electric field with applied voltage. The equivalent gap length increased from 0.28 mm to 0.42 mm for the double gap structure. The equivalent reduced electric field increased from 133 Td to 180 Td.

### C. Ozone Efficiency at different applied voltages

Figure 5.10 shows the ozone concentration measured at different applied voltages. Two peaks were observed in the ozone measurement. The first one corresponds to the ozone produced between grounded mesh and the quartz plate, which flows to the ozone analyser first; while the second peak corresponds to the ozone produced between the high voltage mesh and the quartz plate, which flows to the ozone analyser after a short delay. The amount of ozone produced in the two gaps is approximately the same. The total ozone production can be calculated by integrating the ozone concentration curve with time. The peak value of the ozone concentration increased from 31 ppm to 300 ppm.

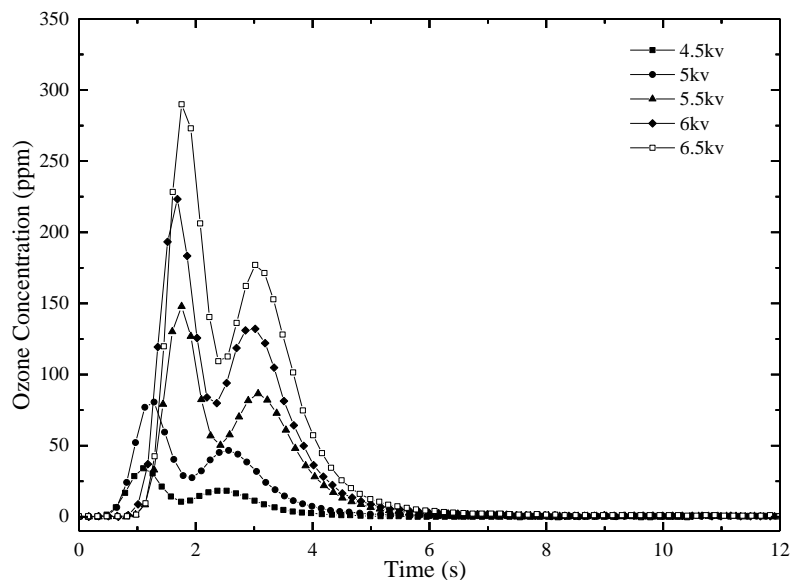


Figure 5.10 The corresponding ozone concentration in real time with mesh electrodes that have an aperture size of 0.96 mm, 0.5 slpm, at 298 K and 1 bar absolute.

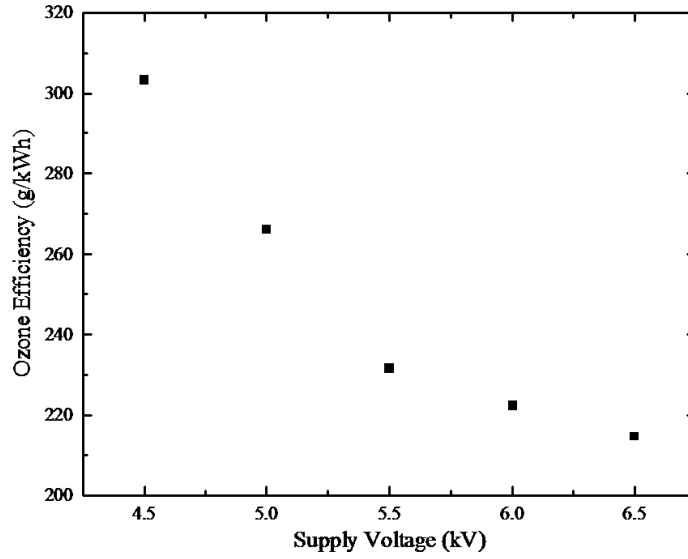


Figure 5.11 The ozone efficiency with different applied voltages (from 4.5 kV<sub>p</sub> to 6.5 kV<sub>p</sub>) at 1 bar absolute. The dielectric barrier is 1 mm thick, and the mesh has an aperture size of 0.96 mm.

In Figure 5.11, with the increase in the applied voltage from 4.5 kV<sub>p</sub> to 6.5 kV<sub>p</sub>, the ozone efficiency drops from 303 g/kWh to 214 g/kWh. By increasing the applied voltage, the average peak current and the charge transfer per filament increase. The charge transfer per filament can be described as (5.4) [30]:

$$Q_c = e \cdot F_c \cdot \int_0^{t_d} v_d \cdot N_e dt \quad (5.4)$$

where  $N_e$ ,  $v_d$  and  $F_c$  are the electron density, electron drift velocity, and the cross-section of the micro-discharge channel, respectively. Assuming that the volume of each filament is the same, the cross-section of the micro-discharge channel and the electron drift velocity are the same, the increasing of charge transfer  $Q_c$  means the increment of electron density  $N_e$ .

The reduced electric field is an important parameter for ozone generation, which is proportional to the mean energy of the electrons [56]. Due to the increase of the reduced electric field, the mean electron energy increases. Based on the electron collision cross-section shown in Figure 4.27, the oxygen molecule dissociation cross section increases with electron energy up to 30 eV. The increase in  $c[O]$  can produce more ozone molecules while the ozone dissociation due to reactions between ozone molecules and atomic oxygen increases as well.

The specific energy ( $J/L$ ) is defined as the injected energy per unit volume of feed gas, calculated using equation (5.5):

$$\text{SpecificEnergy} = \frac{P \cdot 60}{FL} \quad (5.5)$$

where  $FL$  is the flow rate of the feed gas in L/min.

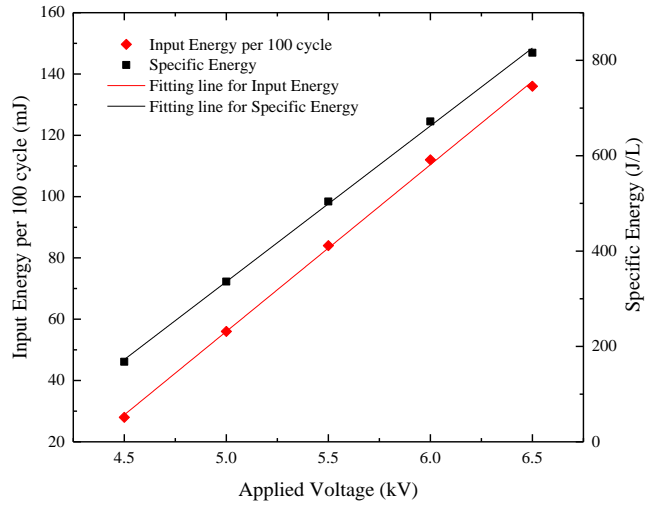


Figure 5.12 The input energy per 100 cycle and the specific energy under different applied voltage (from 4.5 kV<sub>p</sub> to 6.5 kV<sub>p</sub>), using 0.96 mm meshed electrodes, 0.5 slpm, at 298 K and 1 bar absolute.

According to Figure 5.13, the increment of ozone concentration with specific power is not linear. The ratio between ozone concentration and specific power decreases while increasing the specific energy. As a result, the total ozone efficiency decreases when the applied voltage increases.

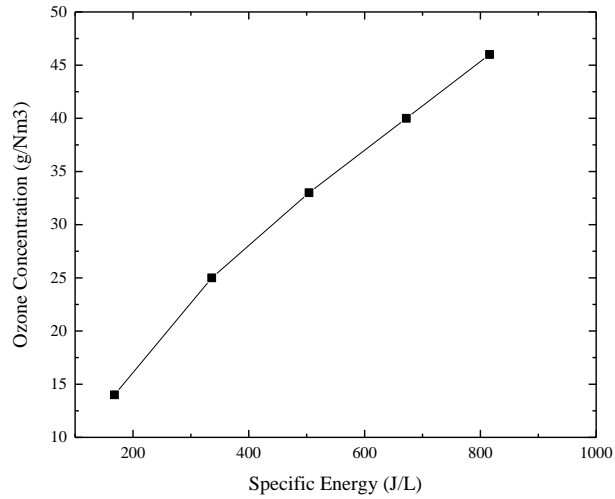


Figure 5.13 The relationship between specific power and ozone concentration under different applied voltage ( $4.5 \text{ kV}_p$  to  $6.5 \text{ kV}_p$ ), with 0.96 mm aperture size meshed electrodes, 0.5 slpm, at 298 K and 1 bar absolute.

#### 5.4.2 Discharges under different gas pressures

##### A. Current amplitude distribution analysis

10,000 single current pulses were captured. The average peak current shown in Figure 5.14 decreased from 4.9 mA at 1.2 bar absolute to 3.3 mA at 2.0 bar absolute. The current amplitude distribution is shown in Figure 5.15; with an increase in the pressure, the distribution became narrower.

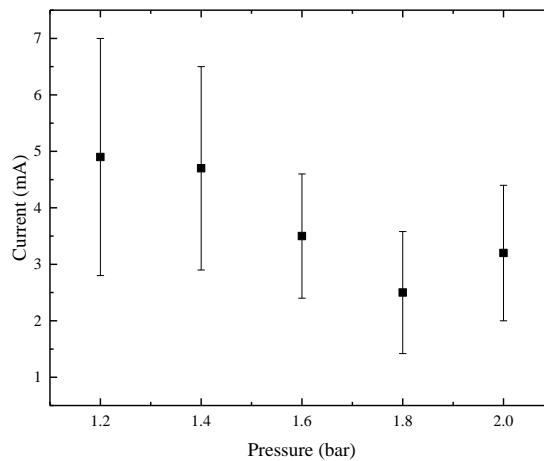


Figure 5.14 The average current with a standard deviation under different pressures with mesh with an aperture size of 0.96 mm, 0.5 slpm, at 298 K and  $6.5 \text{ kV}_p$  applied voltage.

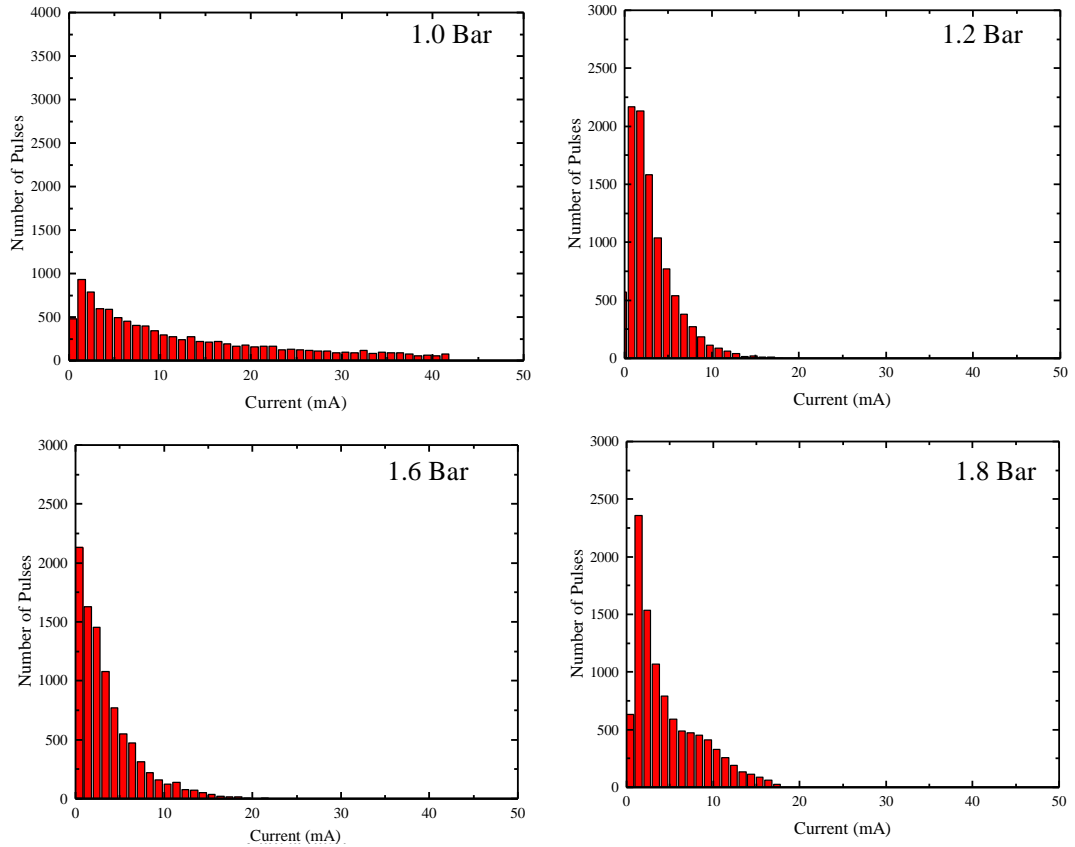


Figure 5.15 The current amplitude distribution under different pressures from 1.2 bar absolute to 2.0 bar absolute with meshed electrodes with an aperture size of 0.96 mm, 0.5 slpm, at 298 K and 6.5 kV<sub>p</sub> applied voltage.

It is found that the average peak current changes from ~ 13 mA at 1.0 bar absolute to ~5 mA at 1.2 bar absolute. With continuous increasing the pressure to 1.8 bar, the average peak current decreases from 5 mA to less than 3 mA. The narrower distribution is observed with increasing the absolute pressure from 1.0 bar to 1.2 bar.

### B. Discharge parameters at different gas pressure

Figure 5.16 shows the sampled Lissajous figures under different absolute pressure.

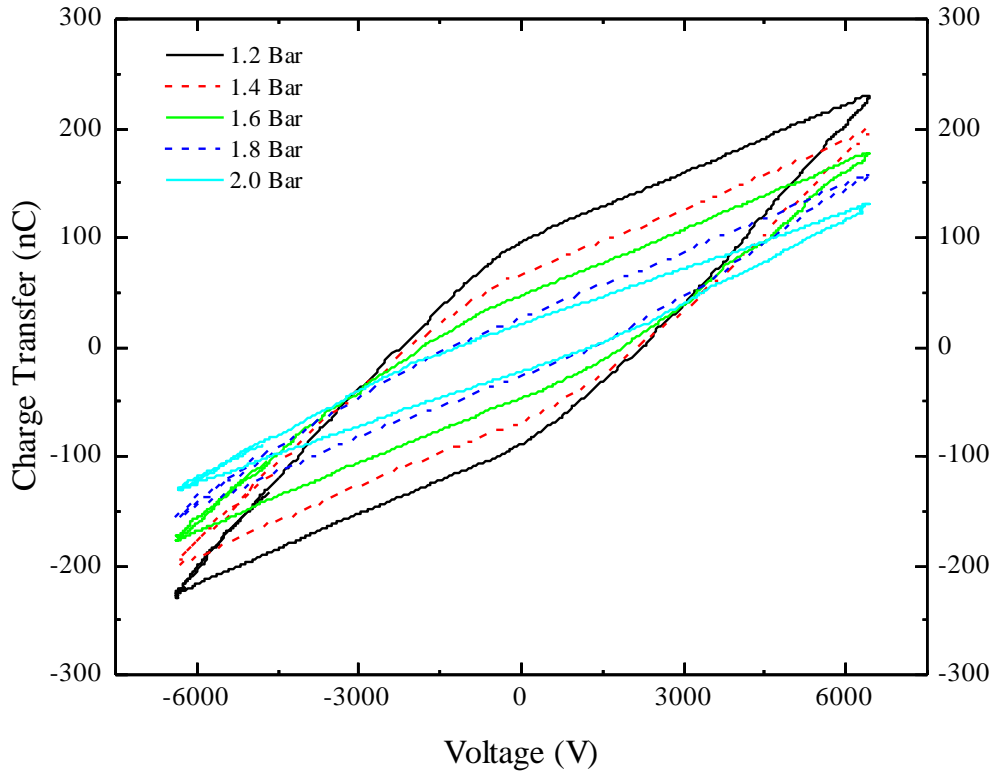


Figure 5.16 The Lissajous figure under different absolute pressure under 0.96 mm aperture size meshed electrodes, 0.5 slpm, at 298 K and 6.5 kV<sub>p</sub> applied voltage.

With 6.5 kV<sub>p</sub> applied voltage, by changing the gas pressure from 1.2 bar to 2.0 bar, the breakdown voltage decreases from 2011 V to 1419 V. According to Paschen curve, with increasing gas pressure at the same gap length, the required breakdown voltage increases. Nevertheless, the breakdown voltage shown in Figure 5.16 is decreasing with the increase of gas pressure. Due to the uneven gap length, with increasing the gas pressure, the required breakdown voltage increases. Under the same applied voltage, the gas breakdown can only happen in a short gap length. As a result, the equivalent breakdown voltage decreases.

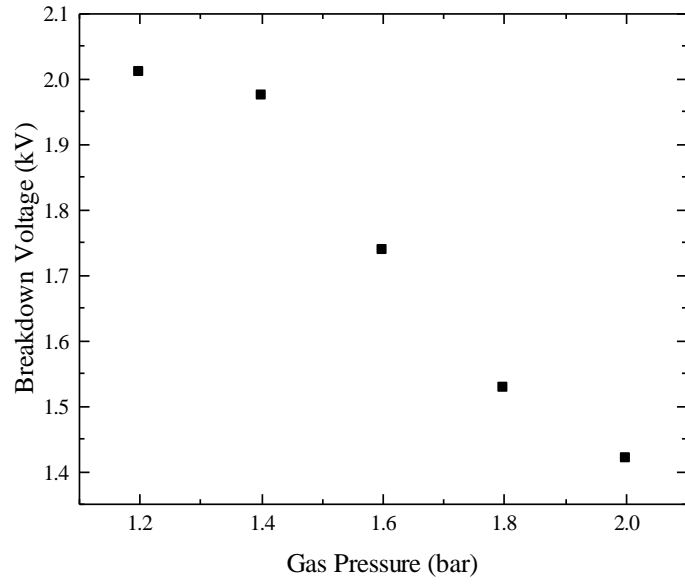


Figure 5.17 Breakdown voltage versus gas pressure with 0.96 mm aperture size meshed electrodes, 0.5 slpm, at 298 K and 6.5 kV<sub>p</sub>.

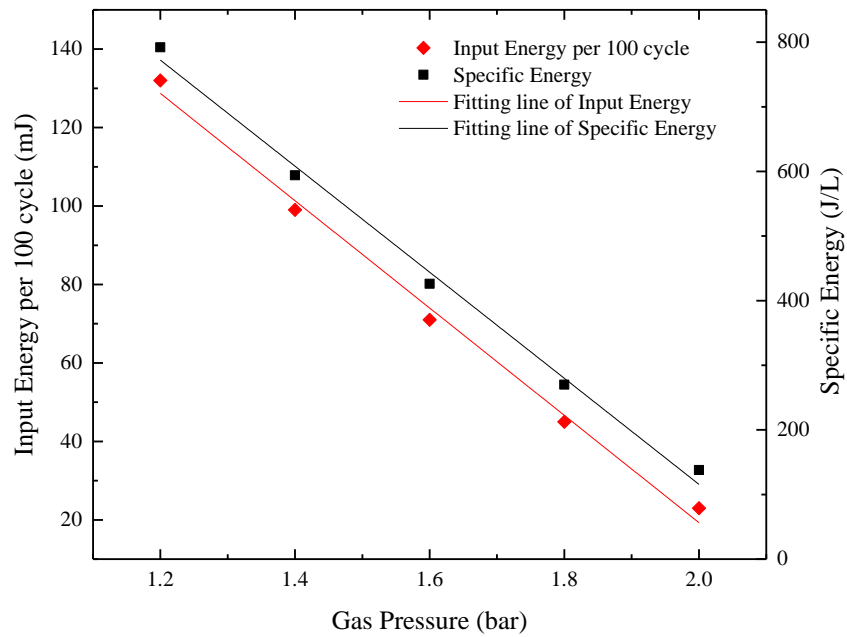


Figure 5.18 The input energy per 100 cycle and the specific energy under different gas pressure (from 1.2 Bar to 2.0 Bar) with 0.96 mm aperture size meshed electrodes, 0.5 slpm, at 298 K and 6.5 kV<sub>p</sub>.

Figure 5.18 shows the input energy and the specific energy decrease linearly with the increasing of gas pressure. The results prove that the discharge under meshed electrode always develop in shorter gaps first and expand to longer gaps with the increase of voltage.

The parameters are calculated under different absolute pressure from 1.2 bar absolute to 1.8 bar absolute with 6.5 kV<sub>p</sub> as shown in Table 5.2.

Table 5.2 The discharge parameters under different pressures with applied voltage of 6.5 kV<sub>p</sub>.

<b>Absolute Pressure (Bar)</b>	<b>Input Energy per 100 cycle (mJ)</b>	<b>Breakdown Voltage (V)</b>	<b>Equivalent length (mm)</b>	<b>Gap Reduced Electric Field (Td)</b>
1.2	132	2011	0.42	166
1.4	99	1973	0.40	142
1.6	71	1737	0.34	130
1.8	45	1526	0.30	113
2.0	23	1479	0.25	108

With 6.5 kV<sub>p</sub> applied voltage, the reduced electric field is decreasing from 166 Td to 108 Td, while the equivalent gap length decreases from 0.42 mm to 0.25 mm. With increasing gas pressure, the discharge is limited to short gaps below 0.3 mm. The majority of the discharge filaments should develop at much shorter gap length.

### **C. Ozone efficiency at different gas pressure**

Figure 5.19 shows the transient ozone concentration with 6.5 kV<sub>p</sub> applied voltage for 100 cycles energy generation. With the increase of gas pressure, the ozone concentration decreases. The peak value of the ozone concentration shown in Figure 5.19 decreased from nearly 300 ppm to 50 ppm.

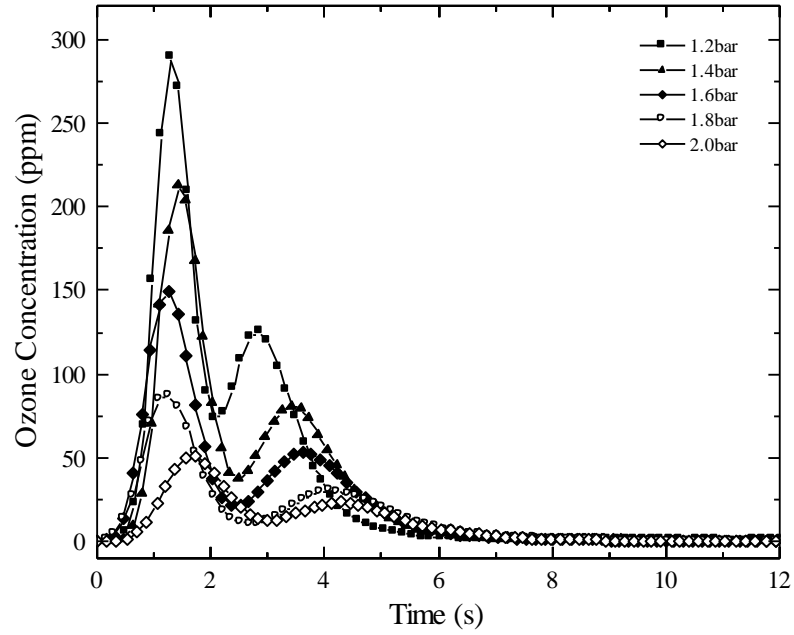


Figure 5.19 the corresponding ozone concentration in real-time under 0.96 mm aperture size meshed-plates, 0.5 slpm, at 298 K and 6.5 kV<sub>p</sub> applied voltage.

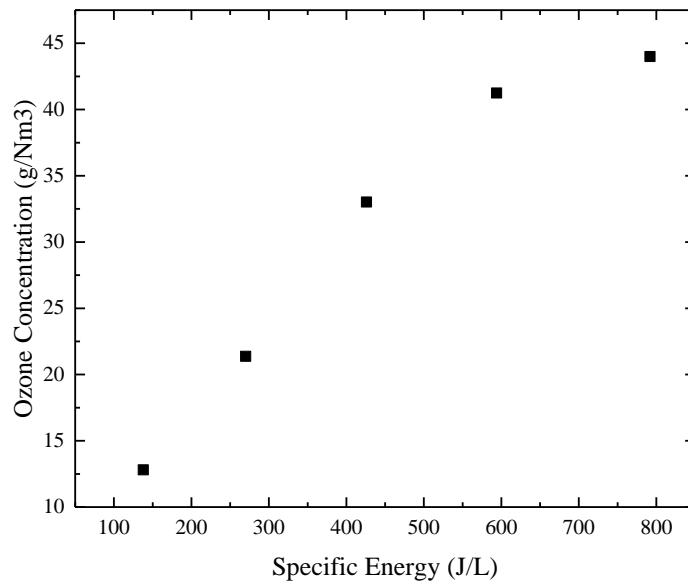


Figure 5.20 Ozone concentration with specific energy under different gas pressure (from 1.2 bar to 2.0 bar) with 0.96 mm aperture size meshed-plates, 0.5 slpm, at 298 K and 6.5 kV<sub>p</sub> applied voltage.

The ozone concentration increases non-linearly with increasing specific energy. With increasing gas pressure, the ratio between ozone concentration and specific energy increases. Figure 5.21 shows that the ozone efficiency increases with increasing gas pressure at 6.5 kV<sub>p</sub>. The best ozone efficiency is 334 g/kWh at 2 bar absolute. With increasing gas pressure, the gas density increases. The non-uniform gap length leads to the majority discharges happening across shorter gap. According to Braun's research [83], the pressure increasing can reduce the filament radius therefore the diffusion area of the charges accumulated on the barrier surface decreases, as a result, the reversed electric field can be established faster to extinguish the discharge. For the same charge transfer, the discharge time increases leading to a more uniform distribution of electrons to collide with oxygen molecules to produce ozone molecules. The dissociation of ozone is related to the ozone concentration, which means that higher ozone concentration can increase the ozone dissociation speed. The more uniform distribution of ozone in the gas gap can decrease the ozone dissociation.

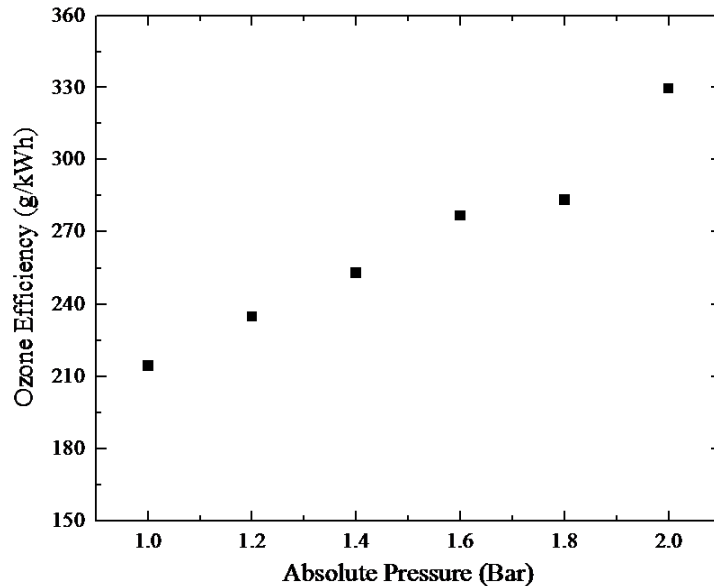


Figure 5.21 The average ozone efficiency at different pressure from 1 bar absolute to 2 bar absolute.

### 5.5 Ozone efficiency versus reduced electric field

In this section, the relationship between ozone efficiency and reduced electric field has been characterised by changing the applied voltage from 4.5 kV<sub>p</sub> to 6.5 kV<sub>p</sub> in 0.5 kV increments and changing the pressure from 1 bar absolute to 2 bar absolute in 0.2 bar absolute increments under 5.5 kV<sub>p</sub> to 6.5 kV<sub>p</sub> applied voltage as shown in Figure 5.22.

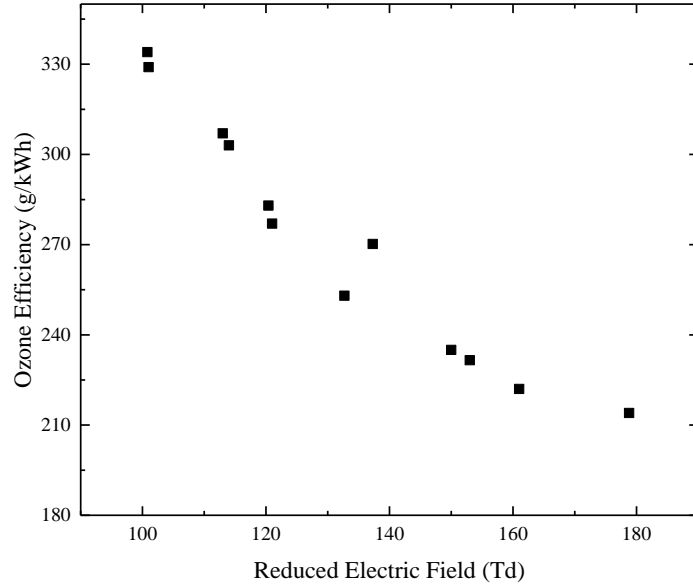
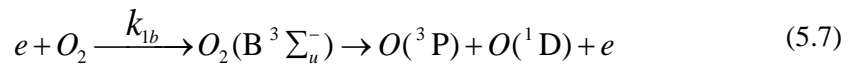
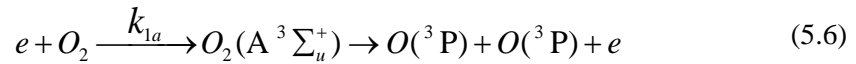


Figure 5.22 The relationship between reduced electric field (Td) and ozone efficiency (g/kWh) using 0.96 mm aperture size meshed electrodes.

The highest ozone efficiency achieved in this experiment is 334 g/kWh at 101 Td under 6.5 kV<sub>p</sub> applied voltage and 2 bar absolute. After that, the ozone efficiency gradually drops to 214 g/kWh when the reduced electric field increases to 180 Td.

The *O* atoms are generated by collisions between *O*<sub>2</sub> molecules and electrons as shown in reactions (5.6) and (5.7).



The number of oxygen atoms produced by one electron per cm of path can be calculated as shown in (5.8):

$$N(O) = 2(k_{1a} + k_{1b}) \cdot N(O_2) \cdot v_d^{-1} \quad (5.8)$$

where  $N(O_2)$  is the initial concentration of *O*<sub>2</sub> molecules in particles per cm<sup>3</sup>, and  $v_d$  is the drift velocity of electrons in cm/s.

The production of vibrationally-excited ozone molecules:



The production of ground state ozone molecules:



The dissociation of ozone molecules:



The conversion ratio of atomic oxygen to ozone molecules can be calculated based on the reaction rate ( $k_{1a}$  to  $k_5$ ) as shown (5.13):

$$\begin{aligned} C_{O_3} &= \frac{k_3 N(O)N(O_3^*) + k_4 N(O_2)N(O_3^*)}{k_3 N(O)N(O_3^*) + k_4 N(O_2)N(O_3^*) + 2k_5 N(O)N(O_3^*)} \\ &= \frac{k_3 N(O) + k_4 N(O_2)}{k_3 N(O) + k_4 N(O_2) + 2k_5 N(O)} \\ &= \frac{1}{2k_5 \frac{N(O)}{N(O_2)} + 1 + \frac{N(O)}{k_3 \frac{N(O)}{N(O_2)} + k_4}} \\ &= \frac{1}{1 + \frac{2k_5 c[O]}{k_3 c[O] + k_4}} \end{aligned} \quad (5.13)$$

Where the relative atomic oxygen concentration is named as  $c[O]$ .

The ozone production  $N[O_3]$  is related to the production of atomic oxygen and its conversion rate, which can be calculated as (5.14):

$$N(O_3) = N(O) \cdot C_{O_3} = 2(k_{1a} + k_{1b}) \cdot N(O_2) \cdot v_d^{-1} \frac{1}{1 + \frac{2k_5 c[O]}{k_3 c[O] + k_4}} \quad (5.14)$$

In an oxygen discharge with the electrical field strength  $E$ , the energy obtained by an electron per cm of path is given by (5.15):

$$\Delta E_e = eE \quad (5.15)$$

Assuming that the portion of energy carried by electrons is  $k_r$ , the total energy that is imparted to the discharge in the electric field per cm of path is given by (5.16)

$$\Delta E_t = \frac{\Delta E_e}{k_r} \quad (5.16)$$

According to [30] [84], the portion of  $k_l$  is estimated to be 0.5 in dielectric barrier discharges, because the dielectric barrier discharge is considered to be developed to the stage of the streamer discharge, where electrons and positive ions are produced evenly along the discharge columns [85]. The ozone generation efficiency is calculated as (5.17):

$$\eta = \frac{N(O_3)}{\Delta E_t} = \frac{1}{2} \cdot \frac{N(O)}{\Delta E_e} \cdot C_{O_3} \quad (5.17)$$

The theoretical ozone efficiency can be calculated using equation (5.18):

$$\eta = \frac{(k_{1a} + k_{1b})}{v_d(E/N)} \cdot \frac{1}{1 + \frac{2k_5 c[O]}{k_3 c[O] + k_4}} O_3 \text{ molecules} / eV \quad (5.18)$$

It can be seen that the ozone efficiency depends on the relative  $O$  atom concentration  $c[O]$ , the reduced electric field ( $E/N$ ), the reaction rate coefficients and the drift velocity of electrons ( $v_d$ ). As the  $O$  atoms are generated during the discharge,  $c[O]$  depends on the energy density of these discharges ( $W$ ) [74].

In this work, the feed gas pressure and applied voltage were adjusted, which leads to the change of the internal gas discharge parameters, as a result, the ozone concentration and ozone efficiency changes. According to Seung-Lok Park's research [86], by using meshed electrodes, the ozone efficiency increases due to the electrode configuration limiting the ozone residence time in the discharge gap. Park concluded that the decomposition of ozone was reduced. Increasing the discharge power or reducing the gas pressure both resulted in increased specific energy. With an increase in specific energy, the gas temperature increases, which results in saturation of the ozone concentration when the ozone dissociation rate is equal to the ozone formation rate. The same trend was found in [87] and [88]. The ozone concentration was found to increase with increasing specific energy but tended to saturate when the specific energy was raised higher than 2 kJ/L, where the ozone concentration was  $\sim 30$  g/Nm<sup>3</sup>. According to

Monge's research [88], when increasing the specific energy, the ozone concentration did not increase linearly. It was found that the ozone concentration under 6 L/h was the same as that under 8 L/h. It was also found that changing the amplitude of the applied voltage resulted in different ozone performance. The ozone efficiency at lower voltage amplitude was higher than that at higher voltage amplitude.

## 5.6 Ozone generation and mesh aperture size

In the following subsection, the meshed electrodes are changed by using different aperture sizes. The diameter of the electrodes is kept the same. In this experiment, meshes with 1.7 mm, 0.56 mm and 0.26 mm aperture sizes are used. The relationship between ozone efficiency and the reduced electric field with different aperture sizes is analysed.

### 5.6.1 Ozone efficiency

To analyse the behaviour of discharges for meshed electrodes with different aperture sizes, the absolute pressure was changed from 1 bar absolute to 1.8 bar absolute in 0.2 bar absolute increments with 6.5 kV<sub>p</sub> applied voltage. All the parameters were investigated, as shown in Table 5.3.

Table 5.3 The discharge parameters under different pressures (1 bar absolute to 1.8 bar absolute in 0.2 bar absolute increments) using meshed electrodes with 1.7 mm, 0.56 mm and 0.26 mm aperture sizes with 6.5 kV<sub>p</sub> applied voltage at 5 kHz.

<b>Aperture Size (mm)</b>	<b>Absolute Pressure (Bar)</b>	<b>Energised Energy (mJ)</b>	<b>Breakdown Voltage (V)</b>	<b>Equivalent Gap length (mm)</b>	<b>Reduced Electric Field (Td)</b>
1.70	1.0	130	2780.9	0.82	140.8
	1.2	89	2519.0	0.72	122.9
	1.4	54	1979.3	0.59	101.3
	1.6	39	1718.5	0.56	103.9
	1.8	20	1331.5	0.34	90.3
0.56	1	101	1748.8	0.32	199.6
	1.2	95	1644.5	0.29	193.78
	1.4	85	165.3	0.29	165.7
	1.6	74	1574.0	0.28	145.7
	1.8	46	1430.1	0.25	135.5
0.26	1	103	1492.7	0.24	257.8
	1.2	104	1612.7	0.29	200.0
	1.4	87	1591.5	0.27	173.8
	1.6	69	1445.5	0.24	155.1
	1.8	48	1371.7	0.21	150.6

For the meshed electrodes with a 1.7 mm aperture size, the equivalent gap length increased dramatically from 0.34 mm to 0.82 mm when decreasing the absolute pressure from 1.8 bar

absolute to 1 bar absolute at 6.5 kV<sub>p</sub> applied voltage, while the energy input increased from 20 mJ to 130 mJ.

For the meshed electrodes with a 0.56 mm aperture size, increasing the pressure caused the breakdown voltage to decrease gradually with the decrease in the power input. The maximum reduced electric field increased from 140.8 Td when using meshed electrodes with a 1.7 mm aperture size to nearly 200 Td when using meshed electrodes with a 0.56 mm aperture size. The equivalent gap length continued to decrease from 0.32 mm at 1 bar absolute to 0.25 mm at 1.8 bar absolute.

For the meshed electrodes with a 0.26 mm aperture size, increasing the pressure caused the breakdown voltage to increase from 1492 V at 1 bar absolute to 1612 V at 1.2 bar absolute, and to then drop to 1371 V at 1.8 bar absolute. Increasing the breakdown voltage indicates that, when using meshed electrodes with the thin wire, the discharge can occur along the entire gas gap. Continuously increasing the pressure causes the discharge distance to reduce with the decrease of the breakdown voltage.

Overall, when decreasing the aperture size, the equivalent reduced electric field increased under the same discharge conditions (the same voltage and pressure).

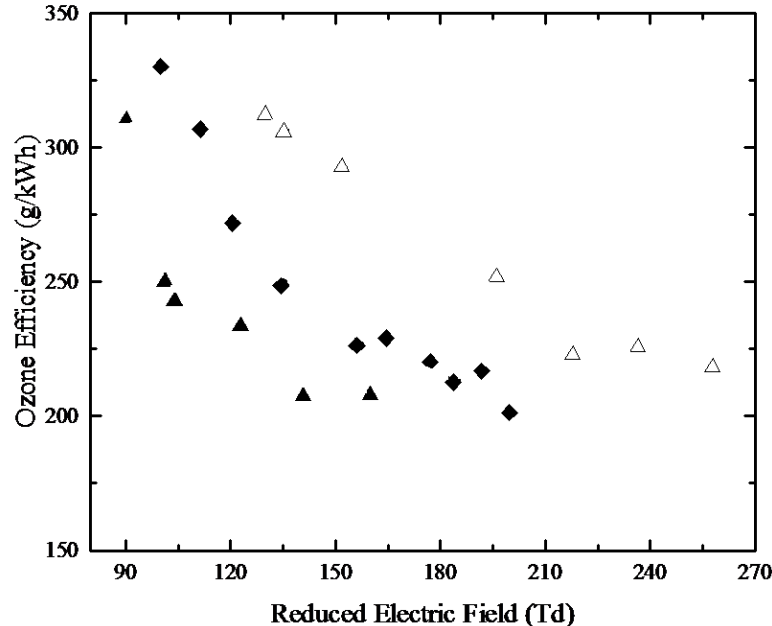


Figure 5.23 The relationship between the reduced electric field (Td) and ozone efficiency (g/kWh) using meshed electrodes with (a) a 1.7 mm aperture size (solid triangles), (b) a 0.56 mm aperture size (solid diamonds) and (c) a 0.26 mm aperture size (open triangles).

In Figure 5.23, the closed triangle points show the result when using a 1.7 mm aperture size. The optimised ozone efficiency can reach 310 g/kWh at 90 Td. After this, the ozone efficiency drops dramatically to 207 g/kWh at a reduced electric field of 161 Td. The closed diamond points indicate the result when using a 0.56 mm aperture size. The maximum ozone efficiency can reach 328 g/kWh at 103 Td and the ozone efficiency drops to 200 g/kWh at 200 Td. The open triangles show the result for the 0.26 mm aperture size. The optimised ozone efficiency can reach 320 g/kWh at 130 Td and drops to below 200 g/kWh at 250 Td. All of the results show that decreasing the reduced electric field can increase the ozone efficiency. In all the experimental conditions, the peak value of the ozone efficiency can reach over 300 g/kWh. On the other hand, for the same reduced electric field, the ozone efficiency increased when decreasing the aperture size. For instance, for the same reduced electric field 140 Td, the ozone efficiency was ~310 g/kWh when using the mesh with a 0.26 mm aperture size, while it was ~250 g/kWh when using the 0.56 mm aperture size and ~200 g/kWh when using the 1.7 mm aperture size. With the increase in the aperture size, the wire thickness increased, leading to a discharge being ignited in a longer equivalent gap length to increase the electron distribution in the discharge gap. The ozone concentration in the gas gap increases to increase the dissociation speed of ozone.

### 5.6.2 Discharge characteristics analysis

The average peak current under different applied voltage is shown in Figure 5.24. Increasing the applied voltage leads to the increment of the average current amplitude. While, the average peak current by using 0.26 mm and 0.56 mm aperture size meshed-electrodes does not show much difference. The average peak current using 1.7 mm size meshed-electrodes increases dramatically from 7 mA to 70 mA at 6.5 kV<sub>p</sub>. The standard deviation increases with the increment of applied voltage to a maximum of 31 mA at 6.5 kV by using 1.7 mm aperture size mesh electrodes.

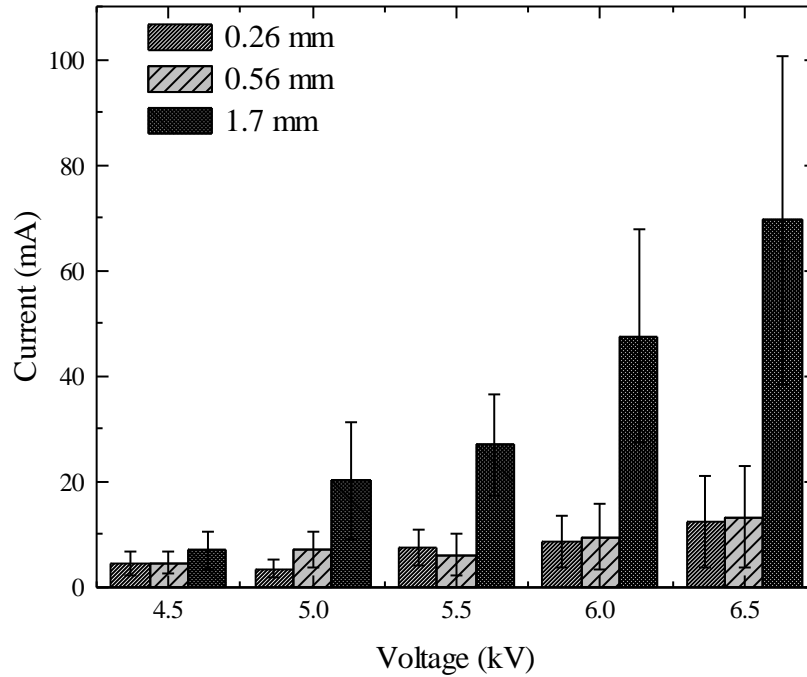


Figure 5.24 Average peak current under different applied voltage with 0.26 mm, 0.56 mm and 1.7 mm aperture size mesh.

The average peak current decreased when decreasing the aperture size. According to the standard deviation analysis, it is clear that the concentrated current amplitude distribution can increase ozone efficiency. With the higher amplitude of the total current, more energy is released by each filament. As a result, ozone efficiency can be reduced.

## 5.7 A comparison of planar electrode and meshed electrode

With 100-cycle power input, for the planar-plates DBD, the best result achieved previously is 220 g/kWh. Compared with the characteristics of the peak current using parallel-plates, the average peak current using meshed electrodes is smaller and the distribution of the peak current is narrower. The more detailed comparison is investigated in the following section.

### 5.7.1 Ozone efficiency versus reduced electric field

In this subsection, the relationship between the reduced electric field and ozone efficiency is investigated by using a meshed electrode (0.96 mm aperture size) and planar-plates electrodes, as shown in Figure 5.25.

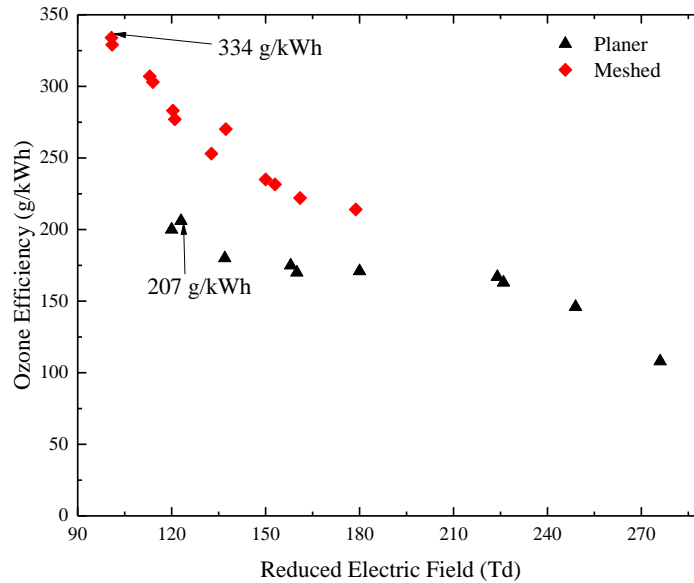


Figure 5.25 The relationship between the reduced electric field (Td) and ozone efficiency (g/kWh) when using meshed electrodes (shown by red diamonds) and planar plates (shown by black triangles).

With the increase in the reduced electric field, the ozone efficiency decreased continuously. The reduced electric field decreased with the increase in the pressure in the test cell. In addition, when increasing the applied voltage, the breakdown voltage increased for both the meshed electrode and the planar electrode.

However, the maximum ozone efficiency can be 334 g/kWh for meshed electrodes compared to the maximum ozone efficiency of 207 g/kWh for planar electrodes. When changing the parameters, such as the applied voltage and the absolute pressure, the ozone efficiency of meshed electrodes decreased from 334 g/kWh to 250 g/kWh with an increase in the reduced electric field from 100 Td to 190 Td. However, the ozone efficiency of planar electrodes decreased dramatically from 207 g/kWh to 100 g/kWh with the increase in the reduced electric field from 120 Td to 280 Td.

Under meshed electrode, the reduced electric field is an average value for the discharge. The exact reduced electric field across the test cell is variable which depends on the gap length at the discharge point. According to the results, the lower the reduced electric field is, the higher the ozone efficiency will be. As the ozone efficiency using meshed-electrodes is, on average, 100 g/kWh higher than that of the planar electrodes, the discharge characteristics by using different electrodes configurations might be different. In the following section, the average

current amplitude at different applied voltage using both meshed electrodes and planar electrodes has been investigated.

The result has an agreement with Takaki's research [89]. Takaki compared ozone synthesis and discharge properties based on DBD by changing the configuration of electrodes. The ozone efficiency increased from 80 g/kWh to 120 g/kWh in pure oxygen by changing the ground electrode from planar to multipoint. Besides, for the same charge transfer, the number of discharges using multipoint reached ~3000 while the number of discharges using planar was 20 times higher.

### 5.7.2 Current amplitude distribution analysis

In this subsection, the current amplitude distribution was considered by changing the applied voltage from 4.5 kV<sub>p</sub> to 6 kV<sub>p</sub> under different electrode configurations. According to the calculated equivalent gap length ( $\approx 0.4$  mm) of meshed electrodes with a 0.96 mm aperture size, a gap length of 0.4 mm was identified. 10,000 single pulses were captured to investigate the distribution of the external current and the average value of the peak current.

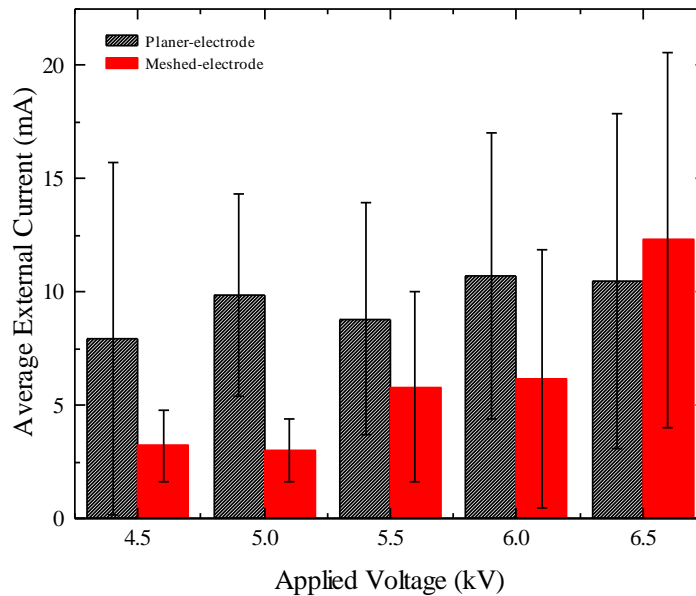


Figure 5.26 The average peak current at different applied voltages using the planar electrode and the meshed electrode with its standard deviation.

When increasing the applied voltage from 4.5 kV<sub>p</sub> to 6.5 kV<sub>p</sub>, the average peak current using planar electrodes did not change dramatically. For 4.5 kV<sub>p</sub> applied voltage, the standard deviation was 7.77 mA. The maximum current captured was 84.6 mA and the minimum

current was only 2.8 mA. With the continuous increase in the applied voltage, the standard deviation varied from 4.48 mA to 7.42 mA.

In the current analysis of meshed-electrodes, when increasing the applied voltage from 4.5 kV<sub>p</sub> to 5 kV<sub>p</sub>, the average peak current did not change significantly, with quite a low standard deviation of ~1.6 mA. With the continuous increase in the applied voltage, the average peak current increased dramatically to 12.3 mA with a large standard deviation of ~8.0 mA. It was observed that the equivalent gap depth increased from ~0.30 mm at 4.5 kV<sub>p</sub> applied voltage to ~0.4 mm at 6.5 kV<sub>p</sub> applied voltage. The increase in the equivalent gap depth led to the development of micro-discharges more completely and the accumulated charges required to form the reversed electric field increased.

Figure 5.27 shows the current amplitude distribution of 0.3 mm planar electrodes at 4.5 kV<sub>p</sub> applied voltage and the current amplitude distribution of 0.96 mm meshed electrodes at 4.5 kV<sub>p</sub> applied voltage with a 1 mm thick quartz barrier. The current amplitude distribution was plotted by capturing 10,000 single pulses. Each column represents 0.5 mA.

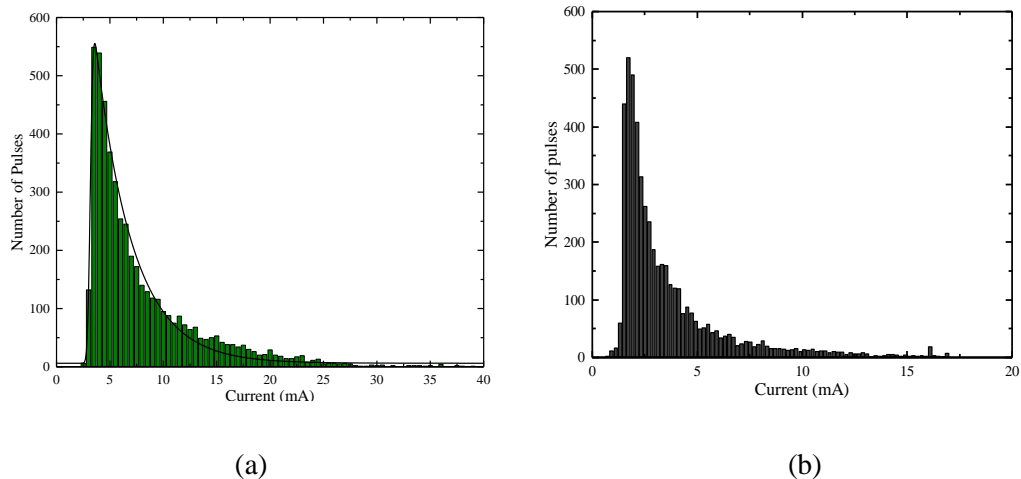


Figure 5.27 The distribution of the peak current at 4.5 kV<sub>p</sub> applied voltage using (a) 0.3 mm planar electrodes and (b) meshed electrodes with a 0.96 mm aperture size.

The current amplitude distribution of 0.3 mm planar electrodes showed that most of the peak current values were between 2.5 mA and 7.5 mA. In the distribution histogram, the maximum peak current was over 35 mA. However, the distribution of meshed electrodes with a 0.96 mm aperture size showed that most of the peak current values were between 1 mA and 3 mA.

Figure 5.28 compares the current and voltage waveforms of the sampled first quarter by using different electrode configurations with the same charge transfer (225 nC). The applied voltage

of the planar electrode was  $\sim 6 \text{ kV}_p$ , while the applied voltage of the meshed electrode was  $\sim 4 \text{ kV}_p$ .

In Figure 5.28 (a), the maximum current was approximately 18 mA. The total discharge number was over 300. In Figure 5.28 (b), the maximum current was approximately 25 mA. The total discharge number was 197. The discharge frequency using meshed electrodes was higher than that of the planar electrodes. The higher charge transfer per filament is indicative of the higher electron density. Once the produced ozone molecules pass through the discharge channel, the atomic oxygen and low energy electrons can dissociate ozone molecules. With higher electron density, the concentration of both atomic oxygen and electrons increase. The dissociation rate of ozone increases as well. As a result, the ozone production decreases significantly with the same energy input.

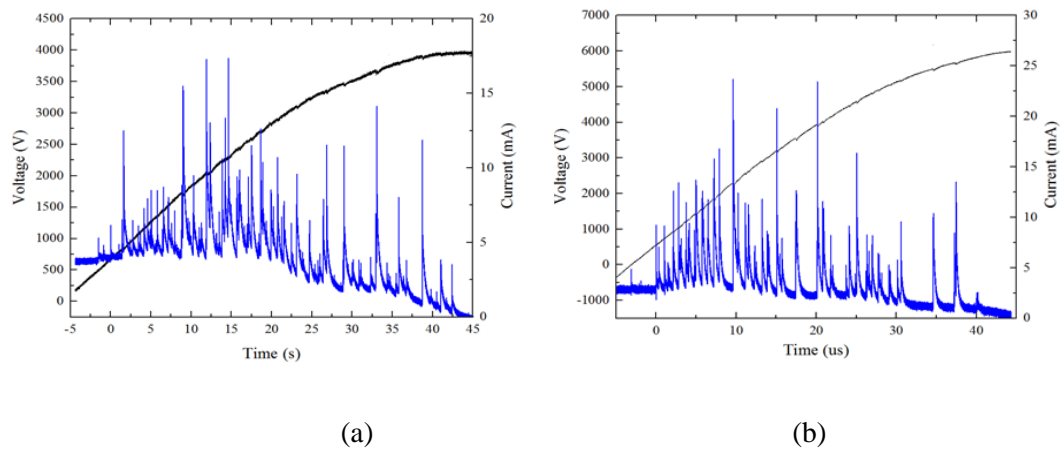


Figure 5.28 The first quarter-cycle current and voltage waveforms of (a) meshed electrodes with a 0.97 mm aperture size with  $4 \text{ kV}_p$  voltage supply and (b) 0.3 mm planar plates with a  $6 \text{ kV}_p$  voltage supply.

## 5.8 Conclusion

According to the Td versus ozone efficiency curve for the 0.96 mm aperture size (Figure 5.22), the maximum ozone efficiency can reach over  $330 \text{ g/kWh}$  at  $100 \text{ Td}$ . Ozone efficiency can be manipulated by changing the applied voltage, changing the pressure in the test cell and changing the aperture size. When increasing the applied voltage, decreasing the pressure and increasing the aperture size of the meshed electrodes, the ozone efficiency decreases.

To establish the relationship between the filament current and the ozone efficiency, the total current at different voltages, under different pressures and with different aperture sizes was

measured. When increasing the applied voltage, the average peak current increased continuously from ~3 mA at 4.5 kV<sub>p</sub> to ~12 mA at 6.5 kV<sub>p</sub>. The distribution was more concentrated for the lower applied voltage. When increasing the pressure, the average peak total current decreased dramatically from ~12 mA at 1.0 bar absolute to ~5 mA at 1.2 bar absolute. With the continuous increase in the pressure, the average current decreased to ~3 mA. The distribution was more concentrated when increasing the pressure. When increasing the aperture sizes, the distribution of the current was wider. All the results indicate that a smaller amplitude of pulsed filament current and a more concentrated distribution of the pulsed filament current can increase the ozone efficiency.

With regard to the ozone formation process, meshed electrodes can increase the discharge times and discharge frequency. This means that there were more discharge points per cycle than when using planar plates with same amount of charge transfer. The comparison was made at the same power density by using 0.96 mm mesh and planar electrodes with a 0.3 mm gap size. The results show that the number of discharges was 398 for meshed electrodes and 118 for planar plates. The ozone efficiency was 230 g/kWh for meshed electrodes and 185 g/kWh for planar electrodes.

For the meshed electrodes DBD, the discharge gap length was variable depending on the amplitude of the voltage in real time. The discharge can be ignited at a low amplitude applied voltage. The low external current magnitude indicates that the filament was easily extinguished. As the electric field across the gap length was variable, the electron diffusion area of the filament was limited. As a result, the radius of the filament channel was limited and the charges transferred by the filament could not expand to a large area. With the same charge transfer, the discharge when using meshed electrodes was more uniform. The electron distribution in the gas gap tended to be more uniform as well. The concentration of atomic oxygen produced was increased to increase the ozone concentration. The different discharge characteristics between meshed-electrodes and planar-electrodes lead to the better performance of ozone efficiency by using meshed-electrodes.

## 6 Ozone Generation Technology below -80 °C

### 6.1 Introduction

#### 6.1.1 Motivation

Considering the investigated results of the last two chapters, the optimized ozone efficiency can reach over 330 g/kWh by using meshed-plates electrodes at 2.0 bar. The corresponding current amplitude distribution is narrow and the amplitude of the external current is below 4 mA. The ozone efficiency increases from 15% to 26% under the same reduced electric field compared with that of the planar electrodes. The water vapour can limit the ozone efficiency, and the lower temperature can increase the reaction rate coefficient of ozone formation. To further increase the ozone efficiency, the low temperature ozone generation needs to be considered. According to the limitations of ozone generation discussed in Chapter 1, the water vapour can produce unwanted species such as  $\text{H}_2\text{O}_2$  and OH to dissociate ozone molecules. At cryogenic temperature, the liquid ozone can be formed which can limit the reaction between ozone molecules and other species. As a result, in this chapter, the dielectric barrier discharge is operating under low temperature (below  $-90^\circ\text{C}$ ) even to cryogenic temperature (normally cryogenic temperature is defined as gas temperature below  $-150^\circ\text{C}$ ). To indicate the relationship between applied frequency and ozone efficiency, the experiment will be carried out using 50 Hz and 5 kHz power supply respectively. In industry, the low concentration ozone is produced by using air. To simulate the industrial performance of ozone generation, both air and oxygen are used to test the ozone generation efficiency result.

#### 6.1.2 Objectives

The main objectives are shown:

When air-fed:

- Investigate the current amplitude distribution under different temperature ( $-80^\circ\text{C}$  to  $-183^\circ\text{C}$ )
- Investigate the ozone efficiency under 50 Hz.

When oxygen-fed:

- Investigate the current amplitude distribution under different temperature ( $-80^\circ\text{C}$  to  $-183^\circ\text{C}$ ).
- Investigate the ozone efficiency under 50 Hz and 5 kHz.

### 6.1.3 Properties of liquid ozone and liquid oxygen

Before describing the experiment, the physical properties of liquid ozone and liquid oxygen will be discussed in detail in the following section, including density, viscosity and surface tension. The boiling point of ozone is -112 °C and the melting point of ozone is -192.2 °C. The boiling point of oxygen is -183 °C and the melting point of oxygen is -218.8 °C.

The density of liquid ozone was measured by Charles K. Hersh *et al.* [90], who used two U-tubes in parallel in liquid nitrogen to prepare liquid ozone and liquid oxygen mixtures.

The density of the saturated solutions at -183 °C and -195 °C was determined. To ensure that no solid was formed, the pressure in the U-tube was adjusted. Table 6.1 shows the results for liquid ozone, liquid oxygen and saturated liquid mixtures.

Based on the results of Table 6.1, decreasing the temperature gradually increases the ozone density.

Table 6.1 The physical properties of liquid oxygen and the mixture of liquid oxygen and liquid ozone [90].

<b>-195 °C</b>		<b>-183 °C</b>	
Ozone wt%	Density (g/L)	Ozone wt%	Density (g/L)
0	1.2	0	1.15
90.8	1.56	30	1.25
100	1.61	100	1.57

## 6.2 Experimental setup

### 6.2.1 Test cell design

In this subsection, the main design of the test cell is introduced clearly and in detail. Figure 6.1 shows the schematic diagram of ozone generation.

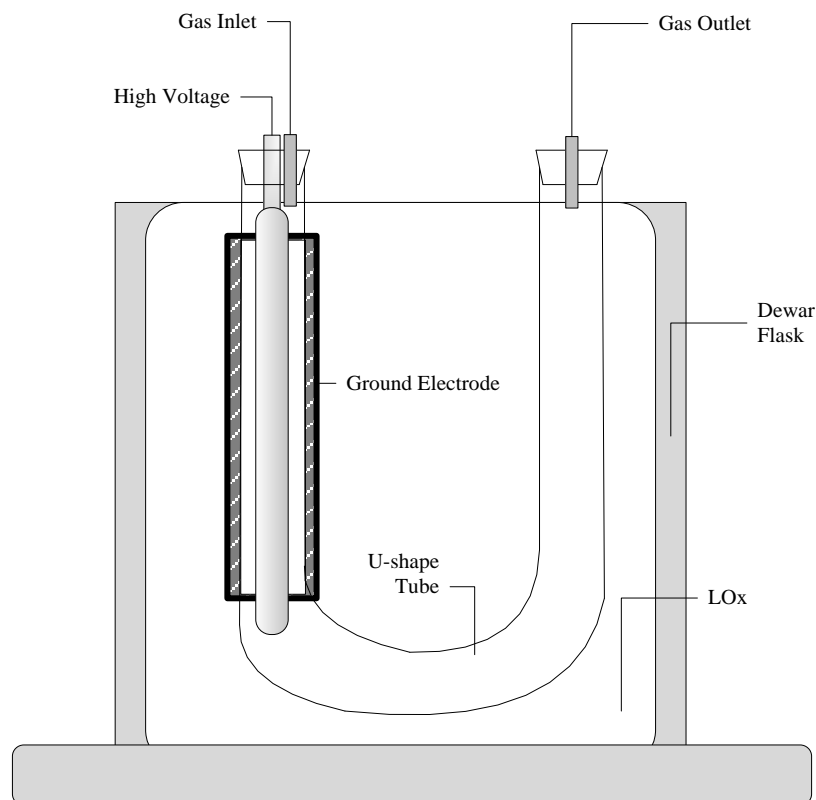


Figure 6.1 The schematic diagram of ozone generation at a low temperature.

A U-shaped tube was used as the dielectric barrier. The U-shaped tube was made from borosilicate glass with an inner diameter of 8 mm and an outer diameter of 10 mm. The straight legs of the U-tube were 200 mm. A silicone rubber stopper was pushed into the tube end with a stainless-steel needle electrode sealed at the centre of the silicon rubber. Slightly to the side of the stainless-steel needle, a 1 mm outer diameter soda-lime tube was used as the gas inlet. The length of the needle was 100 mm and the end of the needle was connected to a 7.5 mm diameter, 60 mm length stainless steel electrode by a banana plug. The outer surface of the U-shaped tube was covered by aluminium foil, which is fixed by a 0.2 mm stainless steel wire. The aluminium foil formed the ground electrode of the test cell. The other end of the tube was sealed with a silicone stopper with the gas outlet through a soda glass tube. At the other end of the U-shaped tube, another piece of silicone rubber was pushed into the tube to seal it. At the centre of the silicone rubber, another 1 mm outer diameter soda-lime tube was pushed into the silicone rubber as the gas outlet. The test cell was submerged in a 1 L dewar flask which was filled with liquid oxygen.

## 6.2.2 Experimental setup

### A. The production of liquid oxygen

In this experiment, liquid oxygen was produced on site and used to cool the ozone test cell. A copper coil tube was used to collect the liquid oxygen by putting it into a dewar flask filled with liquid nitrogen. As the boiling point of liquid nitrogen is lower than that of liquid oxygen, when passing the oxygen gas through the copper coil tube, the oxygen is liquefied. When the pressure in the copper coil tube was high enough, the liquid oxygen was forced out into another dewar flask, which was used as a liquid oxygen collector, as shown in Figure 6.2.

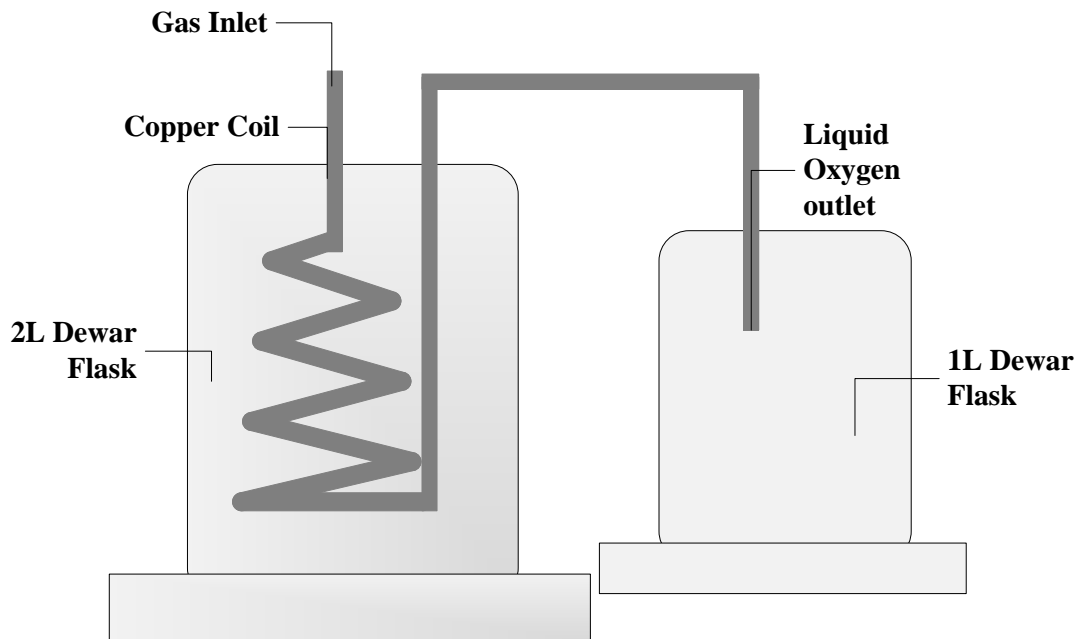


Figure 6.2 Preparation of liquid oxygen using a copper coil and liquid nitrogen.

### B. Preparation of the experiment

Once the dielectric barrier discharge test cell was immersed in liquid oxygen and energized, the liquid ozone was produced in the discharge gap. According to the literature review, if the volume of liquid ozone is more than 1 mL, an explosion might occur [91]. The maximum energisation time at 50 Hz was 3 min and the maximum energisation time at 5 kHz was 1 min in order to reduce the risk of explosion.

### C. Experimental schematic

Figure 6.3 shows the schematic of the experimental setup.

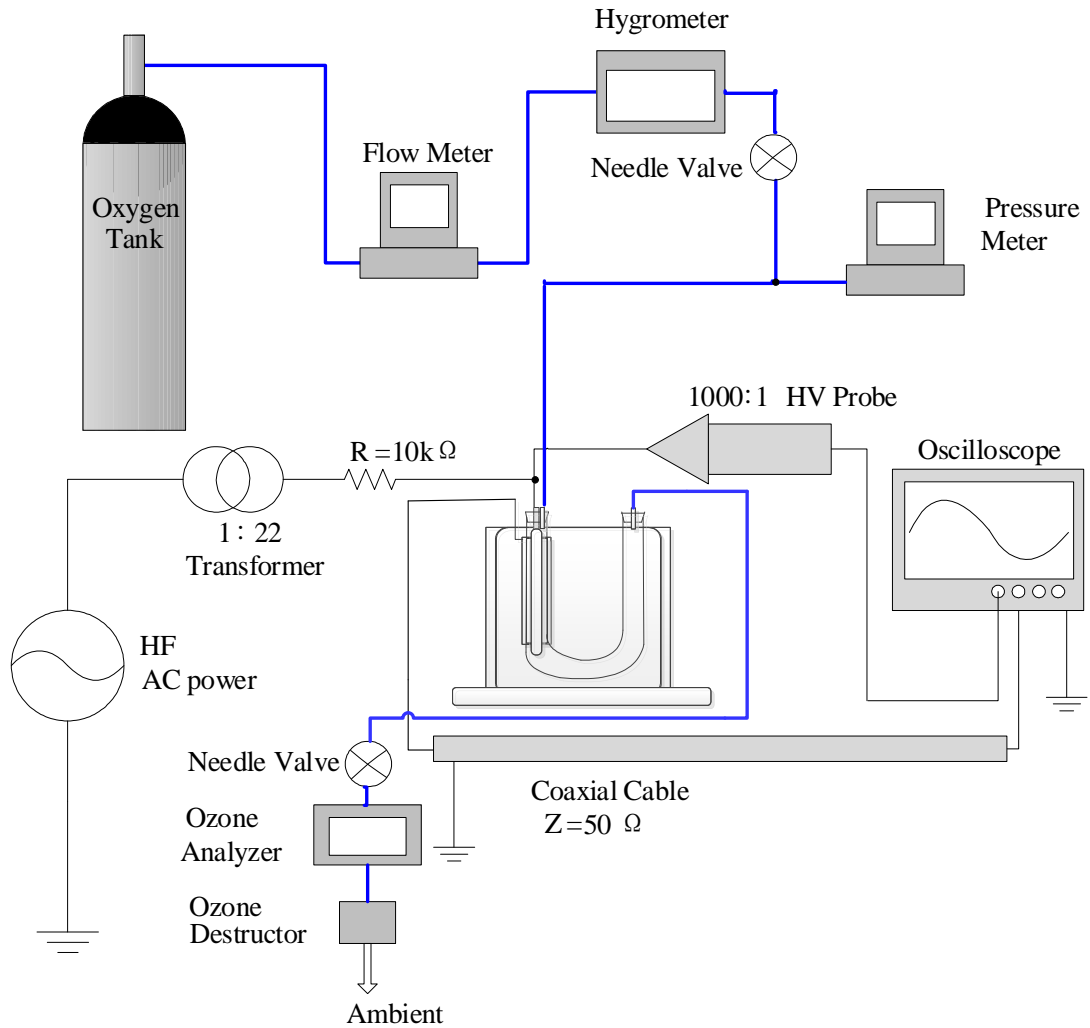


Figure 6.3 The schematic diagram of experiment arrangement.

The current was measured using a 50  $\Omega$  coaxial cable. A measurement capacitor of 15 nF was in series with the test cell to determine the power input using Lissajous figure. The ozone analyser used was BMT 964. Once liquid ozone was formed, when removing the test cell from the liquid oxygen after the discharge, the liquid ozone will vaporize. The transient reading of the ozone analyser was logged by LabVIEW every 0.2 s.

#### D. Experiment procedures

Due to the instability of liquid ozone, the ozone generation process must follow strict procedures for safety reasons. The procedures of the experiment are listed in detail:

- Liquid oxygen was made by cooling gas phase pure oxygen using liquid nitrogen.
- The feed gas was first passed through the U-shaped tube.

- Once the feed gas had filled the U-shaped tube, the test cell was put into the dewar flask.
- A thermometer was used to measure the test cell temperature at the ground electrode.
- After the discharge, the test cell was taken out of the dewar flask gradually.
- Because the temperature of the U-shaped tube was low, the water vapour was in the solid state. Upon taking the U-shaped tube out of the dewar flask, the formed ice becomes water drops. The next experiment should be done after the water drops in the U-shaped tube were blow-dried.

### 6.3 Ozone generation with 50 Hz power supply

The energy input when using a 50 Hz power supply was only mJ meaning that the temperature of the test cell remained stable. In this case, the ozone efficiency at different temperatures can be investigated. The temperature can be adjusted by changing the surface level of the liquid oxygen. The experiment was conducted using both dry air and pure oxygen.

#### 6.3.1 Ozone generation in air

##### A. At low temperature (-80 °C to -130 °C)

The experiment was carried out with an input voltage of 7.5 kV<sub>p</sub> and a 0.4 L/min gas flow rate. The energization time was 1 min. The test cell temperature was intentionally controlled by adjusting the liquid oxygen's surface level. The test result using dry air at different temperatures is shown below.

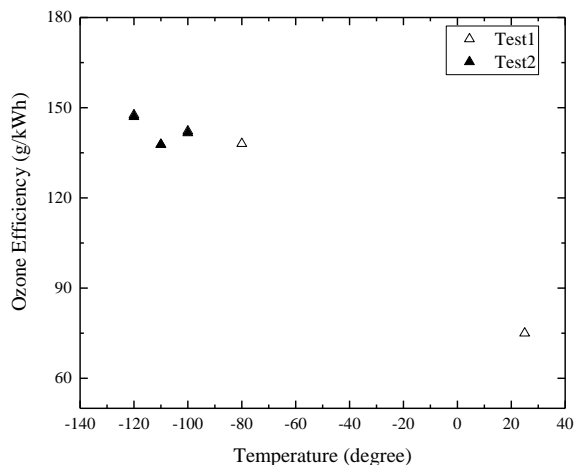


Figure 6.4 The relationship between ozone efficiency and test cell temperature for 50 Hz energisation.

For reference, the ozone efficiency was only 80 g/kWh at room temperature (25°C). In Test 1, when decreasing the test cell temperature to -80 °C, the ozone efficiency increased from 80 g/kWh to 130 g/kWh. With a continuous decrease in the temperature, the ozone efficiency increased to 145 g/kWh at -120 °C (see Appendix D). Overall, the ozone efficiency increased more than 1.6 times when decreasing the temperature to -120 °C. The ozone concentration and the Lissajous figure for different temperatures will be discussed in the following section.

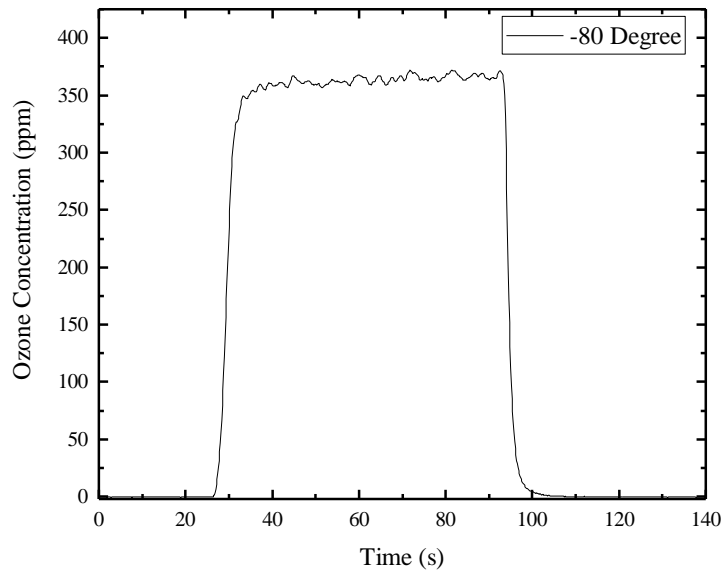


Figure 6.5 The ozone concentration at -80 °C with a 1 min energization time at 50 Hz, 7.5 kV<sub>p</sub> and 0.4 L/min air input.

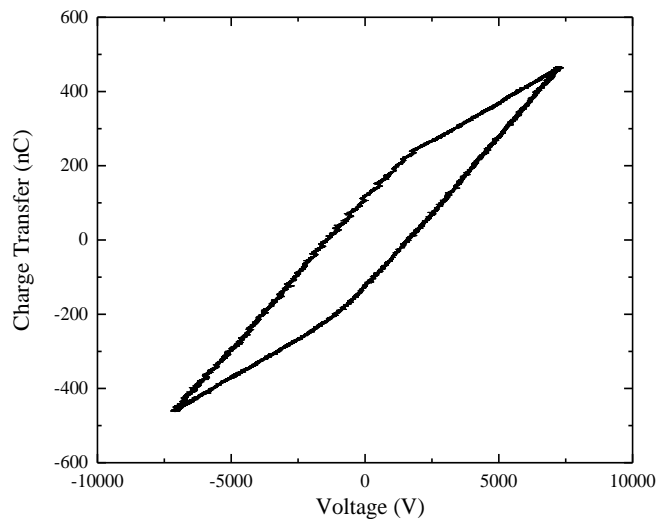


Figure 6.6 The Lissajous figure at -80 °C with a 1 min energization time at 50 Hz, 7.5 kV<sub>p</sub> and 0.4 L/min air input.

Table 6.2 The discharge parameters at different test cell temperatures with 7.5 kV<sub>p</sub> applied voltage.

Temperature	C <sub>d</sub> (pF)	C <sub>g</sub> (pF)	V <sub>b</sub> (V)	Power (mW)
-80	81.2	85.0	1535.5	109
-100	77.7	85.8	1678.4	100
-110	77.4	88.9	1792.6	94
-120	71.2	90.2	1714.5	84

All the relative parameters are shown in Table 6.2. When decreasing the ambient temperature, the ozone concentration decreased from 370 ppm at -80 °C to 275 ppm at -120 °C. The discharge parameters, such as gap capacitance and breakdown voltage, increased with the decrease in the ambient temperature. The dielectric barrier capacitance and the power input decreased with the decrease in the ambient temperature.

According to ideal gas law, when decreasing the ambient temperature, the number of particles,  $N$ , increases. According to the relationship between breakdown voltage and the number of particles based on Paschen's law, the breakdown voltage increases with the increment of the number of particles. For the same applied voltage, the breakdown voltage increasing causes the decrement of the total charge transfer per cycle. The power decreases with the drop in the temperature.

The relative permittivity  $\epsilon_r$  represents the ability to store electrical energy in the electric field. When decreasing the temperature, the space charge polarisation effect decreases. In this case, more electric flux exists in the dielectric barrier with a lower permittivity. According to the equation describing parallel-plate capacitance, the decrease in the relative permittivity causes a decrease in the dielectric barrier capacitance.

With regard to the increment of gap capacitance, a possible reason was the change of the thermal expansion leading to a change in the discharge distance. The thermal expansion is the tendency of matter to change in shape, area and volume in response to a change in temperature [92].

The temperature-dependent linear expansion ( $dL$ ) of the tubes was proportional to the test cell temperature:

$$dL = \alpha L_0 dT \quad (6.1)$$

where  $\alpha$  is the linear thermal expansion coefficient in  $10^{-6} K^{-1}$  and  $L_0$  is the original length of the test cell. In this experiment, as the starting temperature was room temperature (25°C), the original length of the tube can be considered constant. The coefficients of thermal expansion are different for different materials. The coefficient of stainless steel 316 is  $\alpha_{ss316} = 16.0$  [93] and the coefficient of Pyrex glass is  $\alpha_{Pyrex} = 3.2$  [94]. With same change of temperature, the linear expansion of stainless steel was five times greater than was the area expansion of the glass. As a result, the decrease in the temperature will increase the gap length between the stainless-steel tube and the Pyrex tube. Increasing the gap length, the breakdown voltage increases. In this case, increasing the gap length and the number of particles can increase the required breakdown voltage dramatically. The results show that the breakdown voltage only increased from 1535 V at -80 °C to 1793 V at -110 °C, and then decreased to 1715 V at -120 °C. The increase in the gap length requires a higher breakdown voltage. As the gap length was maintained via stainless steel wire around the high-voltage electrode, decreasing the temperature, the thermal expansion of stainless steel decreases more than that of the pyrex. The short gap formed between the stainless-steel wire and the pyrex tube, which was shorter than the gap length between stainless steel tube and pyrex tube. As a result, once decreasing the temperature to -120 °C, the discharge happened between the stainless steel and the pyrex tube with lower breakdown voltage.

Based on the research by Choi *et al.* [95], the discharge mode varied under different temperature (below 300 K). The gap breakdown voltage increased in pure helium DBD from 500 V at 300 K to 800 V at 170 K and then decreased to 650 V at 160 K. The breakdown voltage then gradually increased to 700 V at 100 K. Between 170 K and 230 K, a static pattern was exhibited with a higher breakdown voltage than the expected values. Choi *et al.* concluded that the breakdown voltage was relatively high only in the case when the micro-discharges were static. Compared with the breakdown voltage measured in the experiments, the abrupt increase of the breakdown voltage at -110 °C might be due to the formation of a static pattern. This theory needs to be confirmed using further diagnostics.

For the analysis of ozone efficiency, the chemical reactions in air need to be considered, as they are more complicated than those reactions using pure oxygen. Due to the involvement of nitrogen molecules, the reaction between nitrogen atoms (and nitrogen molecules' excited states  $N_2(A^3\Sigma_u^+)$ ,  $N_2(B^3\Pi_g)$ ) and oxygen atoms, and the reactions between nitrogen atoms (and

nitrogen molecules' excited states  $N_2(A^3\Sigma_u^+)$ ,  $N_2(B^3\Pi_g)$  and ozone molecules are quite complicated.

From the research, the main participant reactions for the formation process of oxygen atoms are shown below [74][96][97]



$$k_1 = 4.4 \times 10^{-12} \exp\left(-\frac{3220}{T}\right)$$



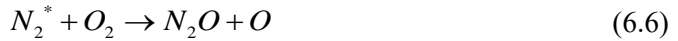
$$k_2 = 3.4 \times 10^{-11} \exp\left(-\frac{24}{T}\right)$$



$$k_3 = 5.8 \times 10^{-11} \exp\left(-\frac{220}{T}\right)$$



$$k_4 = 5.0 \times 10^{-12} \exp\left(-\frac{210}{T}\right)$$



$$k_5 = 4.6 \times 10^{-15}$$

The simulation result from 143 reactions among 30 species [98][99][100] shows that the concentration of nitrogen oxide reaches about 1% of the ozone concentration. The oxygen atoms produced by nitrogen species, apart from the direct reaction between electrons and oxygen molecules, can produce 50% of the ozone. The ozone formation time in air was longer than it was in oxygen, which was around 100  $\mu$ s. Except for oxygen atoms, the resultants  $NO$ ,  $N_2O$  and  $N_2$  are the main species from the micro-discharges. These species can form in 100 ns. The oxygen atoms can react with the oxides to form other nitrogen oxide species such as  $NO_2$ ,  $NO_3$  and  $N_2O_5$ .



$$k_6 = 1.0 \times 10^{-31} \left(\frac{T}{300}\right)^{-1.6} [N_2]$$



$$k_7 = 9.0 \times 10^{-32} \left(\frac{T}{300}\right)^{-2.0} [N_2]$$



$$k_8 = 2.8 \times 10^{-30} \left(\frac{T}{300}\right)^{-3.5} [N_2]$$

Some investigations show that the maximum ozone efficiency reduces to about 0.2 kg/kWh in a higher reduced electric field (200-300 Td). The main reason is the nitrogen oxides. The oxides can also react with ozone to reduce the ozone concentration further, as the following reactions show.



$$k_9 = 1.4 \times 10^{-13} \exp\left(-\frac{2470}{T}\right)$$



$$k_{10} = 1.8 \times 10^{-12} \exp\left(-\frac{1370}{T}\right)$$



$$k_{11} = 5.0 \times 10^{-12} \exp\left(-\frac{650}{T}\right)$$

With regard to the oxygen atom formation process, according to the rate coefficients of related reactions, when decreasing the temperature, the oxygen atom formation rate decreases. The production rate of nitrogen oxides ( $NO$ ,  $N_2O$ ) also decreases. For the oxygen atom dissociation process, the decrease in the temperature can increase the rate coefficients of the related reactions. The concentration of atomic oxygen and the concentration of nitrogen oxides decreased. In general, the reaction rate of the oxygen atom dissociation process decreased with the decrease in the temperature. When decreasing the temperature, in the ozone dissociation

process, the rate coefficients of related reactions also decrease to limit the ozone dissociation. The experimental results closely agree with the theory, with the ozone efficiency increasing from nearly 80 g/kWh to 150 g/kWh at -120 °C.

### B. At cryogenic temperatures

This subsection describes the production of liquid ozone when conducting the experiment at cryogenic temperatures (-183 °C). The test cell was dipped into liquid oxygen. The test cell temperature was -183 °C. The energization time was 3 min. The gas flow rate was 0.4 L/min. During the discharge time, the produced ozone is liquefied. In this case, the ozone production can be measured by removing the test cell from the liquid oxygen environment. With a continuous flow of the gas, the liquid ozone formed is vaporised into the gas phase. The ozone concentration can then be determined.

Figure 6.7 shows the measured ozone concentration:

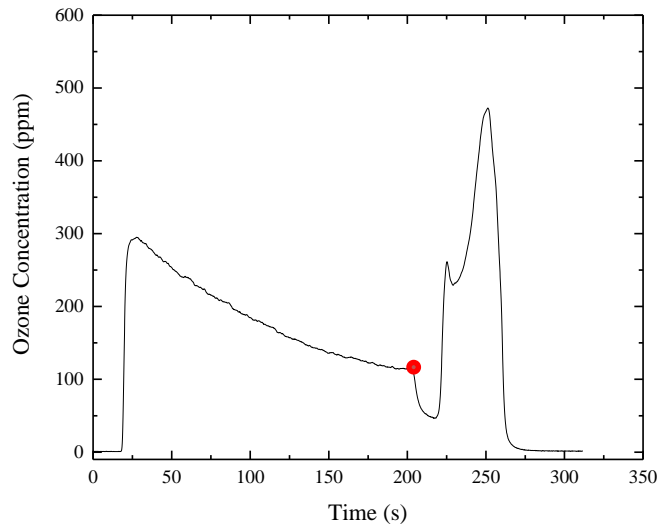


Figure 6.7 Ozone concentration in real time at -183 °C with 7.5 kV<sub>p</sub> voltage and 0.4 L/min air input.

At the beginning of the experiment, gas phase ozone was produced, reaching the maximum ozone concentration of nearly 300 ppm. Then, the ozone concentration gradually decreased to 120 ppm by the end of the energy input (red point). As mentioned previously, the test cell temperature was much lower than the boiling point of ozone. Part of the produced ozone was liquefied. Table 6.3 shows the viscosity and the surface tension of liquid ozone and liquid oxygen at -183 °C and -195 °C [90]. Regarding the units in Table 6.3:

$$1 \text{ cP} = 1 \text{ mPa}\cdot\text{s}$$

$$1 \text{ Dynes/cm} = 1 \text{ mN/m}$$

Table 6.3 Viscosity and surface tension properties of liquid ozone and oxygen mixtures.

Ozone wt%	<b>-183 °C</b>		<b>-195 °C</b>	
	Viscosity (cP)	Surface Tension (Dynes/cm)	Viscosity (cP)	Surface Tension (Dynes/cm)
100	1.57	38.4	4.2	43.8
0	0.189	13.2	0.189	15.7

According to the results shown in Figure 6.7, compared to the parameters of liquid oxygen, the viscosity of ozone was nearly 10 times greater and the surface tension of liquid ozone was nearly three times greater. The viscosity of the liquid ozone was nearly the same as that of a water droplet. In this case, the liquid ozone attached to the barrier surface and the electrode surface. When removing the test cell from the liquid oxygen, the liquid ozone is vaporized. As shown in Figure 6.7, liquid ozone was vaporized to gas phase ozone from 220 s to 260 s. The peak value of the vaporised ozone concentration was nearly 500 ppm.

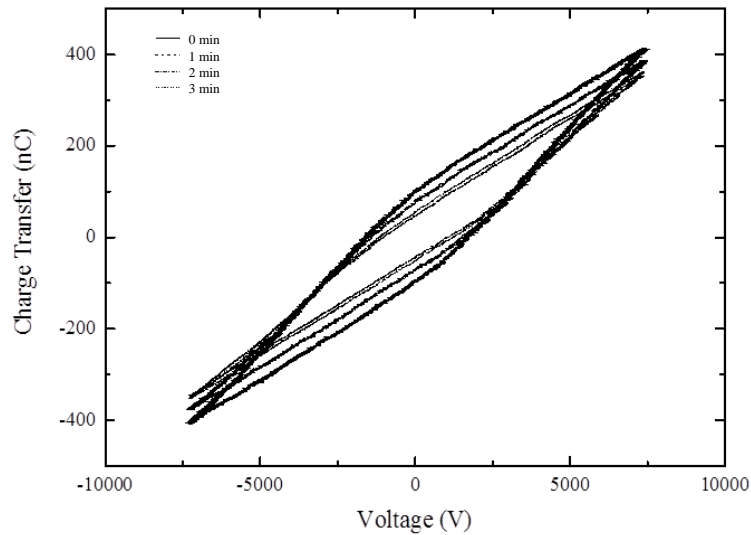


Figure 6.8 Lissajous figures at different energization times at -183 °C.

From the experiments, it is found the area of the Lissajous figure decreases with increasing energisation time. This result confirms that part of the liquid ozone was attached to the surface of the glass tube and the high voltage electrode, reducing the discharge gap. The discharge parameters at different energization time are shown in Table 6.4:

Table 6.4 The discharge parameters at different energization time.

<b>Energization time (min)</b>	<b>C<sub>d</sub> (pF)</b>	<b>C<sub>g</sub> (pF)</b>	<b>V<sub>b</sub>(V)</b>	<b>Power (mW)</b>
0	72.7	105.0	1839.5	109
1	66.2	99.0	1719.2	74
2	64.9	109.4	1697.5	72
3	58.6	134.0	1268.2	47

With the energization time increasing, the breakdown voltage decreased. At the same temperature, the oxygen concentration did not change. The decrease in the gap length decreased the breakdown voltage. If the liquid ozone is attached to the glass and electrode, the total capacitance was the result of the equivalent capacitance of the layer of ozone and the dielectric capacitance in series:

$$C_{d\_total} = \frac{C_d \times C_{liquidozone}}{C_d + C_{liquidozone}} \quad (6.13)$$

The total dielectric capacitance in this case must be lower than the glass capacitance. When increasing the energization time, the produced liquid ozone increased. In this case, the thickness of the liquid ozone layer increases. The equivalent capacitance of the liquid ozone decreased gradually. Consequently, the total dielectric capacitance also decreased. As the discharge gap decreases with time, the corresponding gap capacitance increases.

The calculated power at cryogenic temperatures was measured by averaging the power, which was 74.2 mW. The ozone efficiency at cryogenic temperatures was 135 g/kWh when air-fed.

### 6.3.2 Current amplitude distribution using air

#### A. Current amplitude distribution at different temperatures

Figure 6.9 and Figure 6.10 indicate the current amplitude distribution of both the positive discharges and the negative discharges at different temperatures.

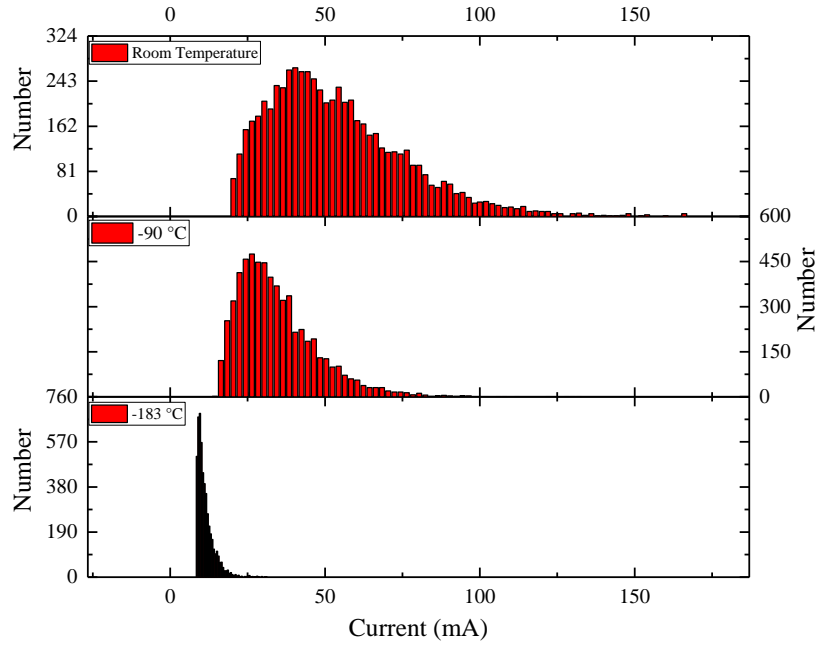


Figure 6.9 The current amplitude distribution of 5,000 single pulses at different test cell temperature for the positive discharge cycle.

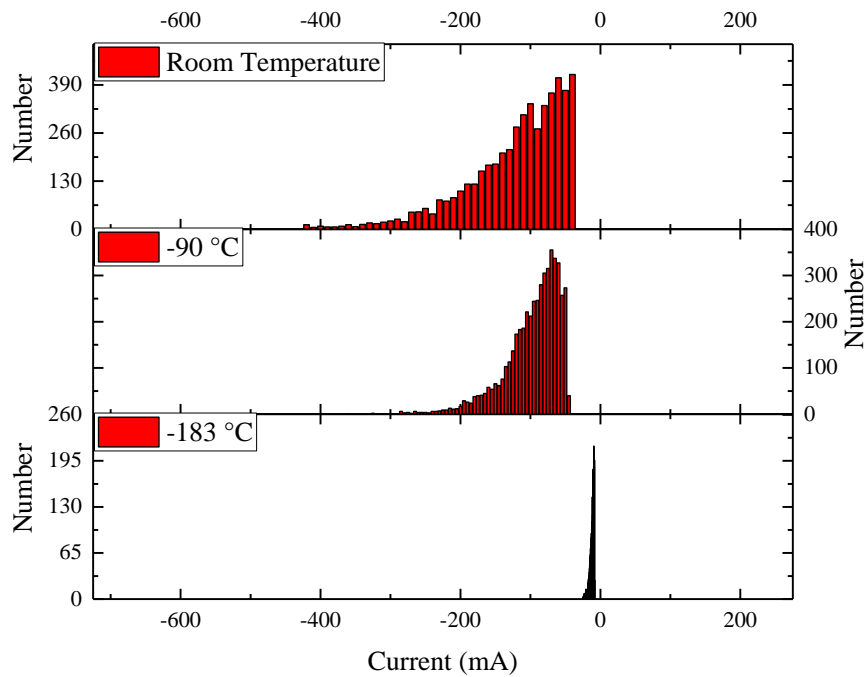


Figure 6.10 The current amplitude distribution of 5,000 single pulses at different test cell temperature for the negative discharge cycle.

For the positive discharge current analysis, the current amplitude was investigated at room temperature, at -90 °C and at -183 °C, respectively. When decreasing the temperature, the current amplitude distribution was narrower.

Table 6.5 Positive current analysis under different temperature.

<b>Temperature (°C)</b>	<b>Minimum Current (mA)</b>	<b>Maximum Current (mA)</b>	<b>Average Current (mA)</b>
25	18.2	159.4	53.8
-90	14.4	132.0	34.7
-183	8.6	31.1	11.4

The current amplitude distribution in the negative discharge cycle was also investigated at room temperature, at -90 °C and at -183 °C. The current amplitude distribution became much narrower once the test cell temperature decreased to -183 °C.

Table 6.6 Negative current analysis under different temperature.

<b>Temperature (°C)</b>	<b>Minimum Current (mA)</b>	<b>Maximum Current (mA)</b>	<b>Average Current (mA)</b>
25	-420	-40	-121.6
-90	-360	-45	-97.5
-183	-25.3	-8.1	-11.9

As a result of decreasing the test cell temperature, the current amplitude distribution was narrower and had a much lower standard deviation. At the temperature above the boiling point of ozone, the negative discharge current was always greater than was the positive discharge current due to the effect of electronegative gas as discussed in Chapter 3. At cryogenic temperatures, the current amplitude distributions of both the positive discharge cycle and the negative discharge cycle were nearly the same.

### **B. Voltage and current waveforms at different temperatures**

In this subsection, the filament development is described. The current and voltage waveforms measured at different temperature are shown in Figure 6.11 to Figure 6.13.

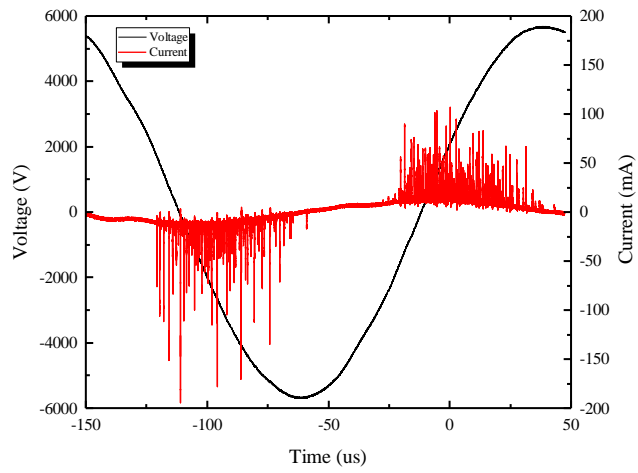


Figure 6.11 The sampled full-cycle current and voltage waveforms at room temperature (25° C).

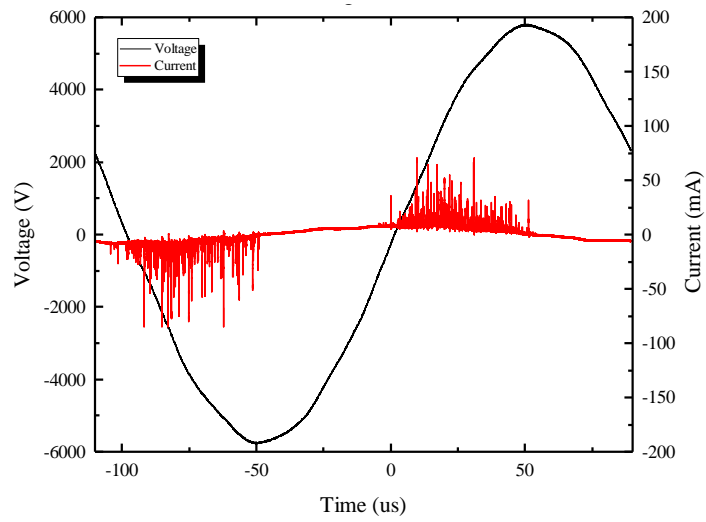


Figure 6.12 The sampled full-cycle current and voltage waveforms at -90 °C.

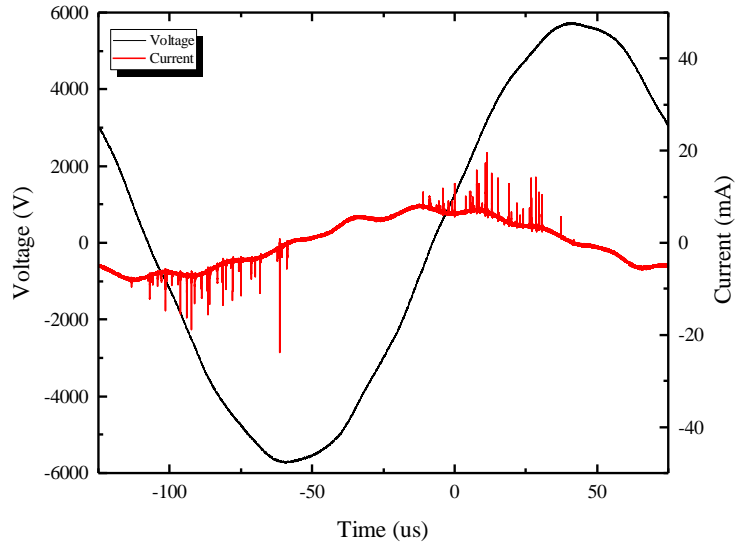


Figure 6.13 The sampled full-cycle current and voltage waveforms at -183 °C.

At 25°C, the maximum current for the positive cycle was 100 mA, while the maximum current for the negative cycle was -200 mA. The ignition voltage of the positive discharge was -1672 V. The average current amplitude for the positive discharge cycle was 48.6 mA and the average current amplitude for the negative discharge cycle was 102 mA. The average discharge duration (10% to 50%) was 21.6 ns.

At -90 °C, the maximum current for the positive cycle was 70 mA, while the maximum current for the negative cycle was -85 mA. The ignition voltage of the positive discharge was -1073.6 V. The average current amplitude of the positive discharge cycle was 33.3 mA and the average current amplitude of the negative discharge cycle was -50.1 mA. The average discharge duration (10% to 50%) was 35 ns.

At -183 °C, the maximum current for the positive cycle was only 19.4 mA and the maximum current for the negative cycle was -23.8 mA. The ignition voltage of the positive discharge was -599 V. The average current amplitude of the positive cycle was only 10.1 mA and the average current amplitude of the negative cycle was -12.5 mA. The average discharge duration (10% to 50%) decreased dramatically to 15 ns.

Overall, when decreasing the temperature, the charge transfer of the single filament decreased dramatically, as the average current amplitude and the discharge duration decreased at same time. On the other hand, the ignition voltage of the discharge decreased dramatically with the decrease in temperature. In this case, the amount of charge accumulated on the barrier after a quarter cycle decreased and the reversed electric field decreased as well.

### 6.3.3 Ozone efficiency in oxygen

In this subsection, ozone efficiency was investigated by using oxygen from -90 °C to -183 °C. The experimental arrangement was the same as it was for air. The test cell temperature was manipulated by adjusting the level of liquid oxygen. The flow rate of the input oxygen gas was 0.4 L/min. The applied voltage was 7 kV<sub>p</sub> at 50 Hz. The energization time was 3 mins. The ozone concentration was measured using the ozone analyzer and the power input was measured by Lissajous figure.

#### A. Ozone efficiency at low temperature

In this section, the ozone efficiency at different low temperatures (-90 °C to -136 °C) was investigated. The ozone concentration, the Lissajous figures at different energization times and the ozone efficiency were calculated.

Figure 6.14 shows the measured ozone concentration sampled at -90 °C.

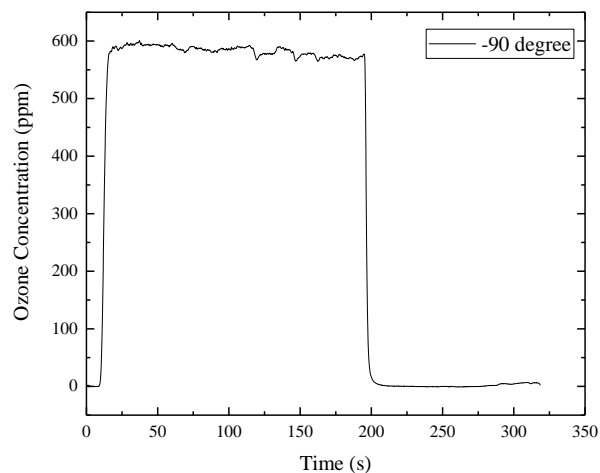


Figure 6.14 The ozone concentration at -90 °C with 3 mins of energization time and oxygen feed.

When operating the test cell at -90 °C (ozone concentration under different temperatures will be shown in Appendix E), the ozone concentration increased to 600 ppm during the discharge time.

When decreasing the test cell temperature below the melting point of ozone, the produced ozone was liquefied. When the discharge was finished and the test cell moved out of the liquid oxygen, the liquefied ozone will be vaporized. With decreasing the temperature to -136 °C, there was a sharp increase of the ozone concentration once the discharge stopped and the test cell was removed from the LO<sub>x</sub> as shown in Figure 6.15.

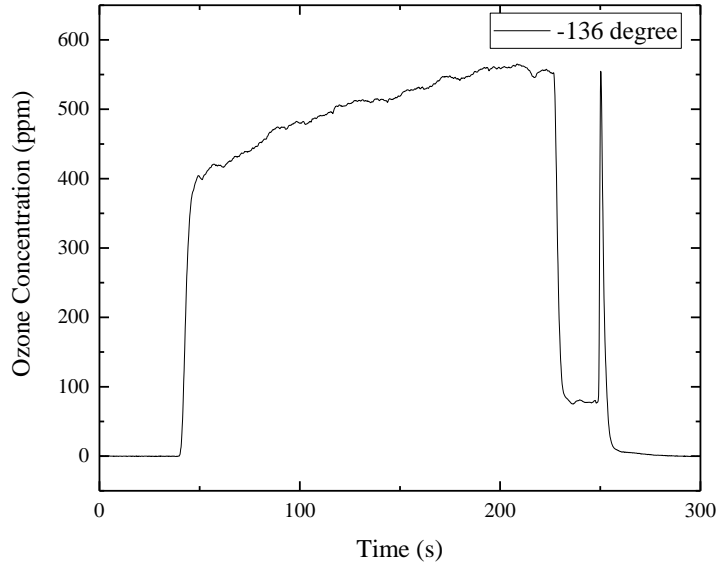


Figure 6.15 The ozone concentration at -136 °C with 3 mins of energization time and oxygen feed.

As mentioned previously, liquid ozone can narrow the discharge gap causing the power input to drop. In this case, the Lissajous figure was measured every minute. The power input was the average of all the Lissajous figures. Figure 6.16 shows the corresponding Lissajous figure at -90° C energized for three minutes.

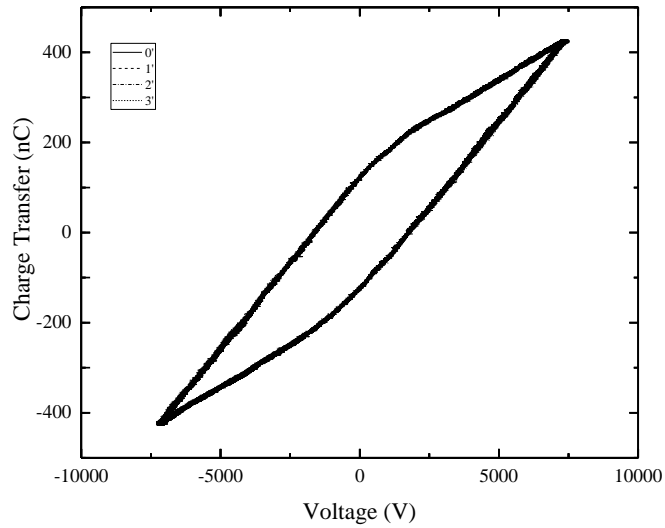


Figure 6.16 The Lissajous figure at -90 °C for 3 mins energization time and oxygen feed.

Table 6.7 shows the calculated parameters:

Table 6.7 The discharge parameters at different test cell temperature.

<b>Temperature (°C)</b>	<b>C<sub>d</sub> (pF)</b>	<b>C<sub>g</sub> (pF)</b>	<b>V<sub>b</sub> (V)</b>	<b>Power (mW)</b>
-90	76.0	67.3	1774.2	100
-110	73.0	68.2	1890.9	99
-124	71.7	78.2	1803.8	66
-130	67.8	80.8	1723.4	90
-136	65.5	94.0	1693.0	70

When decreasing the temperature, the dielectric barrier capacitance decreased while the gap capacitance increased. The breakdown voltage increased from 1774 V to 1890 V when the test cell temperature decreased from -90 °C to -110 °C. With the continuous decrease in the test cell temperature, the breakdown voltage decreased again to 1693 V. At -90 °C, the ozone produced was in the gas phase. With the decrease in the temperature, the number of particles increased and the corresponding breakdown voltage increased as well. When the test cell temperature decreased to below -112 °C, liquid ozone started to form to decrease the discharge gap.

To confirm the relationship between ozone efficiency and the test cell temperature, the experiment was repeated more than twice. Figure 6.17 shows the relationship between the average ozone efficiency and the test cell temperature.

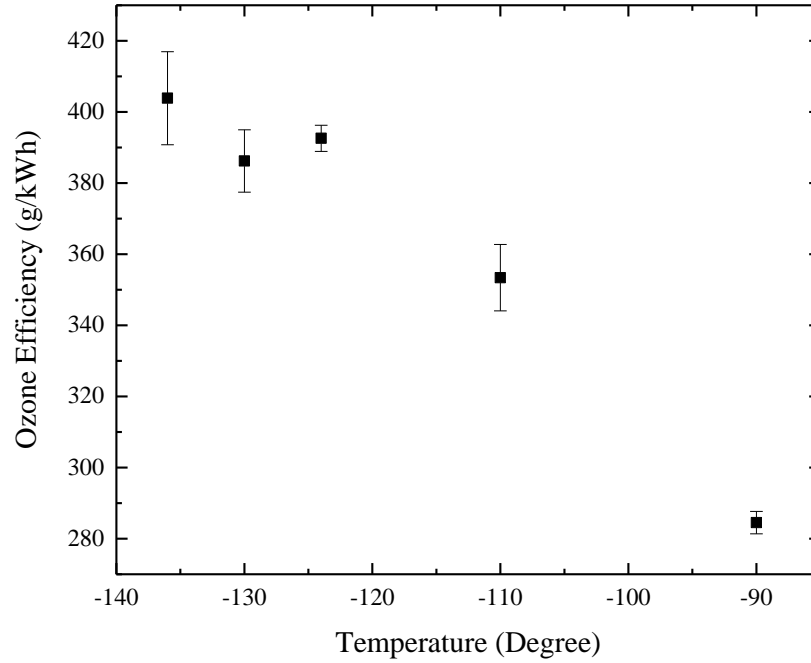


Figure 6.17 The relationship between ozone efficiency (g/kWh) and the test cell temperature (°C).

To indicate the efficiency versus the temperature, the experiment was conducted using five different test cell temperatures. The ozone efficiency at room temperature when using the same test cell was 187 g/kWh. At -90 °C, the ozone efficiency was 287 g/kWh, which was 50% greater than it was at room temperature. With the continuous decrease in temperature to -110 °C, the ozone efficiency increased to 354 g/kWh. The maximum ozone efficiency obtained in the experiment was 400 g/kWh with a 10 g/kWh standard deviation at -136 °C.

As a result, the decrease in the temperature can increase ozone efficiency. Firstly, far below 0 °C, the water vapour is solidified. There is no reaction between water vapour and ozone molecules. According to the dissociation process of ozone generation, when decreasing the temperature, the rate coefficient decreases as well. Some dissociation reactions that occur at the same time are shown below [101]:



$$k_{12} = 1.3 \times 10^{-32} \frac{300}{T} \exp\left(-\frac{170}{T}\right)$$



$$k_{13} = 2.0 \times 10^{-11} \exp\left(-\frac{2300}{T}\right)$$



$$k_{14} = 2.4 \times 10^{-10}$$

where  $k_{14}$  is independent of temperature [100-400 K].

Two oxygen atoms combine to form an oxygen molecule as shown in (6.14); thus, the energy used for the production of atomic oxygen is wasted. Also, an oxygen atom reacts with an ozone molecule to dissociate it to two oxygen molecules as shown in (6.15) and (6.16).

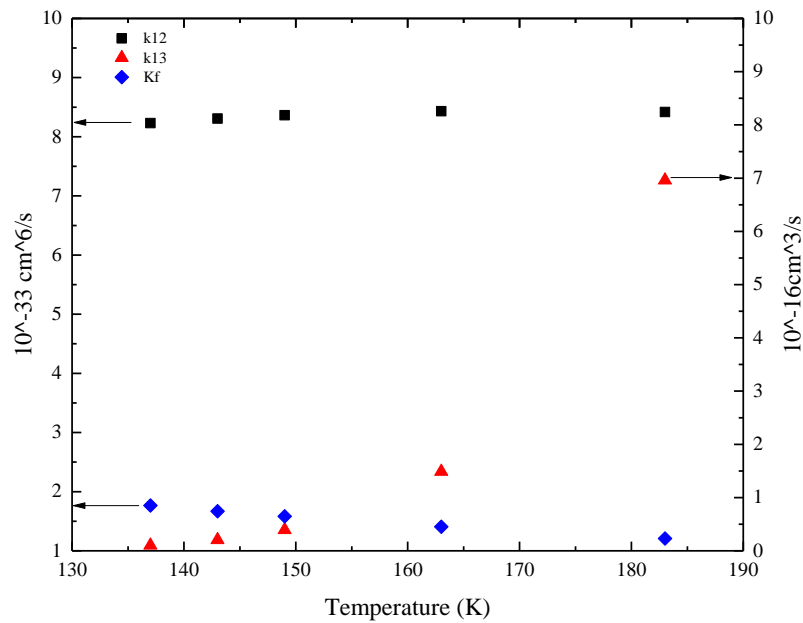


Figure 6.18 The reaction rate coefficients with temperature dependent.

With decreasing the temperature, the ozone generation reaction rate coefficient  $k_f$  shown in (1.36) increases from  $1.2 \times 10^{-33}$  to  $1.9 \times 10^{-33}$ . Meanwhile the coefficient  $k_{12}$  decreases from  $8.4 \times 10^{-33}$  to  $8.2 \times 10^{-33}$  and the coefficient  $k_{13}$  decreases from  $7 \times 10^{-16}$  to  $1 \times 10^{-16}$ . The simultaneous increasing of the ozone formation rate and the decreasing of the ozone dissociation rate leads to the higher ozone efficiency with decreasing temperature.

Compared to the theoretical value, the maximum electron energy efficiency was 9.38 eV. The ozone efficiency at -136 °C was more than twice the ozone efficiency at room temperature. Other factors that may cause ozone efficiency increase at low temperature need to be investigated. In the following section, the discharge property in oxygen is investigated.

### B. Ozone Efficiency at Cryogenic Temperatures

This section discusses the experiment that was carried out at  $-183\text{ °C}$  (the boiling point of oxygen). The gas flow rate was  $0.4\text{ L/min}$ , and the applied voltage was  $8\text{ kV}_p$  at  $50\text{ Hz}$ . The energization time was  $3\text{ min}$ . The ozone concentration and the Lissajous figure were measured and shown in Figure 6.19.

Figure 6.19 shows the ozone concentration at  $-183\text{ °C}$  in real time.

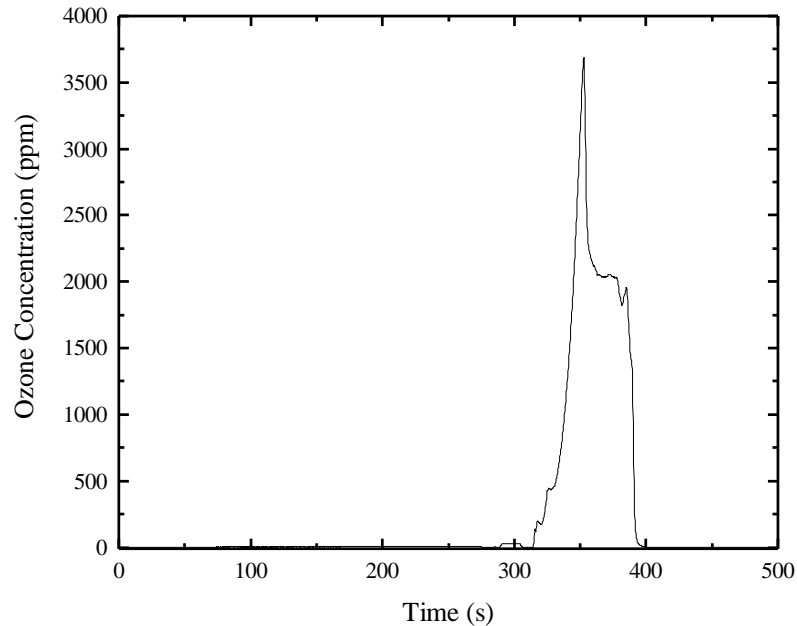


Figure 6.19 The ozone concentration in 3 mins of energization time at  $-183\text{ °C}$ .

From the above ozone concentration curve, within 3 mins energization time, the measured ozone concentration was only  $7.7\text{ ppm}$ . After the discharge, by removing the test cell from the liquid oxygen environment, the ozone concentration increased to over  $3750\text{ ppm}$  and then dropped to zero after one minute. By integrating the ozone concentration in real time, the gas phase ozone produced during the discharge time can be ignored. Most of the ozone produced was in the liquid phase, which was vaporised only when the temperature of the test cell increased.

Compared to the ozone concentration using air at cryogenic temperatures, when only one-third of the ozone produced was in the liquid phase, almost all of the ozone produced using oxygen was in the liquid phase. The boiling point of the feed gas affects the phase of the produced ozone. The boiling point of air is  $-189\text{ °C}$ . In this case, when ozone was produced, most of the ozone molecules can be blown out of the test cell. Meanwhile, with regard to the

oxygen feed, the temperature in the test cell was low enough to liquefy oxygen. The ozone was attached to the glass tube and the electrode and liquefied.

Figure 6.20 shows the Lissajous figure at -183 °C at different energization times.

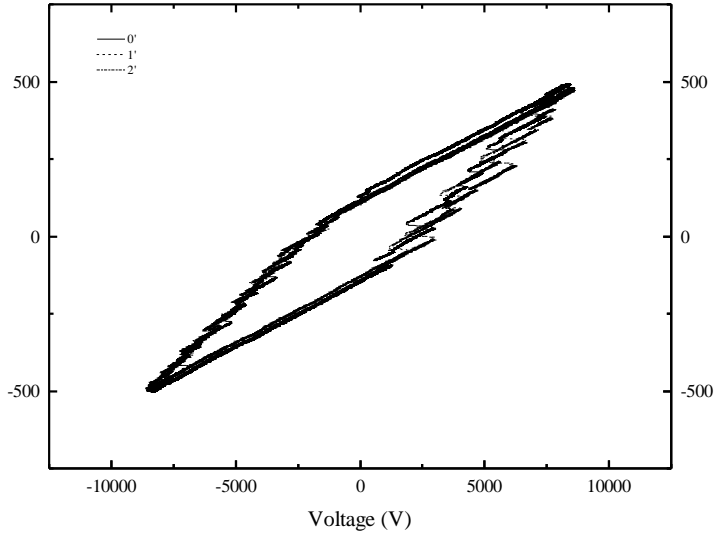


Figure 6.20 The Lissajous figure at different times at -183 °C with 7.5 kV<sub>p</sub> voltage at 0.4 L/min oxygen input.

The discharge parameters at different discharge time were investigated, as Table 6.8 shows:

Table 6.8 The discharge parameters at different times at -183 °C.

<b>Energization time (min)</b>	<b>C<sub>d</sub> (pF)</b>	<b>C<sub>g</sub> (pF)</b>	<b>V<sub>b</sub> (V)</b>	<b>Power (mW)</b>
0	75.6	88.2	2220.1	128
1	66.3	77.9	2068.1	115
2	67.3	79.5	2137.6	113

The average power input in this case was 117.7 mW. The ozone efficiency was 384.4 g/kWh. The breakdown voltage increased to over 2000 V. At the beginning of the discharge, the input power was 128 mW. After two minutes of discharge, the input power was only 113 mW. For a single discharge, the above figure shows that the voltage drop of each discharge at -183 °C was much higher than it was at a low temperature (-90 °C to -136 °C). The discharge at

-183 °C with oxygen feed was quite different from the discharge at -183 °C with air feed. In the next section, the discharge property will be investigated in more detail.

#### 6.3.4 Current amplitude distribution in oxygen

##### A. Current amplitude distribution at low temperature and cryogenic temperature

This section describes the current amplitude distribution that was investigated at -70, -110 and -183 °C, respectively. 5000 current pulses were analysed by the current amplitude distribution and the discharge duration individually.

Figure 6.21 shows the negative current amplitude distribution at different temperatures.

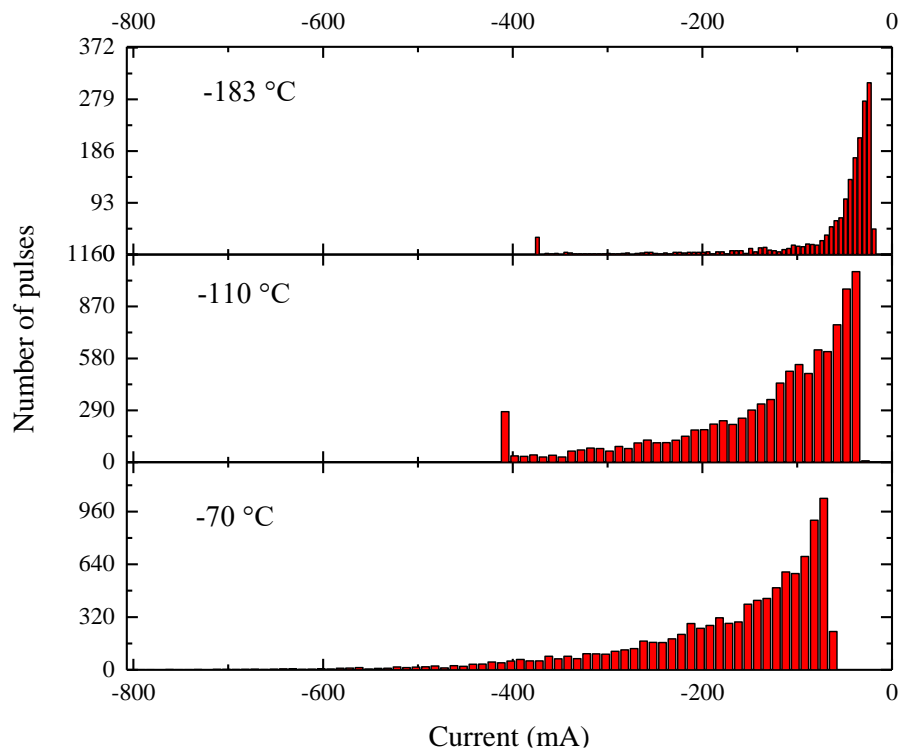


Figure 6.21 The current amplitude distribution of the negative discharge cycle at -70, -110 and -183 °C respectively.

Table 6.9 Negative current analysis under different temperature with oxygen-fed.

Temperature (°C)	Minimum Current (mA)	Maximum Current (mA)	Average Current (mA)
-70	-600	70.0	172.0
-110	-400	28.8	131.3
-183	-360	18.4	116.6

Compared to the current amplitude distribution with air feed, the average current amplitude using oxygen was generally greater than that of air.

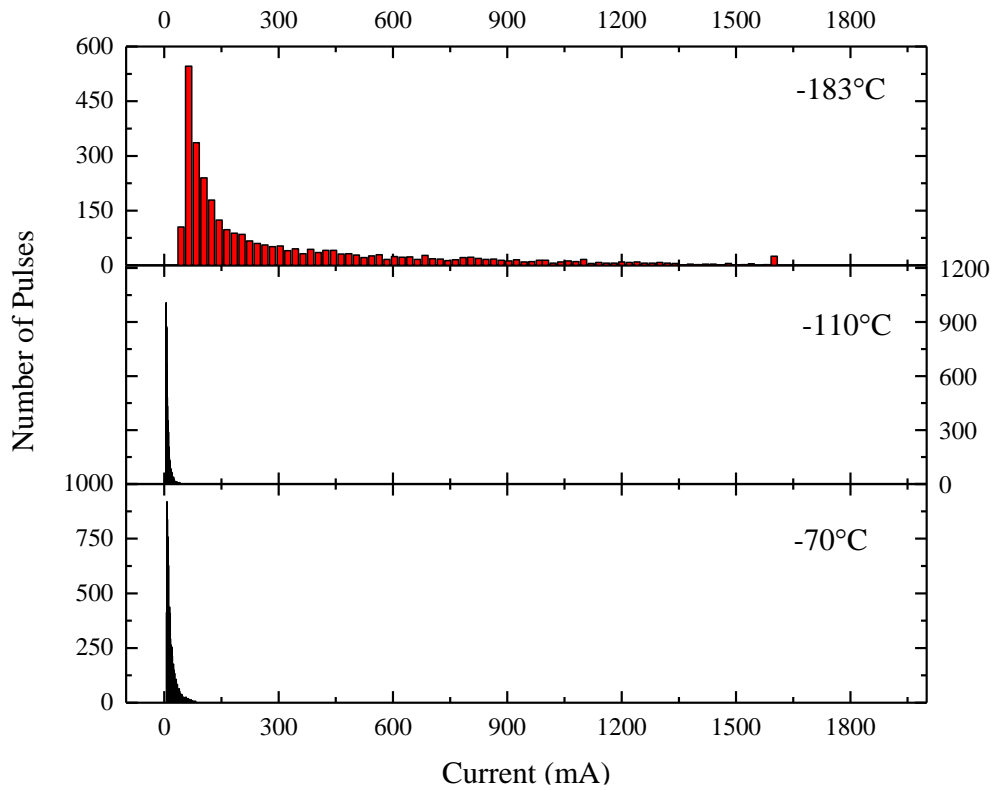


Figure 6.22 The current amplitude distribution of the positive discharge cycle at -70, -110 and -183 °C, respectively.

Figure 6.22 shows the current amplitude distribution at the positive half cycle at different temperatures.

Table 6.10 Positive current analysis under different temperature with oxygen-fed.

Temperature (°C)	Minimum Current (mA)	Maximum Current (mA)	Average Current (mA)
-70	4.8	80	17.3
-110	6.2	43	9.6
-183	30	1500	297.64

At -70 °C, the distribution of the positive current amplitude was relatively narrow. The distribution of the positive current amplitude at -110 °C was even narrower. The narrow

distribution at lower temperatures implies that the filament development tends to be more uniform. Meanwhile, when continuously decreasing the temperature to -183 °C, it was obvious that the current amplitude distribution expanded dramatically. The only difference when compared to the previous experiments (at low temperature) was that liquid ozone was formed. Based on the observation, the power input decreased when the energization time increased. In the following section, the current amplitude distribution at different energization times is discussed.

### B. Current amplitude distribution at -183° C with different energization times

In this section, the variation of current amplitude distribution with time is discussed. As seen in Figure 6.23, the current amplitude distribution at -183 °C was quite different from that at low temperatures (-90 °C to -136 °C). To investigate how liquid ozone formation can affect the discharge, at -183 °C, the current amplitude distribution of both the positive and the negative discharge cycles within 1 min, from 1 min to 2 min and from 2 min to 3 min were investigated.

Figure 6.23 shows the current amplitude distribution of the positive discharge cycle at different time.

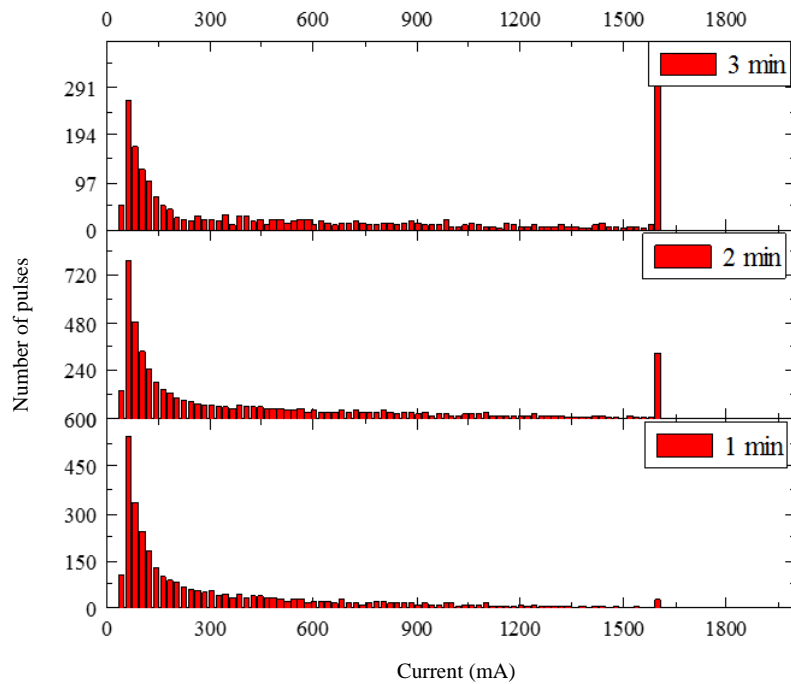


Figure 6.23 The positive current amplitude distribution at different energization time at -183 °C with 9 kV<sub>p</sub> applied voltage at 50 Hz.

The maximum measured current amplitude was 1.7 A. A current amplitude above 1.7 A can only be measured as 1.7 A due to the limitation of the oscilloscope. At different time, the number of pulses with a measured amplitude of 1.7 A increased over time, which means that the discharge becomes more energetic over time. The average current amplitude in the first minute was 297.6 mA and increased continuously to 388.8 mA by the third minute. From the Lissajous figure (shown in Figure 6.20), we can see that the power input decreases, while the charge transfer per half-cycle does not change significantly.

Figure 6.24 shows the current amplitude distribution of the negative discharge cycle at -183 °C.

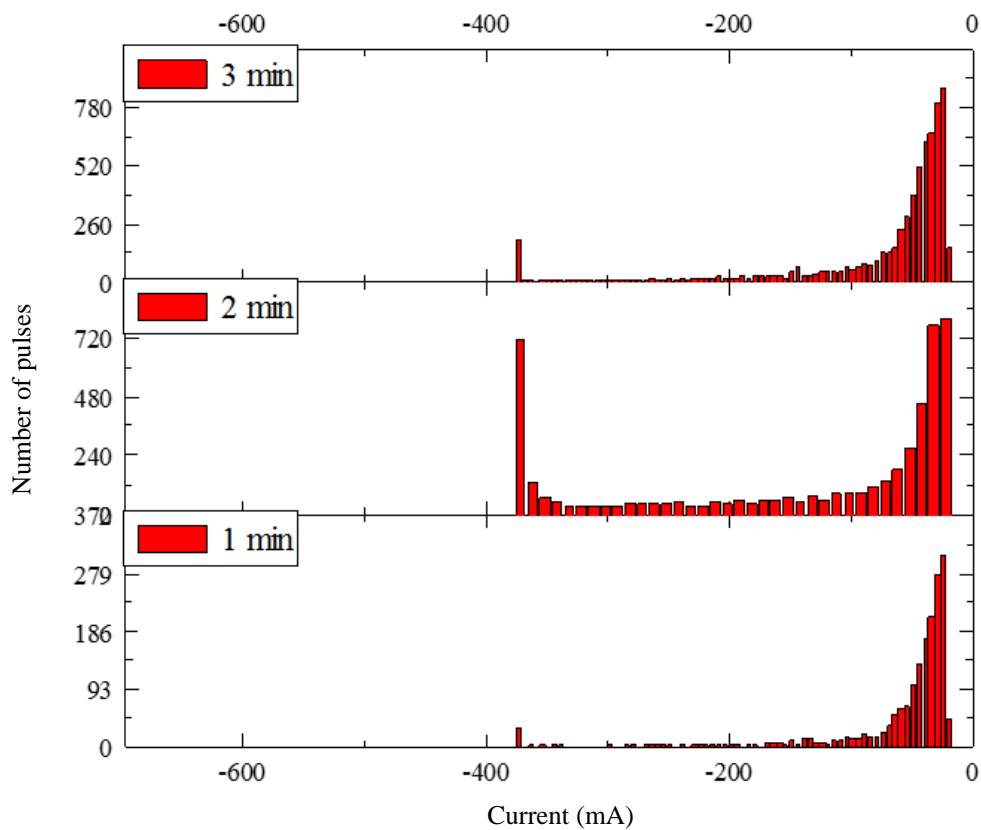


Figure 6.24 The negative current amplitude distribution at different energization time at -183 °C with 9 kV<sub>p</sub> applied voltage at 50 Hz.

The average current amplitude in the first minute was 116.6 mA, and then increased to 142.4 mA in the second minute. Finally, in the third minute, the average current amplitude was 129.1 mA.

According to the Lissajous figure, the charge transfer of the positive cycle was the same as that of the negative cycle. The average current amplitude of the positive cycle was more than twice that of the negative cycle. In this case, the number of discharges in the positive cycle was less than the number of discharge in the negative cycle. It was observed that the discharge property using oxygen input at -183 °C was completely different from the discharge property measured at low temperatures (-90 °C to -136 °C), once the liquid ozone was formed. The current and voltage waveforms at different temperatures are investigated in the next subsection.

### C. Discharge properties at different temperatures

In this section, the current and voltage waveforms at -70 °C, -110 °C and -183 °C are discussed (as shown in Figure 6.25 to Figure 6.27).

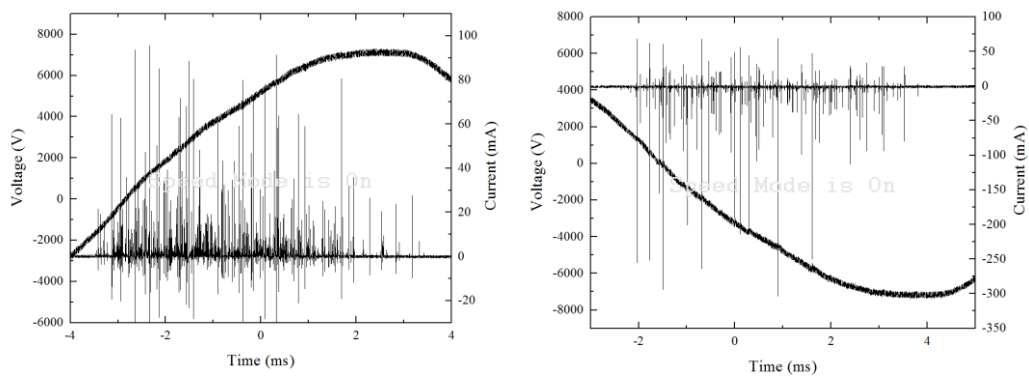


Figure 6.25 The sampled current and voltage waveforms with 0.4 L/min oxygen feed at -70 °C at 7.5 kV<sub>p</sub> voltage, 50 Hz.

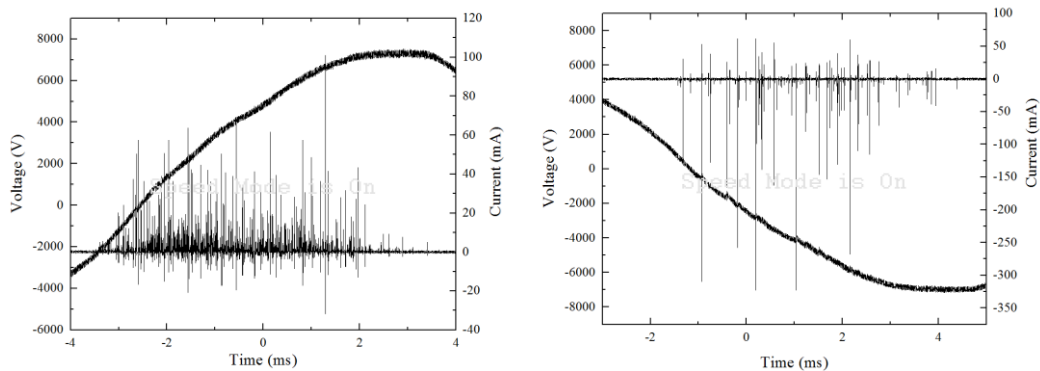


Figure 6.26 The sampled current and voltage waveforms with 0.4 L/min oxygen feed at -110 °C at 7.5 kV<sub>p</sub> voltage, 50 Hz.

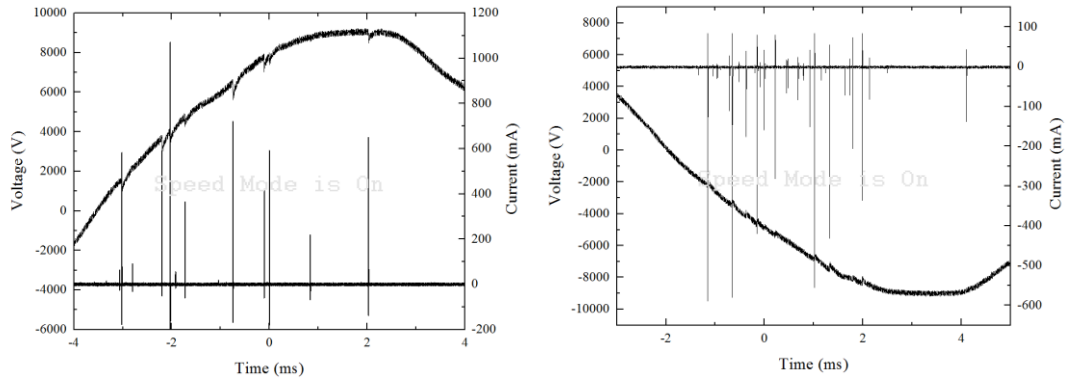


Figure 6.27 The sampled current and voltage waveforms with 0.4 L/min oxygen feed at -183 °C at 7.5 kV<sub>p</sub> voltage, 50 Hz.

At -70 °C, the maximum current amplitude during the positive discharge was approximately 100 mA, while the maximum current amplitude during the negative discharge was over -300 mA. The number of discharge of positive cycle was much higher than was that of the negative cycle.

At -110 °C, the average current amplitude of the positive cycle was much lower than it was at -70 °C. Meanwhile, the average current amplitude of the negative cycle was much greater than it was at -70 °C. The discharge frequency of the negative cycle decreased. With a decrease in the temperature, the number of oxygen particles increases dramatically.

At -183 °C, the discharge properties changed. In the sampled discharge cycle, the maximum current amplitude of the positive cycle was nearly 1 A with a voltage drop of over 200 V. The total number of discharges in the positive cycle was 12, while the total number of discharges in the negative cycle was 29. The increment of the current amplitude in the positive cycle was the result of the formation of liquid ozone. As mentioned previously, the ozone produced at -183 °C was in the liquid phase. A thin layer of liquid ozone can form on either the glass tube or the electrode. Based on the current waveform, the liquid ozone layer should form on the high-voltage electrode. In the positive discharge cycle, the current amplitude value increased dramatically as the temperature decreased. In this case, the charge transfer of each filament increased significantly, which means that the micro-discharge in the positive cycle was difficult to extinguish. As we know, liquid ozone has a strong electronegativity to absorb electrons. Once the electrons move towards the anode, the liquid ozone on the high-voltage electrode can obtain the electrons. In this case, the reversed electric field is quite difficult to establish. As a result, more electrons are required to form the reversed electric field. In this case, the current amplitude of the positive cycle increased significantly. As there was strong

filament development, the electric field across the gas gap decreased dramatically. The next discharge occurs until the electric field has been replenished, which explains why the discharge repetition rate decreases. A proof experiment was undertaken by passing a mixture of ozone and oxygen gas into a U-tube immersed in liquid oxygen; no liquid ozone was detected. The only possible explanation is that the high concentration of ozone was produced during the discharge at -183 °C. The distance between each molecule was close enough to liquefy the ozone.

## 6.4 Ozone generation with 5 kHz power supply

For industrial use such as water treatment and DeNO<sub>x</sub>, ozone concentration above 150 g/Nm<sup>3</sup> is normally required with the most commonly used frequency being between 0.5 and 5 kHz. This section describes the experiment that was conducted using a 5 kHz AC supply. The ozone test cell was immersed directly into the liquid oxygen to maintain the test cell at cryogenic temperature. The input gas was pure oxygen with a flow rate of 0.4 L/min. The applied voltage was 7 kV<sub>p</sub> with 1 min energization time. The test cell and experimental arrangement were exactly the same as that of the 50 Hz experiment. The ozone concentration was measured by the ozone analyser.

### 6.4.1 Ozone concentration analysis

Figure 6.28 shows the ozone concentration after 1 min discharge.

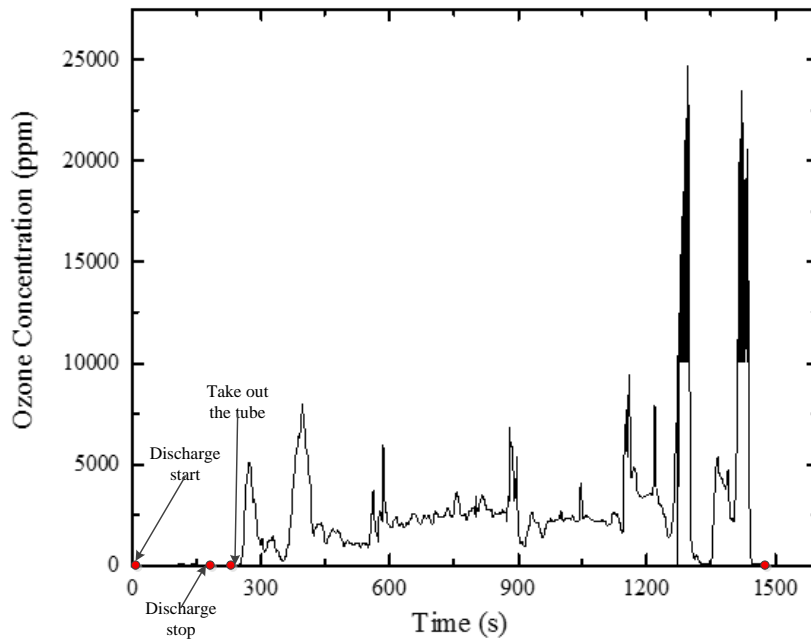


Figure 6.28 The ozone concentration measurement with 1 min of discharge time at 5 kHz, 7 kV<sub>p</sub> with 0.4 L/min oxygen input.

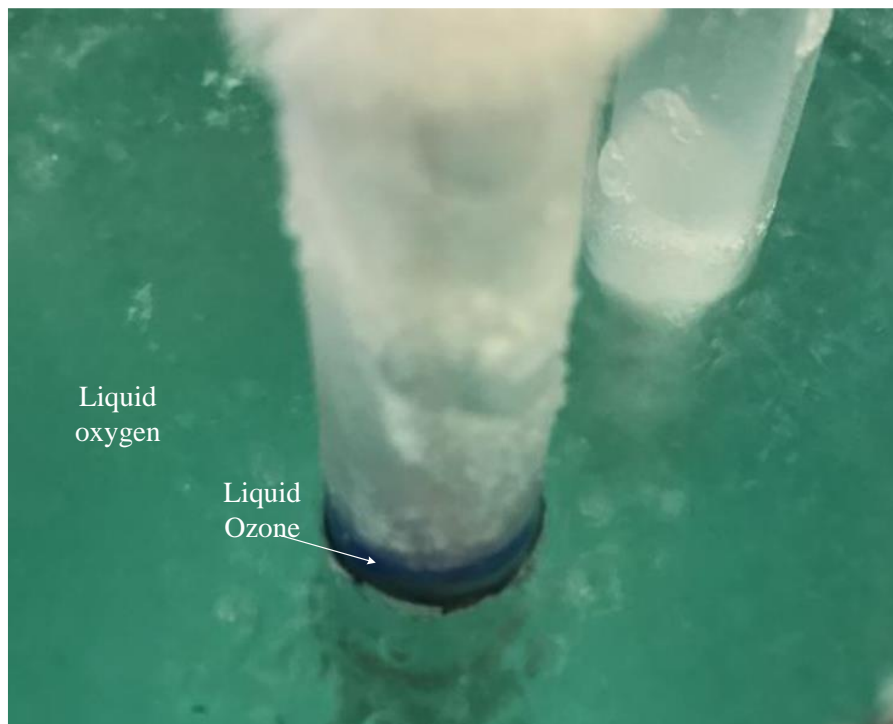


Figure 6.29 Liquid ozone (dark violet) produced under -183 °C with 5 kHz power supply, 7 kV<sub>p</sub> operating 1 min.

In Figure 6.28, during the energization time, the detected ozone concentration remained zero. All the ozone produced was in the liquid phase. After the discharge, when removing the test cell from the liquid oxygen environment, the liquid ozone vaporised gradually. A dark violet liquid could be observed attaching to the high-voltage electrode as shown in Figure 6.29. When removing the test cell, the temperature increased from the top of the test cell to the bottom. The violet liquid that formed could be seen flowing down to the bottom of the U-shaped tube along the high voltage electrode. At this time, a part of the liquid ozone vaporised and the peaks shown in Figure 6.28 were measured. With a continuous increase in the temperature, the remainder of the liquid ozone vaporised partly. As a result, there are several peaks in the gas phase ozone concentration. The total ozone production was the integration of the ozone concentration with time, multiplied by the flow rate.

#### 6.4.2 Ozone efficiency analysis

Figure 6.30 shows the Lissajous figure obtained for every 15 s.

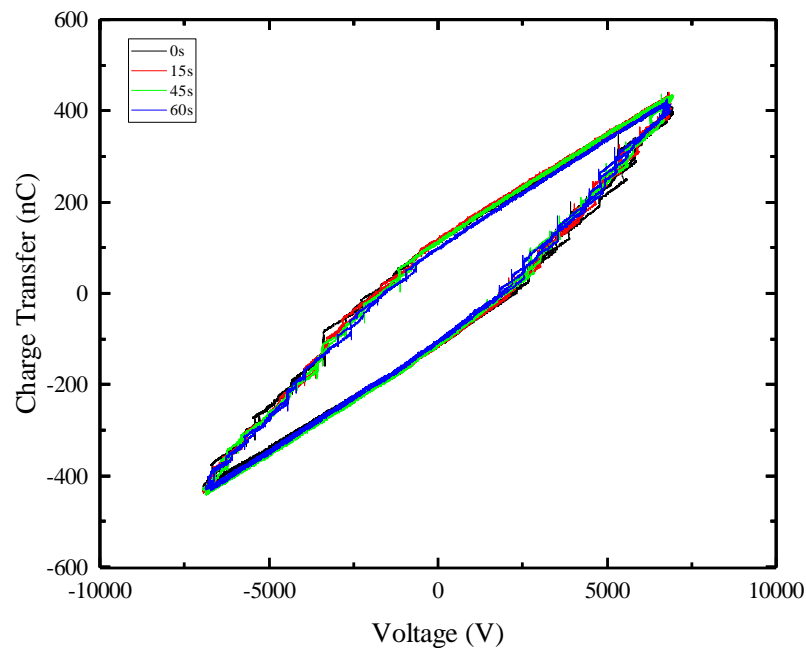


Figure 6.30 The Lissajous figure at different time during the 1 minute energization time with 7 kV<sub>p</sub> power supply at 5 kHz. The reactor temperature was -183 °C.

Table 6.11 The discharge parameters at different times.

<b>Energization Time (s)</b>	<b>C<sub>d</sub> (pF)</b>	<b>C<sub>g</sub> (pF)</b>	<b>V<sub>b</sub>(V)</b>	<b>Power (W)</b>
0	88.3	94.2	1860.0	9.6
15	85.3	89.8	2123.8	9.6
45	85.7	93.4	1990.9	9.7
60	81.1	96.5	1878.4	8.9

In the above Lissajous figures, the area decreased over time. According to Table 6.11, the dielectric capacitance decreased slightly over time. The input power did not change significantly in the first 45 s. The power input at 60 s decreased from 9.7 W to 8.9 W. The average power input in this case was 9.45 W. The ozone efficiency was 396.6 g/kWh which is equal to 9 eV electron energy efficiency.

## 6.5 Discussion

In the past century, ozone generation under low temperature was investigated by Hautefeuille and Chappuis [102], who successfully obtained ozone concentrations of 14.9% by weight of ozone at 0 °C, and 21.4% at -23 °C. High concentration ozone (350 g/Nm<sup>3</sup>) can be achieved at -23°C due to the low ozone decomposition rate. Masuda *et al.* [45][46] recorded the generation of ozone using a glow discharge in oxygen at cryogenic temperatures (liquid nitrogen temperature -190 °C) with a maximum ozone efficiency of 550 g/kWh. The glow discharge takes place in a quartz tube at low pressure of 0.5 to 2.0 Torr, with the distance between two stainless steel electrodes being 100 mm. The test cell was dipped directly into a tank filled with liquid nitrogen. An icy layer of ozone formed on the surface of the tube. After 10 minutes of energization time, the level of the liquid nitrogen was reduced to vaporise the mixed ozone-oxygen gas into another collection tube. The results showed that the ozone efficiency could be more than 300 g/kWh. The increase in the pressure could decrease the ozone efficiency. The best result achieved using glow discharge was 550 g/kWh with a 5 mm diameter tube at 1 Torr. Based on the measurement result, the electron energy efficiency at cryogenic temperature by glow discharge was 45%, which is much higher than the commercial ozone generator efficiency.

Masuda *et al.* [43] also did the research under the high-frequency surface discharge. The cylindrical DBD configuration test cell with liquid nitrogen cooling system was used. The gas

phase ozone was produced. The operating frequency was 10 kHz with different peak applied voltage. The electrode test cell temperature was adjusted by controlling the input of liquid nitrogen. The highest ozone efficiency achieved was 400 g/kWh at -90 °C and 8 kV<sub>p-p</sub> power supply.

Increasing the applied voltage, the ozone generation efficiency, based on Masuda's experiment result, was decreased. At -90 °C and 10 kV<sub>p-p</sub>, the ozone efficiency was only 240 g/kWh, which was only half of that obtained at 8 kV<sub>p-p</sub>. As the produced ozone was in the gas phase, with increasing the voltage input, the energy input increased leading to the higher gas temperature. The ozone dissociation rate increases significantly. While, from this experiment, as the whole test cell was submerged in liquid oxygen, the heat transfer was better. From another point of view, once the produced gas phase ozone transferred to liquid phase, there was no dissociation progress.

Considering the energy efficiency, the theoretical ozone efficiency is 1280 g/kWh with 3 eV to produce two ozone molecules. Without considering the dissociation process or the water vapour effect, to produce two ozone molecules, the energy required is 5.13 eV. In this case, the maximum ozone efficiency achievable is 748 g/kWh. According to the literature review [74], the energy branching of DBD shows that the oxygen dissociation process mostly happens at 8.4 eV. Normally, it is considered that the wasted energy was transferred into molecule vibration and heat. In this case, the maximum ozone efficiency achievable is only 457 g/kWh. The results of ozone production at cryogenic temperature show that the higher ozone efficiency can be achieved which means the electron energy used for the production of two ozone molecules was less than 8.4 eV. The results show that the energy wasted during the process of ozone production can be re-used somehow.

## 6.6 Conclusion

In this chapter, the ozone efficiency at different temperatures was discussed. The experiment was conducted from -90 °C to -183 °C at 50 Hz and 5 kHz, respectively. The maximum ozone efficiency can reach nearly 460 g/kWh at -136 °C with an oxygen feed.

When using a 50 Hz power supply, the ozone efficiency was investigated using an air feed and an oxygen feed, respectively. The ozone efficiency when using the air feed was more than 50% greater than it was at room temperature. The limitation of the ozone dissociation process and the reduction of the water vapour effect led to an increment in the ozone efficiency. With

the air input, the ozone produced was quite difficult to liquefy even when reaching the boiling point.

With the oxygen input at -90 °C, the ozone efficiency was over 280 g/kWh, which was much greater than that of the commercial ozone generator. When continuously decreasing the test cell temperature to -136 °C, the maximum ozone efficiency was 460 g/kWh. Following several repeatable tests, the ozone efficiency increased with the decrease of the test cell temperature. The ozone produced was always in the gas phase. After immersing the test cell in the liquid oxygen, the ozone produced in this case was all in the liquid phase. The discharge became quite intense. The maximum ozone efficiency was 384 g/kWh.

When using the 5 kHz power supply, the maximum ozone efficiency was nearly 400 g/kWh. Theoretically, 2.9 eV can produce an ozone molecule. The ozone efficiency was 1220 g/kWh. According to the simulation results after 76 main reactions after oxygen feed, the most likely oxygen dissociation energy was 8.4 eV. In this case, the ozone efficiency was approximately 440 g/kWh. According to the test results, the ozone efficiency at -183 °C can be 400 g/kWh, which means the waste of the electron energy was quite low. Whether this was due to the decrease in the temperature needs to be confirmed by more detailed experimentation.

The current amplitude distribution at different temperature has been investigated as well. According to the literature review, the lower the temperature, the higher the ozone efficiency. However, the formation of liquid ozone makes the discharge quite unstable. The average current of the positive cycle in this case was at least 15 times greater than was the average current at low temperatures (-70 °C and -110 °C). The discharge area decreased with the increment of the amount of liquid ozone. In this case, the power input was not a constant. Further research needs to be done for a better understanding of the discharge properties when the liquid ozone was formed.

## 7 Conclusion and Future Work

### 7.1 Conclusion

As introduced in Chapter 1, ozone is an environmentally friendly oxidant with wide applications in industry. The research focused on the investigation of the dielectric barrier discharge with oxygen input for ozone generation. The aim of the research was to optimise the ozone generation efficiency based on the dielectric barrier discharge. It included the optimisation of micro-discharges and the creation of advanced ozone generation technology to increase the ozone efficiency. Five different test cells were designed and manufactured. Firstly, a cylindrical DBD test cell was used for the investigation of atmospheric pressure glow discharge. Secondly, the open planar-plate configuration DBD test cell was used for the investigation of filament development. Thirdly, a sealed test cell with planar electrodes configuration was used for comparison with the commercially used ozone generator to determine the current distribution and ozone generation efficiency. Fourthly, the same sealed test cell with meshed electrodes configuration was used to determine the discharge performance of optimised meshed electrodes. Finally, a U-shaped tube was used to investigate the discharge performance and ozone efficiency at cryogenic temperatures. Two types of power input mode were employed in the research, 50 Hz AC and 5 kHz AC. Two ozone analysers with different measurement ranges were used to determine the ozone concentration. Electrical and optical diagnostics were used to investigate the discharge characteristics and behaviour of micro-discharges in the DBD.

Firstly, a literature review that discussed ozone's properties and applications, the ozone generation process and discharge methods was presented. It focused mainly on the chemical reactions involved in the ozone generation process. The critical kinetics of ozone generation were analysed first. With regard to the ozone generation process, it was crucial to analyse the electron energy efficiency. Based on the references concerning the cross section of electron collisions with oxygen molecules, electrons with 10 eV to 20 eV have a higher cross section of oxygen dissociation. Although the cross section of oxygen dissociation increases when the electron energy increases to 30 eV, the unwanted cross section of oxygen ionisation increases to the higher value. Based on the references regarding the cross section of electron collisions with ozone molecules, electrons with energy from 1.06 eV to 3 eV have a higher cross section for ozone dissociation. As a result, reducing the proportion of low-energy electrons and increasing the proportion of high-energy electrons (less than 20 eV) can increase the electron

energy efficiency. The reduced electric field,  $E/N$ , was the key parameter to reflect the mean electron energy in micro-discharges. The reduced electric field between 100 Td to 300 Td was the optimum range for ozone generation. If the reduced electric field was lower than 100 Td, the mean electron energy was too low to dissociate the oxygen molecules but was just sufficient to dissociate the produced ozone. Meanwhile, if the reduced electric field was higher than 300 Td, the mean electron energy was too high to ionise the oxygen molecules and the production of atomic oxygen increased dramatically to accelerate the ozone dissociation. As a result, the concentration of oxygen atoms was an important factor in ozone generation. The optimum range of the concentration of oxygen atoms was  $10^{-5}$  to  $10^{-4}$ . If the atomic oxygen concentration was higher than  $10^{-4}$ , the reaction rate of atomic oxygen and ozone molecules would increase. Based on the literature review, the 8.4 eV electron energy can dissociate oxygen molecules to  $O(3P)$  and  $O(1D)$  with energy branching of over 60% once the reduced electric field was greater than 100 Td. The critical problem was that the excited oxygen atom would react with another oxygen molecule to transfer the energy into heat or react with an ozone molecule to dissociate ozone back to the oxygen molecule. This part of the energy was wasted. Meanwhile, 6 eV electron energy can dissociate oxygen molecules to  $2O(3P)$  with maximum energy branching of only 30%. Most of the electrons reacted with oxygen molecules to cause the vibration of oxygen molecules or to produce excited oxygen molecules. Excited oxygen molecules mainly collide with other oxygen molecules and produce heat. Overall, whether the wasted energy could be reused was worth investigating. If so, the ozone efficiency could increase significantly.

Apart from the energy losses in the filament, the temperature and humidity effects can affect the ozone generation efficiency. The ozone dissociation rate was proportional to the temperature. When increasing the temperature, the ozone dissociation rate increased dramatically. The cooling water (15 °C) was used for a large ozone generator to maintain the gas temperature in the test cell. Moreover, the water vapour in the feed gas affected the ozone generation by producing  $OH$  and  $HO_2$  to react with ozone. The dew point of the feed gas was usually below  $-40^{\circ}\text{C}$ .

The research was based on ozone generation using dielectric barrier discharge which was found as a filamentary discharge. It was found that the single discharge time was 10 ns with milliamps current amplitude, accompanied by a voltage drop across the test cell. It was also found that the transferred charge of a quarter-cycle discharge on the barrier surface distributes to two parts. Part of the charge forms a reversed electric field with opposite polarity charges. The other part of the charges induces charges with the opposite polarity from the ground

electrode. The charge transfer analysis of a full cycle was investigated by measuring the Lissajous figure. The charge accumulation value at the critical points was calculated. The analysis of the single filament focused on the equivalent circuit, which separated the discharge gap capacitance and the discharge barrier capacitance from the total gap capacitance and total barrier capacitance. This indicates that the filament current was formed by the charges increasing the voltage across the discharge barrier capacitance  $C_d''$  and the charges causing the voltage drop across the discharge gap  $C_g''$ . The charges increasing the voltage across  $C_d''$  were the charge transfer from the stray capacitance and the rest of the total capacitance of the test cell  $C_t'$ . Overall, the expression of the filament current was shown in (3.22). The distribution of the current was investigated and found to conform to a normal distribution with the standard deviation. Finally, the transient state dielectric barrier discharge process was analysed. From the result, it can be seen that the dielectric barrier discharge can be balanced quickly in the first few cycles. The discharge waveforms in the first cycle show that the current amplitude was much higher than was that in the steady state. Without the accumulated charges on the barrier surface, the filament developed sufficiently. From the second cycle onwards, the discharge was more harmonious and the establishment of the discharge was made. The current distribution of the planar electrode configuration DBDs was worth investigating.

A sealed planar-plate configuration test cell was used for the investigation of the relationship between the filament current and ozone efficiency. The current distribution was determined by changing the applied voltage, the gas pressure and the barrier thickness. It was found that, when increasing the applied voltage, the average peak external current did not change significantly. The increment of the gas pressure leads the current amplitude distribution to become narrower. With an increase in the barrier thickness, the current amplitude distribution became more concentrated and the average discharge current decreased from 25 mA to 10 mA by increasing the pressure from 1.0 bar to 1.6 bar. After the investigation of the current distribution, the ozone efficiency under different conditions was investigated as well. When increasing the applied voltage, the ozone efficiency decreased because the higher concentration of ozone produced was dissociated by the atomic oxygen. When increasing the pressure, the ozone efficiency increased because the filament development was more uniform. For the same charge transfer, the number of discharges increased, leading to a more uniform distribution of atomic  $O$ . When increasing the barrier thickness, more of the accumulated charges will contribute to the establishment of the reversed electric field to extinguish the filament more easily. Ozone efficiency versus the reduced electric field figures were developed, as shown in Figure 4.26. The ozone efficiency can reach  $\sim 207$  g/kWh at  $\sim 123$  Td.

The ozone efficiency then reduces gradually when the reduced electric field is increased from 140 Td to 210 Td. With the continuing increase of the reduced electric field, the ozone efficiency fell rapidly to ~109 g/kWh at ~277 Td.

It was found that, with low external current magnitude, the filament could easily be extinguished. The power supply will charge the test cell to recover the electric field across the gap, but the local electric field across the previous gap channel is less than the average electric field. The next filament will then form at a different position on the electrode surface. When the filament was easily extinguished, the electron distribution in the gas-gap tended to be more uniform, increasing the ozone efficiency. The electrons are produced in the filament channel and only react with the oxygen molecules in the channel. With a higher energy filament, the discharge number reduces if the charge transfer remains the same. Most of the oxygen molecules in the gap cannot react with the electrons, and the increasing amount of electrons can also react with ozone, reducing the efficiency of the ozone production.

To produce a uniform filamentary discharge, the planar electrodes were replaced by meshed electrodes. The discharge occurred in the gap between the barrier and the wires. When increasing the applied voltage, the discharge area expanded. With the increase in the applied voltage, the average peak current increased from 3 mA to 21 mA. The equivalent gap length increased from 0.28 mm to 0.42 mm and the breakdown voltage increased from 1105 V to 2061 V. This was accompanied by a decrease in the ozone efficiency from 303 g/kWh to 214 g/kWh. It can be seen that the increase in the discharge current led to a decrease in the ozone efficiency. When increasing the applied voltage, the average peak current increased continuously from ~3 mA at 4.5 kV<sub>p</sub> to ~12 mA at 6.5 kV<sub>p</sub>. The current amplitude distribution is narrower for the lower applied voltage. When increasing the pressure, the average peak total current decreased dramatically from ~12 mA at 1.0 bar absolute to ~5 mA at 1.2 bar absolute. With the continuous increase in the pressure, the average current decreased to ~3 mA. A more uniform discharge with a lower amplitude of the external current can increase the ozone efficiency. By decreasing the aperture size, the discharge current amplitude at the same applied voltage and gas pressure decreases. For the same reduced electric field, the ozone efficiency increases when reducing the aperture size. All the results indicate that a smaller amplitude of pulsed filament current and a narrower distribution of the pulsed filament current can increase the ozone efficiency. A comparison was made between the meshed electrode DBD and the planar electrode DBD. At the same reduced electric field, the ozone efficiency using the meshed electrode was 100 g/kWh higher than when using the planar electrode. To investigate the differences in current amplitude distribution using different configurations, the same gap

length as with the planar electrode was used. The result shows that increasing the applied voltage from 4.5 kV<sub>p</sub> to 6.5 kV<sub>p</sub> does not change the average peak current of planar plate dramatically, from 8 mA to 10 mA, while the average peak current of the meshed plate increased from 2 mA to 22 mA.

When using meshed electrodes, the discharge was relatively independent. The diffusion area of the single filament was quite limited due to the uneven gap length. With a nanosecond discharge, there is diffuse discharge using planar electrode. By changing the electrode configuration, the ozone efficiency increased dramatically. Comparing the results of the two electrode configurations, the highest ozone efficiency was achieved by increasing the gas pressure. The increase in the gas pressure decreases the mean free path of the electrons and the faster extinguishing of the filament. In this case, for the same charge transfer, there is increased number of filaments developed in the discharge gap leading to a more uniform electron distribution. The ozone dissociation due to electron effect is limited.

To get better results of ozone efficiency, the temperature effect and the reactions which can dissociate ozone production need to be limited. By reducing the temperature to below - 80 °C, the effect of humidity was removed. Another advantage was that the rate coefficient of ozone formation increased while the dissociation rate decreased. The total ozone reaction efficiency can increase. The test cell was located in a dewar flask that was filled with liquid oxygen. Once the discharge occurred, the heat produced in the test cell transferred to the liquid oxygen to vaporise it to the gas phase. Ozone generation with air input at different temperatures using 50 Hz was tested. With regard to the air input, ozone generation at 25°C was 80 g/kWh. Ozone generation increased to 130 g/kWh at -80 °C. The continuous decrease in the temperature to - 120 °C caused the maximum ozone efficiency to increase to 145 g/kWh, which was 1.6 times greater than was the ozone efficiency at room temperature. With regard to the oxygen input, the maximum ozone efficiency was 460 g/kWh at -136 °C. With decreasing in the temperature, the ozone efficiency increased from 280 g/kWh to more than 400 g/kWh on average. The ozone efficiency at -183 °C was also measured. Because of the production of liquid ozone, the strong surface tension resulted in a high probability for liquid ozone to attach to the surface of the glass tube or to the metal electrode. The formation of liquid ozone decreased the discharge area. When using 5 kHz power supply at -183 °C, all of the ozone produced was in the liquid phase. The ozone output in the gas phase during the discharge was zero. When removing the test cell from the dewar flask after the discharge, it could be seen that the violet-coloured liquid was vaporising. As a result, the ozone concentration was calculated in real time. The

maximum ozone generation efficiency achieved was 396.6 g/kWh which is equal to the 9 eV ozone molecule.

## 7.2 Highlights of the results

Throughout this thesis, the research focused on ozone generation using the AC dielectric barrier discharge. The important findings are listed as follows:

1. The charge transfer of a single filament was composed of the charges leading to the voltage drop across the discharge gap capacitance and the charges produced to increase the voltage across the discharge barrier capacitance.
2. The external current was due to the voltage drop across the stray capacitance. The distribution of the external current can reflect the distribution of the filament current.
3. An optimised meshed electrode was used to replace the planar electrode. The lower amplitude of the external current and a narrower current amplitude distribution can lead to higher ozone efficiency of 330 g/kWh.
4. Ozone generation at cryogenic temperatures was investigated. The highest measured ozone efficiency was 460 g/kWh, which was three times higher than commercial ozone efficiency with the liquid ozone produced. Furthermore, there was no longer a need to use the cooling system. The liquid oxygen can take away the heat in the test cell and the vaporised oxygen can be reused as the gas input.

## 7.3 Future work

There are two major areas in which the author would like to conduct further research. The first is the mechanism of the ozone generation process. The second would be an attempt to commercialise ozone generation technology at cryogenic temperatures.

With regard to the investigation of the mechanisms involved in filamentary discharge, the external current distributions under different parameters have been performed. In the research, a regular external current trend was shown in Figure 7.1. It captured the peak current of 20,000 single discharges with air input. The peak current shows quite an interesting distribution. It would appear that every charge that accumulated on the barrier surface was moving and trying to establish a new balance after a certain period. The phenomenon only occurs when using an open test cell. A more detailed analysis needs to be performed in future work.

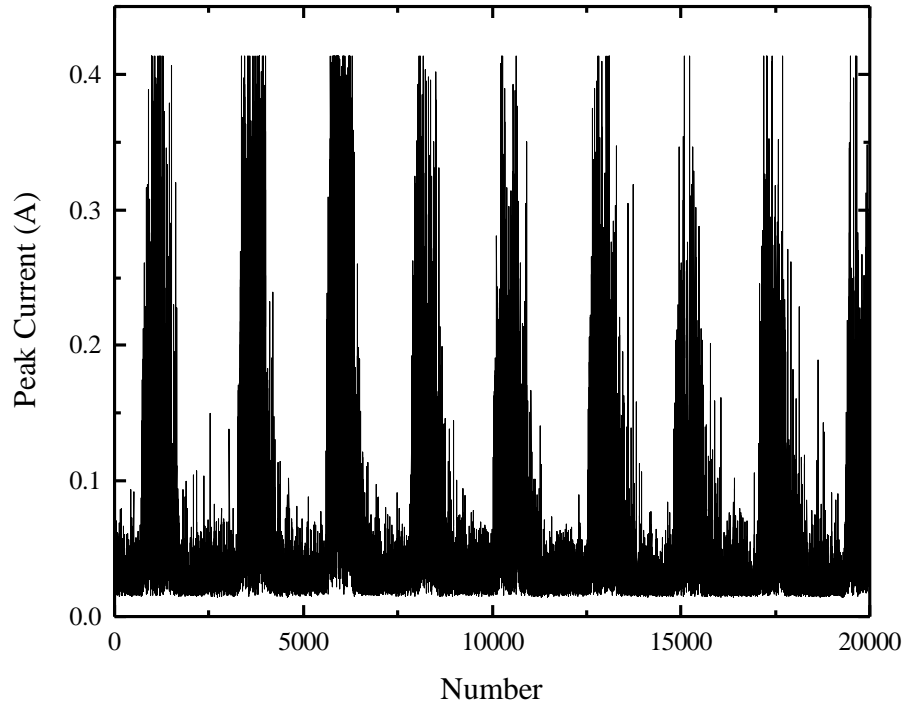


Figure 7.1 The trend of the peak current value using DBD in air.

Secondly, the species produced in the discharge channel with the oxygen feed are crucial for the analysis of the kinetics of ozone generation. The most reliable result was based on the simulation of the 76 main reactions. In this research, the spectra of oxygen during the discharge were measured using the cylindrical test cell. The results at different applied voltages are shown in Appendix F. It would appear that the only line spectra detected was 777 nm. The rest of the spectra were between 300 nm and 400 nm. As the spectra bands of the second positive and first negative systems of the nitrogen molecule were quite close to the line spectra of atomic oxygen, it was difficult to identify the species in the discharge. Whether these are the wavelengths of nitrogen molecules or the wavelengths of atomic oxygen needs to be investigated in detail.

Finally, ozone generation at cryogenic temperatures needs further investigation. The ozone concentration and ozone efficiency results were satisfied in a short operation time. Conditions were unsafe if the liquid ozone in the container was more than 1 mL. A method to collect the liquid ozone is a crucial aspect for future investigation.

## 8 Published Papers

### 8.1 Journal papers

**Y. J. Zhou**, G. M. Huang, T. Wang, S. J. MacGregor, Q. C. Ren, M. P. Wilson and I. V. Timoshkin, “Optimization of ozone generation by investigation of filament current characteristics under dielectric barrier discharges”, *IEEE Transactions on Plasma Science*, vol. 44, No. 10, 2016.

G. M. Huang, **Y. J. Zhou**, T. Wang, I. V. Timoshkin, M. P. Wilson, S. J. MacGregor and M. J. Given, “Statistical analysis of pulsed micro-discharges and ozone generation in dielectric barrier discharges”, *IEEE Transactions on Plasma Science*, vol. 44, No. 10, 2016.

**Y. J. Zhou**, T. Wang, S. J. MacGregor, Q. C. Ren, M. P. Wilson and I. V. Timoshkin, “Experimental investigation of meshed-plates dielectric barrier discharge in ozone generation”, *Journal of Physics D: Applied Physics*, In progress.

### 8.2 Conference papers

**Y. J. Zhou**, G. M. Huang, T. Wang, S. J. MacGregor, M. P. Wilson and I. V. Timoshkin, Pulsed filament current characteristics in dielectric barrier discharge 20 Jun 2015 *2015 IEEE Pulsed Power Conference (PPC)*. Piscataway, NJ.: [IEEE](#), p. 1-4 4 p.

G. M. Huang, **Y. J. Zhou**, M. P. Wilson, T. Wang, I. V. Timoshkin, S. J. MacGregor and M. J. Given, “Investigation of pulsed micro-discharges and ozone production by dielectric barrier discharges”, *Proceedings of 2015 IEEE Pulsed Power Conference*, Austin, TX, 2015.

## 9 Appendix

### A. The calculation of Lissajous figure

```

%Read excel
B = xlsread('H:\LOxExperiment\Mesh\Transient LOx Voltage
Data.xlsx', 'Sheet1', 'B2:C100001');
T = xlsread('H:\LOxExperiment\Mesh\Transient LOx Voltage
Data.xlsx', 'Sheet1', 'A2:A100001');

A = zeros (8,100);
A_con = zeros (8,100);

X = zeros (1000,100);
Y = zeros (1000,100);
T_1 = zeros (1000, 100);
Q_1 = ones (1000, 2)*(-2000);
Q_2 = ones (1000, 2)*2000;
P_1 = [Q_1,Q_2];
P_2 = P_1;
Z = zeros (100, 12);
C = zeros (1000,1);
D = zeros (1000,1);
E = zeros (1000,1);
F = zeros (1000,1);
G = zeros (1000,1);
H = zeros (1000,1);
I = zeros (1000,1);
J = zeros (1000,1);
K = zeros (1000,1);
L = zeros (1000,1);
Z_1 = zeros (100,8);

k = 100000/100;

for i = 1:1:100
for j = 1:1:1000
l = k * (i-1);
X (j,i) = B (j+1, 1);
Y (j,i) = B (j+1, 2);
T (j,i) = T (j+1, 1);
end
end

for i = 1:1:100
C = X (:,i);
D = Y (:,i);
[ymax,index] = max (D);
xmax = C(index);

```

```

Z (i,1) = xmax;
Z (i,2) = ymax;
[ymin,index] = min (D);
xmin = C(index);
Z (i,3) = xmin;
Z (i,4) = ymin;
end

for i = 1:1:100
C = X (:,i);
D = Y (:,i);
[ymax,index] = max (D);
xmax = C(index);
Z_1 (i,1) = xmax;
Z_1 (i,2) = ymax;
if index + 100 <=1000
Z_1 (i,3) = C (index + 100);
Z_1 (i,4) = D (index + 100);
else
Z_1 (i,3) = C (index - 900);
Z_1 (i,4) = D (index - 900);
end
[ymin,index] = min (D);
xmin = C(index);
Z_1 (i,5) = xmin;
Z_1 (i,6) = ymin;
if index + 100 <=1000
Z_1 (i,7) = C (index + 100);
Z_1 (i,8) = D (index + 100);
else
Z_1 (i,7) = C (index - 900);
Z_1 (i,8) = D (index - 900);
end
end

for i = 1:1:100
alpha = 0;
for j = 1:1:999
if Y (j,i) * Y (j+1,i) <= 0 && alpha <=2
alpha = alpha +2;
A (1,i) = Y (j,i);
A (2,i) = Y (j+1,i);
A (3,i) = min (abs(Y(j,i)),abs(Y(j+1,i)));
if A (3,i) == abs(A (1,i))
A_con (alpha,i) = A (1,i);
A_con (alpha-1,i) = X (j,i);
end
if A (3,i) == abs (A (2,i))
A_con (alpha,i) = A (2,i);
A_con (alpha-1,i) = X (j+1,i);
end
end

```

```

end
end
if A_con (1,i) < A_con (3,i)
Z (i,5) = A_con (1,i);
Z (i,6) = A_con (2,i);
Z (i,7) = A_con (3,i);
Z (i,8) = A_con (4,i);
end
if A_con (1,i) > A_con (3,i)
Z (i,7) = A_con (1,i);
Z (i,8) = A_con (2,i);
Z (i,5) = A_con (3,i);
Z (i,6) = A_con (4,i);
end
end

for i = 1:1:100
alpha = 4;
for j = 1:1:999
if X (j,i) * X (j+1,i) <= 0 && alpha <=6
alpha = alpha +2;
A (4,i) = X (j,i);
A (5,i) = X (j+1,i);
A (6,i) = min (abs(X(j,i)),abs(X(j+1,i)));
if A (6,i) == abs(A (4,i))
A_con (alpha-1,i) = A (4,i);
A_con (alpha,i) = Y (j,i);
end
if A (6,i) == abs (A (5,i))
A_con (alpha-1,i) = A (5,i);
A_con (alpha,i) = Y (j+1,i);
end
end
end
end
if A_con (6,i) < A_con (8,i)
Z (i,9) = A_con (5,i);
Z (i,10) = A_con (6,i);
Z (i,11) = A_con (7,i);
Z (i,12) = A_con (8,i);
end
if A_con (6,i) > A_con (8,i)
Z (i,11) = A_con (5,i);
Z (i,12) = A_con (6,i);
Z (i,9) = A_con (7,i);
Z (i,10) = A_con (8,i);
end
end

```

**B. The current and voltage waveforms under APGD with helium input.**

*B.1 With helium gas directly from cylinder.*

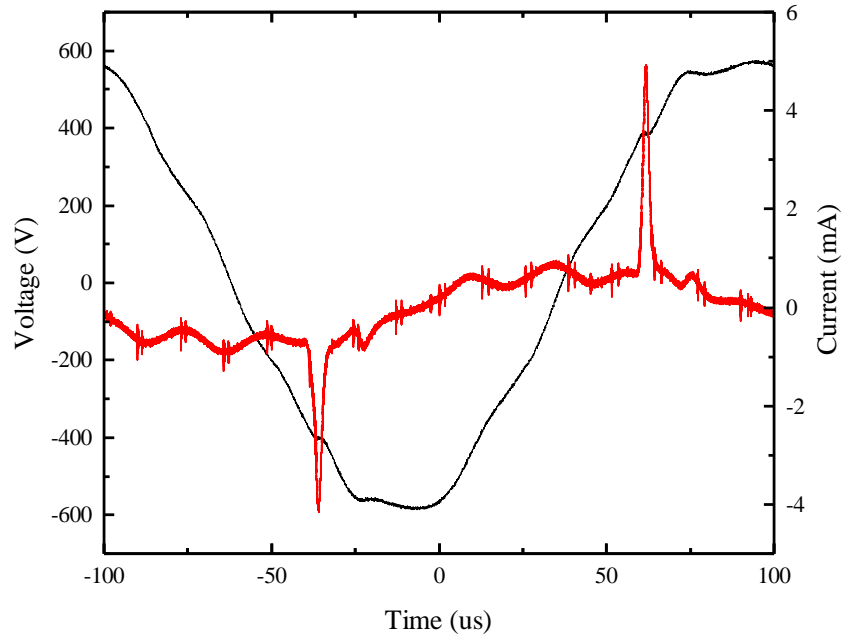


**Figure B.1** The current and voltage waveforms once the discharge ignited with helium.

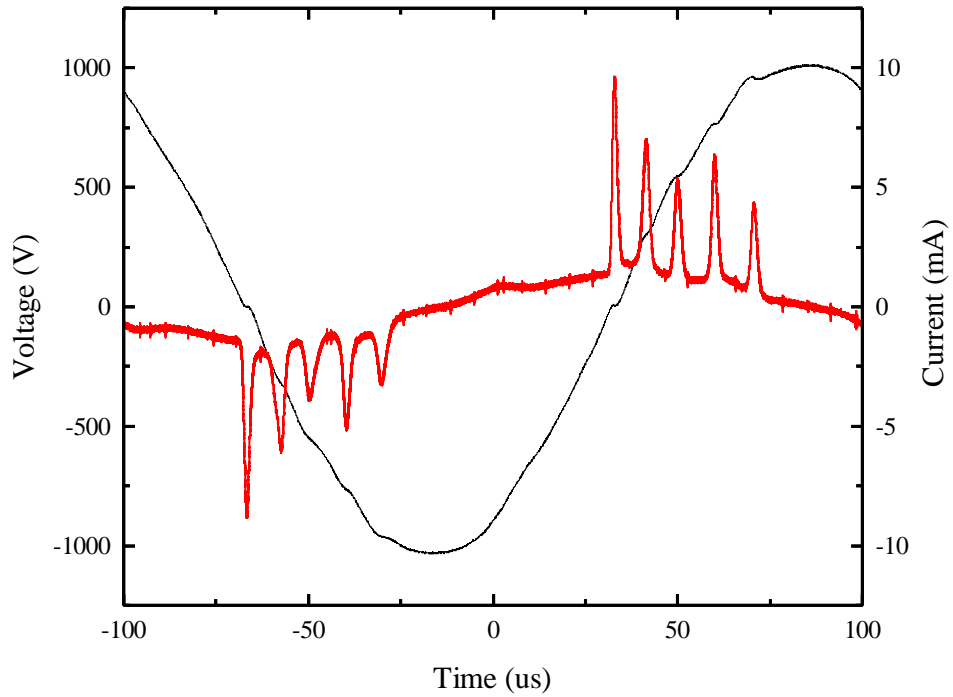


**Figure B.2** The current and voltage waveforms at 1 kV<sub>p</sub> with helium.

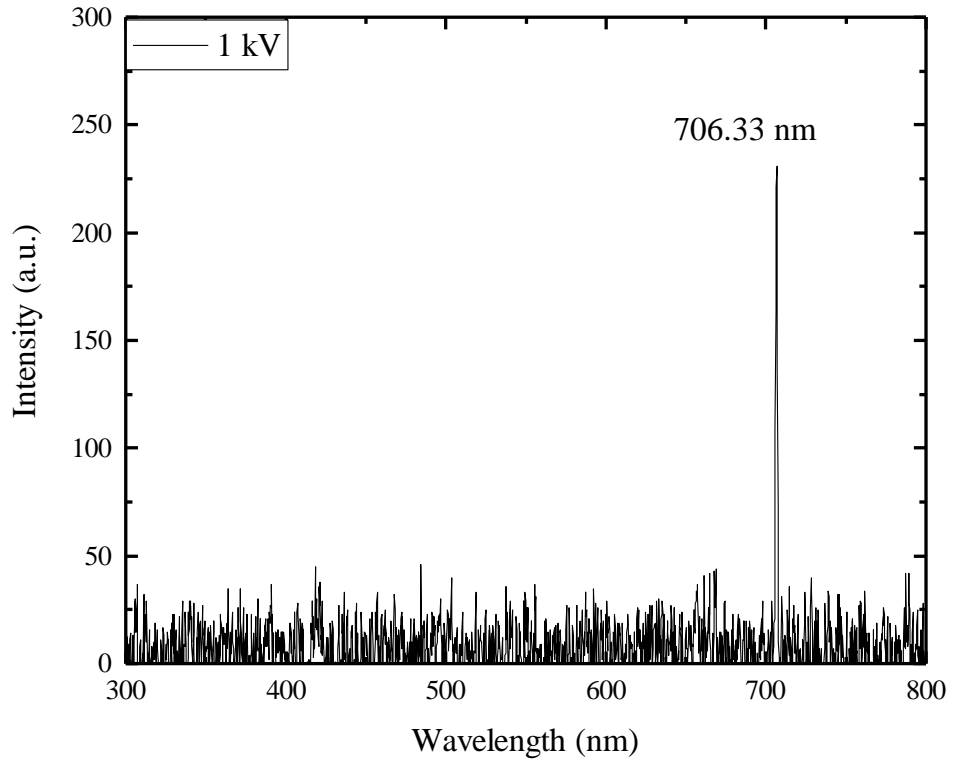


**Figure B.3** The spectra of atomic helium at 1 kV<sub>p</sub> power supply.

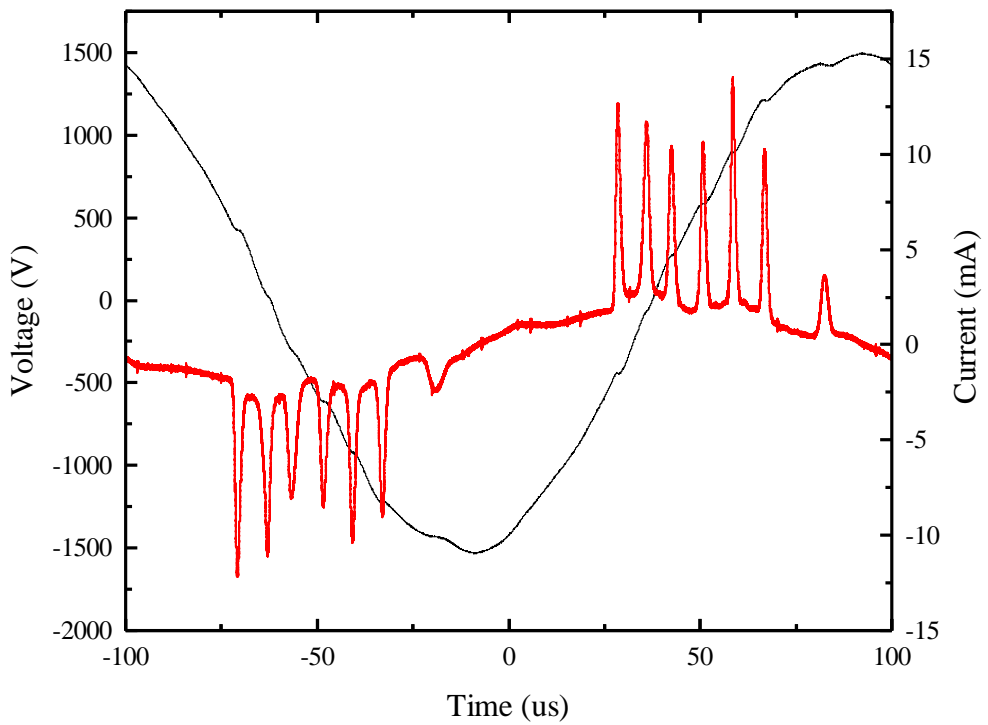


**Figure B.4** The current and voltage waveforms at 1.5 kV<sub>p</sub> with helium.

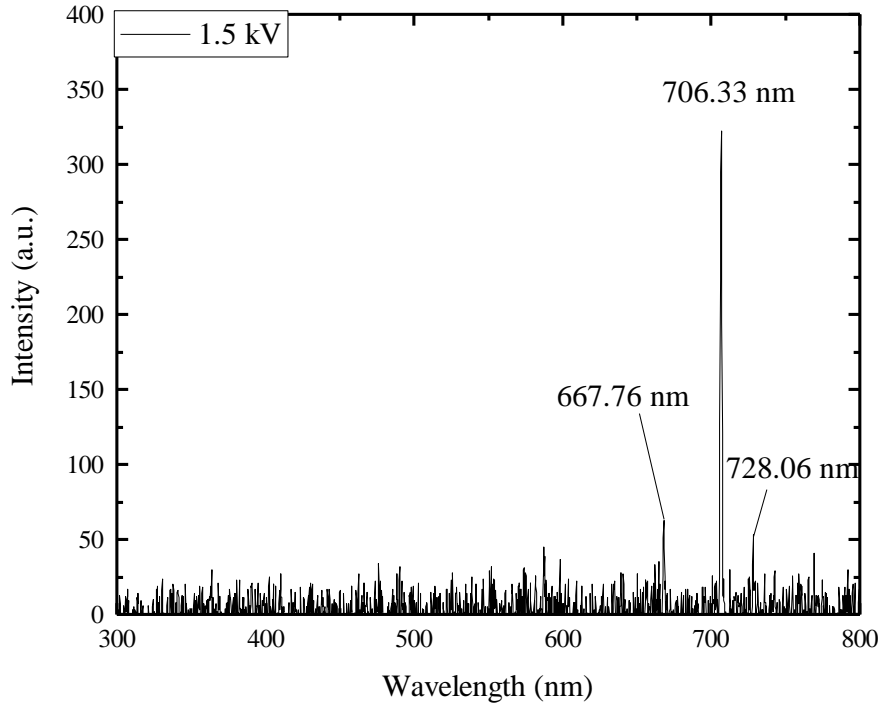


**Figure B.5** The spectra of atomic helium at 1.5 kV<sub>p</sub> power supply.

*B.2 With dried helium gas.*

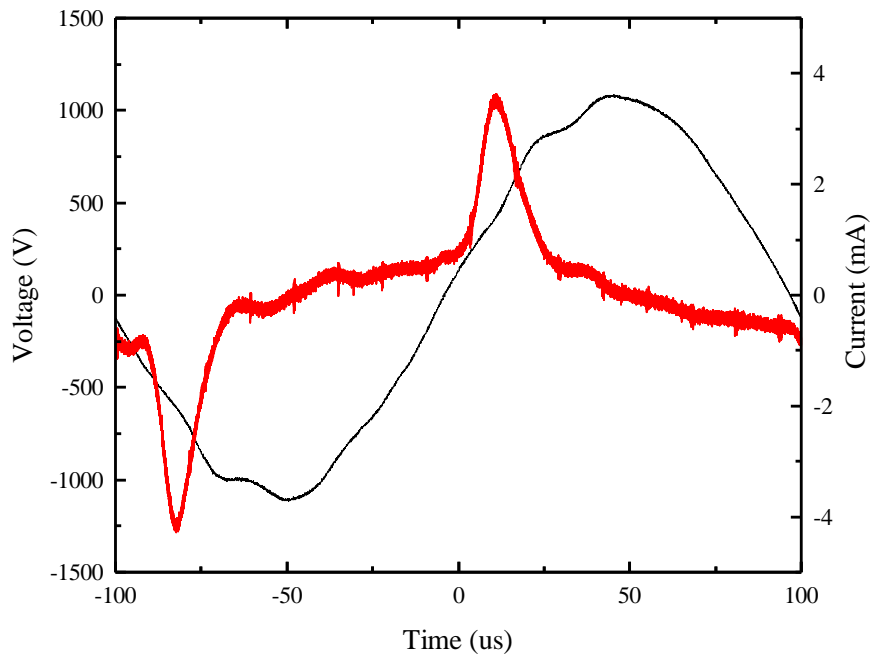


**Figure B.6** The current and voltage waveforms at 1 kV<sub>p</sub> with dried helium gas.

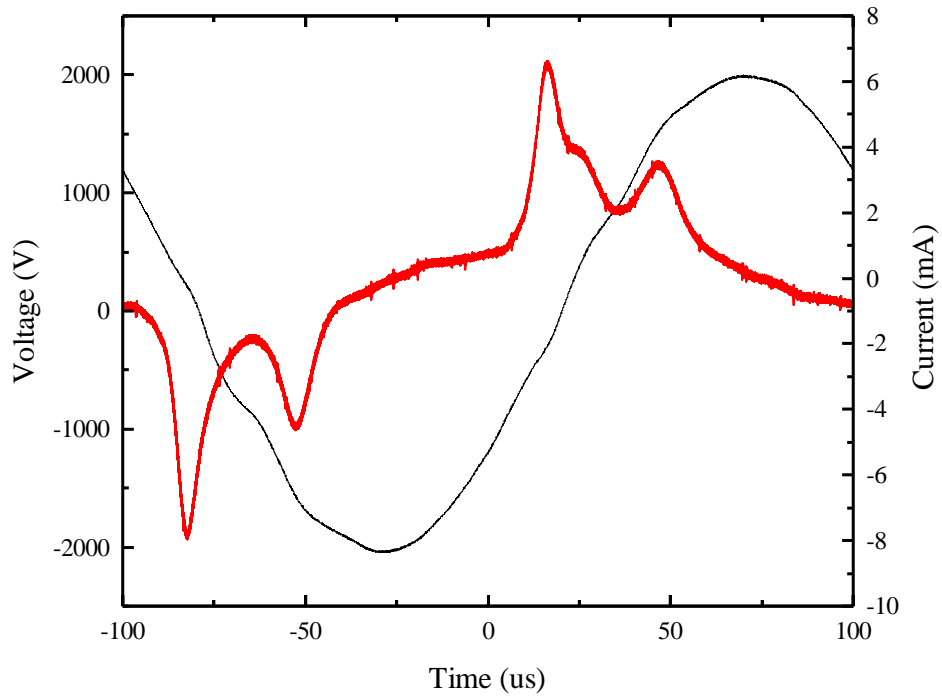


**Figure B.7** The current and voltage waveforms at 2 kV<sub>p</sub> with dried helium gas.

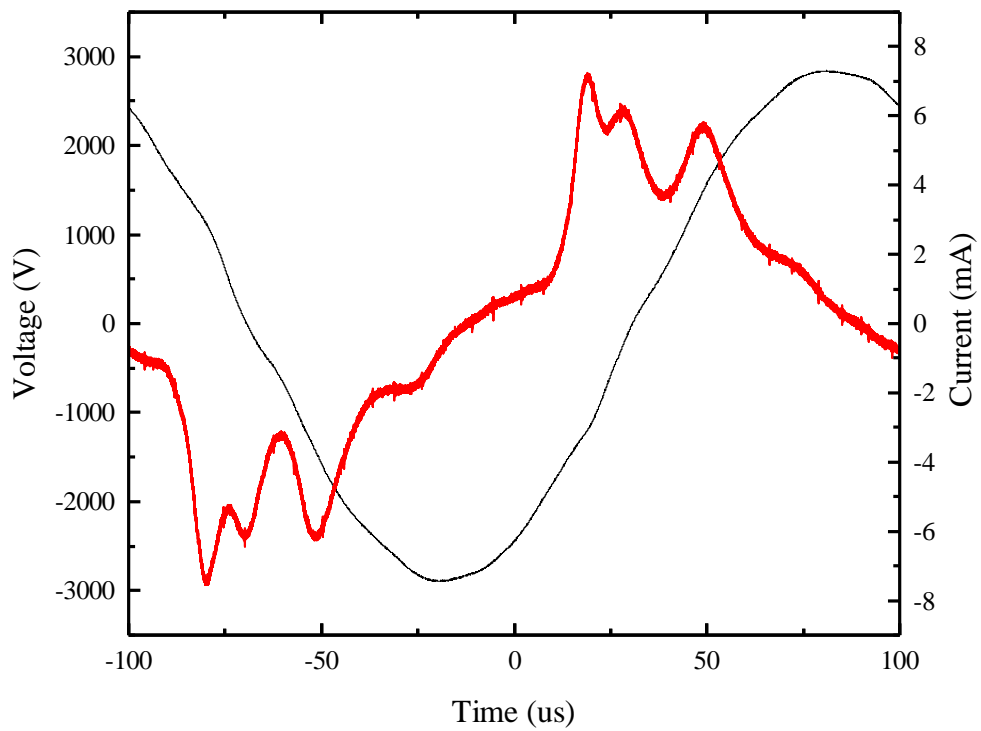
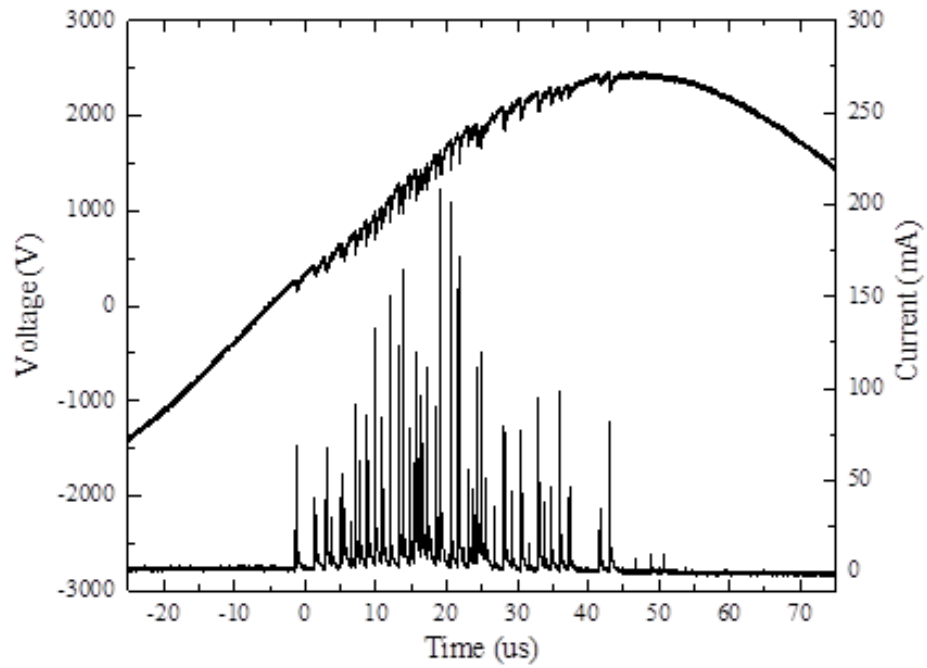
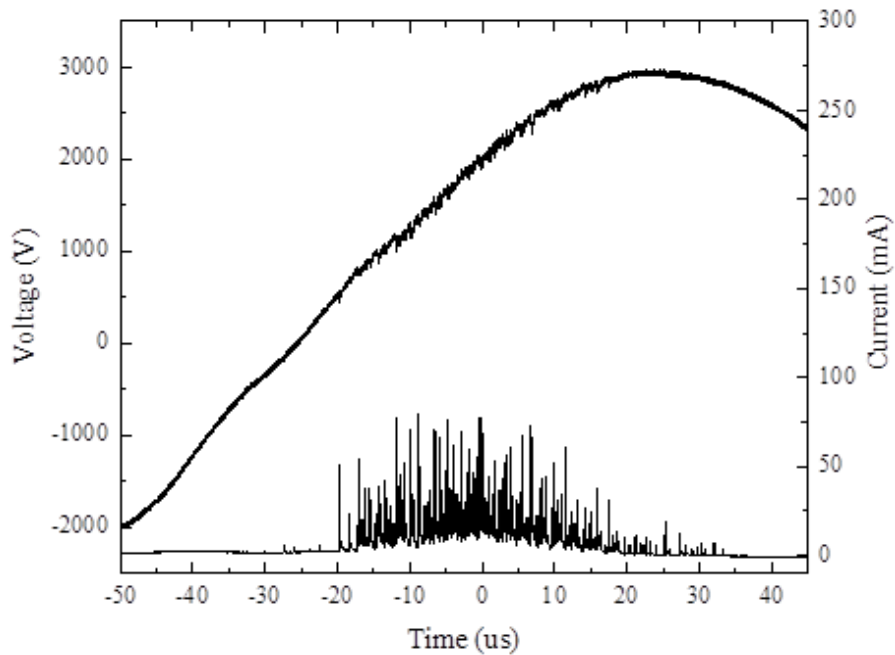


**Figure B.8** The current and voltage waveforms at 3 kV<sub>p</sub> with dried helium gas.

**C. The sampled quarter cycle waveform of voltage and current at different pressure.**



(a)



(b)

**Figure C.1** The example quarter cycle waveform of voltage and current at (a) 1 bar and (b) 1.6 bar. The dielectric barrier is 0.2 mm thick, and the gap length is 0.3 mm with 3 kV<sub>peak</sub> supply voltage.

**D. The Ozone Concentration and Lissajous Figure under Different Temperature with Air Input.**

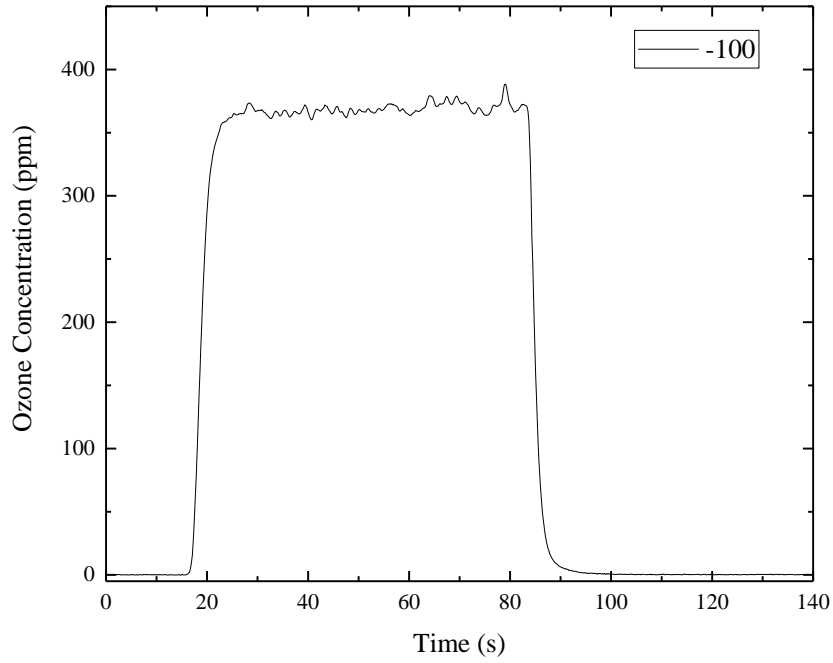


**Figure D.1 The ozone concentration at -100 °C with air input.**

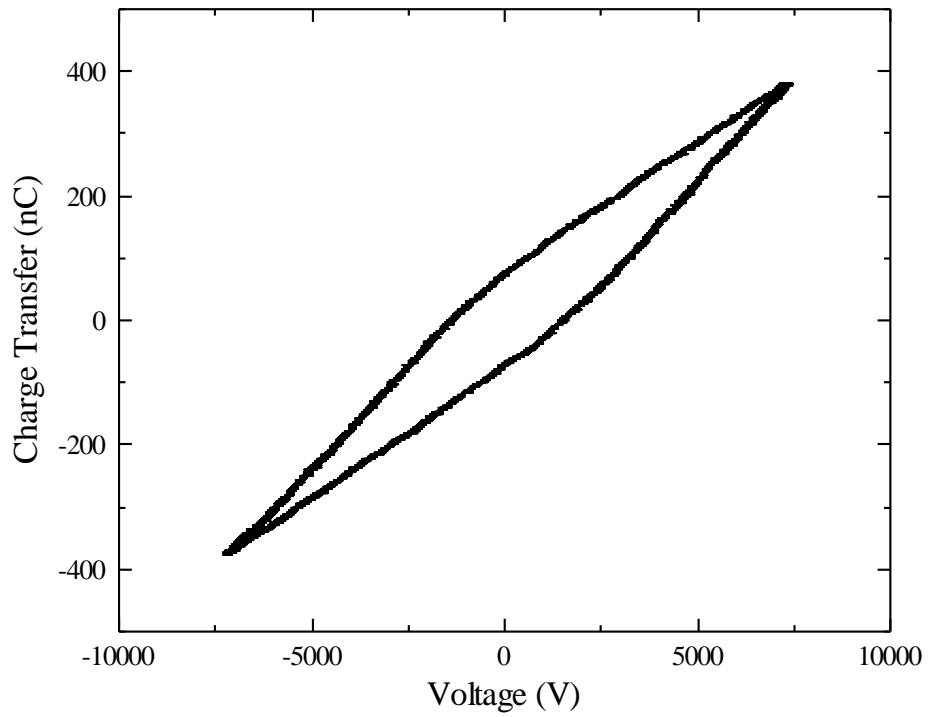


**Figure D.2 The Lissajous figure at -100 °C with air input.**

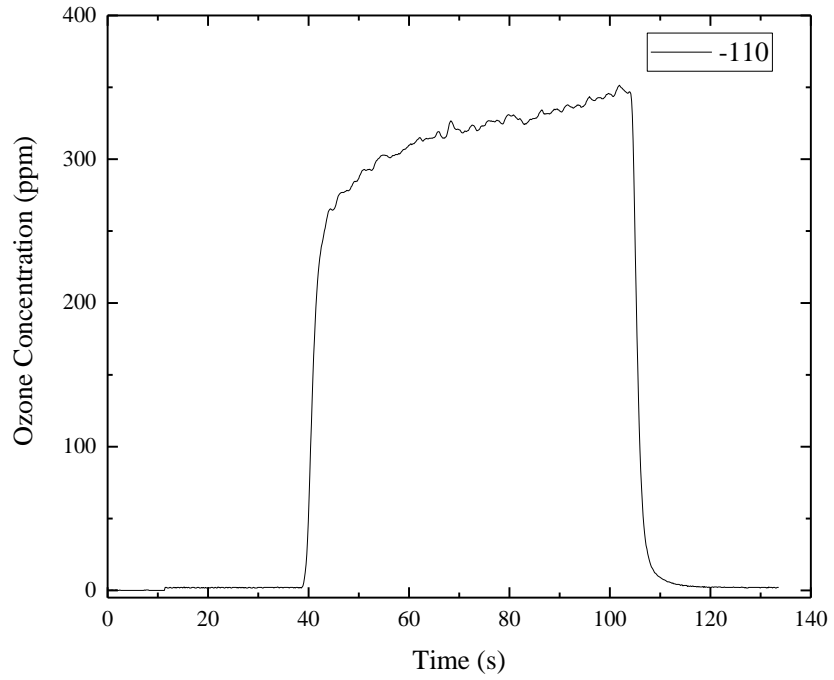


**Figure D.3** The ozone concentration at  $-110^{\circ}\text{C}$  with air input.

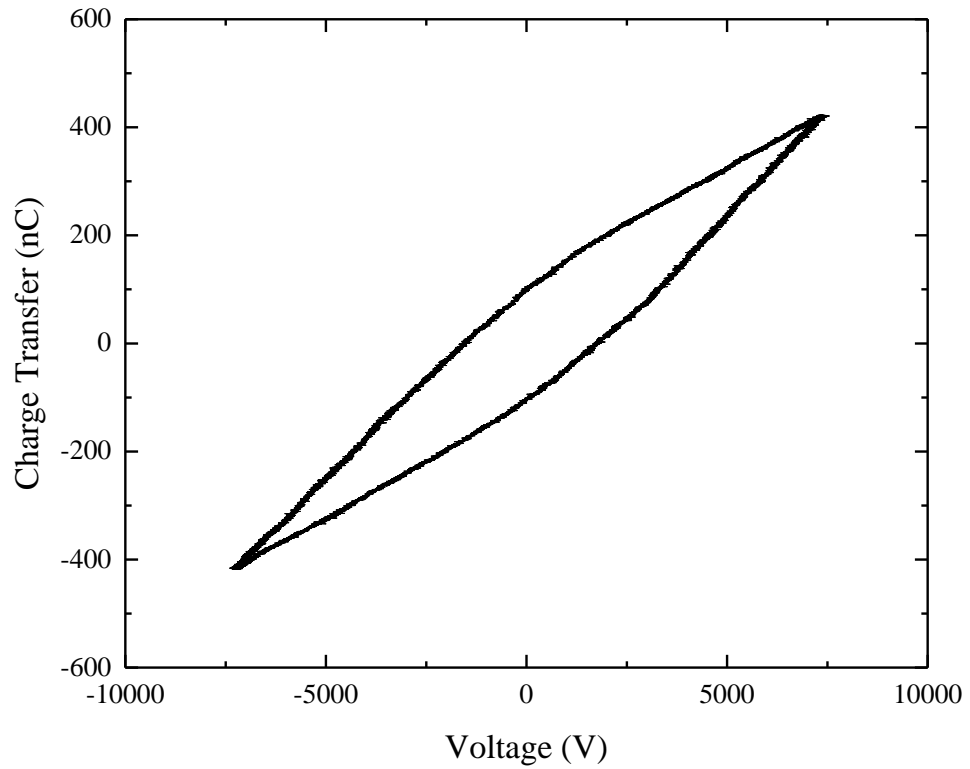


**Figure D.4** The Lissajous figure at  $-110^{\circ}\text{C}$  with air input.

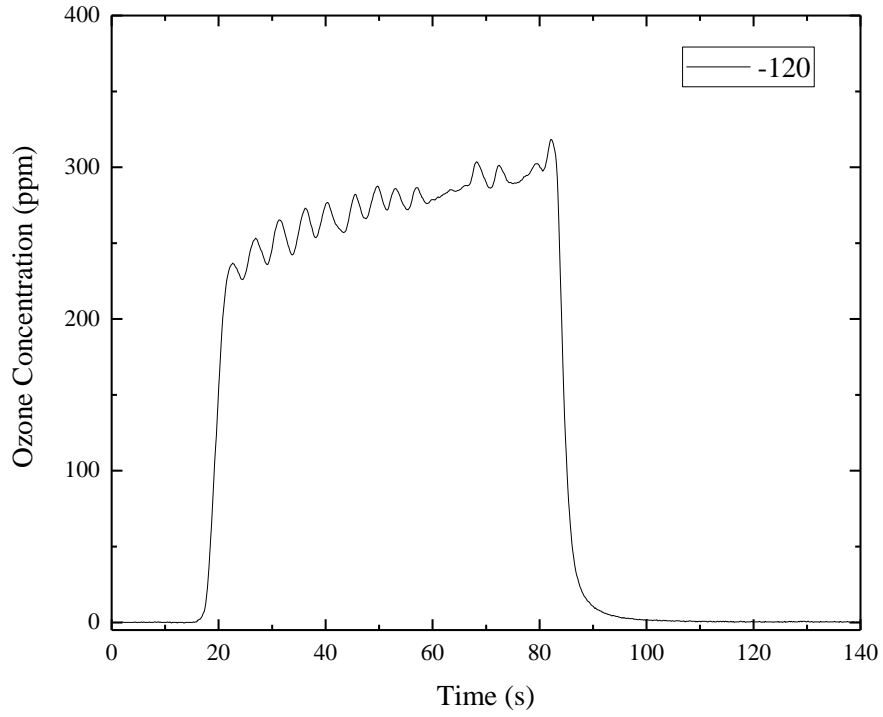


**Figure D.5** The ozone concentration at  $-120^{\circ}\text{C}$  with air input.

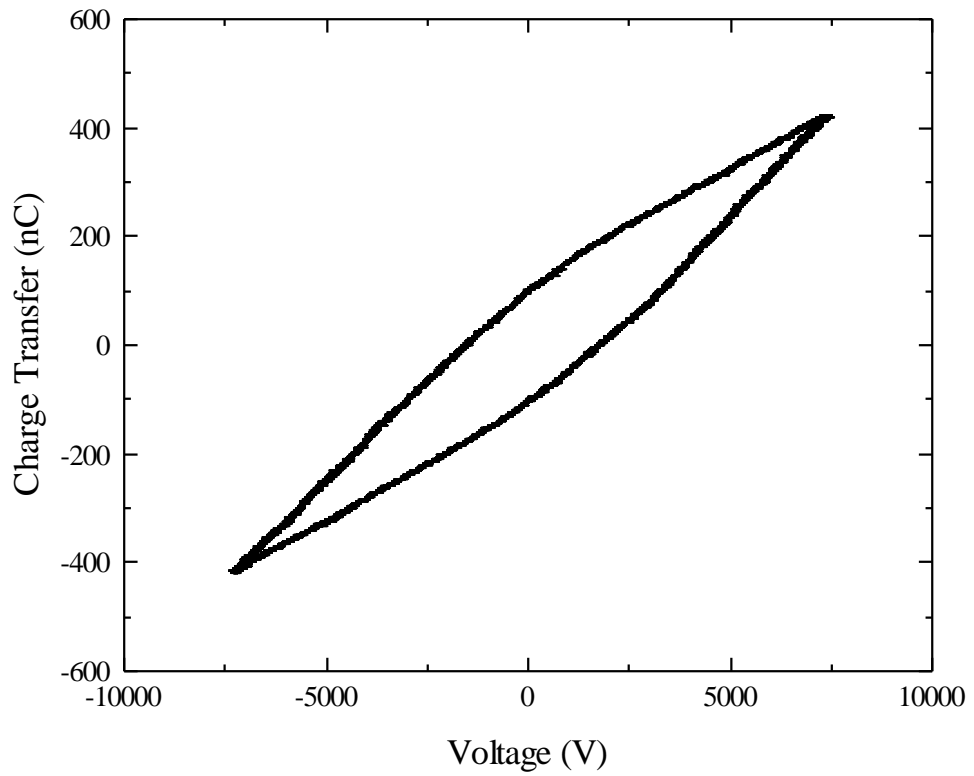


**Figure D.6** The Lissajous figure at  $-120^{\circ}\text{C}$  with air input.

**E. The Ozone Concentration and Lissajous Figure under Different Temperature with Oxygen Input.**

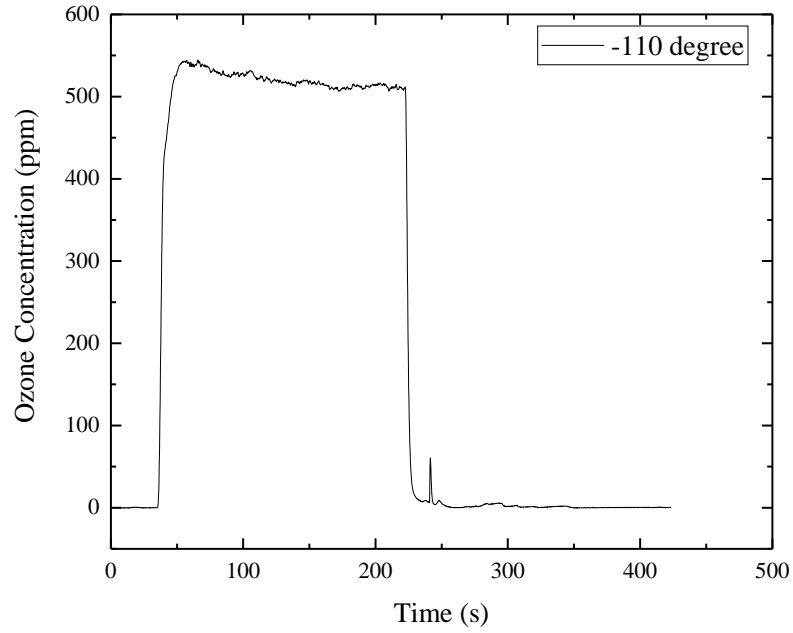


**Figure E.1** The ozone concentration at -110 °C with oxygen input.

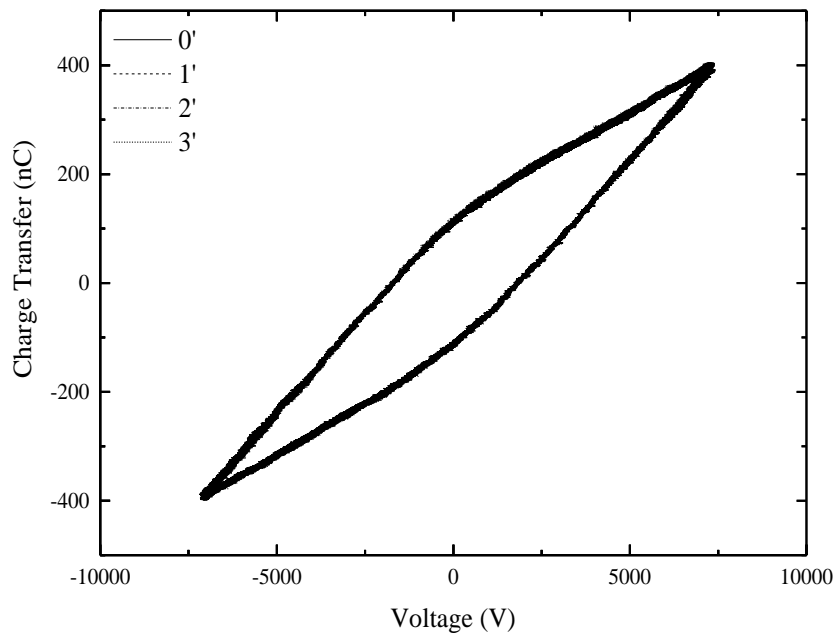


**Figure E.2** The Lissajous figure at -110 °C with oxygen input.

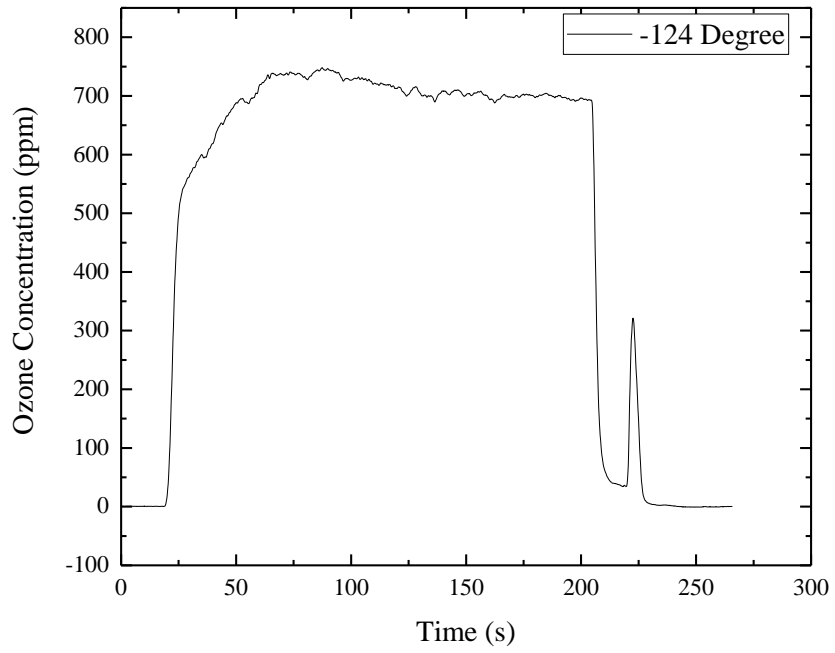


Figure E.3 The ozone concentration at -124 °C with oxygen input.

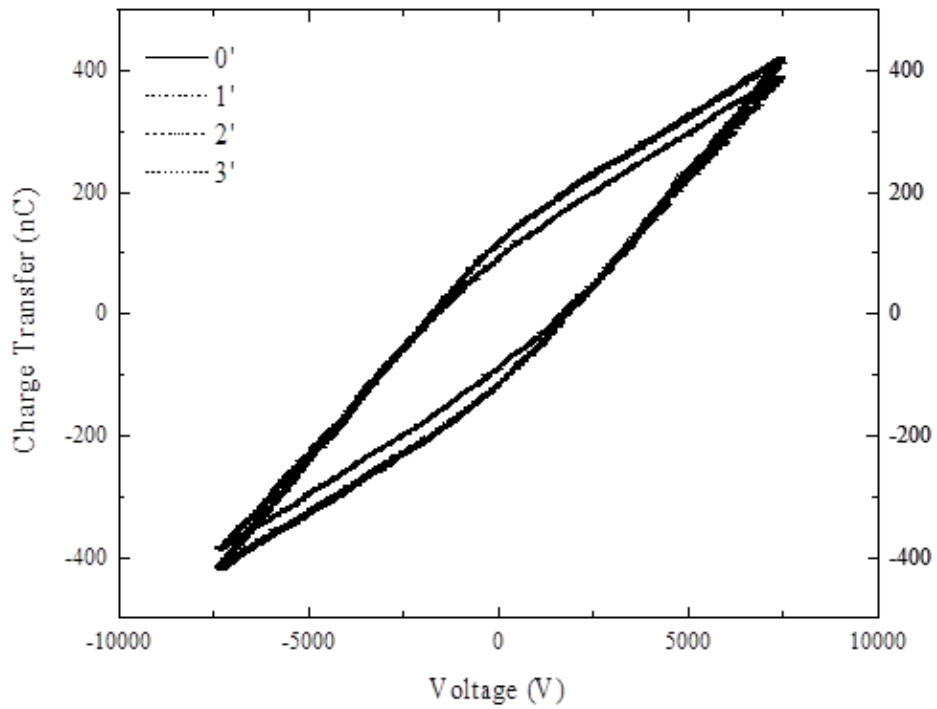
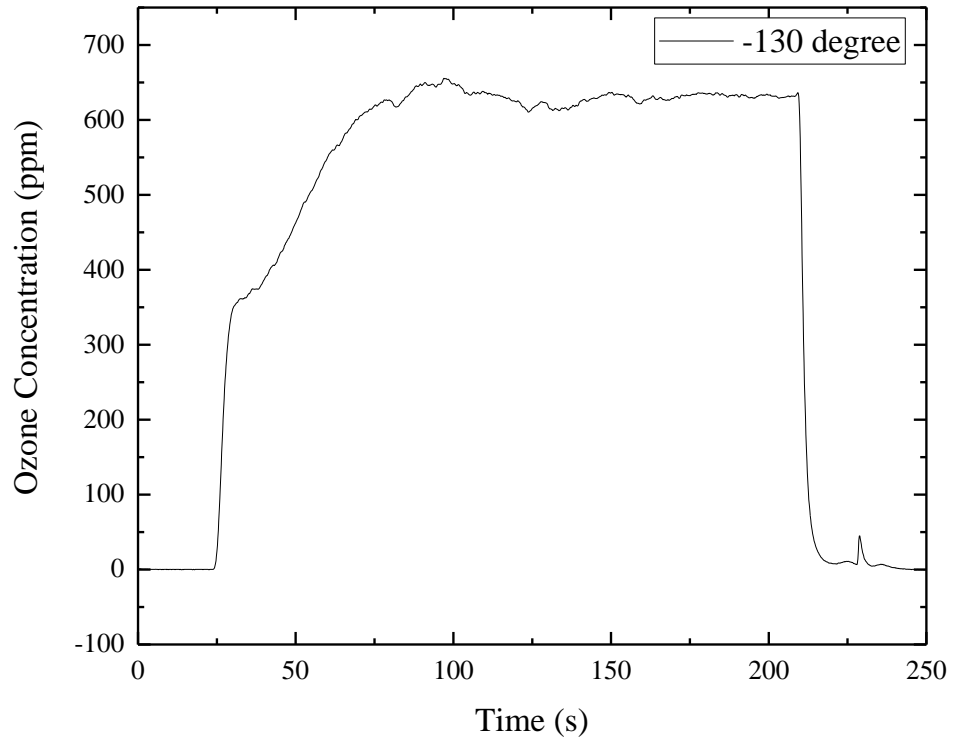
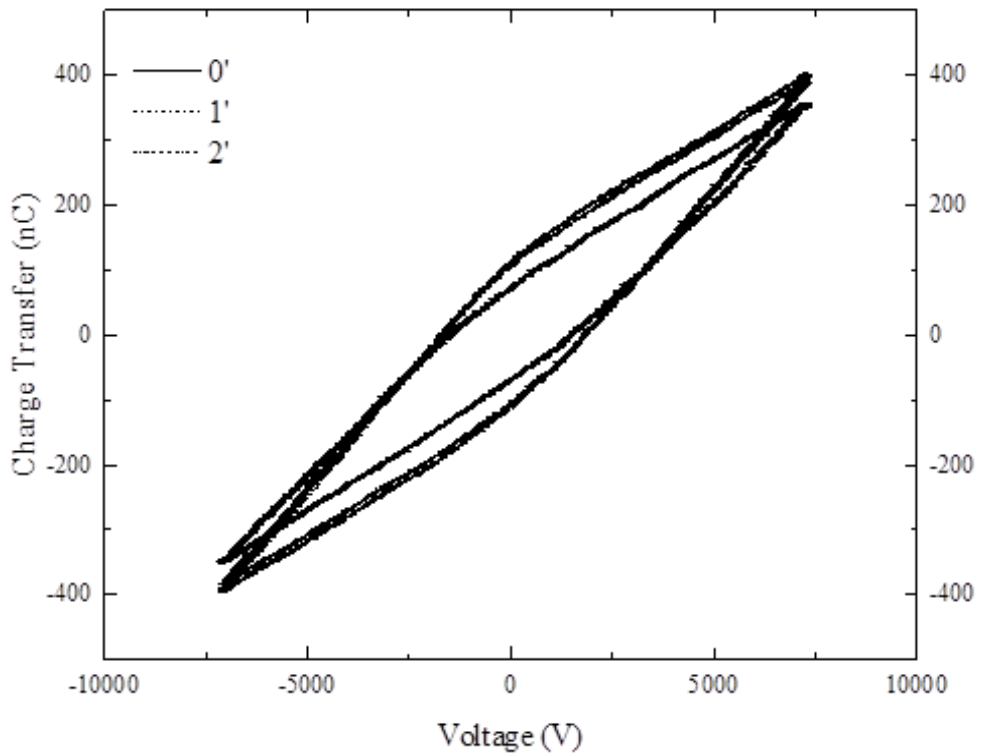


Figure E.4 The Lissajous figure at -124 °C with oxygen input.



**Figure E.5** The ozone concentration at -130 °C with oxygen input.



**Figure E.6** The Lissajous figure at -130 °C with oxygen input.

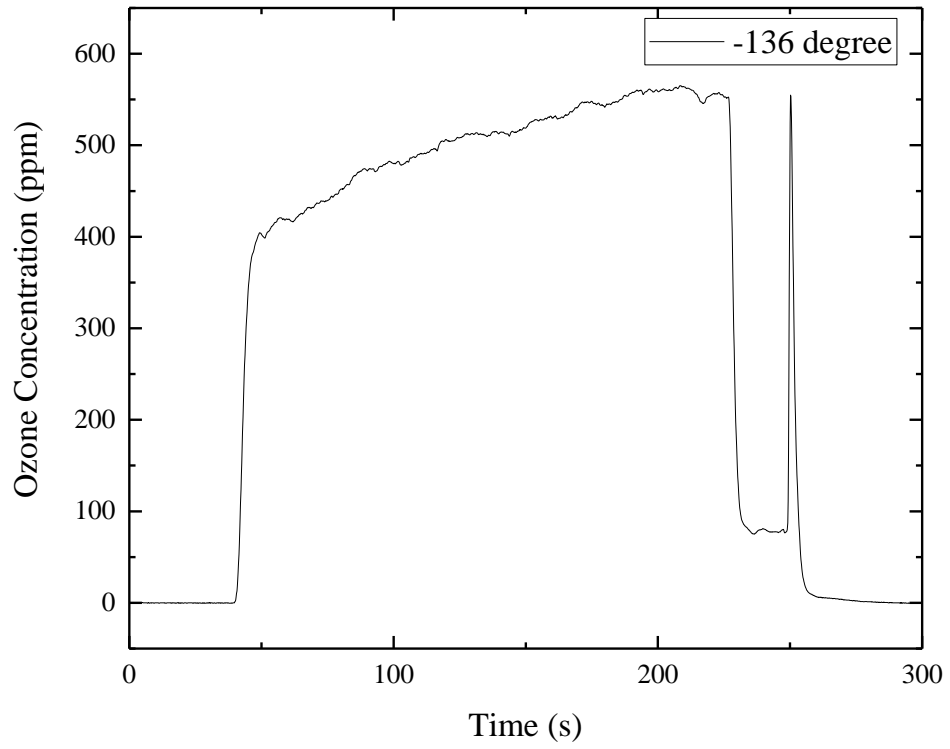


Figure E.7 The ozone concentration at -136 °C with oxygen input.

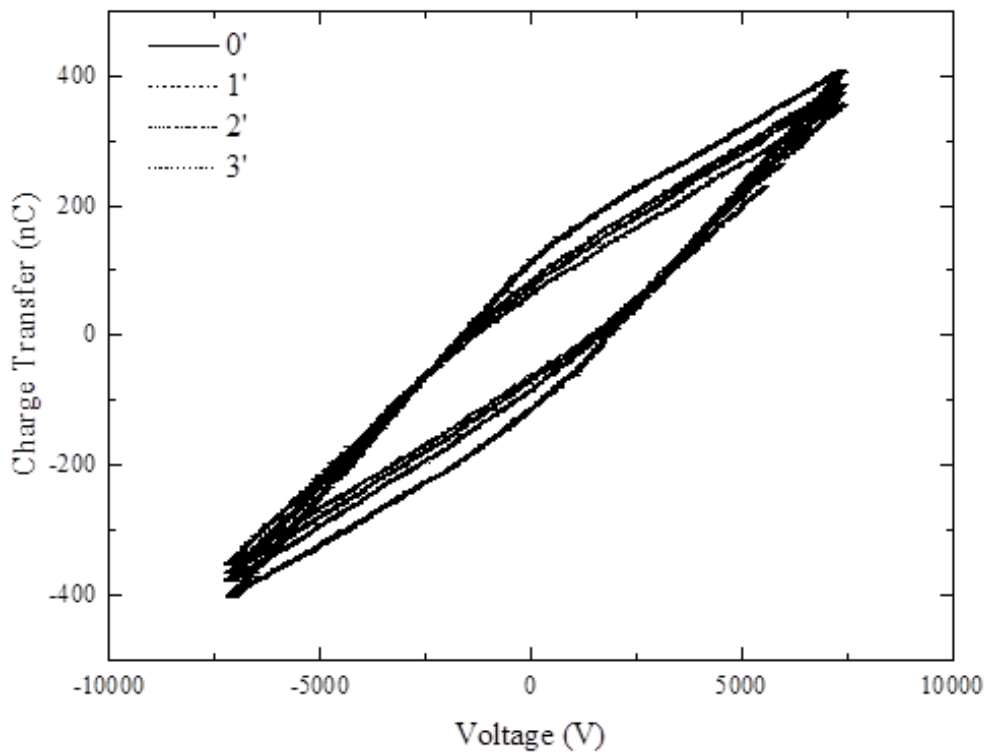
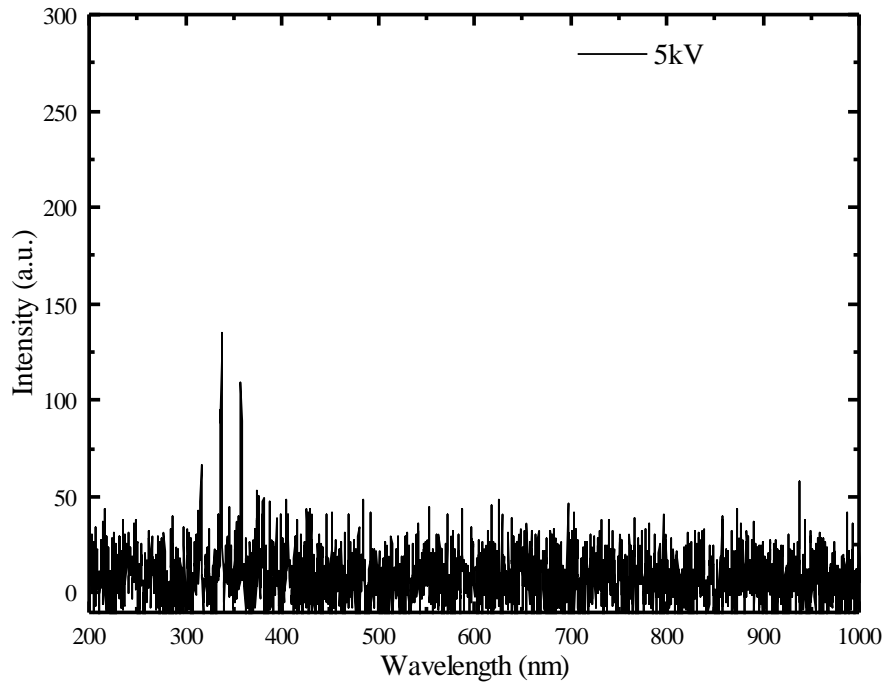
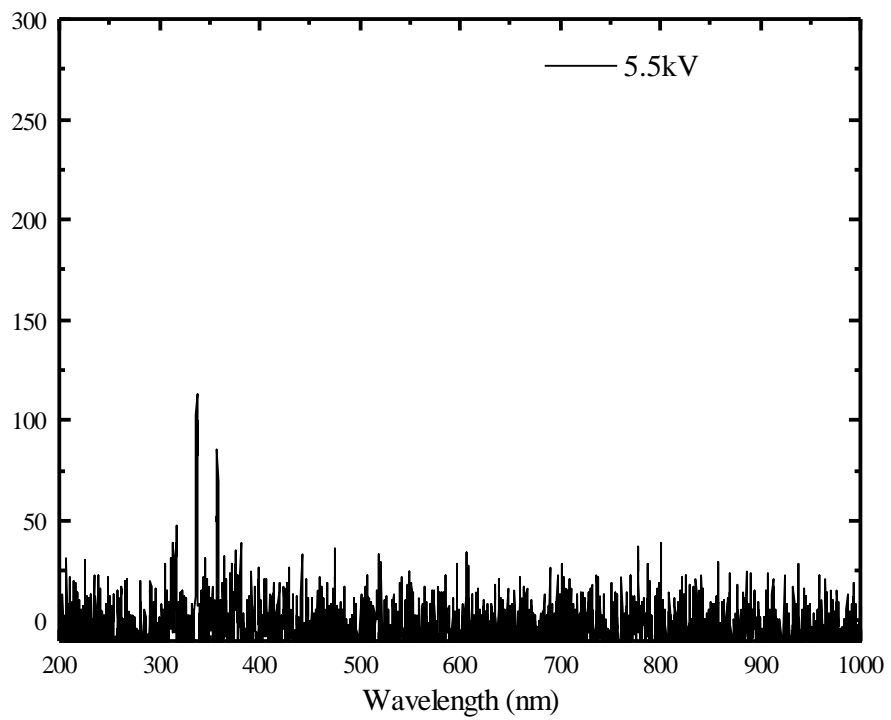


Figure E.8 The Lissajous figure at -136 °C with oxygen input.

**F. The spectra of atomic oxygen under different applied voltage.**



**Figure F.1** The spectra of the discharge gas at 5 kV<sub>p</sub>.



**Figure F.2** The spectra of the discharge gas at 5.5 kV<sub>p</sub>.

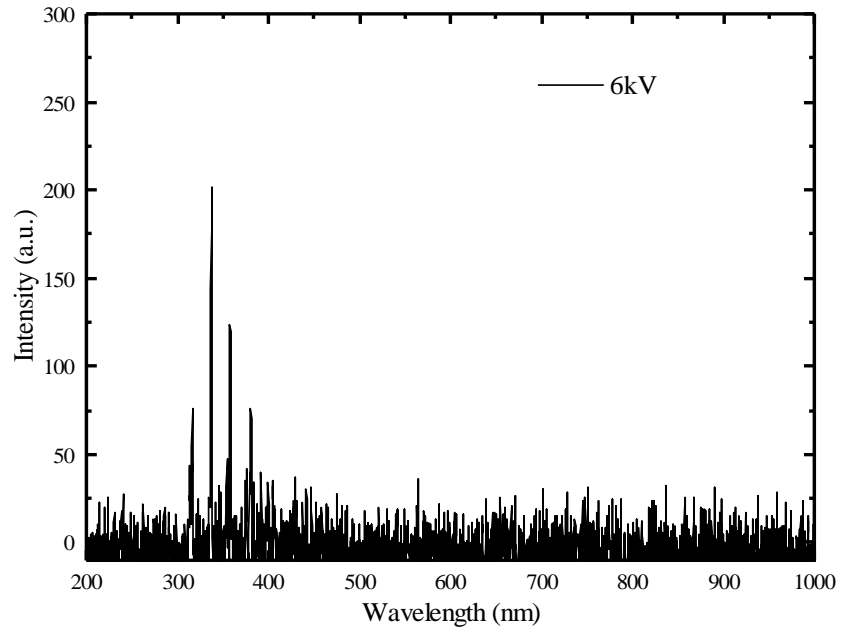


**Figure F.3** The spectra of the discharge gas at 6 kV<sub>p</sub>.

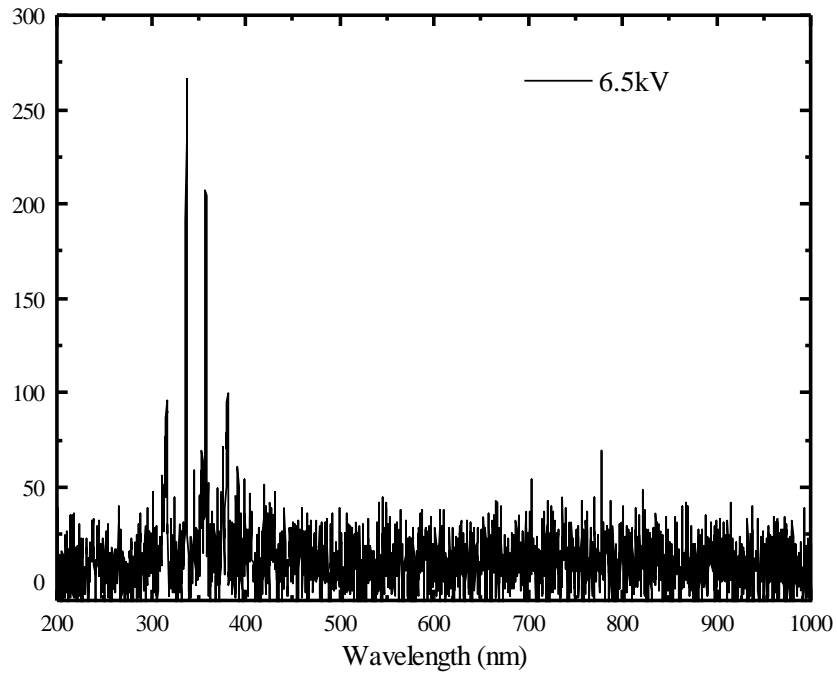


**Figure F.4** The spectra of the discharge gas at 6.5 kV<sub>p</sub>.

## 10 Reference

- [1] Tanaka, Takehiko, and Yonezo Morino. "Coriolis interaction and anharmonic potential function of ozone from the microwave spectra in the excited vibrational states." *Journal of Molecular Spectroscopy* 33.3 (1970): 538-551.
- [2] Mack, K.M. and Muentner, J.S., 1977. Stark and Zeeman properties of ozone from molecular beam spectroscopy. *The Journal of Chemical Physics*, 66(12), pp.5278-5283.
- [3] Craun, G.F. and Craun, G.F., DISINFECTANTS AND DISINFECTANT BY-PRODUCTS. *Toxicology*, 1, p.9.
- [4] Katzenelson, E., B. Kletter, and H. I. Shuval. "Inactivation kinetics of viruses and bacteria in water by use of ozone." *Journal (American Water Works Association)* (1974): 725-729
- [5] Vosmaer, A. 1916. *Ozone: Its Manufacture, Properties , and Uses*. Van Nostrand Publishers, New York.
- [6] Lowndes, M.R. 1985. Ozone and the (British) Consumer- Organoleptic Considerations. Proc. Intl. Conf.: The Role of Ozone in Water and Wastewater Treatment. Edited by R. Perry and A.E. McIntyre Selper Ltd., London (pp. 189-194).
- [7] Pascal, O. 1986. Ozone Disinfection in Drinking Water. Presented ad Workshop on Water and Wastewater. USEPA Water Engrg. Res. Lab., Cincinnati. Ohio (pp.63-84).
- [8] Deborde, M., Rabouan, S., Mazellier, P., Duguet, J.P. and Legube, B., 2008. Oxidation of bisphenol A by ozone in aqueous solution. *Water research*, 42(16), pp.4299-4308.
- [9] Bourbigot, M.M., 1989. Ozone disinfection in drinking water. *Journal of New England Water Works Association*, 103(1), pp.1-12.
- [10] Barry L. Loeb , Craig M. Thompson , Joseph Drago , Hirofumi Takahara & Sylvie Baig (2012) Worldwide Ozone Capacity for Treatment of Drinking Water and Wastewater: A Review, *Ozone: Science & Engineering*, 34:1, 64-77.
- [11] Loeb, B.L., Thompson, C.M., Drago, J., Takahara, H. and Baig, S., 2012. Worldwide ozone capacity for treatment of drinking water and wastewater: a review. *Ozone: Science & Engineering*, 34(1), pp.64-77.
- [12] Fujikawa, E.G., et al. 1989. Ozonation in America: An Evolution of Success. *Wtr. Engrn. Mgmt.*, Oct.: 20-24.
- [13] Robson, P.M. et al. 1990. Status of U.S. Drinking Water Treatment Ozonation Systems.
- [14] Am Water Works Res, F., Langlais, B., Reckhow, D.A. and Brink, D.R., 1991. *Ozone in water treatment: application and engineering*. CRC press.
- [15] Le Paulouë, J. and B. Langlais, "State of the Art of Ozonation in France", *Ozone Sci. Eng.*, 21(2):153-162 (1999)
- [16] Geering, F. 1987. Experiences With Ozone Treatment of Water in Switzerland. Proc. 8th Ozone World Congress. International Ozone Association. Zurich, Switzerland. (pp. B59-B75).

- [17] Geering, F. 1988. Experiences With Ozone Treatment of Water in Switzerland. *Ozone News*, 16:5:18-24.
- [18] Loeb, B.L., Thompson, C.M., Drago, J., Takahara, H. and Baig, S., 2012. Worldwide ozone capacity for treatment of drinking water and wastewater: a review. *Ozone: Science & Engineering*, 34(1), pp.64-77.
- [19] Takahara, H., Y. Kato, S. Nakayama, Y. Kobayashi, Y. Kudo, H. Tsuno, and I. Somiya, "Estimation of an Appropriate Ozonation System in Water Purification Plant", Proceedings of 19th Ozone World Congress, Tokyo, Japan, Paper 17–2 (2009).
- [20] Ishii, K., and K. Sato, "Current Situation and Future Estimation of Ozonation in Water Treatment in Japan", Proceedings of 18th Ozone World Congress, Las Vegas, NV, 652–667 (2003)
- [21] Skalska, K., Miller, J.S. and Ledakowicz, S., 2010. Trends in NO<sub>x</sub> abatement: a review. *Science of the total environment*, 408(19), pp.3976-3989.
- [22] Farman, J. C., B. G. Gardiner, and J. D. Shanklin. "Large losses of total ozone in Antarctica reveal seasonal ClO<sub>x</sub>/NO<sub>x</sub> interaction." (1985): 207-210.
- [23] Meichsner, Jurgen, et al., eds. Nonthermal plasma chemistry and physics. CRC Press, 2012.
- [24] Fu, Y. and Diwekar, U.M., 2004. Cost effective environmental control technology for utilities. *Advances in Environmental Research*, 8(2), pp.173-196.
- [25] Zhang, J., Zhang, R., Chen, X., Tong, M., Kang, W., Guo, S., Zhou, Y. and Lu, J., 2014. Simultaneous removal of NO and SO<sub>2</sub> from flue gas by ozone oxidation and NaOH absorption. *Industrial & Engineering Chemistry Research*, 53(15), pp.6450-6456.
- [26] Jakubiak, M.P., 2012. Pilot-scale studies on NO<sub>x</sub> removal from flue gas via NO ozonation and absorption into NaOH solution. *Chemical and Process Engineering*, 33(3), pp.345-358.
- [27] W. Siemens, Poggendorff's Ann. Phys. Chem., vol. 102, pp. 66-122, 1857.
- [28] Diaper, E. W. J. *Practical Aspects of Water and Wastewater Treatment of Ozone*. Crane Company, Cochrane Division, 1972.
- [29] Hosselet, L.M.L.F., 1973. Increased efficiency of ozone-production by electric discharges. *Electrochimica acta*, 18(12), pp.1033-1041.
- [30] Eliasson, B., M. Hirth, and U. Kogelschatz. "Ozone synthesis from oxygen in dielectric barrier discharges." *Journal of Physics D: Applied Physics* 20.11 (1987): 1421.
- [31] Becker, Kurt H., et al., eds. *Non-equilibrium air plasmas at atmospheric pressure*. CRC press, 2004.
- [32] Chang, J-S., Phil A. Lawless, and Toshiaki Yamamoto. "Corona discharge processes." *IEEE Transactions on plasma science* 19.6 (1991): 1152-1166.
- [33] Braun, D., and G. Pietsch. "On the efficiency of ozone generation." Proc. 10th Int. Symp. Plasma Chemistry (Bochum, Germany, 1991). 1991.
- [34] Boeuf, J. P. "Plasma display panels: physics, recent developments and key issues." *Journal of physics D: Applied physics* 36.6 (2003): R53.

- [35]Allan, Michael, et al. "Production of vibrationally autodetaching in low-energy electron impact on ozone." *Journal of Physics B: Atomic, Molecular and Optical Physics* 29.15 (1996): 3487.
- [36]Rangwala, S. A., et al. "Cross sections for the dissociative electron attachment to ozone." *Journal of Physics B: Atomic, Molecular and Optical Physics* 32.15 (1999): 3795.
- [37] Hammond, C. R. "CRC handbook of chemistry and physics." by *Lide DR, CRC Press, Boca Raton, FL* (1997): 4.
- [38] Cicman, P., et al. "Dissociative electron attachment to ozone at very low energies revisited." *International Journal of Mass Spectrometry* 260.1 (2007): 85-87.
- [39]Rideal, E. K. "Ozone, Constable and Co." *LTD: London* (1920).
- [40]W. S. Sease, "Supplementary Material, Short Course on Ozone Technology," The Center For Professional Advancement, Somerville, NJ, 1975.
- [41]Eliasson, B., M. Hirth, and U. Kogelschatz. "Ozone Formation in Dielectric Barrier Discharges in Oxygen." *Proc. 7th Intl. Symposium on Plasma Chemistry. Eindhoven.* 1985.
- [42]Jodzis, Sławomir, and Jan Petryk. "Gas temperature in an ozonizer. The computer modeling of an actual discharge system." *IEEE Transactions on Plasma Science* 39.11 (2011): 2120-2121.
- [43]Jodzis, Sławomir. "Temperature effects under ozone synthesis process conditions." *The European Physical Journal Applied Physics* 61.2 (2013): 24319.
- [44]Kitayama, J., and M. Kuzumoto. "Theoretical and experimental study on ozone generation characteristics of an oxygen-fed ozone generator in silent discharge." *Journal of Physics D: Applied Physics* 30.17 (1997): 2453.
- [45]Chang, Jen-Shih, and S. Masuda. "Mechanism of the ozone formations in a near liquid nitrogen temperature medium pressure glow discharge positive column." *Pure and Applied Chemistry* 60.5 (1988): 645-650.
- [46]Masuda, Senichi, et al. "Production of ozone by surface and glow discharge at cryogenic temperatures." *IEEE transactions on industry applications* 24.5 (1988): 928-933.
- [47]Salvermoser, Manfred, Daniel E. Murnick, and Ulrich Kogelschatz. "Influence of water vapor on photochemical ozone generation with efficient 172 nm xenon excimer lamps." *Ozone: Science and Engineering* 30.3 (2008): 228-237.
- [48]Pure oxygen datasheet from BOC: <http://www.boconline.co.uk/en/products-and-supply/speciality-gas/pure-gases/pure-oxygen/pure-oxygen.html>
- [49]Allicat Mass Flow meter Model M-10SLPM-D  
<http://www.alicat.com/products/mass-flow-meters-and-controllers/mass-flow-meters/>
- [50]Allicat Pressure Gauge Model P-2 Bar- D  
<http://www.alicat.com/products/pressure-controllers/digital-pressure-vacuum-transducers-gauges/>
- [51]Easidew Hygrometer <http://www.kahn.com/hygrometers/manuals/easidewonlinemanual.pdf>
- [52]Pacific Power Instrument 112 AMX power supply datasheet  
[https://pacificpower.com/Resources/Documents/112AMX\\_Datasheet.pdf](https://pacificpower.com/Resources/Documents/112AMX_Datasheet.pdf)

- [53] Ashpis, D. E., M. C. Laun, and E. L. Griebeler. "Progress toward accurate measurements of power consumptions of DBD plasma actuators 50th AIAA Aerospace Sciences Meeting Including the New Horizons Forum and Aerospace Exposition, art. no." (2012).
- [54] Ackerman, Marcel. "Ultraviolet solar radiation related to mesospheric processes." *Mesospheric models and related experiments*. Springer Netherlands, 1971. 149-159.
- [55] Anderson, Stuart M., Peter Hupalo, and Konrad Mauersberger. "Ozone absorption cross section measurements in the Wulf bands." *Geophysical research letters* 20.15 (1993): 1579-1582.
- [56] Kogelschatz, Ulrich. "Dielectric-barrier discharges: their history, discharge physics, and industrial applications." *Plasma chemistry and plasma processing* 23.1 (2003): 1-46.
- [57] A. V. Pipa, J. Koskulics, R. Brandenburg, and T. Hoder, "The simplest equivalent circuit of a pulsed dielectric barrier discharge and the determination of the gas gap charge transfer," *Rev Sci Instrum*, vol. 83, p. 115112, Nov 2012
- [58] Becker, Kurt H., et al., eds. *Non-equilibrium air plasmas at atmospheric pressure*. CRC press, 2004.
- [59] Massines, F., Rabehi, A., Decomps, P., Gadri, R.B., Ségur, P. and Mayoux, C., 1998. Experimental and theoretical study of a glow discharge at atmospheric pressure controlled by dielectric barrier. *Journal of Applied Physics*, 83(6), pp.2950-2957.
- [60] Drake, Gordon WF. "Theory of Relativistic Magnetic Dipole Transitions: Lifetime of the Metastable  $2S\ 3S$  State of the Heliumlike Ions." *Physical Review A* 3.3 (1971): 908.
- [61] Van Dyck Jr, Robert S., Charles E. Johnson, and Howard A. Shugart. "Radiative Lifetime of the  $2S\ 0\ 1$  Metastable State of Helium." *Physical Review A* 4.4 (1971): 1327.
- [62] Kramida, A., Ralchenko, Yu., Reader, J., and NIST ASD Team (2014). NIST Atomic Spectra Database (ver. 5.2), [Online]. Available: <http://physics.nist.gov/asd> [2017, May 18]. National Institute of Standards and Technology, Gaithersburg, MD.
- [63] Phelps, A. V., and J. P. Molnar. "Lifetimes of metastable states of noble gases." *Physical Review* 89.6 (1953): 1202
- [64] Mangolini, L., et al. "Effects of current limitation through the dielectric in atmospheric pressure glows in helium." *Journal of Physics D: Applied Physics* 37.7 (2004): 1021.
- [65] Boeuf, J. P. "Plasma display panels: physics, recent developments and key issues." *Journal of physics D: Applied physics* 36.6 (2003): R53.
- [66] Kramida, A., Ralchenko, Yu., Reader, J., and NIST ASD Team (2015). NIST Atomic Spectra Database (ver. 5.3), [Online]. Available: <http://physics.nist.gov/asd> [2017, June 28]. National Institute of Standards and Technology, Gaithersburg, MD.
- [67] Kanazawa, S., et al. "Stable glow plasma at atmospheric pressure." *Journal of Physics D: Applied Physics* 21.5 (1988): 838.
- [68] Okazaki, Satiko, et al. "Appearance of stable glow discharge in air, argon, oxygen and nitrogen at atmospheric pressure using a 50 Hz source." *Journal of Physics D: Applied Physics* 26.5 (1993): 889.

- [ 69 ]Kogoma, Masuhiro, and Satiko Okazaki. "Raising of ozone formation efficiency in a homogeneous glow discharge plasma at atmospheric pressure." *Journal of Physics D: Applied Physics* 27.9 (1994): 1985.
- [70]Osawa, N., et al. "Generation of Low Frequency Atmospheric-Pressure Uniform Discharge in Air." *Proc of the 19th Int. Conf. Plasma Chemistry (ISPC-19) P. Vol. 1.* 2009.
- [71]Nakai, Y., Takashi, A., Osawa, N., Yoshioka, Y., & Hanaoka, R. (2011). Comparison of ozone generation characteristics by filamentary discharge mode and townsend discharge mode of dielectric barrier discharge in oxygen. *Journal of Chemistry and Chemical Engineering*, 5(12).
- [ 72 ] Kogelschatz, U., 2002. Filamentary, patterned, and diffuse barrier discharges. *IEEE Transactions on plasma science*, 30(4), pp.1400-1408.
- [73]U. Kogelschatz, "Advanced ozone generation," *Process Technologies for Water Treatment*, pp. 87-120, 1988.Eliasson, Baldur, and Ulrich Kogelschatz. "Nonequilibrium volume plasma chemical processing." *IEEE transactions on plasma science* 19.6 (1991): 1063-1077.
- [ 74 ] Eliasson, Baldur, and Ulrich Kogelschatz. "Nonequilibrium volume plasma chemical processing." *IEEE transactions on plasma science* 19.6 (1991): 1063-1077.
- []75 U. Kogelschatz, B. Eliasson, and W. Egli, "Dielectric-barrier discharges. Principle and applications," *Journal de Physique IV (Colloque)*, vol. 7, pp. 47-66, 1997.
- [ 76 ] Salvermoser, M. J., U. Kogelschatz, and D. E. Murnick. "Influence of humidity on photochemical ozone generation with 172 nm xenon excimer lamps." *The European Physical Journal Applied Physics* 47.2 (2009): 22812.
- [77]A. Fridman and L. A. Kennedy, *Plasma Physics and Engineering*. United States: Taylor and Francis Group, 2011.
- [78] I. Radu, R. Bartnikas, and M. R. Wertheimer, "Diagnostics and modelling of noble gas atmospheric pressure dielectric barrier discharges in homogeneous or diverging electric fields," *Journal of Physics D: Applied Physics*, vol. 38, pp. 539-546, 2005
- [79] H. C. Kim, F. Iza, S. S. Yang, M. Radmilović-Radjenović, and J. K. Lee, "Particle and fluid simulations of low-temperature plasma discharges: benchmarks and kinetic effects," *Journal of Physics D: Applied Physics*, vol. 38, pp. R283-R301, 2005.
- [80]Itikawa, Yukikazu. "Cross sections for electron collisions with oxygen molecules." *Journal of Physical and Chemical Reference Data* 38.1 (2009): 1-20.
- [81]Penkin, N. P., V. V. Smirnov, and O. D. Tsygir. "Investigation of the electrokinetic properties and of the dissociation of O<sub>2</sub> molecules in an oxygen discharge." *Zhurnal Tekhnicheskoi Fiziki* 52 (1982): 1542-1548.
- [82]Eliasson, B., and U. Kogelschatz. "Electron impact dissociation in oxygen." *Journal of Physics B: Atomic and Molecular Physics* 19.8 (1986): 1241.
- [83]Braun, Dieter, and G. Pietsch. "Microdischarges in air-fed ozonizers." *Journal of Physics D: Applied Physics* 24.4 (1991): 564.

- [84] J. Kitayama and M. Kuzumoto, "Theoretical and experimental study on ozone generation characteristics of an oxygen-fed ozone generator in silent discharge," *Journal of Physics D: Applied Physics*, vol. 30, p. 2453, 1997.
- [85] S. Yagi and M. Tanaka, "Mechanism of ozone generation in air-fed ozonisers," *J. Phys. D: Appl. Phys.*, vol. 20, pp. 1421-37, 1979.
- [86] Park, Seung-Lok, et al. "Effective ozone generation utilizing a meshed-plate electrode in a dielectric-barrier discharge type ozone generator." *Journal of Electrostatics* 64.5 (2006): 275-282.
- [ 87 ]T. Namihira, K. Shinozaki, S. Katsuki, R. Hackam, H. Akiyama, and T. Sakugawa, "Characteristics of ozonizer using pulsed power," in *IEEE Pulsed Power & Plasma Science Conference*, pp. 1090-1093, 2001.
- [88]C. Monge, R. Peyrous, and B. Held, "Optimization of a corona wire-to-cylinder ozone generator. Comparison with economical criteria. part I: Oxygen.," *Ozone Science & Engineering*, vol. 19, pp. 533-547, 1997.
- [89] Takaki, K., Hatanaka, Y., Arima, K., Mukaigawa, S. and Fujiwara, T., 2008. Influence of electrode configuration on ozone synthesis and microdischarge property in dielectric barrier discharge test cell. *Vacuum*, 83(1), pp.128-132.
- [90]HERSH, CHARLES K., ABRAHAM W. BERGER, and JR Callaway Brown. "Physical Properties of Liquid Ozone-Oxygen Mixtures: Density, Viscosity, and Surface Tension." 1959. 22-27.
- [91]HERSH, CHARLES K., ABRAHAM W. BERGER, and JR Callaway Brown. "Physical Properties of Liquid Ozone-Oxygen Mixtures: Density, Viscosity, and Surface Tension." 1959. 22-27.
- [92] "Thermal Expansion". Western Washington University. Archived from the original on 2009-04-17
- [93] Tipler, P.A. and Mosca, G., 2007. *Physics for scientists and engineers*. Macmillan.
- [94] Serway, R. and Jewett, J., 2012. *Principles of physics: a calculus-based text* (Vol. 1). Nelson Education.
- [95] Shi, L. and Danielewicz, P., 2000. Effect of cluster formation on isospin asymmetry in the liquid-gas phase transition region. *EPL (Europhysics Letters)*, 51(1), p.34.
- [96] Becker, Kurt H., et al., eds. *Non-equilibrium air plasmas at atmospheric pressure*. CRC press, 2004.
- [97] Braun, D., and G. Pietsch. "On the efficiency of ozone generation." *Proc. 10th Int. Symp. Plasma Chemistry (Bochum, Germany, 1991)*. 1991.
- [98]Yagi, S., and M. Tanaka. "Mechanism of ozone generation in air-fed ozonisers." *Journal of Physics D: Applied Physics* 12.9 (1979): 1509.
- [ 99 ]Eliasson, B., and U. Kogelschatz. "N<sub>2</sub>O formation in ozonizers." *Journal de chimie physique* 83.4 (1986): 279-282.

- [100]Gibalov, V. I., V. G. Samoilovich, and M. Wronski. "Electrosynthesis of nitrogen oxides and ozone in ozonizer." *Proc. 7th Int. Symp. on Plasma Chem. (ISPC-7)*. 1985.
- [101]Eliasson, B., 1986. Basic data for modelling of electrical discharges in gases: oxygen. *Asea Brown Boveri Corporate Research Report*, pp.KLR-86.
- [102] *Encyclopedia Britannica*, 9th ed. vol. XVIII (ORN-PHT). New York: Charles Scribner's Sons, 1885.